Microlenses

Edited by

Hongrui Jiang

Printed Edition of the Special Issue Published in *Micromachines*

www.mdpi.com/journal/micromachines

Hongrui Jiang (Ed.)

Microlenses

This book is a reprint of the special issue that appeared in the online open access journal *Micromachines* (ISSN 2072-666X) in 2014 (available at:
http://www.mdpi.com/journal/micromachines/special_issues/microlenses).

Guest Editor
Hongrui Jiang
Department of Electrical and Computer Engineering
University of Wisconsin – Madison
3440 Engineering Hall, 1415 Engineering Drive
Madison, WI 53706
USA

Editorial Office
MDPI AG
Klybeckstrasse 64
Basel, Switzerland

Publisher
Shu-Kun Lin

Assistant Editor
Lang Zhou

1. Edition 2015

MDPI • Basel • Beijing • Wuhan

ISBN 978-3-03842-051-4

Table of Contents

List of Contributors

Bader Aldalali: Department of Electrical and Computer Engineering, University of Wisconsin-Madison, Madison, WI 53707, USA; Department of Electrical Engineering, Kuwait University, Khaldiya 13060, Kuwait

Andreas Bräuer: Fraunhofer Institute for Applied Optics and Precision Engineering, Albert-Einstein-Str. 7, D-07745 Jena, Germany

Andreas Brückner: Fraunhofer Institute for Applied Optics and Precision Engineering, Albert-Einstein-Str. 7, D-07745 Jena, Germany

Patrizio Candeloro: Department of Experimental and Clinical Medicine, University Magna Graecia of Catanzaro, 88100 Catanzaro, Italy

Chia-Ming Chang: Department of Photonics, National Chiao Tung University, Hsinchu 30010, Taiwan

Hung-Shan Chen: Department of Photonics, National Chiao Tung University, Hsinchu 30010, Taiwan

Michael Chen: Department of Photonics, National Chiao Tung University, Hsinchu 30010, Taiwan

Nikos Chronis: Macromolecular Science and Engineering, University of Michigan, Ann Arbor, MI 48109, USA; Department of Mechanical Engineering, University of Michigan, Ann Arbor, MI 48109, USA; Department of Biomedical Engineering, University of Michigan, Ann Arbor, MI 48109, USA

Maria Laura Coluccio: Department of Experimental and Clinical Medicine, University Magna Graecia of Catanzaro, 88100 Catanzaro, Italy

Peter Dannberg: Fraunhofer Institute for Applied Optics and Precision Engineering, Albert-Einstein-Str. 7, D-07745 Jena, Germany

Marc Phillipe Yves Desmulliez: Earl Mountbatten Building, School of Engineering & Physical Sciences, Research Institute of Sensors, Signals and Systems, MicroSystems Engineering Centre (MISEC), Heriot-Watt University, Edinburgh EH14 4AS, Scotland, UK

Enzo Di Fabrizio: Department of Experimental and Clinical Medicine, University Magna Graecia of Catanzaro, 88100 Catanzaro, Italy; Department of Physical Sciences and Engineering, King Abdullah University of Science and Technology (KAUST), Thuwal 23955-6900, Kingdom of Saudi Arabia

Jayer Fernandes: Department of Electrical and Computer Engineering, University of Wisconsin-Madison, Madison, WI 53707, USA

Francesco Gentile: Istituto Italiano di Tecnologia, 16163 Genova, Italy; Department of Experimental and Clinical Medicine, University Magna Graecia of Catanzaro, 88100 Catanzaro, Italy

Mostafa Ghannad-Rezaie: Department of Biomedical Engineering, University of Michigan, Ann Arbor, MI 48109, USA

Mayurachat Ning Gulari: Macromolecular Science and Engineering, University of Michigan, Ann Arbor, MI 48109, USA

Chi-Chieh Huang: Department of Electrical and Computer Engineering, University of Wisconsin-Madison, Madison, WI 53706, USA

Hongrui Jiang: Department of Electrical and Computer Engineering, University of Wisconsin-Madison, Madison, WI 53707, USA; McPherson Eye Research Institute, University of Wisconsin-Madison, Madison, WI 53706 USA; Materials Science Program, University of Wisconsin-Madison, Madison, WI 53706, USA; Department of Biomedical Engineering, University of Wisconsin-Madison, Madison, WI 53706, USA

Aditi Kanhere: Department of Electrical and Computer Engineering, University of Wisconsin-Madison, Madison, WI 53707, USA

Chenhui Li: Department of Electrical and Computer Engineering, University of Wisconsin-Madison, Madison, WI 53707, USA

Yan Li: National Engineering Lab for TFT-LCD Materials and Technologies, Department of Electronic Engineering, Shanghai Jiao Tong University, Shanghai 200240, China

Tania Limongi: Department of Physical Sciences and Engineering, King Abdullah University of Science and Technology (KAUST), Thuwal 23955-6900, Kingdom of Saudi Arabia

Yi-Hsin Lin: Department of Photonics, National Chiao Tung University, Hsinchu 30010, Taiwan

Chao Liu: School of Electronics and Information Engineering, Sichuan University, Chengdu 610065, China

Yifan Liu: CREOL, The College of Optics and Photonics, University of Central Florida, 4000 Central Florida Blvd, Orlando, FL 32816, USA

Andre Matthes: Fraunhofer Institute for Applied Optics and Precision Engineering, Albert-Einstein-Str. 7, D-07745 Jena, Germany

Mazher-Iqbal Mohammed: Earl Mountbatten Building, School of Engineering & Physical Sciences, Research Institute of Sensors, Signals and Systems, MicroSystems Engineering Centre (MISEC), Heriot-Watt University, Edinburgh EH14 4AS, Scotland, UK

Gerardo Perozziello: Department of Experimental and Clinical Medicine, University Magna Graecia of Catanzaro, 88100 Catanzaro, Italy

Hongwen Ren: Department of Polymer-Nano Science and Technology, Chonbuk National University, Jeonju, Jeonbuk 561-756, Korea

Peter Schreiber: Fraunhofer Institute for Applied Optics and Precision Engineering, Albert-Einstein-Str. 7, D-07745 Jena, Germany

Jie Sun: CREOL, The College of Optics and Photonics, University of Central Florida, 4000 Central Florida Blvd, Orlando, FL 32816, USA

Anurag Tripathi: Department of Mechanical Engineering, University of Michigan, Ann Arbor, MI 48109, USA

Ming-Huan Wang: School of Electronics and Information Engineering, Sichuan University, Chengdu 610065, China

Qiong-Hua Wang: School of Electronics and Information Engineering, Sichuan University, Chengdu 610065, China

Yu-Jen Wang: Department of Photonics, National Chiao Tung University, Hsinchu 30010, Taiwan

Frank Wippermann: Fraunhofer Institute for Applied Optics and Precision Engineering, Albert-Einstein-Str. 7, D-07745 Jena, Germany

Shin-Tson Wu: CREOL, The College of Optics and Photonics, University of Central Florida, 4000 Central Florida Blvd, Orlando, FL 32816, USA

Su Xu: CREOL, The College of Optics and Photonics, University of Central Florida, 4000 Central Florida Blvd, Orlando, FL 32816, USA

Li-Xiao Yao: School of Electronics and Information Engineering, Sichuan University, Chengdu 610065, China

Preface

Special Issue on Microlenses

Hongrui Jiang

Reprinted from *Micromachines*. Cite as: Jiang, H. Special Issue on Microlenses. *Micromachines* **2014**, *5*, 1342–1343.

The study and application of microscale lenses and lens arrays have been actively researched in recent years; new approaches in the fabrication of microlenses and microlens arrays have emerged. Also, novel applications of these microlenses and microlens arrays have been demonstrated. In an effort to disseminate the current advances in this specialized field of microlenses and microlens arrays, and to encourage discussion on the future research directions while stimulating research interests in this area, a Special Issue of *Micromachines* has been dedicated to “Microlenses”.

This Special Issue presents a total of ten papers covering most of the active areas of research in microlenses and microlens arrays. Specifically, eight papers are on the fabrication and characterization of microlenses and microlens arrays, one focuses on integration of microlenses into complex micro-optical modules, and the last one deals with the super-hydrophobic surface that is often important to realize droplet-based microlenses.

The fabrication and realization of microlenses and microlens arrays reported in these papers, cover a wide range of mechanisms, technologies, materials, and optical designs. Xu *et al.* [1] provide a thorough review of how to improve the response time of liquid crystal (LC) based tunable-focus microlenses. The basic operating principles and recent progress are introduced and reviewed for two types of fast-response microlenses based on LC/polymer composites: polymer dispersed/stabilized nematic LC and polymer-stabilized blue phase LC. Chen *et al.* [2] propose a polarization independent LC microlens arrays based on controlling the spatial distribution of the Kerr constants of blue phase LC; the concept is supported by simulation. Two papers are on adaptive liquid lenses actuated via electrowetting. Liu *et al.* [3] report a design in which the liquid lens is tuned by electrowetting-driven movement of a droplet. Li *et al.* the authors of [4] describe a variable-focus liquid microlens that is actuated by electrowetting on dielectric (EWOD). The microlens is fabricated on a flexible and curved polydimethylsiloxane (PDMS) substrate. Mohammed *et al.* [5] utilize CO_2 laser to manufacture miniaturized plano-convex lenses by an engraving process in poly(methyl methacrylate) (PMMA) substrates. Such lenses can be integrated into lab-on-chip systems. Gulari *et al.* [6] demonstrate a microfluidic-based oil-immersion lenses (μOIL) chip as an add-on chip-based optical module to provide high-resolution and large field of view to a stereo microscope. Aldalali *et al.* [7] report an approach to fabricating PDMS microlenses and mirolens arrays through a single molding step. The mold is formed by photo-polymerization, and the resultant shrinkage, of polyacrylamide (PAAm) hydrogel. Finally, Huang *et al.* [8] present a wide-angle, broad-spectrum cylindrical lens based on reflections from a micro-mirror array, rather than refraction. This intriguing mechanism is inspired by the reflecting superposition compound eyes of some decapods.

There are two papers in this Special Issue covering different aspects of research related to microlenses and microlens arrays. Dannberg *et al.* [9] discuss wafer-level hybrid integration of complex micro-optical modules. Microlenses play a critical role in the formation of these modules. Gentile *et al.* [10] provide a review of super-hydrophobic surfaces (SHSs)—bio-inspired, artificial microfabricated interfaces consisting of nanoengineered micropillars. Such SHSs could benefit many optical components and modules, including microlenses.

I wish to thank all authors who submitted their papers for publication in this Special Issue. I would also like to thank all the reviewers for their tremendous efforts in completing the tasks on time.

Hongrui Jiang
Guest Editor
Department of Electrical and Computer Engineering, University of Wisconsin-Madison,
Madison, WI 53706, USA.

18 December 2014

References

1. Xu, S.; Li, Y.; Liu, Y.; Sun, J.; Ren, H.; Wu, S. Fast-response liquid crystal microlens. *Micromachines* **2014**, *5*, 300–324.
2. Chen, H.; Chen, M.; Chang, C.; Wang, Y.; Lin, Y. Simulation study on polarization-independent microlens arrays utilizing blue phase liquid crystals with spatially-distributed Kerr constants. *Micromachines* **2014**, *5*, 859–867.
3. Liu, C.; Wang, Q.; Yao, L.; Wang, M. Adaptive liquid lens actuated by droplet movement. *Micromachines* **2014**, *5*, 496–504.
4. Li, C.; Jiang, H. Fabrication and characterization of flexible electrowetting on dielectrics (EWOD) microlens. *Micromachines* **2014**, *5*, 432–441.
5. Mohammed, M.; Desmulliez, M. CO_2 laser manufacturing of miniaturised lenses for lab-on-a-chip systems. *Micromachines* **2014**, *5*, 457–471.
6. Gulari, M.; Tripathi, A.; Ghannad-Rezaie, M.; Chronis, N. An optofluidic lens array microchip for high resolution stereo microscopy. *Micromachines* **2014**, *5*, 607–621.
7. Aldalali, B.; Kanhere, A.; Fernandes, J.; Huang, C.; Jiang, H. Fabrication of polydimethylsiloxane microlenses utilizing hydrogel shrinkage and a single molding step. *Micromachines* **2014**, *5*, 275–288.
8. Huang, C.; Jiang, H. Bio-inspired wide-angle broad-spectrum cylindrical lens based on reflections from micro-mirror array on a cylindrical elastomeric membrane. *Micromachines* **2014**, *5*, 373–384.
9. Dannberg, P.; Wippermann, F.; Brückner, A.; Matthes, A.; Schreiber, P.; Bräuer, A. Wafer-level hybrid integration of complex micro-optical modules. *Micromachines* **2014**, *5*, 325–340.
10. Gentile, F.; Coluccio, M.; Limongi, T.; Perozziello, G.; Candeloro, P.; Di Fabrizio, E. The five Ws (and one H) of super-hydrophobic surfaces in medicine. *Micromachines* **2014**, *5*, 239–262.

Fast-Response Liquid Crystal Microlens

Su Xu, Yan Li, Yifan Liu, Jie Sun, Hongwen Ren and Shin-Tson Wu

Abstract: Electrically tunable liquid crystal microlenses have attracted strong research attention due to their advantages of tunable focusing, voltage actuation, low power consumption, simple fabrication, compact structure, and good stability. They are expected to be essential optical devices with widespread applications. However, the slow response time of nematic liquid crystal (LC) microlenses has been a significant technical barrier to practical applications and commercialization. LC/polymer composites, consisting of LC and monomer, are an important extension of pure LC systems, which offer more flexibility and much richer functionality than LC alone. Due to the anchoring effect of a polymer network, microlenses, based on LC/polymer composites, have relatively fast response time in comparison with pure nematic LC microlenses. In addition, polymer-stabilized blue phase liquid crystal (PS-BPLC) based on Kerr effect is emerging as a promising candidate for new photonics application. The major attractions of PS-BPLC are submillisecond response time and no need for surface alignment layer. In this paper, we review two types of fast-response microlenses based on LC/polymer composites: polymer dispersed/stabilized nematic LC and polymer-stabilized blue phase LC. Their basic operating principles are introduced and recent progress is reviewed by examples from recent literature. Finally, the major challenges and future perspectives are discussed.

Reprinted from *Micromachines*. Cite as: Xu, S.; Li, Y.; Liu, Y.; Sun, J.; Ren, H.; Wu, S.-T. Fast-Response Liquid Crystal Microlens. *Micromachines* **2014**, *5*, 300–324.

1. Introduction

Liquid crystals (LCs) exhibit unique material properties ranging between those of conventional isotropic liquids and solid-state crystals. The operation mechanisms of an LC device can be roughly grouped into two categories: molecular reorientation under the influence of an electric field [1] and field-induced mechanical deformation of the droplet shape [2]. The former was pioneered by Schadt and Helfrich, enabling today's liquid crystal displays (LCDs), phase modulators, adaptive lenses, optical switches, and other photonic devices [1].

Since the first concept was demonstrated in 1977 by Bricot [3], adaptive LC lenses have attracted strong research attention due to their advantages of tunable focusing, voltage actuation, low power consumption, simple fabrication, compact structure, and good stability. They are expected to be essential optical devices with widespread applications. Generally speaking, LC lenses can be divided into two categories according to their aperture size: those with a large aperture size (>1 mm) are suitable for portable devices, such as pico projectors, imaging system for cell phones, endoscopic system, and ophthalmic lenses [4–8], while those with a small aperture size (<1 mm) are suitable for microlens arrays and their applications include image processing [9–19], optical communication [20,21], lab on a chip, switchable 2D/3D displays [22,23], *etc*. The progresses of LC lenses with a large aperture size have been reviewed by Fowler *et al.* in 1990 [24] and more recently by Lin *et al.* in 2011 [25]. In the present review article, we focus on LC microlenses, especially those with fast response times.

Most LC lenses/microlenses developed thus far employ nematic LCs (NLCs), which offer a large birefringence to achieve a short focal length. Two major technical challenges have severely limited their practical applications and commercialization: polarization dependency and slow response time (several seconds or hundreds of milliseconds). The former can be solved by using residual phase modulations [26,27], and optical isotropic materials, such as blue phase LC [28–34], double-layered structure [35–37], or axially symmetric photoalignment [38]. Due to the intrinsic speed of NLCs, the response time of a LC microlens is usually in the order of 100 ms, which is obviously not fast enough for image processing, optical communication, *etc.* Several approaches have been proposed to improve the response time. Dual frequency LCs (DFLCs), which exhibit a positive dielectric anisotropy ($\Delta\varepsilon$) at low frequencies and negative $\Delta\varepsilon$ at high frequencies, have been adopted to speed up both rise and decay times of an LC device by controlling the applied frequency [36,39,40]. However, the driving scheme is relatively complicated, and dielectric heating may shift the crossover frequency and lead to performance instability at high frequency operation [41]. Surface-stabilized ferroelectric LCs (SSFLCs) can be switched in 100 μs and the response time of SSFLC microlenses is approximately 1000 times faster than that of nematic devices, however, they are only good for binary optical modulation because of the hysteresis characteristics [42,43]. Microlenses based on chiral sematic A (SmA*) LCs could tune the focal length in several microseconds, which is 10× to 1000× faster than that using SSFLCs or NLCs, respectively [44], but the alignment of LC molecules is not stable. In comparison to the abovementioned approaches, microlenses based on LC/polymer composites provide a relatively fast response time, continuous variable optical power, simple fabrication, and driving scheme, as well as good mechanical stability. These attractive features make them more promising for practical applications. In addition, polymer-stabilized blue phase liquid crystal (BPLC) based on the Kerr effect [45–50] is emerging as a promising candidate for new photonics applications. The major attractions of BPLC are twofold: (1) submillisecond response time due to its self-assembled nanostructure [33,48,51], which is ~10× faster than that of NLCs and (2) free of a molecular alignment layer, which means a simpler fabrication process.

In this review article, we first explain the basic principles of LC microlenses. Then, we illustrate the recent progress on the development of fast-response LC microlenses based on LC/polymer composites by the examples from recent literature, covering topics of polymer-dispersed/stabilized nematic LC microlenses and BPLC microlenses. For each type of microlens, the cell structure, lens performance, focal length tunability, and dynamic response are described, as well as their advantages and disadvantages. Challenges and future perspectives are also discussed.

2. Polymer-Dispersed/Stabilized Nematic Liquid Crystal Microlens

2.1. Principles

Nematic LCs are rod-like molecules, which exhibit optical and dielectric anisotropies due to their anisotropic molecular structures. When properly aligned in an LC cell, their long axes are approximately parallel to each other, and this averaged alignment direction is called LC director, as shown in Figure 1a [52]. Light polarized along the LC director (e-ray, polarization direction is represented by blue arrow) sees extraordinary refractive index n_e, while that polarized perpendicular (o-ray, polarization direction is represented by pink arrow) to the LC director sees ordinary refractive index n_o. Then, if the light is polarized at a θ angle with respect to the director (represented by red arrow), it sees an effective refractive index n_{eff}, expressed as:

$$n_{\mathrm{eff}} = \frac{n_e n_o}{\sqrt{(n_e \sin\theta)^2 + (n_o \cos\theta)^2}} \tag{1}$$

The birefringence (optical anisotropy) of the LC is defined as:

$$\Delta n = n_e - n_o \tag{2}$$

and the dielectric anisotropy is defined as:

$$\Delta\varepsilon = \varepsilon_{/\!/} - \varepsilon_{\perp} \tag{3}$$

where $\varepsilon_{/\!/}$ and $\varepsilon_{\perp}$ are the dielectric constant (or relative permittivity) along and perpendicular to the LC director, respectively.

In a typical cell, LC material is sandwiched between two substrates coated with electrodes (e.g., indium tin oxide, ITO) and surface alignment layers (e.g., polyimide, PI) [53]. Buffed PI introduces the alignment of LC directors while spacers control the cell gap. Figure 1b shows the schematic structure of a homogeneous LC cell, where the top and bottom substrates are rubbed in anti-parallel directions and LC directors are aligned along the substrates in the static state. Let us assume the normally incident light is polarized along the rubbing direction. It will experience an optical path of $L = dn_e$ after passing the cell, where d is the cell gap. When a sufficiently high voltage is applied to the ITO electrodes, the LC directors will be reoriented in vertical direction and the optical path becomes $L = dn_o$ (Figure 1b). If the voltage is not high enough and the LC directors are only reoriented by a θ angle (Figure 1c), the corresponding optical path is $L = \int_0^d n_{\mathrm{eff}}(\theta)\, \mathrm{d}z$, where $n_{\mathrm{eff}}(\theta)$ is the effective refractive index expressed by Equation (1). If the LC molecules, located at different positions, could be controlled to have various reorientation angles, then the light will experience various refractive indices accordingly, as shown in Figure 1d. Here, the light incident on the center and border experience $n_{\mathrm{eff}}(\theta)$ and n_e, respectively, the optical path difference (OPD) between the center and border can be expressed as:

$$\mathrm{OPD} = d(n_{\mathrm{eff}}(\theta) - n_o) \tag{4}$$

At a given wavelength (λ), the corresponding phase difference ΔØ is:

$$\Delta\varnothing = \int_0^d \frac{2\pi}{\lambda} (n_{\mathrm{eff}}(\theta) - n_o)\, \mathrm{d}z \tag{5}$$

Such an effect is equivalent to an isotropic medium with different thickness. It is well known that if the surface of the isotropic medium is polished with a spherical shape, then it functions as a lens. Similarly, if the LC layer exhibits a lens-like gradient refractive index distribution or phase profile, then it has a lens characteristic. For example, in Figure 1e, the normally incident e-ray experiences a gradually increased refractive index distribution from the border to center, and the LC layer functions as a positive lens. *Vice versa*, the LC layer would function as a negative lens if the refractive index gradually decreases from the border to center, as shown in Figure 1f. Gradient refractive index distribution or phase profile within the LC layer forms the foundation of an LC lens. Various approaches for fabricating LC microlens array have been proposed. The common is to create a gradient refractive index distribution among LC directors either by an inhomogeneous electric field [9,10,15–17,20,22,23,54] or by an inhomogeneous LC morphology [11–14,18,19,21,55,56].

Focal length (or optical power) and response time are two very important factors. The focal length is related to the lens radius (*r*), refractive index difference between center and boarder of the lens (Δ*n*), and thickness of LC layer (*d*) as [53]:

$$f = \frac{r^2}{2d\cdot\Delta n} \tag{6}$$

The response time (decay and rise) of a nematic LC lens is determined by the visco-elastic coefficient (γ/*K*), LC layer thickness of (*d*), applied voltage (*V*), and threshold voltage (V_{th}) as [52]:

$$\tau_{\mathrm{decay}} = \frac{r}{K}\left(\frac{d}{\pi}\right)^2 \tag{7}$$

$$\tau_{\mathrm{rise}} = \frac{1}{\frac{V^2}{V_{\mathrm{th}}^2} - 1}\cdot\tau_{\mathrm{decay}} \tag{8}$$

Although the rise time can be greatly shortened by applying an overdrive voltage, the decay time is still determined by the restoring elastic torque. This problem gets even worse as the wavelength increases, e.g., infrared region, since a thicker cell gap is required to compensate the longer wavelength and lower birefringence. To obtain a short focal length, we could increase *d*Δ*n* or reduce the lens aperture. Most of high birefringence LCs have Δ*n* ~0.4 [57]. Some ultra-high Δ*n* (>0.6) LCs have been developed, but their large viscosity leads to a slow response time [58]. Similarly, increasing the LC layer thickness also causes a sluggish response time, as Equation (7) indicates.

Figure 1. Operation principle of a nematic LC lens: (**a**) LC molecular and polarization dependent refractive index; (**b**) schematic structure of a homogeneous LC cell, the incident light sees n_e; (**c**) LC directors are reoriented along the electric field and the incident light sees n_o; (**d**) LC directors are reoriented by a θ angle and the incident light sees $n_{\mathrm{eff}}(\theta)$; (**e**) positive LC lens, and (**f**) negative LC lens.

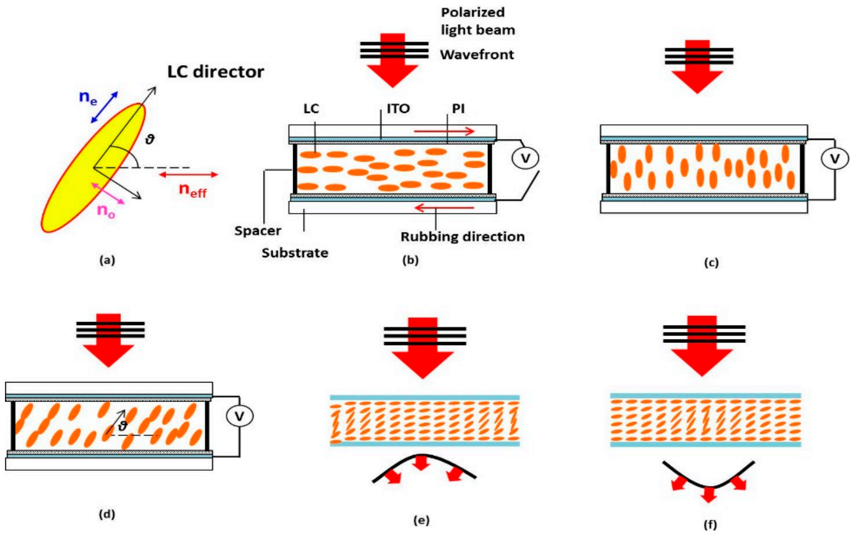

LC/polymer composites, consisting of LC and polymer, are an important extension of pure LC systems, which offer more flexibility and much richer functionality than LC alone. Depending on the monomer concentration, LC/polymer composites can be divided into three major categories: polymer-dispersed LCs (PDLCs) [59], polymer-stabilized LCs (PSLCs) [60], and polymer-network LCs (PNLCs) [61]. PDLC consists of a higher percentage of monomer (>20 wt %), while PSLC consists of a lower percentage of monomer (<10 wt %), PNLC consists of a medium percentage of monomer (10 wt % ~ 20 wt %). Due to the anchoring effect of polymer network, microlenses, based on PDLC/PSLC/PNLC, offer a relatively fast response time in comparison with pure nematic LC microlenses. Nevertheless, the domain size needs to be carefully controlled to avoid scattering.

2.2. Microlens Using Nanosized Polymer-Dispersed Liquid Crystal Droplets

In 2005, Ren *et al.* demonstrated a fast-response microlens array using nanosized PDLC droplets [54], as Figure 2 shows. UV-curable monomer NOA65 is first molded to form plano-concave microlens arrays on the bottom ITO substrate. The plano-concave cavities are filled with nano-PDLC material, which consists of 35 wt % NOA65 ($n_p = 1.524$) and 65 wt % Merck nematic LC E48 ($n_o = 1.523$, $\Delta n = 0.23$). The ordinary refractive index of the LC material matches well with that of the polymer matrix. After UV curing at 15 $\mathrm{mW{\cdot}cm^{-2}}$ and 50 °C for 30 min, a saturated phase separation between NOA65 and E48 is obtained, and LC droplets are uniformly dispersed in polymer matrix. In the voltage-off state, the LC droplets are randomly oriented, and the average refractive index of the nano-PDLC is larger than that of the NOA65 ($n_p = 1.524$), and the incident light can be focused (Figure 2a). At the voltage-on state, the LC directors are reoriented along the electric field direction, and effective refractive index in the plane perpendicular to the electric field is decreased. According to Equation (6), the focal length increases. When the voltage is high enough, the focusing effect will disappear since all the LC directors have been reoriented along the electric field (Figure 2b). For the LC microlens with a 450 μm aperture and 45 μm cell gap, its focal length was continuously tunable from 3.3 cm to 3.5 cm ($\lambda = 633$ nm) when the voltage increased to 200 V_{rms}. The τ_{rise} (from focusing to less-focusing) and τ_{fall} (from less-focusing to focusing) were measured to be ~0.25 ms and ~0.15 ms, under 200 V_{rms} square pulses. Due to the randomly oriented LC droplets in the polymer matrix, such microlenses are polarization independent. Moreover, the LC droplet size is smaller than a visible wavelength, thus it doesn't scatter light. However, the operating voltage is quite high and it is difficult to further tune the focal length to infinity even the voltage keeps increasing. Besides, in PDLC microlens the refractive index difference between the microlens center and border is relatively small, *i.e.*, $\Delta n = c\Delta n/3$, where Δn is the LC birefringence and c is the LC concentration. In this microlens array, the theoretical δn is only ~0.027, which is much smaller than the LC birefringence ($\Delta n = 0.23$). As a result, the dynamic range is rather limited.

Figure 2. Side view of the nano-PDLC lens in the: (**a**) voltage-off state; and (**b**) voltage-on state.

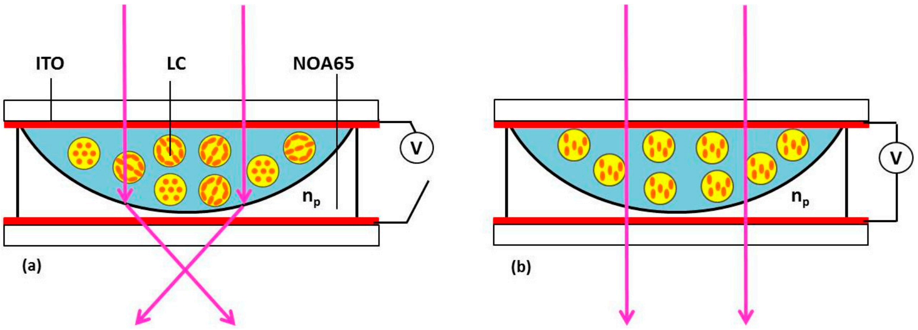

2.3. Polymer-Stabilized Liquid Crystal (PSLC) Microlens

2.3.1. PSLC Microlens Using a Patterned Photomask

To lower the operating voltage, increase the phase shift and improve the dynamic response time during focus change, PSLC is a feasible approach [60]. Different from nano-PDLC, monomers used in PSLC usually have a rod-like structure with a reactive double bond at both sides, similar to the structure of nematic LC molecules. In addition, the monomer concentration in PSLC is 10 wt % or less. When an LC/monomer mixture is filled into the cell, both LC molecules and monomers will exhibit the same alignment property, if the inner surface of the substrate is properly rubbed. Under UV exposure, the double bonds of the monomer are opened and the molecules are linked together, forming a stable polymer network [53].

A PSLC microlens array is usually prepared through a spatially inhomogeneous UV exposure, which can be generated by two methods: (1) UV laser beam with a Gaussian-shaped profile [55]; (2) a uniform UV laser beam passing through an optical density filter, e.g., hole-array patterned photomask [56,61,62]. The latter is much simpler and more suitable for making microlens array.

Figure 3. (**a**) Fabrication setup of PSLC microlens array; (**b**) recorded UV intensity profile after passing through Ø25 µm hole and (**c**) formed polymer network after UV exposure.

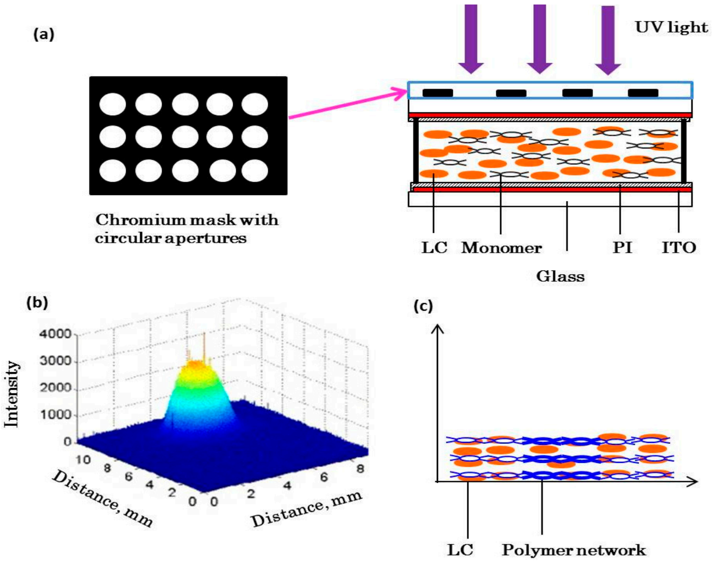

Figure 3a depicts the fabrication setup of PSLC microlens array using a hole-array patterned photomask [56]. The LC/monomer mixture consists of 3 wt % BAB6 monomer and 97 wt % E48 nematic LC ($\Delta n = 0.231$ at $\lambda = 589$ nm and $T = 20$ °C), as well as a small amount of photoinitiators. The cell gap and substrate thickness are 15 μm and 1.1 mm, respectively. The substrates are rubbed in anti-parallel directions. A chromium photomask having hole-array apertures is placed on the top a substrate. The diameter of each hole is 25 μm. When the UV beam ($\lambda = 365$ nm) passes through the holes, diffraction appears. Figure 3b shows the measured UV intensity profile after the beam passing through the single hole. The formed diffraction pattern consists of a series of rings, but most of light energy concentrates on the 0th order ring, which presents a parabolic-like profile. When the LC/monomer mixture is exposed to such a UV intensity distribution, the stronger intensity in the central region will accelerate the polymerization rate and form a denser polymer network (*i.e.*, the polymer-rich region). On the contrary, the weaker intensity at the borders will have a slower polymerization rate and form a looser polymer network (*i.e.*, LC-rich region). Therefore, a centro-symmetric inhomogeneous polymer network is formed, as shown in Figure 3c. The polymer-rich region exhibits a higher threshold voltage than that of the border LC-rich region. Therefore, the LC molecules on the border are reoriented first under a uniform electric field. This gradient refractive index distribution makes the PSLC function like a positive microlens. At $V = 0$, the PSLC exhibits a homogeneous alignment and no focusing effect occurs. As the voltage increases, the focal length first decreases to ~2 cm at ~5 V_{rms}, and then increases again. Because at a higher voltage, the LC molecules in the polymer-rich and LC-rich regions are all reoriented towards the electric field, the gradient refractive index profile is gradually flattened. The focal length was measured to be ~3.3 cm at 20 V_{rms} and response time <20 ms. Theoretically, a sufficiently high voltage could reorient all the LC molecules along the electric field, leading to an infinity focal length. However, LC molecules at the border of the microlens experience the weakest stabilization; thus, the microlens aperture has a tendency to shrink at high voltage. On the other hand, LC molecules in the center may be strongly anchored by the polymer network and cannot contribute to the phase change. In this PSLC microlens array, the focal length gradually saturates as the voltage exceeds 10 V_{rms} and cannot be further tuned. Besides, the refractive index difference between center and boarder of the lens (Δn) is usually much smaller than the LC birefringence since a large gradient distribution of LC domains is not preferred in the PSLC [11,13,21]. Otherwise, large LC domains would cause light scattering, nonuniform response, and mechanical instability.

2.3.2. PNLC Microlens Using Patterned Electrode

To utilize the maximum intrinsic birefringence of the LC material and present the shortest possible focal length, in 2013, Ren *et al.* demonstrated a PNLC microlens array using a ring-array-patterned electrode in a homogeneous cell [63]. Figure 4 shows the cell structure; the top substrate has a planar ITO electrode, while the bottom substrate has two patterned ITO electrodes (electrode-1 and electrode-2) for generating fringing field (V_F) and uniform longitudinal field (V_L) individually. The inner and outer radii of the ring are 50 μm and 70 μm, respectively. These two substrates are antiparallel rubbed and the cell gap is ~15 μm (Figure 4b). The LC/monomer layer consists of 90 wt % Merck BL-009 ($n_o = 1.529$, $\Delta n = 0.281$) and ~10 wt % RM257 (containing a small amount of photoinitiators). RM257 has a rod-like structure and can be easily aligned with LCs. The desired gradient refractive index profile in the

LC/monomer layer is introduced by the fringing field (V_F), and later stabilized by UV exposure to form polymer networks (Figure 4c). For the microlens with a 50 μm aperture, the shortest focal length is ~378 μm at $V_F = 6$ V_{rms} and λ ~550 nm. Then, the LC/monomer mixture was photo-polymerized at $V_F = 6$ V_{rms}, under UV exposure (λ ~365 nm, ~10 mW·cm^{-2}) for 20 min. Once the PNLC is formed, it is difficult to be actuated by the fringing field. Instead, a uniform longitudinal electric field is adopted by applying a voltage (V_L) between the top electrode and bottom electrode-2, which in turn changes the focal length (Figure 4d). As V_L increases, the focal length increases gradually. When $V_L > 115$ V_{rms}, the focal length is too long to be estimated. The response time from focusing to non-focusing and from non-focusing to focusing was measured to be ~3.6 ms and ~0.9 ms, respectively, under $V_L = 100$ V_{rms}. As no photomask is employed during the UV polymerization process, the formed PNLC has a uniform morphology. Such a PNLC microlens array offers several attractive features, such as fast response time, good stability, and weak light scattering in the visible spectral range.

Figure 4. PNLC microlens structure and fabrication procedures: (**a**) microlens structure; (**b**) LC/monomer mixture present a homogeneous alignment; (**c**) central-symmetric gradient refractive index distribution is introduced by inhomogeneous fringe field along with UV exposure and (**d**) the formed PNLC microlens after removing the voltage is actuated by a uniform longitudinal electric field.

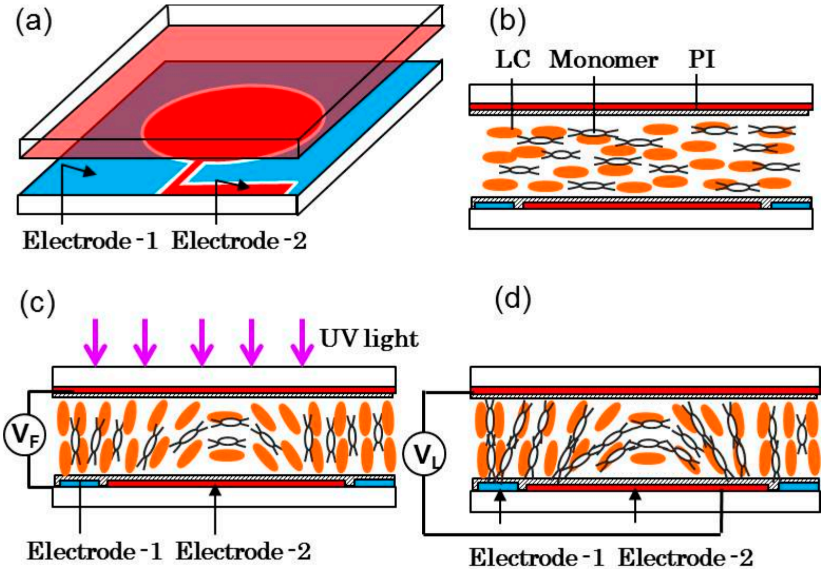

2.3.3. Reconfigurable Fabrication of PNLC Lens/Microlens

To fabricate the PSLC/PNLC microlens shown in Figures 3,4, a pre-patterned template, such as patterned photomask or electrode, is commonly used. The current fabrication techniques heavily involve photolithography procedure, which is expensive, time consuming and environmentally unfriendly (*i.e.*, photoresistors and developers are toxic). In 2013, Sun *et al.* demonstrated a one-step printing technique to fabricate submillisecond-response and scattering-free PNLC lens [21]. Figure 5a depicts the experimental setup. A photomask, either an iris diaphragm (for circular lens) or a rectangular mask (for prism, cylindrical lens, or grating), is placed right above the LC cell and connected to a motion controller. The duration and amplitude of the applied voltages is controlled by LabVIEW. A UV lamp is used for stabilizing the polymer network. The essential part of this method is to control the LC tilt angle (through controlling voltage applied to the mixture) along with the exposure area (through controlling a movable shield), while a desired tilt angle at a specific position is fixed by UV exposure [64]. By repeating the same process at different positions and different voltages, various tilt angle distribution of the LC molecules can be obtained. Figure 5b,c show the fabrication procedures of a lens using an iris diaphragm. Here, the LC/monomer layer consists of 90 wt % HTG135200 (γ_1/K_{11} ~119.6 ms·μm^{-2} at 22 °C) and 10 wt % RM257. By specifically selecting such a high viscosity LC host and performing UV curing at a low temperature (11 °C) [65], the light scattering in the visible region is negligible at 633 nm (and ~3% at 480 nm). For the PNLC lens with a 2.6 mm aperture and 15 μm cell gaps, its focal length can be tuned from 15 cm to 32 cm when the voltage increases from 0 to 100 V_{rms}. In comparison with conventional microfabrication techniques for adaptive LC photonic devices, this approach shows advantages in: (1) short fabrication time; (2) flexibility for designing and fabricating the desired refractive index profile of an LC device; (3) low cost and environmentally friendly; (4) large panel capability and (5) submillisecond device response time. This printing technique enables rapid design iterations for display and photonic devices.

Figure 5. (**a**) Schematic drawing of the fabrication setup; (**b**) dynamic control of the iris diaphragm and exposure for generating spatial gradient refractive index at V_1 and (**c**) at V_2.

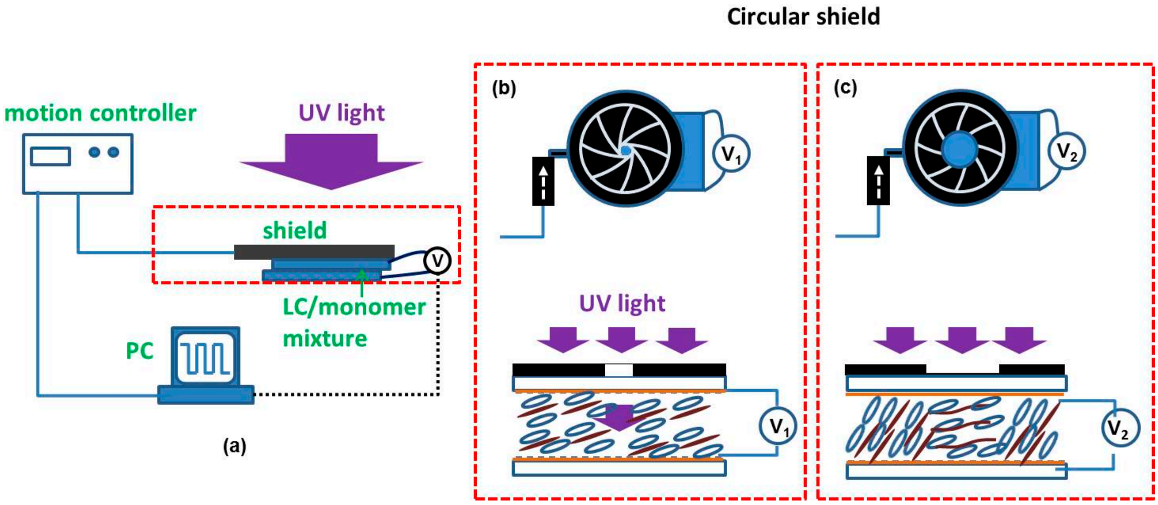

2.3.4. Polymeric Lenticular Microlens Array for 2D/3D Switchable Displays

Electrically switchable two-dimensional (2D) and three-dimensional (3D) displays have attracted great attention lately and various approaches have been proposed [66–72]. Among them, liquid crystal display (LCD) integrated with a lenticular microlens array provides an autostereoscopic multi-view 3D display with high brightness [68–71]. In the 2D mode, each LC microlens has no focusing effect and the microlens array functions as an optical flat. In the 3D mode, each LC microlens exhibits a focusing effect. By turning on and off the microlens focusing effect, the display can be electrically switched between 2D and 3D modes. Therefore, LC lenticular microlens array has become a key component in switchable 2D/3D displays.

The abovementioned PDLC/PSLC/PNLC microlenses could provide a reasonable fast response time, however, the operating voltage is relatively high. To overcome these issues, Flack *et al.* proposed to indirectly actuate the LC lenticular microlens array through a twisted-nematic (TN) LC cell (also called a polarization converter) [1] to achieve 2D/3D switchable displays [73], as shown in Figure 6. Each LC microlens in the array covers two pixels: left and right. An isotropic polymer with a concave shape is used as the base for the LC microlens array. Let us assume the refractive index (n_p) of the isotropic polymer matches the ordinary refractive index (n_o) of the LC material. The LC in the lens cell presents homogeneous alignment. The optical axis of the polarizer is parallel to the rubbing direction of the bottom TN cell. In the voltage-off state, the polarization direction of the incident beam is rotated by 90° after passing through the TN cell, becoming orthogonal to the LC directors in the microlens. As a result, this beam will not be focused because $n_p \sim n_o$. The images from the left pixel and the right pixel can be seen by two eyes at the same time, and the display remains the original 2D display (Figure 6a). When a high voltage is applied to the TN cell, the LC directors are reoriented along the electric field direction and the polarization rotation effect vanishes. The outgoing beam from the TN cell behaves like an extraordinary ray to the microlens array. Because of $n_e > n_p$ and the convex shape of the LC microlens, the focusing effect occurs. For each microlens, the image coming from the right pixel can only be seen by the left eye, while that from the left pixel can only be detected by the right eye (Figure 6b). By combining these two images, our eyes will see 3D images out of the 2D panel.

Figure 6. Operation principle of a switchable 2D/3D display with a TN broadband polarization rotator (middle) and a polymeric microlens array (top): (**a**) voltage-off and (**b**) voltage-on.

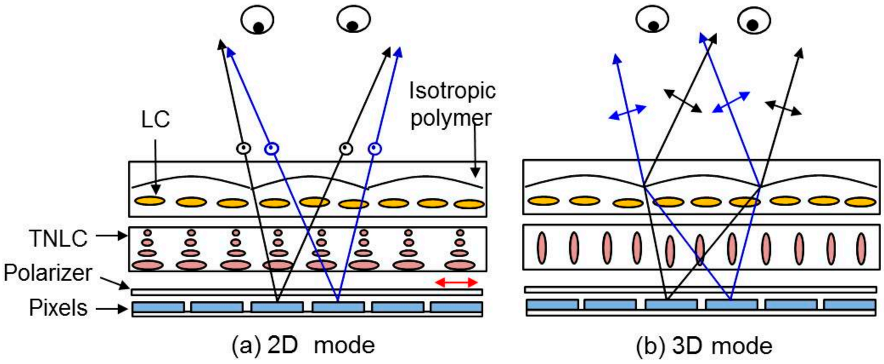

However, such a system requires a total of four glass substrates (Figure 5), which is too bulky and heavy. Ren *et al.* proposed to replace the LC microlens array with a lightweight polymeric microlens array film without compromising the performance [74]. This film was made of a mixture of rod-like diacrylate monomer (~80 wt % RM 257) and positive dielectric anisotropy nematic LC (~20 wt % Merck BL038). RM257 has a rod-like structure with reactive double bonds at both sides. Its nematic phase is from 70 °C to 130 °C. Compared to RM257 itself, the mixture exhibits two desired features: (1) positive $\Delta\varepsilon$ and (2) increased Δn. The mixture was filled into an antiparallel-rubbed cell at 75 °C (Figure 7a), and gradient refractive index profile in one microlens was induced by the fringing fields generated from a planar top electrode and striped bottom electrodes (Figure 7b). After UV stabilization, the polymerized film can be easily peeled from the substrate. Due to the crossed linking of the monomers, the nano-sized LC domains are tightly sealed in the film bulk and the film is optically anisotropic. Integrating with a 90° TN cell, the polymeric film exhibits focusing effect only to the extraordinary ray top sub-figure in (Figure 7c), and five focusing lines could be observed by the CCD camera, bottom sub-figure in Figure 7c.

Turning off the TN cell, the polymeric film presents uniform refractive index to the ordinary ray, top sub-figure in Figure 7d, and no residual focusing effect is observed on the CCD camera, bottom sub-figure in Figure 7d. Under a 10 V pulse, the time from non-focusing (focusing) to focusing (non-focusing) was measured to be ~12 (~40) ms. In comparison to previous switchable LC lenses, Ren's integrated TN/polymeric microlens film exhibits several unique features: (1) compact size; (2) temperature insensitivity; (3) large size capability; (4) switching with a low operating voltage (~5 V) and fast response time (<10 ms). The response time can be further reduced by using a low viscosity LC mixture in the TN cell. Since the film is first formed in a glass cell, and then peeled off from the substrate after opening the cell, this may cause defects or damages in the film. Meanwhile, the fabrication procedures are somewhat sophisticated.

Figure 7. Operation principle of a switchable 2D/3D display with a TN broadband polarization rotator (middle) and a polymeric microlens array (top): (**a**) voltage-off, (**b**) voltage-on, (**c**) focusing state and (**d**) non-focusing state.

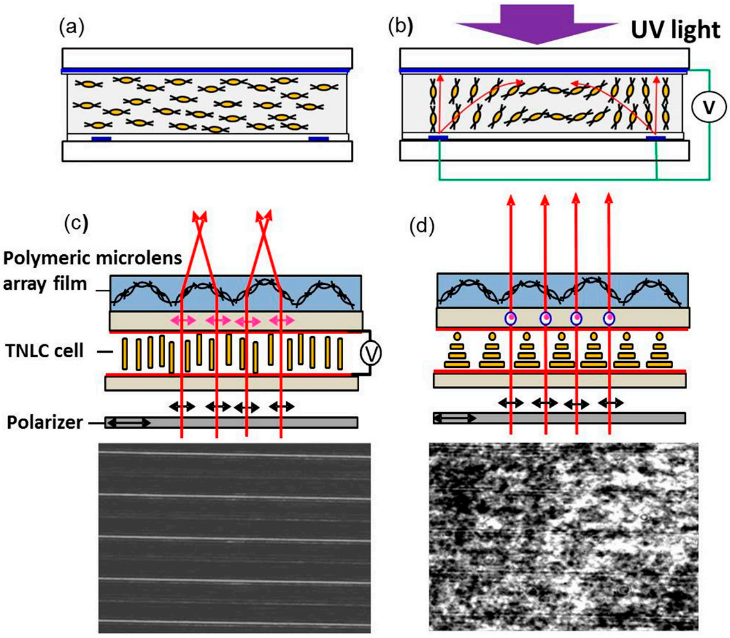

Ren *et al.* further simplified the fabrication procedures through directly forming the polymeric microlens array film on a single substrate with interdigitated ITO electrodes (Figure 8a) [75]. The coated PI layer was buffed along the *x*-direction, perpendicular to the electrode stripes. A droplet of LC/monomer mixture (~80 wt % RM 257 and ~20 wt % Merck BL009) was spread to be a thin film by a blade (Figure 8b). When the voltage is on, the LC molecules experience a dielectric force at the LC-air interface due to the fringing field, which is expressed as [76]:

$$\vec{F}_{\mathrm{d}}=\int_{\mathrm{V}}\frac{1}{2}\varepsilon_0(\varepsilon_{\mathrm{d}}-\varepsilon_{\mathrm{m}})\nabla(\vec{E}\cdot\vec{E})\mathrm{d}V \tag{9}$$

where ε_0 represents the permittivity of free space, V is volume of the droplet, ε_{LC} and ε_{air} (~1) are the dielectric constants of LC and air, respectively, and E is the electric field intensity. Since ε_{LC} is larger than ε_{air}, the dielectric force will pull the LC molecules to the region with higher electric field intensity. If the film is relatively thin, *i.e.*, within the region where the gradient of the electric field intensity is still strong enough to generate a dielectric force comparable with the interfacial tension, it can be effectively flattened by the dielectric force. As a comparison, the LC molecules inside the film do not experience any dielectric force because of the same medium; instead, they are reoriented by the electric field, if they are located within the penetration depth of the electric field (Figure 6c). The gradient orientations of LC molecules in each period lead to a periodic gradient refractive index (GRIN) distribution in the film. As a result, the film exhibits a lens characteristic, which is later stabilized thorough UV polymerization (Figure 8d). It is found that the GRIN distribution within the film is mainly dependent on the applied voltage during UV exposure. If the generated fringing field is too weak to reorient the monomers/LCs, disclination lines and non-uniform GRIN distribution within each stripe appear (Figure 8e,f). When the voltage is sufficiently high, the generated fringing field is able to reorient the monomers/LCs and the stripes present a uniform color change (Figure 8g). Figure 8h is a magnified image showing several stripes. In one period, w is the width of the ITO stripe (8 µm) and A is the diameter of the lens aperture (20 µm). The uniform periodic color stripes imply that the surface of the polymeric film is very flat and each polymeric stripe has a GRIN distribution within it. Therefore, the film functions as a lenticular microlens array. When it is integrated with a 90° TN cell in a lens system, its focal length can be switched by actuating the TN cell.

Figure 8. (**a**) A glass substrate with interdigitated ITO electrodes; (**b**) the droplet is spread to form a thin film with a blade; (**c**) voltage is applied to the electrodes and fringing field induced molecule reorientation is polymerized through UV exposure; (**d**) GRIN distribution remains after removing the voltage; (**e**) film textures observed on the IPS-8/12 substrate at $V = 50\ \mathrm{V_{rm}}$; (**f**) $V = 65\ \mathrm{V_{rms}}$ to the fluidic film; (**g**) solidified after applying 80 $\mathrm{V_{rms}}$ and (**h**) magnified image of (**f**).

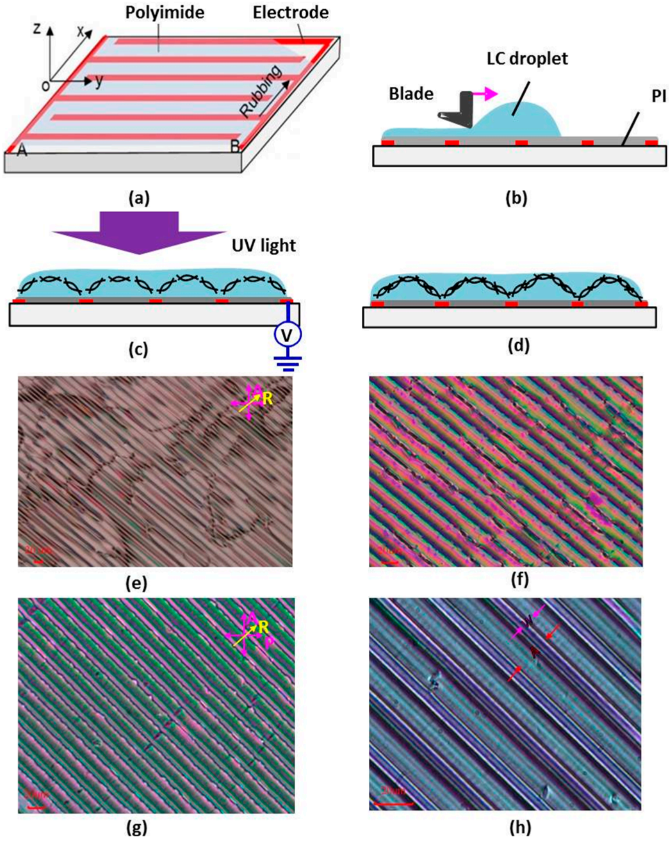

3. Polymer-Stabilized Blue Phase LC Microlens

3.1. Operation Principles

Polymer-stabilized blue phase liquid crystal (PS-BPLC) microlenses [28–34] have been developed with several attractive features: (1) submillisecond response time, (2) alignment-free, and (3) polarization insensitive. Blue phase [47–50] exists over a narrow temperature range (1–2 °C) between chiral nematic and isotropic phases. It is a self-assembled structure consisting of double-twist cylinders arranged in cubic lattice, as show in Figure 9. The pitch length of double twist structure measures several hundreds of nanometers. Due to the short coherent length, BPLC exhibits submillisecond response time [77]. Due to the symmetric three-dimensional cubic structure, it appears optically isotropic. For years, blue phase has been found scientifically interesting but has limited applications mainly due to its narrow temperature range. In 2002, Kikuchi *et al.* used polymer to successfully stabilize the double-twist structure and extended the temperature range of blue phase to more than 60 K (including room temperature) [48], which ushered a new era for blue phase.

Figure 9. (**a**) Double twist cylinder structure and (**b**) cubic lattice of a blue phase.

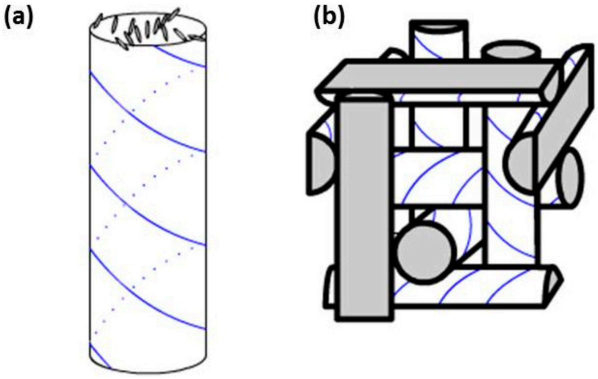

When no voltage is applied, BPLC appears optically isotropic with refractive indices being the same in all directions n_i. As an electric field is applied, birefringence is induced along the direction of electric field. The induced birefringence Δn_{ind} can be described by the Kerr effect in the low field region:

$$\Delta n_{\mathrm{ind}} = \lambda K E^2 \tag{10}$$

where λ is the wavelength and K is the Kerr constant. As the electric field increases, the induced birefringence gradually saturates and can be described by the extended Kerr model [78]:

$$\Delta n_{\mathrm{ind}} = \Delta n_{\mathrm{sat}}\left[1 - e^{-(E/E_{\mathrm{s}})^2}\right] \tag{11}$$

where Δn_{sat} stands for saturated induced birefringence, and E_s represents the saturation field. Along the direction of the electric field, the refractive index is $n_e(E) = n_i + 2\Delta n(E)/3$, and in the orthogonal directions, the refractive indices are $n_o(E) = n_i - \Delta n(E)/3$.

3.2. PS-BPLC Microlens with Planar Electrode

The first PS-BPLC microlens was demonstrated by Lin *et al.* in 2010 [16]. The fast response time and polarization insensitivity were experimentally verified. The structure is shown in Figure 10a. The PS-BPLC is confined between two glass substrates with a cell gap of 20 μm. The top electrode has a hole pattern (diameter = 250 μm) in the center, while the bottom electrode is continuous. In the voltage-off state, the effective refractive index of BPLC is spherical. When voltage is applied between top and bottom electrodes, the effective optical index-ellipsoid of PS-BPLC turns out ellipsoidal due to induced birefringence. The index is more elongated ellipsoid at the edge than in the center due to the non-uniform electric field distribution (*i.e.*, $E_3 > E_2 > E_1$). Since the optic axes are in the direction of light propagation (z direction), both x and y polarizations experience ordinary refractive index $n_o = n_i - \Delta n(E)/3$. At the edge of the aperture, the effective refractive index n_o is lower than that in the center, because of larger induced birefringence $\Delta n(E)$. Such a spatial distribution of refractive indices forms a positive-lens-like phase profile. To characterize the microlens array, a collimated unpolarized green (λ = 532 nm) laser beam was used for illumination. Figure 10b shows the 2D images captured by a charge-coupled device (CCD) without voltage, and no obvious focusing is observed. Figure 10c shows the focusing (measured as 13 cm) at 100 V_{rms}. Moreover, this focusing effect is not affected by the incident polarization, therefore it is polarization insensitive. Such a BPLC microlens array is simple, fast responding, polarization insensitive and alignment free. However, such a simple structure has difficulty to generate ideal phase profile for achieving good image quality.

Figure 10. **(a)** The cross section of a PS- microlens using a hole-patterned electrode; **(b)** measured CCD images of the 2D microlens array at 0 V_{rms} and **(c)** 100 V_{rms}.

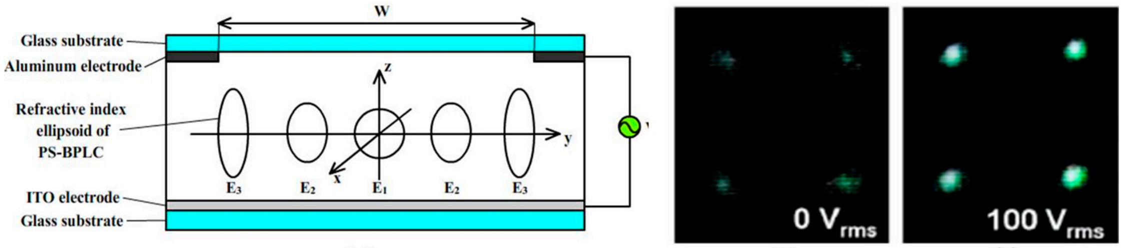

(a) (b) (c)

3.3. BPLC Microlens with Curved Electrode

In 2011, Li *et al.* proposed another BPLC lens structure with curved electrode to improve the phase profile [33]. Figure 11 depicts the cross section (x-z plane) of the microlens array. The top glass substrate has a plano-concave microlens array profile. Its inner surface is coated with an ITO electrode, and then flattened by a polymer layer. The inner surface of the bottom substrate is coated with a planar ITO electrode A BPLC layer is sandwiched between these two substrates. The thickness of the polymer layer in the center of the lens d_1 is much larger than that at the edge d_2. In Figure 11a, At $V = 0$, the BPLC is optically isotropic and does not contribute to the optical power. So the propagation direction of the traversing light is not changed. In Figure 11b, as the applied voltage increases, vertical electric fields are generated across the aperture. Because of the curved shape of top ITO electrodes, the electric fields are much weaker in the center than at the edge, and consequently the induced birefringence is much smaller in the center. Therefore, the accumulated phase profile is like a positive lens, and the outgoing light is converged. Figure 12a–c depicts three microlens structures with different top electrode shapes. The black, pink and blue curves in Figure 12d are phase profiles of structure depicted in Figure 12a–c, respectively, and the red dashed line is an ideal parabolic shape. By controlling the shape of the curved ITO electrode, they can control the phase profile to approach parabolic shape so that the spherical aberration could be suppressed.

Figure 11. The configuration and working principle of a PS-BPLC microlens using a curved ITO electrode, (**a**) voltage-off state and (**b**) voltage-on state.

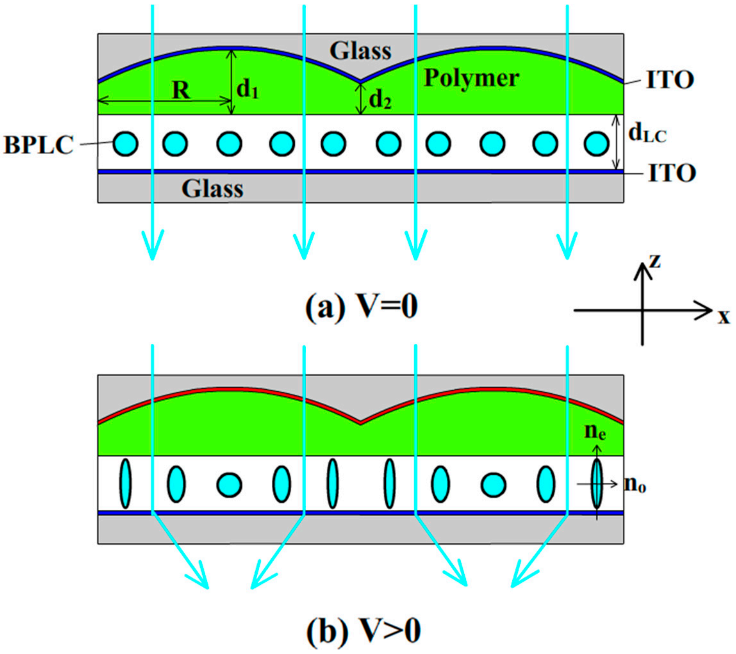

Figure 12. (**a**), (**b**) and (**c**) Microlens structures with different top ITO electrode shapes, and (**d**) the simulated phase profiles: black line for structure (**a**), pink for structure (**b**), blue line for structure (**c**), and red dashed lines for an ideal parabolic shape.

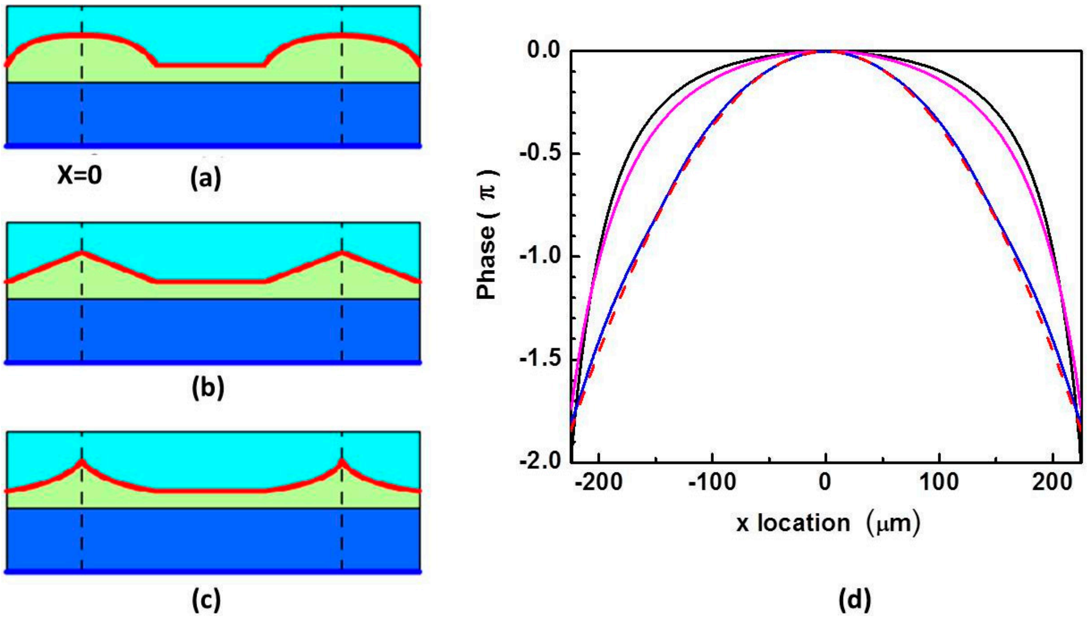

The focal length of the microlens could be calculated using the following formula:

$$f_{\mathrm{LC}} = \frac{R^2}{2\Delta n(E) d_{\mathrm{LC}}} \tag{12}$$

where $\Delta n(E)$ is refractive index difference between the center and edge of the lens, d_{LC} the cell gap, and R the semi-diameter of the lens. Figure 13 plots the focal lengths at different voltages for a specific structure (R = 225 mm, d_1 = 76 mm, d_2 = 2 mm, d_{LC} = 17 µm), employing a blue phase material with a saturation birefringence Δn = 0.2 and saturation field E_s = 5.6 V·µm^{-1}. The blue curve and pink curve are for TM (x polarization) and TE (y polarization) waves, respectively. As shown in the figure, the two curves overlap very well and this lens is indeed polarization independent. With parabolic phase profile and polarization independency, it is an attractive design; however, the fabrication of such curved electrode is relatively difficult.

Figure 13. Simulated focal lengths of a PS-BPLC microlens at different voltages.

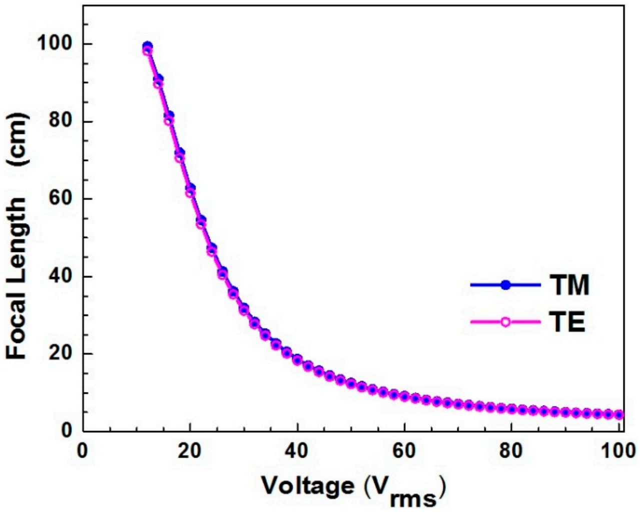

3.4. PS-PBLC Microlens with Multi-Electrode

To simplify the structure, Lee *et al*. proposed a multi-electrode-structure PS-BPLC lens as shown in Figure 14 [32]. The bottom substrate has a planar electrode while the top glass substrate has multiple electrodes with different widths and different voltages. Below these electrodes, there is a high dielectric layer to smoothen the phase profile across the lens without shielding much of voltage. By individually controlling the voltage of each electrode, an ideally parabolic phase profile can be obtained. The planar structure of multi-electrode greatly simplifies the fabrication process. This lens remains polarization independent, fast response and has a parabolic phase shape. However, it requires multiple data addressing for multiple electrodes.

Figure 14. The cross section of a PS-BPLC microlens with multiple electrodes.

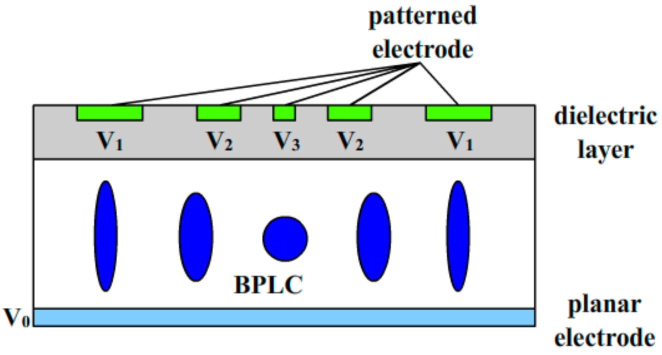

To further simplify the lens structure, a PS-BPLC cylindrical lens with a resistive film electrode was proposed [31]. As depicted in Figure 15, on the inner surface of top substrate, there is a center ITO electrode stripe at the center of the lens, and two ITO electrode stripes on the two edges, respectively. The aperture of the lens is further coated with a thin transparent high-resistive film. On the inner surface of the bottom substrate, a planar ITO electrode is coated. The resistive film has a linearly changing potential when different voltages are applied on two ends. As a result, the vertical electric field distribution also linearly varies from center to edge. In the low field region, where the Kerr effect dominates, the induced birefringence ($\Delta n = \lambda KE^2$) distribution is approximately parabolic, and so is the accumulated phase profile. Therefore, with only two electrodes, a natural parabolic phase profile is obtained. However, if the electric field further increases, saturation effect takes place, and the phase profile starts to deviate from parabolic shape gradually. Overall, this is simple design for achieving good lens performances: fast response, approximately parabolic phase profile, and polarization independency.

Figure 15. The cross section of PS-BPLC microlens using a resistive film electrode.

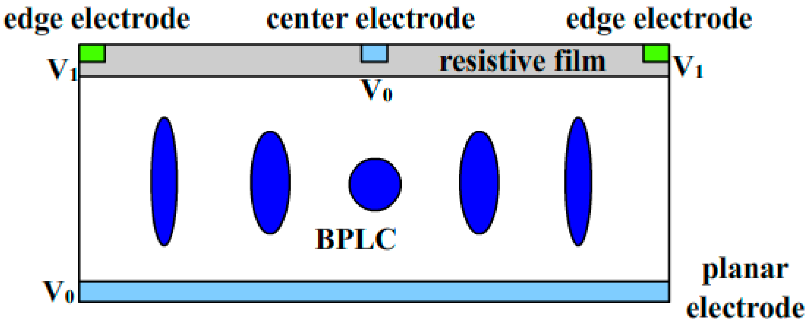

3.5. Fresnel PS-PBLC Microlens

For a BPLC lens, usually the focal length is relatively long comparing to its nematic LC counterpart, and also the required voltage is high. To increase the dynamic range, Fresnel type BPLC lenses have been developed [28,29]. Figure 16 shows the configuration and working principle of the Fresnel BPLC lens [29]. An even-zone electrode is formed on one of the substrates, and a planar common electrode is formed on the other. At voltage-off state, BPLC is optically isotropic, and there is no lensing effect. When a voltage is applied between even-zone electrode and common electrode, the refractive index in the even zones is elongated in vertical direction, while the refractive index in the odd zones remains isotropic. As a result, phase difference between the odd and even zones is generated, and the BPLC Fresnel lens is switched on.

Recently, another Fresnel BPLC lens fabricated by holography was demonstrated [28]. Figure 17 depicts the schematic of experimental setup for fabricating such a lens. The interference between a planar and a spherical wavefronts generated by the plano-convex lens naturally produces a Fresnel pattern. A polymer/LC Fresnel lens was generated upon exposure, and then the LC was washed out and a BPLC mixture was refilled into the cell. When a voltage is applied between the planar electrodes, a focusing effect occurs.

Figure 16. The device configuration and working principle of a Fresnel BPLC lens: (**a**) voltage-off state and (**b**) voltage-on state.

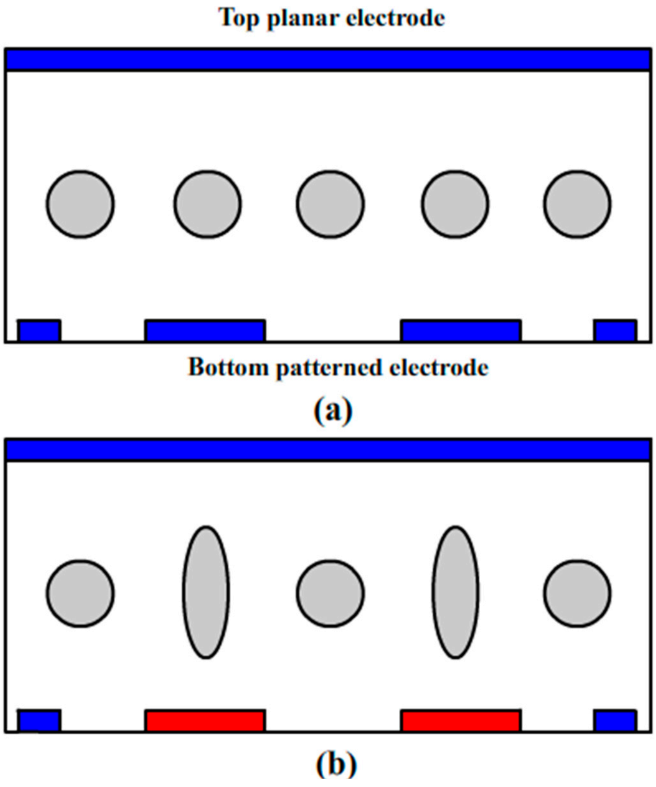

Figure 17. Schematic of experimental setup for making a Fresnel BPLC lens by holography.

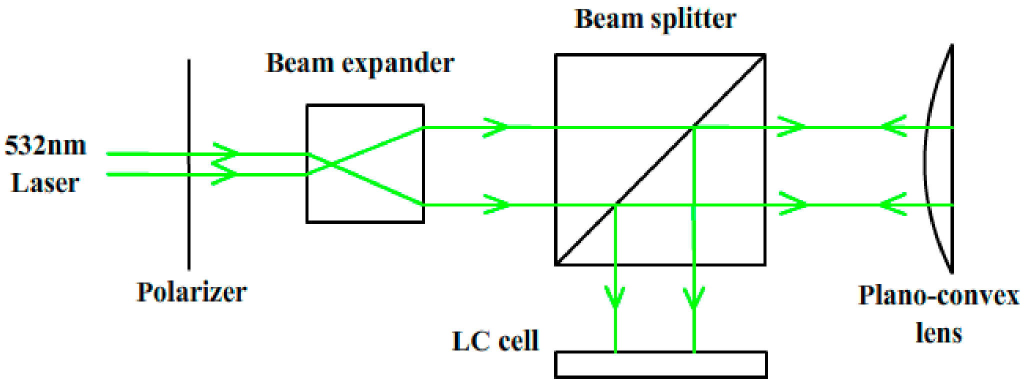

4. Conclusions and Outlook

This paper gives an overview on the state-of-the-art, fast-response LC microlenses based on LC/polymer composites. As an important extension of pure LC systems, the LC/polymer composites offer more flexibility and much richer functionalities than the LC alone. Depending on the monomer concentration, three types of LC/polymer composites have been proposed for photonic applications: PDLC, PSLC, and PNLC. Benefiting from the anchoring effect of polymer networks, these microlenses exhibit much faster response times than pure nematic LC ones. Of particular interest, we reported on four types of microlenses: nano-PDLC microlens, PSLC microlens based on patterned photomask, PDLC microlens based on patterned electrode/reconfigurable fabrications, and polymeric lenticular microlens array for 2D/3D displays, and explained their device structures, operation mechanisms, and electro-optical performances.

To advance their emerging applications and transfer the laboratory prototypes to commercial products, several technical challenges still need to be addressed. An important limitation is the relatively high operating voltage. To suppress the light scattering in visible wavelength range, a small LC droplet/domain size is preferred, which usually requires a high voltage to actuate. For example, PNLC's light scattering in the visible region is negligible at 633 nm (and ~3% at 480 nm) by selecting a high viscosity LC host and performing UV curing at a low temperature (11 °C), but the operating voltage is as high as 100 V_{rms} [65]. For nano-PDLC, the operating voltage is even higher, ~200 V_{rms}. Such a high operating voltage is not favorable for portable devices. Phase loss is a concern for PDLC/PSLC microlenses, since some LC molecules are strongly anchored by the polymer network and cannot contribute to the phase change. Therefore, the focal length tunability is rather limited. Another concern is the long-term stability of the polymer network. During the actuation, the reoriented LC domains may cause the polymer network to distort, and these distorted polymer networks may not recover to their original states. As a result, hysteresis occurs. Moreover, the distorted polymer network may lead to light scattering, which in turn degrades the lens quality. To achieve a good optical performance, the phase profile of the microlens needs to be optimized. Some PNLC microlenses suffer from astigmatism [63]. It can be reduced by using a thinner LC layer [79] or minimized by selecting a specific lens shape factor [80]. However, this shape factor is significantly different from that for minimizing its spherical aberration and coma [80]. To balance all the possible aberration arising in an LC lens, a proper shape factor should be chosen.

In addition to nematic LC/polymer composites, PS-BPLC, based on the Kerr effect, is an emerging candidate for new photonic applications. Compared with PDLC/PSLC/PNLC, BPLC microlenses have submillisecond response time. Additionally, they do not require any alignment layer, which could greatly simplify the fabrication process and improve the performance of microlenses with curved electrodes [34]. The scattering of PS-BPLC is determined by its Bragg reflection wavelength. By shifting the Bragg reflection band to UV, the scattering loss of PS-BPLC in the visible/IR band is negligible [81]. However, several problems remain to be overcome for blue phases. Firstly, due to the existence of polymer network, it is more difficult for the LC molecules to reorient in accordance to the electric field. Thus, a relatively high voltage is needed to drive the BPLC devices [16,29]. Secondly, in most tunable LC lenses, it is the variation of refractive index, rather than induced birefringence of LCs, determines the dynamic range of the focal length. For BPLC lens, however, the variations of both ordinary and extraordinary refractive indices are smaller than the induced birefringence so the dynamic range of the BPLC adaptive lens is narrower than its nematic counterpart [77]. Thirdly, all polymer-stabilized LC materials may have the long-term stability issue, if the driving voltage is higher than the onset of the electrostriction effect. Under such a circumstance, after multiple driving loops the bonding between LC molecules and polymer network might be undermined, and the polymer network itself might also be damaged. Therefore, the electro-optic properties of the LC devices will vary slowly during its entire lifetime [82]. Due to the narrow temperature range of the blue phase before stabilization, the temperature of BPLC precursor inside the LC lens chamber has to be controlled precisely during the UV exposure process, which makes mass production a challenge and increases the fabrication cost [48]. In order to solve this problem, a better BPLC material that is more tolerant to temperature variation has to be developed.

In conclusion, several types of fast-response microlenses have been demonstrated by introducing polymer networks into the pure LC system. They are attractive for practical applications in terms of fast response time, variable/switchable optical power, rapid prototyping, easy integration, low power consumption, simple driving, good mechanical stability, as well as reasonable operating voltage. As the advance of new LC/polymer materials, novel device designs, and fabrication approaches, their optical performances, as well as the electro-optical properties are expected to be more competitive. In the future, dielectrophoretically tunable optofluidic devices are foreseen to be low-cost, yet high-quality alternatives to various conventional solid-state photonic devices, and play a key role in the optical systems for imaging, information processing, sensing, optical communication, lab-on-a-chip, and biomedical engineering.

Acknowledgments

The UCF group is indebted to the U.S. Air Force Office of Scientific Research (AFOSR) for financial support under Contract No. FA95550-09-1-0170. H. Ren is supported by the National Research Foundation of Korea under Grant 2014001345.

Author Contributions

All authors helped conceive the idea and prepared the manuscript.

Conflicts of Interest

The authors declare no conflict of interest.

References

1. Schadt, M.; Helfrich, W. Voltage-dependent optical activity of a twisted nematic liquid crystal. *Appl. Phys. Lett.* **1971**, *18*, 127–128.
2. Ren, H.; Xu, S.; Wu, S.T. Voltage-expandable liquid crystal surface. *Lab Chip.* **2011**, *11*, 3426–3430.
3. Bricot, C.; Hareng, M.; Spitz, E. Optical Projection Device and an Optical Reader Incorporating This Device. U.S. Patent 4,037,929, 29 January 1980.
4. Li, L.; Bryant, D.; Heugten Van, T.; Bos, P.J. Near-diffraction-limited and low-haze electro-optical tunable liquid crystal lens with floating electrodes. *Opt. Express* **2013**, *21*, 8371–8381.

5. Lin, H.C.; Collings, N.; Chen, M.S.; Lin, Y.H. A holographic projection system with an electrically tuning and continuously adjustable optical zoom. *Opt. Express* **2012**, *20*, 27222–27229.
6. Lin, Y.H.; Chen, M.S.; Lin, H.C. An electrically tunable optical zoom system using two composite liquid crystal lenses with a large zoom ratio. *Opt. Express* **2011**, *19*, 4714–4721.
7. Lin, Y.H.; Chen, H.S. Electrically tunable-focusing and polarizer-free liquid crystal lenses for ophthalmic applications. *Opt. Express* **2013**, *21*, 9428–9436.
8. Lin, H.C.; Lin, Y.H. A fast response and large electrically tunable-focusing imaging system based on switching of two modes of a liquid crystal lens. *Appl. Phys. Lett.* **2010**, *97*, 063505; doi:10.1063/1.3479051.
9. Nose, T.; Masuda, S.; Sato, S.; Li, J.; Chien, L.C.; Bos, P.J. Effects of low polymer content in a liquid-crystal microlens. *Opt. Lett.* **1997**, *22*, 351–353.
10. Naumov, A.F.; Loktev, M.Y.; Guralnik, I.R.; Vdovin, G. Liquid-crystal adaptive lenses with modal control. *Opt. Lett.* **1998**, *23*, 992–994.
11. Ji, H.S.; Kim, J.H.; Kumar, S. Electrically controllable microlens array fabricated by anisotropic phase separation from liquid-crystal and polymer composite materials. *Opt. Lett.* **2003**, *28*, 1147–1149.
12. Choi, Y.; Park, J.H.; Kim, J.H.; Lee, S.D. Fabrication of a focal length variable microlens array based on a nematic liquid crystal. *Opt. Mater.* **2003**, *21*, 643–646.
13. Ren, H.; Wu, S.T. Tunable electronic lens using a gradient polymer network liquid crystal. *Appl. Phys. Lett.* **2003**, *82*, 22–24.
14. Presnyakov, V.V.; Galstian, T.V. Electrically tunable polymer stabilized liquid-crystal lens. *J. Appl. Phys.* **2005**, *97*, 103101–103106.
15. Kawamura, M.; Ye, M.; Sato, S. Optical particle manipulation using an LC device with eight-divided circularly hole-patterned electrodes. *Opt. Express* **2008**, *16*, 10059–10065.
16. Lin, Y.H.; Chen, H.S.; Lin, H.C.; Tsou, Y.S.; Hsu, H.K.; Li, W.Y. Polarizer-free and fast response microlens arrays using polymer-stabilized blue phase liquid crystals. *Appl. Phys. Lett.* **2010**, *96*, 113505; doi:10.1063/1.3360860.
17. Kao, Y.Y.; Chao, P.C.P.; Hsueh, C.W. A new low-voltage-driven GRIN liquid crystal lens with multiple ring electrodes in unequal widths. *Opt. Express* **2010**, *18*, 18506–18518.
18. Tseng, M.C.; Fan, F.; Lee, C.Y.; Murauski, A.; Chigrinov, V.; Kwok, H.S. Tunable lens by spatially varying liquid crystal pretilt angles. *J. Appl. Phys.* **2011**, *109*, 083109; doi:10.1063/1.3567937.
19. Lu, L.; Sergan, V.; Van Heugten, T.; Duston, D.; Bhowmik, A.; Bos, P.J. Surface localized polymer aligned liquid crystal lens. *Opt. Express* **2013**, *21*, 7133–7138.
20. Masuda, S.; Takahashi, S.; Nose, T.; Sato, S.; Ito, H. Liquid-crystal microlens with a beam-steering function. *Appl. Opt.* **1997**, *36*, 4772–4778.
21. Sun, J.; Xu, S.; Ren, H.; Wu, S.T. Reconfigurable fabrication of scattering-free polymer network liquid crystal prism/grating/lens. *Appl. Phys. Lett.* **2013**, *102*, 161106; doi:10.1063/1.4802919.
22. Na, J.H.; Park, S.C.; Kim, S.U.; Choi, Y.; Lee, S.D. Physical mechanism for flat-to-lenticular lens conversion in homogeneous liquid crystal cell with periodically undulated electrode. *Opt. Express* **2012**, *20*, 864–869.
23. Chen, C.W.; Huang, Y.P.; Chen, P.C. Dual direction overdriving method for accelerating 2D/3D switching time of liquid crystal lens on auto-stereoscopic display. *J. Disp. Technol.* **2012**, *8*, 559–561.
24. Fowler, C.W.; Pateras, E.S. Liquid crystal lens review. *Ophthal. Physiol. Opt.* **1990**, *10*, 186–194.

25. Lin, H.C.; Chen, M.S.; Lin, Y.H. A review of electrically tunable focusing liquid crystal lenses. *Trans. Electr. Electron. Mater.* **2011**, *12*, 234–240.
26. Ren, H.; Lin, Y.H.; Fan, Y.H.; Wu, S.T. Polarization-independent phase modulation using a polymer-dispersed liquid crystal. *Appl. Phys. Lett.* **2005**, *86*, 141110; doi:10.1063/1.1899749.
27. Lin, Y.H.; Ren, H.; Wu, Y.H.; Zhao, Y.; Fang, J.; Ge, Z.; Wu, S.T. Polarization-independent liquid crystal phase modulator using a thin polymer-separated double-layered structure. *Opt. Express* **2005**, *13*, 8746–8752.
28. Tian, J.; Song, Y.; Zhu, J.L.; Ni, S.B.; Wang, Y.J.; Sun, X.Y.; Lu, J.G.; Yang, B.R.; Shieh, H.P.D. Blue phase LC/polymer fresnel lens fabricated by holographics. *J. Disp. Technol.* **2014**, *10*, 157–161.
29. Lin, C.H.; Wang, Y.Y.; Hsieh, C.W. Polarization-independent and high-diffraction-efficiency Fresnel lenses based on blue phase liquid crystals. *Opt. Lett.* **2011**, *36*, 502–504.
30. Liu, Y.; Li, Y.; Wu, S.T. Polarization-independent adaptive lens with two different blue-phase liquid-crystal layers. *Appl. Opt.* **2013**, *52*, 3216–3220.
31. Li, Y.; Liu, Y.; Li, Q.; Wu, S.T. Polarization independent blue-phase liquid crystal cylindrical lens with a resistive film. *Appl. Opt.* **2012**, *51*, 2568–2572.
32. Lee, C.T.; Li, Y.; Lin, H.Y.; Wu, S.T. Design of polarization-insensitive multi-electrode GRIN lens with a blue-phase liquid crystal. *Opt. Express* **2011**, *19*, 17402–17407.
33. Li, Y.; Wu, S.T. Polarization independent adaptive microlens with a blue-phase liquid crystal. *Opt. Express* **2011**, *19*, 8045–8050.
34. Lin, S.H.; Huang, L.S.; Lin, C.H.; Kuo, C.T. Polarization-independent and fast tunable microlens array based on blue phase liquid crystals. *Opt. Express* **2014**, *22*, 925–930.
35. Wang, B.; Ye, M.; Sato, S. Liquid crystal lens with stacked structure of liquid-crystal layers. *Opt. Commun.* **2005**, *250*, 266–273.
36. Huang, Y.; Wen, C.H.; Wu, S.T. Polarization-independent and submillisecond response phase modulators using a 90° twisted dual-frequency liquid crystal. *Appl. Phys. Lett.* **2006**, *89*, 021103; doi:10.1063/1.2219998.
37. Ren, H.; Lin, Y.H.; Wu, S.T. Polarization-independent and fast-response phase modulators using double-layered liquid crystal gels. *Appl. Phys. Lett.* **2006**, *88*, 061123; doi:10.1063/1.2173248.
38. Fuh, A.Y.G.; Ko, S.W.; Huang, S.H.; Chen, Y.Y.; Lin, T.H. Polarization-independent liquid crystal lens based on axially symmetric photoalignment. *Opt. Express* **2011**, *19*, 2294–2300.
39. Kao, Y.Y.; Chao, P.C.P. A new fual-grequency liquid crystal lens with ring-and-pie electrodes and a driving scheme to prevent disclination lines and improve recovery time. *Sensors* **2011**, *11*, 5402–5415.
40. Pishnyak, O.; Sato, S.; Lavrentovich, O.D. Electrically tunable lens based on a dual-frequency nematic liquid crystal. *Appl. Opt.* **2006**, *45*, 4576–4582.
41. Schadt, M. Dielectric heating and relaxations in nematic liquid crystals. *Mol. Cryst. Liq. Cryst.* **1981**, *66*, 319–336.
42. Kim, J.H.; Kumar, S. Fabrication of electrically controllable microlens array using liquid crystals. *J. Lightwave Technol.* **2005**, *23*, 628–632.
43. Kim, J.H.; Kumar, S. Fast switchable and bistable microlens array using ferroelectric liquid crystals. *Jpn. J. Appl. Phys.* **2004**, *43*, 7050; doi:10.1143/JJAP.43.7050.

44. Lee, Y.M.; Gwag, J.; Choi, Y.; Lee, K.H.; Yu, C.J.; Kim, J.H. Fast switching characteristics of a microlens array using the electroclinic effect of SmA* liquid crystals. *Appl. Opt.* **2009**, *48*, 3737–3741.
45. Rao, L.; Ge, Z.; Wu, S.T.; Lee, S.H. Low voltage blue-phase liquid crystal displays. *Appl. Phys. Lett.* **2009**, *95*, 231101; doi:10.1063/1.3271771.
46. Ge, Z.; Gauza, S.; Jiao, M.; Xianyu, H.; Wu, S.T. Electro-optics of polymer-stabilized blue phase liquid crystal displays. *Appl. Phys. Lett.* **2009**, *94*, 101104; doi:10.1063/1.3097355.
47. Haseba, Y.; Kikuchi, H.; Nagamura, T.; Kajiyama, T. Large electro-optic Kerr effect in nanostructured chiral liquid-crystal composites over a wide temperature range. *Adv. Mater.* **2005**, *17*, 2311–2315.
48. Kikuchi, H.; Yokota, M.; Hisakado, Y.; Yang, H.; Kajiyama, T. Polymer-stabilized liquid crystal blue phases. *Nat. Mater.* **2002**, *1*, 64–68.
49. Yan, J.; Rao, L.; Jiao, M.; Li, Y.; Cheng, H.C.; Wu, S.T. Polymer-stabilized optically isotropic liquid crystals for next-generation display and photonics applications. *J. Mater. Chem.* **2011**, *21*, 7870–7877.
50. Yan, J.; Wu, S.T. Polymer-stabilized blue phase liquid crystals: a tutorial. *Opt. Mater. Express* **2011**, *1*, 1527–1535.
51. Chen, Y.; Xianyu, H.; Sun, J.; Kula, P.; Dabrowski, R.; Tripathi, S.; Twieg, R.J.; Wu, S.T. Low absorption liquid crystals for mid-wave infrared applications. *Opt. Expr.* **2011**, *19*, 10843–10848.
52. Khoo, I.C.; Wu, S.T. *Optics and Nonlinear Optics of Liquid Crystals*; World Scientific: Singapore, 1993.
53. Ren, H.; Wu, S.T. *Introduction to Adaptive Lenses*; Wiley: Hoboken, New Jersey, NY, US, 2012.
54. Ren, H.; Fan, Y.H.; Lin, Y.H.; Wu, S.T. Tunable-focus microlens arrays using nanosized polymer-dispersed liquid crystal droplets. *Opt. Commun.* **2005**, *247*, 101–106.
55. Presnyakov, V.; Asatryan, K.; Galstian, T.; Tork, A. Polymer-stabilized liquid crystal for tunable microlens applications. *Opt. Express* **2002**, *10*, 865–870.
56. Ren, H.; Fan, Y.H.; Gauza, S.; Wu, S.T. Tunable microlens arrays using polymer network liquid crystal. *Opt. Commun.* **2004**, *230*, 267–271.
57. Gauza, S.; Wang, H.; Wen, C.H.; Wu, S.T.; Seed, A.J.; Dabrowski, R. High birefringence isothiocyanato tolane liquid crystals. *Jpn. J. Appl. Phys.* **2003**, *42*, 3463–3466.
58. Gauza, S.; Wen, C.H.; Wu, S.T.; Janarthanan, N.; Hsu, C.S. Super high birefringence isothiocyanato biphenyl-bistolane liquid crystals. *Jpn. J. Appl. Phys.* **2004**, *43*, 7634–7638.
59. Doane, J.W.; Vaz, N.A.; Wu, B.G.; Žumer, S. Field controlled light scattering from nematic microdroplets. *Appl. Phys. Lett.* **1986**, *48*, 269–271.
60. Rajaram, C.V.; Hudson, S.D.; Chien, L.C. Morphology of polymer-stabilized liquid crystals. *Chem. Mater.* **1995**, *7*, 2300–2308.
61. Ren, H.; Fan, Y.H.; Wu, S.T. Polymer network liquid crystals for tunable microlens arrays. *J. Phys. D Appl. Phys.* **2004**, *37*, 400–403.
62. Xu, M.; Zhou, Z.; Ren, H.; Seung, H.; Wang, Q. A microlens array based on polymer network liquid crystal. *J. Appl. Phys.* **2013**, *113*, 053105; doi:10.1063/1.4790303.
63. Ren, H.; Xu, S.; Wu, S.T. Polymer-stabilized liquid crystal microlens array with large dynamic range and fast response time. *Opt. Lett.* **2013**, *38*, 3144–3147.

64. Ren, H.; Xu, S.; Wu, S.T. Gradient polymer network liquid crystal with a large refractive index change. *Opt. Express* **2012**, *20*, 26464–26472.
65. Sun, J.; Chen, Y.; Wu, S.T. Submillisecond-response and scattering-free infrared liquid crystal phase modulators. *Opt. Express* **2012**, *20*, 20124–20129.
66. Woodgate, G.J.; Harrold, J.; Jacobs, A.M.S.; Moseley, R.R.; Ezra, D. Flat-panel autostereoscopic displays: characterization and enhancement. In Proceedings of the SPIE 3957, Stereoscopic Displays and Virtual Reality Systems VII, 153, San Jose, CA, USA, 22 January 2000.
67. Choi, H.; Park, J.H.; Kim, J.; Cho, S.W.; Lee, B. Wide-viewing-angle 3D/2D convertible display system using two display devices and a lens array. *Opt. Express* **2005**, *13*, 8424–8432.
68. Dekker, T.; de Zwart, S.T.; Willemsen, O.H.; Hiddink, M.G.H.; Ijzerman, W.L. 2D/3D switchable displays. In proceedings of SPIE 6196, Photonics in Multimedia, 61960H, Strasbourg, France, 3 April 2006.
69. Krijn, M.P.C.M.; de Zwart, S.T.; de Boer, D.K.G.; Willemsen, O.H.; Sluijter, M. 2D/3D displays based on switchable lenticulars. *J. Soc. Inf. Disp.* **2008**, *16*, 847–855.
70. Takagi, A.; Saishu, T.; Kashiwagi, M.; Taira, K.; Hirayama, Y. Autostereoscopic partial 2-D/3-D switchable display using liquid-crystal gradient index lens. *SID Symp. Dig.* **2010**, *41*, 436–439.
71. Chen, C.W.; Huang, Y.C.; Huang, Y.P.; Huang, J.F. Fast switching fresnel liquid crystal lens for autostereoscopic 2D/3D display. *SID Symp. Dig.* **2010**, *41*, 428–431.
72. Lai, Y.K.; Lai, Y.F.; Chen, Y.C. An effective hybrid depth-generation algorithm for 2D-to-3D conversion in 3D displays. *J. Disp. Technol.* **2013**, *9*, 154–161.
73. Flack, J.; Harrold, J.; Woodgate, G.J. A prototype 3D mobile phone equipped with a next-generation autostereoscopic display. In Proceedings of SPIE 6490, Stereoscopic Displays and Virtual Reality Systems XIV, San Jose, CA, USA, 28 January 2007.
74. Ren, H.; Xu, S.; Liu, Y.; Wu, S.T. Switchable focus using a polymeric lenticular microlens array and a polarization rotator. *Opt. Express* **2013**, *21*, 7916–7925.
75. Ren, H.; Xu, S.; Liu, Y.; Wu, S.T. Optically anisotropic microlens array film directly formed on a single substrate. *Opt. Express* **2013**, *21*, 29304–29312.
76. Jones, T.B. *Electromechanics of Particles*; Cambridge Universtiy Press: Cambridge, UK, 1995.
77. Chen, K.M.; Gauza, S.; Xianyu, H.; Wu, S.T. Submillisecond gray-level response time of a polymer-stabilized blue-phase liquid crystal. *J. Disp. Technol.* **2010**, *6*, 49–51.
78. Yan, J.; Cheng, H.C.; Gauza, S.; Li, Y.; Jiao, M.; Rao, L.; Wu, S.T. Extended Kerr effect of polymer-stabilized blue-phase liquid crystals. *Appl. Phys. Lett.* **2010**, *96*, 071105; doi:10.1063/1.3318288.
79. Kikuta, H.; Iwata, K.; Shimomura, H. First-order aberration of a double-focus lens made of a uniaxial crystal. *J. Opt. Soc. Am. A* **1992**, *9*, 814–819.
80. Lesso, J.P.; Duncan, A.J.; Sibbett, W.; Padgett, M.J. Aberrations introduced by a lens made from a birefringent material. *Appl. Opt.* **2000**, *39*, 592–598.
81. Kikuchi, H.; Higuchi, H.; Haseba, Y.; Iwata, T. Fast electro-Optical switching in polymer-stabilized liquid crystalline blue ohases for display application. *SID Symp. Dig.* **2007**, *38*, 1737–1740.
82. Lan, Y.F.; Tsai, C.Y.; Lu, J.K.; Sugiura, N. Mechanism of hysteresis in polymer-network stabilized blue phase liquid crystal. *Polymer* **2013**, *54*, 1876–1879.

Simulation Study on Polarization-Independent Microlens Arrays Utilizing Blue Phase Liquid Crystals with Spatially-Distributed Kerr Constants

Hung-Shan Chen, Michael Chen, Chia-Ming Chang, Yu-Jen Wang and Yi-Hsin Lin

Abstract: Polarization independent liquid crystal (LC) microlens arrays based on controlling the spatial distribution of the Kerr constants of blue phase LC are simulated. Each sub-lens with a parabolic distribution of Kerr constants results in a parabolic phase profile when a homogeneous electric field is applied. We evaluate the phase distribution under different applied voltages, and the focusing properties of the microlens arrays are simulated. We also calculate polarization dependency of the microlenses arrays at oblique incidence of light. The impact of this study is to provide polarizer-free, electrically tunable focusing microlens arrays with simple electrode design based on the Kerr effect.

Reprinted from *Micromachines*. Cite as: Chen, H.-S.; Chen, M.; Chang, C.-M.; Wang, Y.-J.; Lin, Y.-H. Simulation Study on Polarization-Independent Microlens Arrays Utilizing Blue Phase Liquid Crystals with Spatially-Distributed Kerr Constants. *Micromachines* **2014**, *5*, 859–867.

1. Introduction

Liquid crystal (LC) microlens arrays are important in applications of 2D/3D switching, fiber coupling, and sensors [1–3]. Most of proposed structures of LC microlens arrays require at least one polarizer. To remove the usage of a polarizer, polarization independent LC phase modulations are developed. Three types of polarization independent LC phase modulations have been proposed: the type of the double-layered structure, the type of the residual phase structure, and the mixed type [4–10]. However, the structures were relatively complicated and the response times were slow. In 2010, we proposed a polarization independent polymer stabilized blue phase liquid crystal (PSBP-LC) microlens arrays based on the electric-field-induced Kerr effect, the field-induced birefringence is proportional to the electric field squared [11]. The Kerr effect exists in many LC materials, such as polymer stabilized isotropic phase liquid crystals, nematic liquid crystals, blue phase liquid crystals, and even ferroelectric liquid crystals [12–14]. In this paper, we proposed polarization independent LC microlens arrays based on controlling the distribution of the Kerr constants of blue phase LC (BPLC). The simulated results indicate the distribution of the Kerr constants of BPLC results in a parabolic optical phase shift and the proposed microlens arrays are capable of imaging. The polarization dependency of the LC microlens arrays is also discussed. The purpose of this study is mainly to provide a way to achieve polarizer-free, electrically tunable focusing microlens arrays with simple electrode design based on the Kerr effect.

2. Operating Principle and Lens Design

The Kerr medium, such as BPLC and PSBP-LC, is optically isotropic without an external electric field [11]. Under an external electric field (*E*), the optical axis of the field-induced birefringence is parallel to the electric field. The field-induced birefringence (Δn) is written as [15]:

$$\Delta n = n_e(E) - n_o(E) = \lambda \cdot K \cdot E^2 \tag{1}$$

where n_o is ordinary refractive index, n_e is extraordinary refractive index, K is the Kerr constant of the LC materials, and λ is wavelength of the incident light. Regarding the local orientations of LC molecules of BPLC under external electric field, $n_o(E)$ and $n_e(E)$ can be further expressed in Equations (2) and (3):

$$n_{\mathrm{o}}(E) = n_{\mathrm{ave}} - \frac{\lambda \cdot K \cdot E^2}{3} \tag{2}$$

$$n_{\mathrm{e}}(E) = n_{\mathrm{ave}} + \frac{2}{3} \cdot \lambda \cdot K \cdot E^2 \tag{3}$$

where n_{ave} represents the average refractive index without any applied electric field (*i.e.*, $n_{\mathrm{ave}} = (n_{\mathrm{e}} + 2n_{\mathrm{o}})/3$). As a result, polarization independent phase modulation based on the Kerr effect of LC materials can be achieved. To generate a corresponding polarization independent phase profile of a lens, an inhomogeneous electric field is a way to be adopted [11]. However, the patterned electrodes are required. Instead of patterned electrodes, we proposed a spatially-distributed Kerr constant to achieve polarization independent microlens arrays. The structure and operating principles are depicted in Figure 1a,b. The structure primary consists of LC materials and two glass substrates coated with a layer of indium-tin-oxide (ITO). Without an applied voltage (*V*), an incident unpolarized light propagating along *z*-direction sees the average refractive index of n_{ave} because the effective optical index-ellipsoids are spherical which means the LC material is optically isotropic due to the cubic symmetry of the lattice structure, as depicted in Figure 1a [11,16]. With an applied voltage, an incident unpolarized light sees a spatial optical phase difference originating from a spatial distribution of Kerr constants, as depicted in Figure 1b. Assume the Kerr constant is spatially distributed in a parabolic form which can be expressed as:

$$K(r) = K_{\mathrm{c}} - \frac{K_{\mathrm{c}} - K_{\mathrm{b}}}{r_0^2} \cdot r^2 \tag{4}$$

where r_0 is the radius of aperture of a sub-lens, r is position, K_c is the Kerr constant at the center of the aperture, and K_b is the Kerr constant around the peripheral region. Optical phase difference (OPD) under an applied voltage ($\delta(r)$) is $2\pi / \lambda \cdot [n_{\mathrm{o}}(E) \cdot d]$, where d is the cell gap. From Equations (2) and (4), OPD is:

$$\delta(r) = \frac{2\pi}{\lambda} \times d \times \left[n_{\mathrm{ave}} - \frac{\lambda \times E^2}{3} \times \left(K_{\mathrm{c}} - \frac{K_{\mathrm{c}} - K_{\mathrm{b}}}{r_0^2} r^2 \right) \right] \tag{5}$$

r^2 term in Equation (4) is related to the focal length (*f*), inverse of lens power (*P*) [17,18]. Lens power is the degree that a lens converges or diverges light. The unit of lens power is diopter (D or m^{-1}). Thereafter, the lens power is written as:

$$P(E) = -\frac{2 \times \lambda \times d \times E^2 \times (K_{\mathrm{c}} - K_{\mathrm{b}})}{3 \times r_0^2} = -\frac{2 \times \lambda \times d \times E^2 \times \Delta K}{3 \times r_0^2} \tag{6}$$

where ΔK is defined as $(K_{\mathrm{c}} - K_{\mathrm{b}})$. Thus, we can realize microlens arrays based on spatially- distributed Kerr constants whose lens power is electrically tunable. The lens power of the mocrolens arrays is larger as both the applied electric field and ΔK are larger.

Figure 1. The structure and operating principles of the LC (liquid crystal) microlens arrays (**a**) without an applied voltage and (**b**) with an applied voltage.

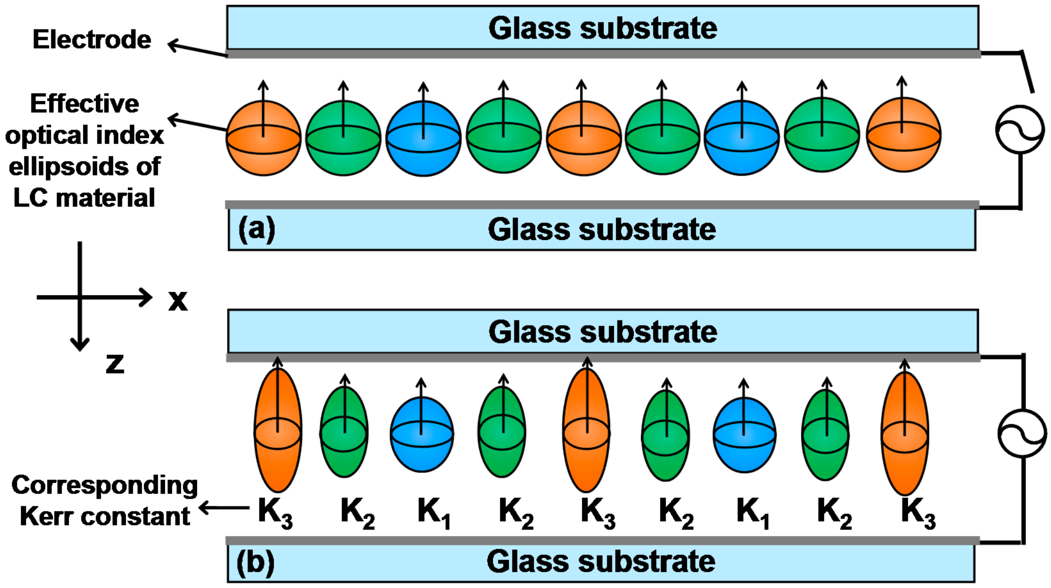

3. Simulation Results and Discussion

Here we simulate LC microlens arrays with spatially-distributed Kerr constants. The designed aperture size and the spacing between adjacent sub-lenses are 100 µm. The cell gap of the LC lenses is 25 µm. Usually Kerr constant is in a range between 10^{-8} and 10^{-10} V^2/m [19–21]. To demonstrate microlens arrays with a positive focal length, we design the Kerr constant in the center of a sub-lens (K_c) is 10^{-8} V^2/m while the Kerr constant at the peripheral region of a sub-lens (K_b) is 10^{-9} V^2/m. Figure 2 plots the parabolic distribution of Kerr constants of the microlens arrays based on the parameters we designed. We defined the phase shift as the difference between OPD at an applied voltage (V) and at $V = 0$. From Figure 2a and Equation (5), the phase shift as a function of position is shown in Figure 2b. The curve of phase shift in Figure 2b exhibits a periodically parabolic form at $V > 0$ due to the parabolic distribution of Kerr constant of the LC layer. The phase shift increases with an applied voltage. Based on Equation (6) and the parabolic distribution we designed, the simulated voltage-dependent lens power is depicted in Figure 2c. The lens power increases with an applied voltage. The lens power at $V = 100$ V_{rms} is around 650 m^{-1}, which is corresponding to the focal length of ~1.54 mm.

Figure 2. (**a**) The spatial distribution of Kerr constants of the LC microlens arrays based on the parameters we designed; (**b**) the corresponding spatial phase shift of the LC microlens arrays at $V = 0$ (red line), 50 V_{rms} (green line), and 100 V_{rms} (blue line); and (**c**) the simulated voltage- dependent lens power.

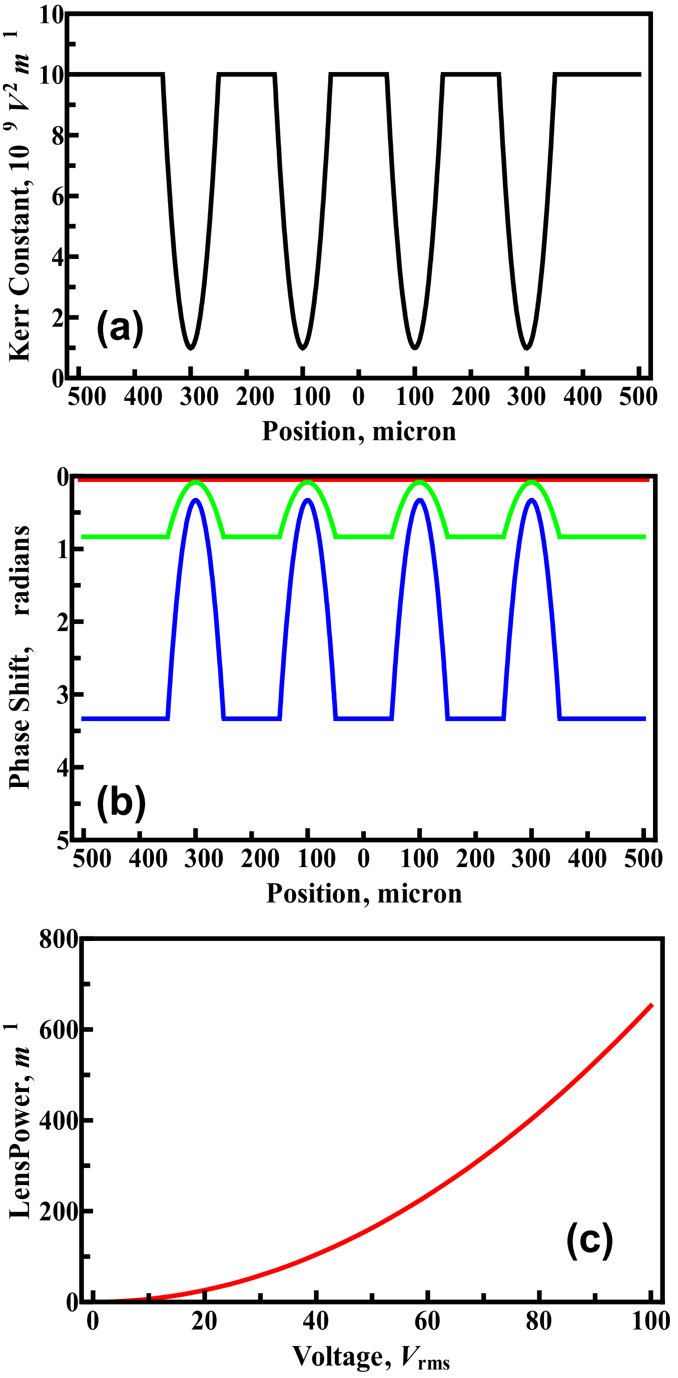

To simulate the focusing properties of the microlens arrays at the focal plane, we adopted the Fresnel approximation [22]. Figure 3a,b shows the spatial phase shift and corresponding intensity distribution at the focal plane of the micolens arrays. As we can see, the parabolic phase shift (red line in Figure 3a results in sharp peaks at the focal plane (red line in Figure 3b). In contrast, the trapezoid-like phase shift (blue dotted line in Figure 3a) results in relatively broad peaks at the focal plane (blue dotted line in Figure 3b). Therefore, the parabolic phase distribution is necessary to realize good imaging quality which also means the distribution of Kerr constants should be parabolic. In 2011, Wu *et al.* proposed an Eiffel-Tower-like ITO electrode to generate an ideal phase distribution in BPLC [23]. However, the Eiffel-Tower-like ITO electrode is difficult to fabricate. The method of the spatial distribution of Kerr constants that we proposed is more practical because our method does not require complex electrodes.

Figure 3. (**a**) The simulated spatial phase shifts of the LC microlens arrays. Blue dotted line stands for periodically trapezoid-like phase shift and red line stands for periodically parabolic phase shift; (**b**) the corresponding intensity distribution at the focal plane for the periodically trapezoid-like phase shift (dotted blue line) and the periodically parabolic phase shift (red line).

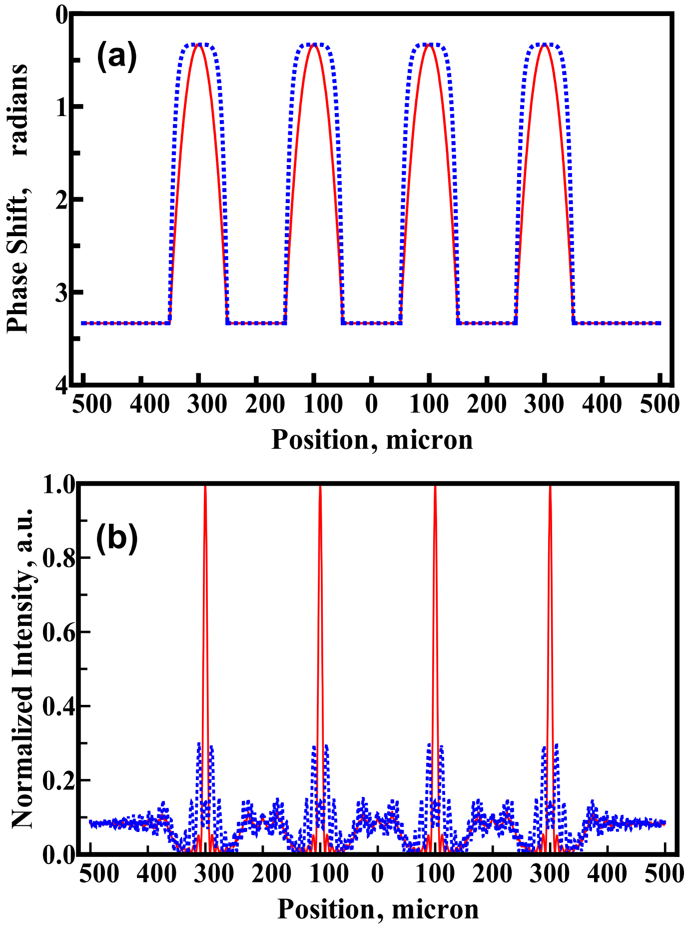

The LC microlens arrays as incident light is at the oblique angle (*i.e.*, off-axis) is also important in applications. Assume the incident angle is θ_i with respect to *z*-direction and the light propagates in LC cell with an angle of θ_{LC}. Because the change of the refractive index of the Kerr medium is very small (normally < 0.05), we can assume the incident light propagates in a straight way in the medium and θ_{LC} is able to be deduced from Snell's law (*i.e.*, $n_{air} \times \sin\theta_i = n_{ave} \times \sin\theta_{LC}$). Two eigenmodes propagating in the LC medium are defined as e-mode and the o-mode. The polarization of e-mode lies in the plane of *x*-*z* plane and that of o-mode is perpendicular to *x*-*z* plane. Thereafter, we can calculate the phase shift of the e-mode as:

$$\delta_{e-\mathrm{mode}e}(E,x)=\frac{2\pi}{\lambda}\int n_{\mathrm{e,eff}}(E,\theta_{\mathrm{LC}},x)\cdot dk=\frac{2\pi}{\lambda}\int n_{\mathrm{e,eff}}(E,\theta_{\mathrm{LC}},x)\cdot\csc\theta_{\mathrm{LC}}\cdot dx \tag{7}$$

where the effective extraordinary refractive index ($n_{\mathrm{e,eff}}$) can be expressed as:

$$n_{\mathrm{e,eff}}(E,\theta_{\mathrm{LC}},x)=\left(\frac{n_{\mathrm{e}}^2(E,x)}{\sin^2(\theta_{\mathrm{LC}})}+\frac{n_{\mathrm{o}}^2(E,x)}{\cos^2(\theta_{\mathrm{LC}})}\right)^{-0.5} \tag{8}$$

The phase shift of the o-mode can also be expressed as:

$$\delta_{\mathrm{o\text{-}mode}}(E,x)=\frac{2\pi}{\lambda}\int n_{\mathrm{o}}(E,x)\cdot dk=\frac{2\pi}{\lambda}\int n_{\mathrm{o}}(E,x)\cdot\csc\theta_{\mathrm{LC}}\cdot dx \tag{9}$$

To simplify the discussion, a single sub-lens is considered in the following discussions. The diameter of the sub-lens and the cell gap are 100 and 25 μm, respectively. The simulated phase shifts as incident light is at the oblique angle are shown in Figure 4. The dotted line represents the phase shift of e-mode while the solid line represents the o-mode at $V = 100$ V_{rms}. The blue and the red represent θ_{LC} of ~+10° and −10°, respectively. From Snell's law, θ_{i} is ~±15.7° when corresponding θ_{LC} is ±10° and n_{ave} is around 1.56. From the simulation results, the phase shift between the center and the peripheral region for the e-mode is around 3π radians. As to the o-mode, the phase shift between the center and the peripheral region is around ~2.8π. This also indicates the micorlens arrays are polarization dependent at the oblique incidence because the refractive index changes more for o-ray than that for e-ray. To reduce the polarization dependency of the phase shift at oblique incidence, we can use other electrically tunable LC cells for phase compensation.

To experimentally realize the spatial distribution of the Kerr constants of the LC materials, one can produce the spatial distribution of Kerr constants of the Kerr medium, such as BPLC, in terms of fabrication method of spatial temperature gradient. Based on previous research results, the Kerr constant is proportional to the coherent length squared (ξ^2), inversely proportional to $T-T^*$, where T is temperature and T^* represents the temperature as the coherent length of the LC become infinite (*i.e.*, $K \propto \xi^2 \propto 1/T-T^*$) [19–21]. As a result, the Kerr constant of BPLC strongly depends on the temperature. Therefore, the spatial distribution of the Kerr constant can be controlled by means of temperature gradient, and then we can use photo-polymerization to stabilize BPLC in order to regulate the distribution of phase separation and further to generate spatially-distributed Kerr constants. To demonstrate the proposed idea, we step-controlled the curing temperatures of the PSBP-LC materials, and we realized the Kerr constant difference check by phase retardation measurement three times. However, due to the limit of the temperature gradient controlling instrument, we are not able to put such a big Kerr constant difference within this small aperture region. For further implementation of this concept, one might need step masks or more precision thermal controlling machines to get steep phase distribution within the aperture.

Figure 4. The simulated phase shift at the oblique angle. The dotted line represents the phase shift of o-mode and the solid line represents the phase shift of e-mode. The blue and red represent the incident angle θi is +15.7° and −15.7°, respectively.

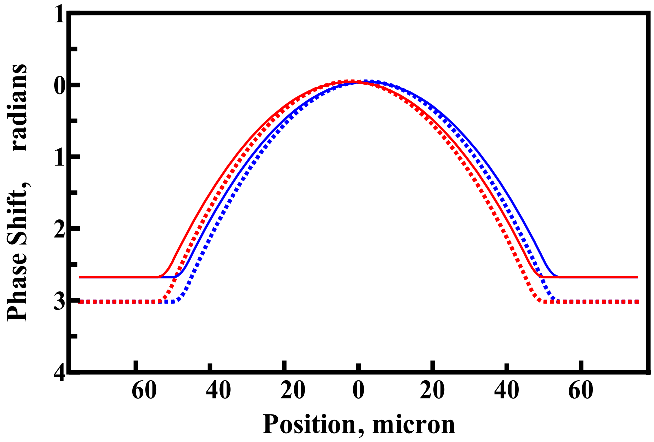

4. Conclusions

We proposed a polarization independent LC microlens arrays based on spatially distributed Kerr constants of the LC material. The mechanism and simulated performance are discussed. In addition, we also evaluate the polarization dependency of the microlens arrays at oblique angle of incidence. This study provides a method to realize polarizer-free and electrically tunable microlens arrays with simple electrodes based on the Kerr effect.

Acknowledgments

This research was supported partially by the Ministry of Science and Technology (MOST) in Taiwan under the contract No. NSC 101-2112-M-009-011-MY3.

Author Contributions

Hung-Shan Chen proposed the concept, did the simulation and wrote the manuscript. Michael Chen, Chia-Ming Chang, and Yu-Jen Wang helped in the simulations and discussions. Yi-Hsin Lin discussed the concept and results with Hung-Shan Chen, and also revised the manuscript.

Conflicts of Interest

The authors declare no conflict of interest

References

1. Liu, Y.F.; Ren, H.W.; Xu, S.; Li, Y.; Wu, S.T. Fast-response liquid crystal lens for 3D displays. *SPIE Proc.* **2014**, *9005*, 1–10.
2. Chen, M.; Chen, C.H.; Lai, Y.; Lu, Y.C.; Lin, Y.H. An electrically tunable polarizer for a fiber system based on a polarization-dependent beam size derived from a liquid crystal lens. *IEEE Photonics J.* **2014**, *6*, 1–8.

3. Klaus, W.; Ide, M.; Hayano, Y.; Morokawa, S.; Arimoto, Y. Adaptive LC lens array and its application. *SPIE Proc.* **1999**, *3635*, 66–73.
4. Lin, Y.H.; Ren, H.W.; Wu, Y.H.; Zhao, Y.; Fang, J.Y.; Ge, B.Z.; Wu, S.H. Polarization-independent liquid crystal phase modulator using a thin polymer-separated double-layered structure. *Opt. Express* **2005**, *13*, 8746–8752.
5. Lin, Y.H.; Ren, H.W.; Fan, Y.H.; Wu, Y.H.; Wu, S.T. Polarization-independent and fast-response phase modulation using a normal-mode polymer-stabilized cholesteric texture. *J. Appl. Phys. Lett.* **2005**, *98*, doi:10.1063/1.2037191.
6. Ren, H.W.; Lin, Y.H.; Fan, Y.H.; Wu, S.T. Polarization-independent phase modulation using a polymer-dispersed liquid crystal. *Appl. Phys. Lett.* **2005**, *86*, doi:10.1063/1.1899749.
7. Wu, Y.H.; Lin, Y.H.; Lu, Y.Q.; Ren, H.; Fan, Y.H.; Wu, J.R.; Wu, S.T. Submillisecond response variable optical attenuator based on sheared polymer network liquid crystal. *Opt. Express* **2004**, *12*, 6382–6389.
8. West, J.L.; Zhang, G.Q.; Reznikov, Y.; Glushchenko, A. Fast birefringent mode of stressed liquid crystal. *Appl. Phys. Lett.* **2005**, *86*, doi:10.1063/1.1852720.
9. Ren, H.; Lin, Y.H.; Wen, C.H.; Wu S.T. Polarization-independent phase modulation of a homeotropic liquid crystal gel. *Appl. Phys. Lett.* **2005**, *87*, doi:10.1063/1.2126107.
10. Lin, T.H.; Chen, M.S.; Lin, W.C.; Tsou, Y.S. A polarization-independent liquid crystal phase modulation using polymer-network liquid crystals in a 90° twisted cell. *J. Appl. Phys. Lett.* **2012**, *112*, doi:10.1063/1.4737260.
11. Lin, Y.H.; Chen, H.S.; Lin, H.C.; Tsou, Y.S.; Hsu, H.K.; Li, W.Y. Polarizer-free and fast response microlens arrays using polymer-stabilized blue phase liquid crystals. *Appl. Phys. Lett.* **2010**, *96*, doi:10.1063/1.3360860.
12. Yang, Y.C.; Yang, D.K. Electro-optic Kerr effect in polymer-stabilized isotropic liquid crystals. *Appl. Phys. Lett.* **2011**, *98*, doi:10.1063/1.3533396.
13. Khoshsima, H.; Tajalli, H.; Ghanadzadeh Gilani, A.; Dabrowski, R. Electro-optical Kerr effect of two high birefringence nematic liquid crystals. *Appl. Phys. Lett.* **2006**, *39*, 1495–1499.
14. Pozhidaev, E.P.; Kiselev, A.D.; Srivastave, A.K.; Chigrinov, V.G.; Kwok, H.S.; Minchenko, M.V. Orientational “Kerr effect” and phase modulaion of light in deformed-helix ferroelectric liquid crystals with subwavelength pitch. *Phys. Rev.* **2013**, *87*, doi:10.1103/PhysRevE.87.052502.
15. Lin, Y.H.; Chen, H.S.; Wu, C.H.; Hsu, H.K. Measuring electric-field-induced birefringence in polymer stabilized blue phase liquid crystal based on phase shift measurement. *J. Appl. Phys.* **2011**, *109*, doi:10.1063/1.3583572.
16. Amnon, Y.; Yeh, P. *Optical Waves in Crystals: Propagation and Control of Laser Radiation*; Wiley: New York, NY, USA, 1984; p. 83.
17. Lin, H.C.; Chen, M.S.; Lin, Y.H. A review of electrically tunable focusing liquid crystal lenses. *Trans. Electr. Electron. Mater.* **2011**, *12*, 234–240.
18. Lin, Y.H.; Chen, H.S. Electrically tunable-focusing and polarizer-free liquid crystal lenses for ophthalmic applications. *Opt. Express* **2013**, *21*, 9428–9436.
19. Haseba, Y.; Kikuchi, H.; Nagamura, T.; Kajiyama, T. Large electr-optic Kerr effect in nanostructures chiral liquid-crystal composites over a wide temperature range. *Adv. Mater.* **2005**, *17*, 2311–2315.

20. Tian, L.; Goodby, J.W.; Gortz, V.; Gleeson, H.F. The magnitude and tmeperature dependence of the Kerr constant in liquid crystal blue phases and the dark conglomerate phase. *Liq. Crys.* **2013**, *40*, 1446–1454.
21. Majles Ara, M.H.; Mousavi, S.H.; Rafiee, M.; Zakerhamidi, M.S. Dtermination of temperature dependence of Kerr constant for nematic liquid crystal. *Mol. Cryst. Liq. Cryst.* **2011**, *544*, 227/[1215]–231/[1219]
22. Goodman, J.W. *Introduction to Fourier Optics*, 3rd ed.; Roberts and Company Publishers: Greenwood Village, CO, USA, 2005; p. 67.
23. Li, Y.; Wu, S.T. Polarization independent adaptive microlens with a blue-phase liquid crystal. *Opt. Express* **2011**, *19*, 8045–8050.

Adaptive Liquid Lens Actuated by Droplet Movement

Chao Liu, Qiong-Hua Wang, Li-Xiao Yao and Ming-Huan Wang

Abstract: In this paper we report an adaptive liquid lens actuated by droplet movement. Four rectangular PMMA (Polymethyl Methacrylate) substrates are stacked to form the device structure. Two ITO (Indium Tin Oxide) sheets stick on the bottom substrate. One PMMA sheet with a light hole is inserted in the middle of the device. A conductive droplet is placed on the substrate and touches the PMMA sheet to form a small closed reservoir. The reservoir is filled with another immiscible non-conductive liquid. The non-conductive liquid can form a smooth concave interface with the light hole. When the device is applied with voltage, the droplet stretches towards the reservoir. The volume of the reservoir reduces, changing the curvature of the interface. The device can thus achieve the function of an adaptive lens. Our experiments show that the focal length can be varied from −10 to −159 mm as the applied voltage changes from 0 to 65 V. The response time of the liquid lens is ~75 ms. The proposed device has potential applications in many fields such as information displays, imaging systems, and laser scanning systems.

Reprinted from *Micromachines*. Cite as: Liu, C.; Wang, Q.-H.; Yao, L.-X.; Wang, M.-H. Adaptive Liquid Lens Actuated by Droplet Movement. *Micromachines* **2014**, *5*, 496–504.

1. Introduction

Adaptive microlens has received considerable attention for the wide range of applications such as information displays, cameras, laser scanning systems, and wavefront distortion compensation. According to the difference of the filled materials, it can be roughly classified into two categories: liquid crystal (LC) lens [1–5] and liquid lens [6–24]. An adaptive LC lens usually employs an inhomogeneous electric field to make the LC molecules reorient to produce a gradient refractive index profile. The LC lens is polarization-dependent which means that the lens has low spectral transmission. Since the response time depends on the LC layer thickness and the size of the LC lens, it is more suitable for making microlens which constrains the real applications in imaging systems. There are three common operating mechanisms to design a liquid lens: electrowetting effect [6–14], dielectric force [15–18], and fluidic pressure [19–24].

A dielectric lens uses two non-conductive liquids of different dielectric constants to form a smooth liquid-liquid interface. It can bear high operating voltage and has lower power consumption. However, the dielectric lens needs be applied with inhomogeneous electric field. So the electrodes of the dielectric lens should be etched with holes or rings which make the device fabrication more complicated. A fluidic pressure based liquid lens usually makes use of a PDMS (polydimethylsiloxane) membrane to control the volume of the liquids. The membrane lens can achieve a large lens aperture and the focal length can be varied within a wide range. However, the disadvantages of this type of lens cannot be ignored. For example, the gravity effect may exist in the membrane lens when it is placed in vertical position, which may degrade the imaging performance. By applying an external driving system, the lens would have a bulk volume and high power consumption. Compared with the liquid lens discussed above, electrowetting-based liquid lens has the advantages of polarization independent, fast response, and simple fabrication.

In this paper we demonstrate an adaptive liquid lens actuated by droplet movement. Compared with other adaptive liquid lenses, our lens has the competitive advantages in simple structure, reasonably fast response time and low power consumption. In our device, the volume change of the reservoir is actuated by liquid pressure. So it is possible to significantly actuate a large-aperture lens or microlens array at a relatively low operating voltage. Furthermore, the proposed lens can maintain a better liquid interface compared with the lens whose electrode structure is rings [14,15]. Because the rings-shape electrode could cause the different frictions for the droplet, the curvature of the lens would be nonuniform. One experiments show that the focal length can be varied from −10 to −159 mm as the applied voltage changes from 0 to 65 V. The response time of the liquid lens is ~75 ms.

2. Device Mechanism and Fabrication

Figure 1 shows the schematic of the proposed device and the operation mechanism. Two ITO sheets are fabricated on the bottom substrate. The left-ITO sheet is coated with a dielectric layer whose dielectric constant is ~3.5. A PMMA sheet with a light hole is inserted in the middle of the PMMA structure. A conductive droplet (Liquid-1) is placed on the substrate and its left side touches the PMMA sheet to form a closed reservoir. Then we inject another immiscible non-conductive liquid (Liquid-2) from the light hole. The droplet touches the PMMA sheet and completely seals the right-hand side of the device. The space of the oil phase is just like a reservoir. The droplet extrudes the reservoir to make a liquid pressure. When the droplet moves towards the left side of the device, the volume of the oil phase can be changed. That is to say, the volume of the oil phase determines the range of achievable focal lengths. At initial state, the non-conductive liquid can form a smooth concave surface, as shown in Figure 1a. In this state, the light beam is divergent when it passes through the device. When we apply voltage V to the right-ITO sheet, the droplet stretches towards the reservoir due to electrowetting effect, making its volume decrease. So the curvature of the interface is changed, as shown in Figure 1b. The top view of the device is also depicted in Figure 1c. Figure 2 shows the electrowetting effect mechanism in the device. At initial state, as shown in Figure 2a, the balance of the interface between Liquid-1, Liquid-2 and the dielectric layer tri-junction line is governed by the equations as below [25]:

$$\cos\theta_1 = \cos\theta_0 + \frac{U^2\varepsilon}{2d\gamma_{12}} \tag{1}$$

$$\gamma_{D2} + \gamma_{12}\cos\theta_0 = \gamma_{1D} \tag{2}$$

where θ_0 is the initial contact angle without applied voltage, θ_1 is the contact angle when voltage is applied to the device, U is the external voltage to the ITO sheet, d is the thickness of the dielectric insulator, $\varepsilon = \varepsilon_0\varepsilon_r$ is the dielectric constant of the dielectric insulator, γ_{12} is the surface tension between Liquid-1 and Liquid-2, γ_{1D} is the surface tension between Liquid-1 and dielectric insulator, and γ_{D2} is the surface tension between dielectric insulator and Liquid-2. When the external force is applied to the droplet reaches to balance, as shown in Figure 2b, the droplet satisfies the following equation:

$$F + \gamma_{D2} = \gamma_{12}\cos\theta_1 + \gamma_{1D} \tag{3}$$

where F represents the electric force of per meter.

To fabricate the device shown in Figure 1, four PMMA substrates are stacked to form the structure using glue UV-331. The whole size of the structure is 15 mm × 8 mm × 8 mm. First, two ITO sheets with the size of 8 mm × 7 mm are made on the bottom substrate and the gap between them is 0.5 mm. The left-ITO sheet is coated with a SU8 layer (~1 μm) as an insulator, followed by a thin Teflon layer (AF-1600, from DuPont, Wilmington, DE, USA). The surface tension of the Teflon layer is ~18 mN·m^{-1} at 20 °C. Then a PMMA sheet is inserted in the middle of the device. The size of the PMMA sheet is 8 mm × 7 mm and the diameter of the light hole is 3 mm. Next, we place a droplet of NaCl solution (Liquid-1: the density is 1.05 g·cm^{-3}, viscosity is ~12 mPa s at room temperature) on the substrate and filled the channel, as shown in Figure 1c. Finally, the silicon oil (Liquid-2: the density is 0.98 g·cm^{-3}, surface tension is ~19 mN·m^{-1} at 20 °C, viscosity is ~10 mPa s at room temperature, refractive index is 1.40) is injected from the light hole.

Figure 1. Schematic of the proposed device and the operation mechanism: (**a**) Initial state; (**b**) Applied voltage to the device; (**c**) Top view of the device.

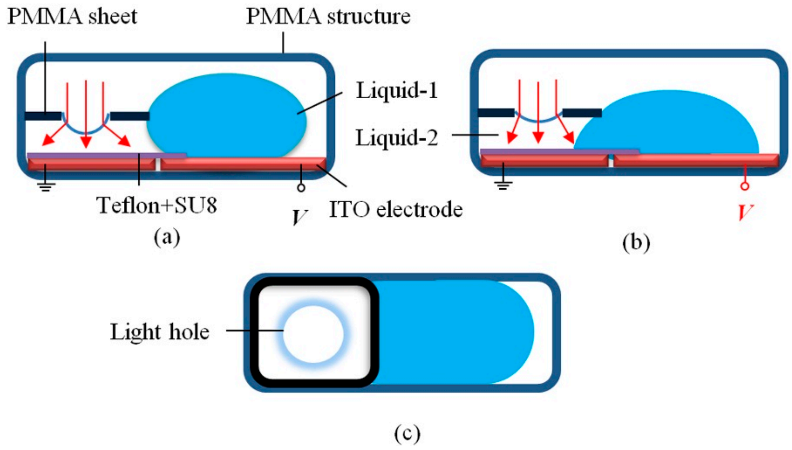

Figure 2. Electrowetting effect mechanism in the device: (**a**) Initial state; (**b**) External force reaching to balance.

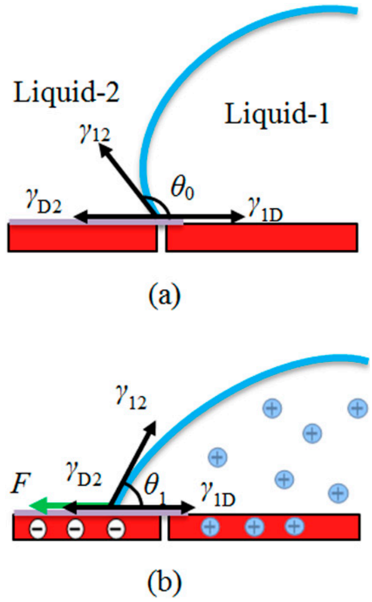

3. Experiment and Discussion

To evaluate the device performance during actuation process, we recorded the image of an object through the lens. The optical setup is shown in Figure 3. We placed a printed letter “A” 5 mm below the device; thus, the object was always within the focal length of the lens. Therefore, we can observe an upright virtual image. A CCD (charge coupled device) camera was used to record the image-change. When we applied voltage $U < 30$ V to the device, the droplet could not move. The liquid lens has the shortest negative focal length, as shown in Figure 4a. When the voltage $30 \text{ V} < U < 65$ V, the droplet started to move towards the reservoir, the image-change was shown in Figure 4b–d. When the voltage $U = 65$ V, the magnification reached maximum. When we removed the external voltage, the droplet moved backwards to its original position automatically due to the high interface tension with the sidewall of the structure.

Figure 3. Optical setup of the device.

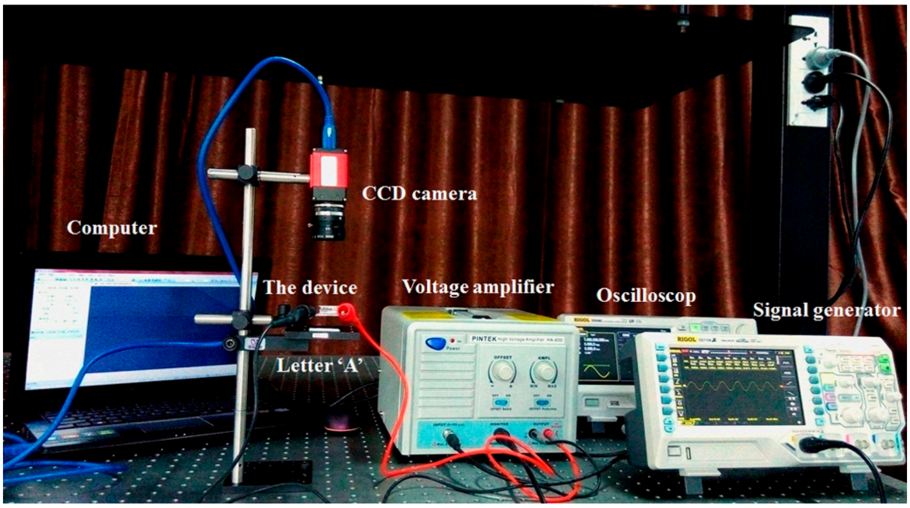

Figure 4. Images for different focal lengths under different voltages: (**a**) Initial state; (**b**) State 1; (**c**) State 2; (**d**) State 3.

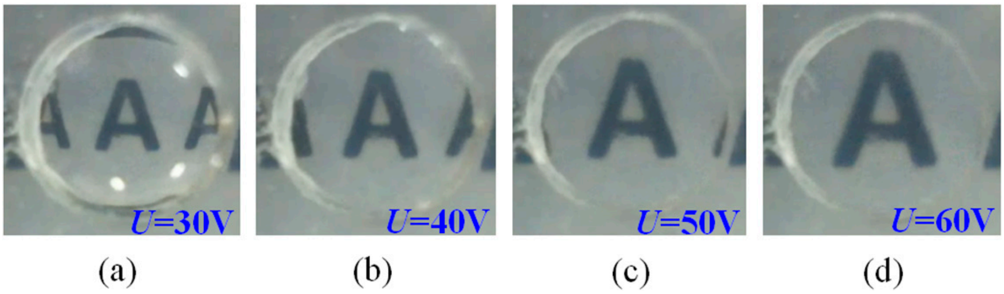

To measure the focal length of the liquid lens, we expanded and collimated a He-Ne laser beam ($\lambda = 632.8$ nm) to ~3 mm in diameter and let it normally pass through the liquid lens. The focal length is determined by a geometrical imaging method, as shown in Figure 5a. So $f = (d_2 - d_1) \times l_1/(l_2 - l_1) - d_1$. Every measurement was repeated three times and the results were averaged. In our experiment, the focal length can be changed from −10 to −159 mm with the voltage changing from 0 to 65 V. As we can see from Figure 5b, the focal length changes differently between voltage-on state and voltage-off state. The main reason for this may be explained as follows: regarding the droplet movement, it is more difficult to extrude the reservoir than move freely backward to its original position. Furthermore, the frictional force between the droplet and the structure may be changed several times after the droplet movement on the substrate.

Response time is another key point to measure the optical performance of the device. We take the absolute value of the focal length and normalize it. Figure 6 shows the response time of the device. As we can see, it takes a time of ~75 ms (~63 ms) for the device changing the focal length from −10 (−159) to −159 mm (−10 mm). The device has a relatively fast response time.

Figure 5. Protocol adopted for the determination of focal length (**a**) and focal length *versus* applied voltage (**b**).

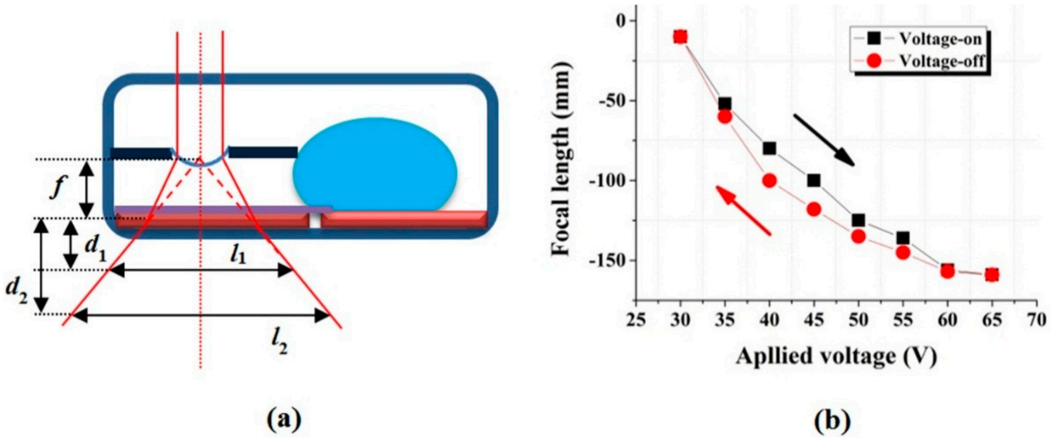

(a) **(b)**

Figure 6. Response time of the device ($U = 65$ V).

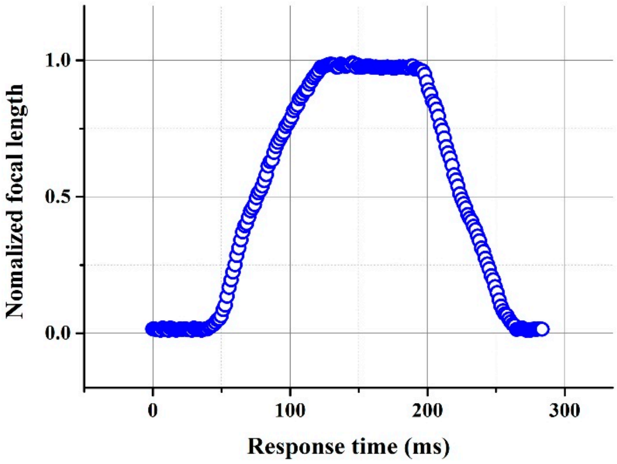

Liquid viscosity plays a significant role in response time of a device. First we define the total response time as the sum of the rise time and descend time. We did another experiment at the voltage of 60 V to study the relationship between the liquid viscosity and the total response time. In the experiment, we choose three silicone oils with different viscosities (10 mPa s, 20 mPa s, and 50 mPa s) as Liquid-2, respectively. Liquid-1 remained the same. The measured response time of different liquids are 146 ms, 205 ms, and 311 ms, respectively. The measured maximum focal lengths are 156 mm, 124 mm, and 42 mm, respectively. As shown in Figure 7, the response time prolongs as the viscosity increases. Thus, the viscosity of the oil plays a significant role in changing the focal length of the liquid lens, as shown in Figure 7. High liquid viscosity means low flow ability. So the movement of Liquid-1 will be restrained, which leads to the decrease of the maximum focal length.

Figure 7. Response time and the maximum focal length under different liquid viscosities.

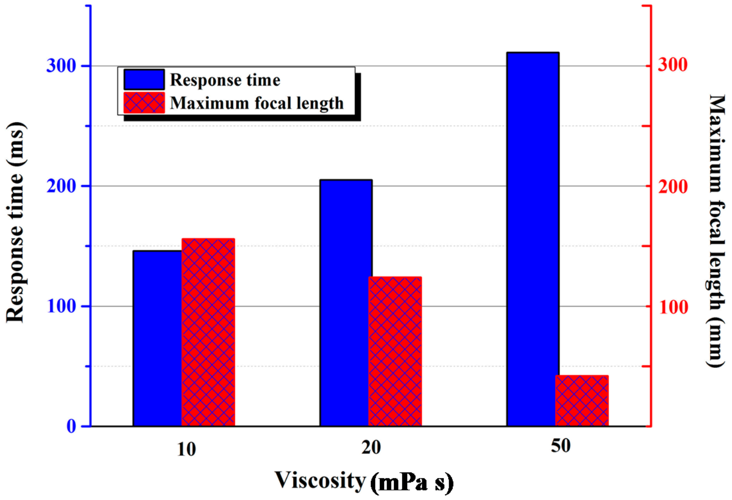

The curvature of the interface of the proposed adaptive liquid lens cannot change from concave surface to convex surface which constrains the varied range of the focal length. The main reason is that in our device the droplet actuated by electrowetting extrudes the reservoir to make a liquid pressure. In the experiment, the electrostatic force is not large enough to make the droplet move a relatively long distance towards the PMMA sheet. So the volume change of the reservoir is limited. Thus, the configuration of the lens cannot change from divergent to convergent. If we decrease the thickness of the dielectric layer and the whole size of the device, the device can obtain a robust optical performance. We can also increase the external voltage to solve this issue. However, the high applied voltage will decrease the lifetime of the device. So we should choose the proper voltage and carefully design the device. Our device also suffers from gravity effect when placed in vertical position. We can choose three immiscible density-matched liquids filled with the device to solve this issue. This will form the basis for our further work.

4. Conclusions

In this paper we reported an adaptive liquid lens actuated by droplet movement. The device is fabricated with four rectangular PMMA substrates. Two ITO sheets are stacked on the bottom substrate with a small gap between them. One sheet with a light hole is inserted in the middle of the device. A conductive droplet touches the sheet to form a small closed reservoir which is filled with another immiscible non-conductive liquid. When we apply a DC (direct current) voltage to the device, the droplet stretches towards the reservoir making the curvature of the interface changed. Our experiments show that the focal length can be varied from −10 to −159 mm as the applied voltage changes from 0 to 65 V. The response time of the liquid lens is ~75 ms. The proposed device has potential applications such as information displays, cameras, imaging systems and laser scanning systems.

Acknowledgments

The work is supported by the NSFC under Grant Nos. 61225022 and 61320106015, the “973” Program under Grant No. 2013CB328802, and the “863” Program under Grant Nos. 2012AA011901 and 2012AA03A301.

Author Contributions

Study concepts, design experimental studies, manuscript editing: Chao Liu. Data acquisition, analysis, interpretation, statistical analysis: Li-Xiao Yao and Ming-Huan Wang. Manuscript revision, review, final version approval: Qiong-Hua Wang.

Conflicts of Interest

The authors declare no conflict of interest.

References

1. Xu, M.; Zhou, Z.W.; Ren, H.; Lee, S.H.; Wang, Q.H. Tunable liquid microlens. *J. Appl. Phys.* **2013**, *113*, doi:10.1063/1.1536033.
2. Wang, B.; Ye, M.; Sato, S. Liquid crystal lens with focal length variable from negative to positive values. *IEEE Photonics Technol. Lett.* **2006**, *18*, 79–81.
3. Hwang, S.J.; Liu, Y.X.; Porter, G.A. Tunable liquid crystal microlenses with crater polymer prepared by droplet evaporation. *Opt. Express* **2013**, *21*, 30731–30738.
4. Ren, H.; Xu, S.; Wu, S.T. Polymer-stabilized liquid crystal microlens array with large dynamic range and fast response time. *Opt. Lett.* **2013**, *38*, 3144–3147.
5. Ye, M.; Wang, B.; Sato, S. Liquid-crystal lens with a focal length that is variable in a wide range. *Appl. Opt.* **2004**, *43*, 6407–6412.
6. Bergea, B.; Peseux, J. Variable focal lens controlled by an external voltage: An application of electrowetting. *Eur. Phys. J. E.* **2000**, *3*, 159–163.
7. Peng, R.; Wang, D.Z.; Hu, Z.W.; Chen, J.B.; Zhuang, S.L. Focal length hysteresis of a double-liquid lens based on electrowetting. *J. Opt.* **2013**, *15*, doi:10.1088/2040-8978/15/2/025707.
8. Kuipera S.; Hendriks, B.H.W. Variable-focus liquid lens for miniature cameras. *Appl. Phys. Lett.* **2004**, *99*, doi:10.1063/1.1779954.
9. Krupenkin, T.; Yang, S.; Mach, P. Tunable liquid microlens. *Appl. Phys. Lett.* **2003**, *82*, 316–318.
10. Grilli, S.; Miccio, L.; Vespini, V.; Finizio, A.; Nicola, S.D.; Ferraro, P. Liquid micro-lens array activated by selective electrowetting on lithium niobate substrates. *Opt. Express* **2008**, *16*, 8084–8093.
11. Murade, C.U.; Ende, D.V.D.; Mugele, F. High speed adaptive liquid microlens array. *Opt. Express* **2012**, *20*, 18180–18187.
12. Choi, H.; Won, Y. Fluidic lens of floating oil using round-pot chamber based on electrowetting. *Opt. Lett.* **2013**, *38*, 2197–2199.
13. Li, C.H.; Jiang, H.R. Electrowetting-driven variable-focus microlens on flexible surfaces. *Appl. Phys. Lett.* **2012**, *100*, doi:10.1063/1.4726038.

14. Liu, C.X.; Park, J.; Choi, J.W. A planar lens based on the electrowetting of two immiscible liquids. *J. Micromech. Microeng.* **2008**, *18*, doi:10.1088/2040-8978/13/11/115503.
15. Cheng, C.C.; Yeh, J.A. Dielectrically actuated liquid lens. *Opt. Express* **2007**, *15*, 7140–7145.
16. Ren, H.; Xianyu, H.; Xu, S.; Wu, S.T. Adaptive dielectric liquid lens. *Opt. Express* **2008**, *16*, 14954–14960.
17. Tsai, C.G.; Chen, C.N.; Cheng, L.S.; Cheng, C.C.; Yang, J.T.; Yeh, J.A. Planar liquid confinement for optical centering of dielectric liquid lenses. *IEEE Photonics Technol. Lett.* **2009**, *21*, 1396–1398.
18. Yang, C.C.; Tsai, C.G.; Yeh, J.A. Dynamic behavior of liquid microlenses actuated using dielectric force. *J. Microelectromech. Syst.* **2011**, *20*, 1143–1149.
19. Li, L.; Wang, Q.H.; Jiang, W. Liquid lens with double tunable surfaces for large power tunability and improved optical performance. *J. Opt.* **2011**, *13*, doi:10.1063/1.2168245.
20. Xu, S.; Ren, H.; Wu, S.T. Adaptive liquid lens actuated by liquid crystal pistons. *Opt. Express* **2012**, *20*, 28518–28523.
21. Moran, P.M.; Dharmatilleke, S.; Khaw, A.H.; Tan, K.W.; Chan, M.L.; Rodrigueza, I. Fluidic lenses with variable focal length. *Appl. Phys. Lett.* **2006**, *88*, doi:10.1063/1.2168245.
22. Mao, X.; Stratton, Z.I.; Nawaz, A.A.; Lin, S.C.S.; Huang, T.J. Optofluidic tunable microlens by manipulating the liquid meniscus using a flared microfluidic structure. *Biomicrofluidics* **2010**, *4*, doi:10.1063/1.3497934.
23. Dong, L.; Agarwal, A.K.; Beebe, D.J.; Jiang, H. Adaptive liquid microlenses activated by stimuli-responsive hydrogels. *Nature* **2006**, *442*, 551–554.
24. Song, C.L.; Nguyen, N.T.; Asundi, A.K.; Low, C.L.N. Biconcave micro-optofluidic lens with low-refractive-index liquids. *Opt. Lett.* **2009**, *34*, 3622–3624.
25. Mugele, F.; Baret, J.C. Electrowetting: From basics to applications. *J. Phys Condens. Matter.* **2005**, *17*, R705–R774.

Fabrication and Characterization of Flexible Electrowetting on Dielectrics (EWOD) Microlens

Chenhui Li and Hongrui Jiang

Abstract: We present a flexible variable-focus converging microlens actuated by electrowetting on dielectric (EWOD). The microlens is made of two immiscible liquids and a soft polymer, polydimethylsiloxane (PDMS). Parylene intermediate layer is used to produce robust flexible electrode on PDMS. A low-temperature PDMS-compatible fabrication process has been developed to reduce the stress on the lens structure. The lens has been demonstrated to be able to conform to curved surfaces smoothly. The focal length of the microlens is 29–38 mm on a flat surface, and 31–41 mm on a curved surface, varying with the voltage applied. The resolving power of the microlens is 25.39 line pairs per mm by a 1951 United States Air Force (USAF) resolution chart and the lens aberrations are measured by a Shack-Hartmann wavefront sensor. The focal length behavior on a curved surface is discussed and for the current lens demonstrated the focal length is slightly longer on the curved surface as a result of the effect of the curved PDMS substrate.

Reprinted from *Micromachines*. Cite as: Li, C.; Jiang, H. Fabrication and Characterization of Flexible Electrowetting on Dielectrics (EWOD) Microlens. *Micromachines* **2014**, *5*, 432–441.

1. Introduction

Liquid lenses do not require complicated mechanical systems to change their focal lengths, and they are widely used in photonics, display and biomedical systems [1–4]. Another rapidly-developing area in micro-optics is the fabrication of microlenses made on flexible polymer substrates [5,6], because microlens array on a curved substrate have some significant advantages over planar microlenses, including wider field of view [6,7], creating 3-D effect [8,9] and mimicking artificial compound eyes [10]. In virtue of these developments, emerging liquid-based variable-focus microlenses have become important components in modern miniaturized optical systems. Benefitting from the quick response, the low power consumption, and the robustness under voltage cycling, liquid microlenses based on electrowetting on dielectric (EWOD) have drawn much attention [1,11]. However, traditional EWOD microlenses are fabricated on rigid materials like glass, silicon and polyethylene terephthalate, and are consequently not compatible with curved surfaces.

We have previously reported a flexible EWOD liquid lens design [12], in which a water droplet is covered by silicone oil and the water droplet has to turn concave to form a converging lens. Therefore, the electrode, dielectric and hydrophobic layers were deposited on the sidewall of a polymer chamber to change the water surface from convex to concave shape and the water-oil interface is pinned on the sidewall of the chamber. This design raises two problems: (1) When the lens is wrapped onto a curved surface, the sidewall will be stretched and it is difficult to determine how the water-oil interface will be distorted; (2) The electrode and hydrophobic coating on the sidewall cannot be easily patterned. In addition, the indium tin oxide (ITO) electrode is fragile due to the weak adhesion of ITO on polydimethylsiloxane (PDMS), a soft polymer.

Here, we present a flexible EWOD microlens made of PDMS with improved lens design and robust flexible electrodes. We also discuss the focal length of the microlens on a spherical surface in comparison to that of the same lens on a flat surface. The center of the lens is a silicone oil droplet covered by surrounding water. The thin flexible PDMS substrate is compatible with curved surfaces and the effect of chamber sidewall distortion on the water-oil interface is reduced. The modified low-temperature fabrication process is also reported. A parylene C layer is coated directly onto PDMS to promote aluminum-PDMS bonding and to reduce the problem associated with the porosity of PDMS. The focal length is measured on both flat and curved substrates. When the applied voltage increases up to 100 V, the focal length changes from 38 mm to 29 mm on a flat substrate and it is slightly longer on a curved substrate (*f*: 41–31 mm). The Zernike coefficients of the lens were measured by a Shack-Hartmann wavefront sensor.

2. Mechanism and Fabrication

2.1. Mechanism

Figure 1a shows a 3D schematic of a flexible microlens wrapped onto a spherical surface. The lens substrate and lens chamber are both made of PDMS, which is transparent, flexible, and bio-compatible. The substrate is designed to be much thinner than the chamber. Therefore, the lens can be easily wrapped onto curved surfaces and the stress on the chamber is significantly reduced [6]. Figure 1b illustrates the cross-section of a flexible EWOD microlens. A silicone oil droplet (refractive index $n_1 = 1.47$) is placed at the center of the chamber and it is covered by water (refractive index $n_2 = 1.33$). The electrode, dielectric and hydrophobic layers are sequentially coated on the PDMS substrate and they were patterned by photolithography techniques. The water is in contact with another electrode on the chamber. The applied voltage between the two electrodes controls the surface energy on the substrate and therefore varies the radius of curvature of the water-oil interface [1]. Figure 1c shows the change of the water-oil interface when a voltage is applied. At low voltages, the substrate is hydrophobic and the oil droplet spreads on it, forming a small contact angle. As the voltage increases, the substrate turns relatively hydrophilic and water squeezes the oil droplet to a more convex shape, which has a larger contact angle with the substrate. The varying contact angle (θ) of the lens can be expressed by Equation (1) [11].

$$\cos(\theta) = \cos(\theta_0) + \frac{\varepsilon}{2d\gamma_{12}} V_0^2 \tag{1}$$

where θ_0 is the contact angle at $V_0 = 0$, ε is the dielectric constant of the dielectric layer, d is its thickness, γ_{12} is the water-oil interfacial tension and V_0 is the applied voltage.

Figure 1. (**a**) 3D schematic of a flexible liquid lens on a hemisphere. The lens structure is made of a soft polymer, polydimethylsiloxane (PDMS). The thin flexible PDMS substrate can be wrapped onto curved surfaces; (**b**) aross-section schematic of the microlens. The PDMS substrate is deposited with an electrode, a dielectric layer, and a hydrophobic coating subsequently, and the PDMS chamberf is coated with another electrode. The liquid lens is the liquid-to-liquid interface formed by a silicone oil droplet and its surrounding water. The voltage applied on the electrodes modifies the effective surface energy, and thus changes the radius of curvature of the water-oil interface; (**c**) at zero or low voltage, the silicone oil droplet spreads out on the substrate due to the hydrophobic coating. As the voltage increases, the substrate surface turns more hydrophilic and the water squeezes the oil droplet to a shape with smaller radius of curvature.

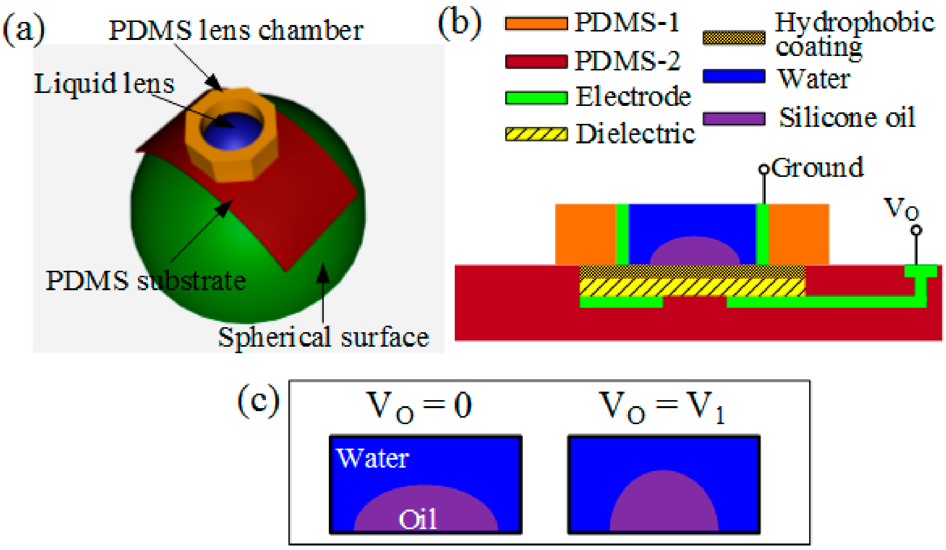

2.2. Fabrication

It is difficult to create strong permanent bonding between metal and PDMS surface due to the low surface energy of PDMS [13] and the different degrees of thermal expansion of the metal and PDMS layers during the metal deposition process [14]. Therefore, surface treatment is necessary to increase the surface energy of PDMS; otherwise, the weak adhesion between electrodes and PDMS substrate often cause device failure during the following electrode patterning or substrate bending. A few approaches have been tried out and proved to significantly strengthen the electrode-PDMS bonding: (1) oxygen plasma treatment increases the bond strength by activating layers of cross-linked PDMS in oxygen plasma; surface oxidation is believed to expose silanol groups (OH) at the surface of the PDMS layers that when brought together form covalent siloxane bonds (Si–O–Si) [15,16]; (2) polyimide intermediate layer, which is widely used in flexible electronic devices [17,18]; (3) parylene C coating, on which metal layers can be deposited and patterned [19,20]. Besides promoting electrode-PDMS adhesion, parylene C layer also improves the overall device robustness. Parylene has attractive properties, such as optical transparency, pinhole-free conformal deposition process [21], chemical and biological inertness, good mechanical strength (Young's modulus of 3.1–4.75 GPa and tensile strength of 40–110 MPa) [21–23], low permeability to moisture and gases [24] and low intrinsic film stress. The parylene C coating addresses the porosity problem of PDMS which could cause bubble formation, sample evaporation and absorption of organic solvents and small hydrophobic molecules from solution [25]. Therefore, deposition of parylene C coatings onto PDMS film is used as the surface treatment method in the fabrication process.

The fabrication process starts with preparing the PDMS substrate. A clean microscope slide is coated with a hydrophobic layer, trichloro(octadecyl)silane (Sigma-Aldrich Co., Saint Louis, MO, USA), to facilitate the separation of PDMS film from the microscope slide later on. The microscope slide is then spin-coated with PDMS prepolymer at 1000 rpm for 60 s and then baked on a hotplate at 70 °C for 4 h to cure the prepolymer. Figure 2 illustrates subsequent fabrication processes on the PDMS substrate. In Figure 2a, a thin parylene C film (~2 μm) is deposited on the PDMS substrate to strengthen electrode adhesion and to mitigate the porosity problem of PDMS as discussed above. In Figure 2b, aluminum film (~200 nm) is sputtered on the parylene-coated PDMS in a sputtering system (Discovery 24, Denton Vacuum, Moorestown, NJ, USA). In Figure 2c, the aluminum electrode is photopatterned with photoresist AZ4620 (Clariant Corporation, Somerville, NJ, USA) and then wet-etched in a commercially prepared defreckling aluminum etchant for 5 min. SU-8 is used as the dielectric material, because it has high dielectric constant (~3) and can be deposited by spin-coating method. In Figure 2d, the substrate is spin-coated with SU-8 prepolymer solution (SU-8 2002, MicroChem Corp., Newton, MA, USA) at 500 rpm for 8 s and then at 2000 rpm for 30 s. Next, the SU-8 undergoes UV exposure at 20 mW for 40 s, followed by hard bake at 120 °C for 5 h, forming a ~2.4 μm SU-8 film. In Figure 2e, the SU-8 dielectric layer is spin-coated with Teflon solution (Teflon® AF 1600, DuPont, Wilmington, DE, USA) at 1000 rpm for 30 s and then baked at 120 °C for 10 h. To avoid damages to the PDMS, the baking temperature is much lower than that used in standard procedure (up to 330 °C) [26], and therefore the baking time is extended to remove the solvents thoroughly. The Teflon film formed (~400 nm thick) is hydrophobic, smooth and chemical-inert. In Figure 2f, the Teflon film is photopatterned with photoresist AZ4620 and then etched by oxygen plasma at 200 W for 2 min in a reactive ion etching (RIE) chamber (Unaxis 790, Plasma-Therm, St Petersburg, FL, USA). In Figure 2g, a PDMS chamber is bonded to the substrate by an acrylic, low durometer, flexible, UV-cure adhesive (Loctite 3108, Henkel Corp., Rocky Hill, CT, USA). The adhesive is cured under 30 mW UV radiance for 20 s to form a rubbery bonding. The chamber is first filled with water and then the silicone oil droplet is squeezed to the center by a syringe pipette with a sharp tip.

Figure 2. Fabrication process of the flexible electrowetting on dielectric (EWOD) microlens. (**a**) Deposit parylene C layer (~2 µm) on PDMS substrate. Parylene strengthens the boding between PDMS and electrodes; (**b**) and (**c**) sputter aluminum electrode (~200 nm) and pattern it by photolithography and wet etch; (**d**) spin-coat SU-8 dielectric layer (~2.4 µm) and post-bake it at 120 °C for 5 h; (**e**) spin-coat Teflon hydrophobic thin film (~400 nm) and post-bake it at 120 °C for 10 h to remove the solvent; (**f**) sattern the Teflon coating with photolithography and reactive ion etching; (**g**) sond a PDMS chamber onto the substrate using a flexible, UV-cure adhesive.

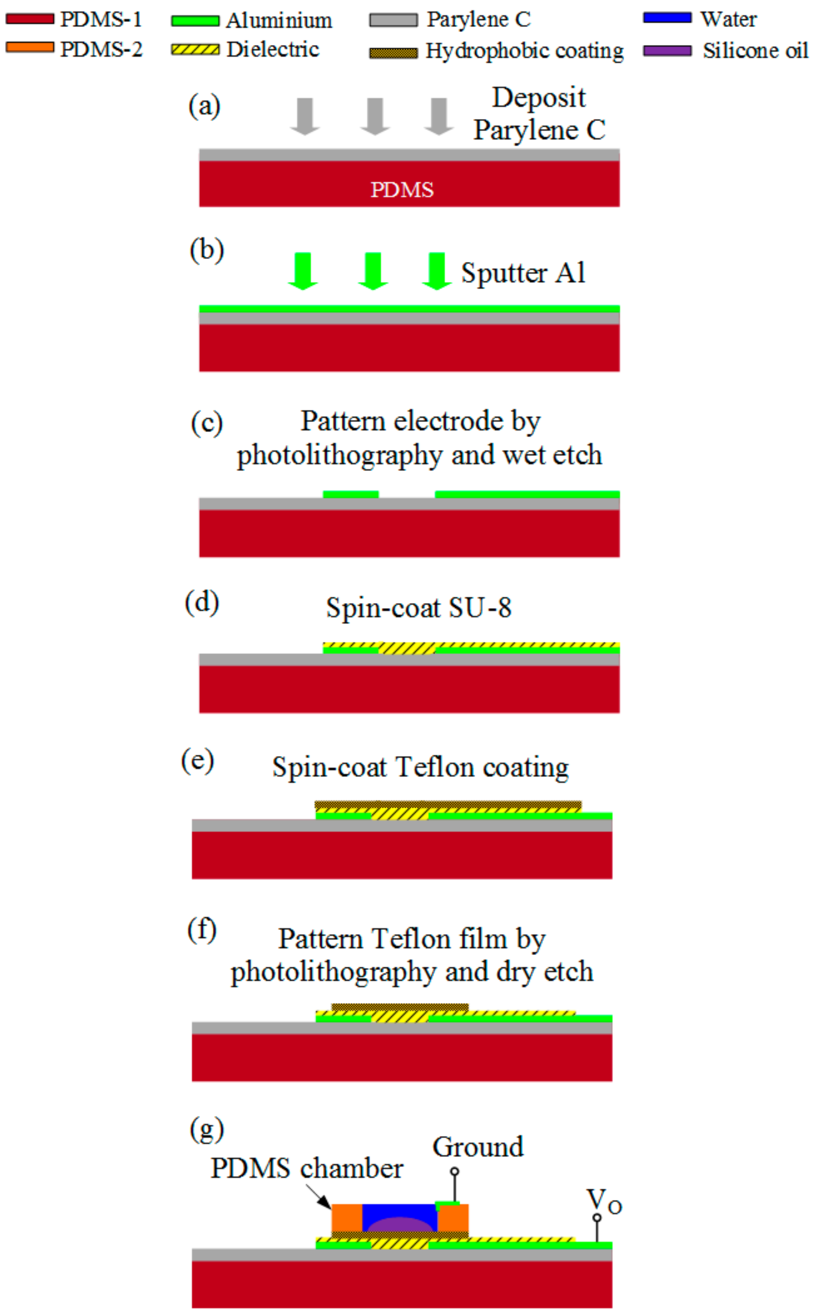

Figure 3 demonstrates the flexible EWOD microlens and its compatibility with curved surfaces. Figure 3a shows the thin PDMS substrate after it is deposited with aluminum electrode, SU-8 dielectric and Teflon hydrophobic coating. Figure 3b,c shows the EWOD lens wrapped onto a cylinder and an eyeglass, respectively. The aperture (circular opening on the substrate) is 2 mm in diameter and the diameter of the PDMS chamber is around 8 mm. The PDMS lens structure exhibits excellent flexibility and transparency.

Figure 3. Demonstration of the flexible PDMS lens structure: (**a**) Bending a PDMS substrate (already coated with Al electrode, SU-8 dielectric layer and Teflon coating); (**b**) a flexible EWOD lens wrapped on a cylinder; (**c**) a flexible EWOD lens bonded with a protection glass, which has almost zero optical power.

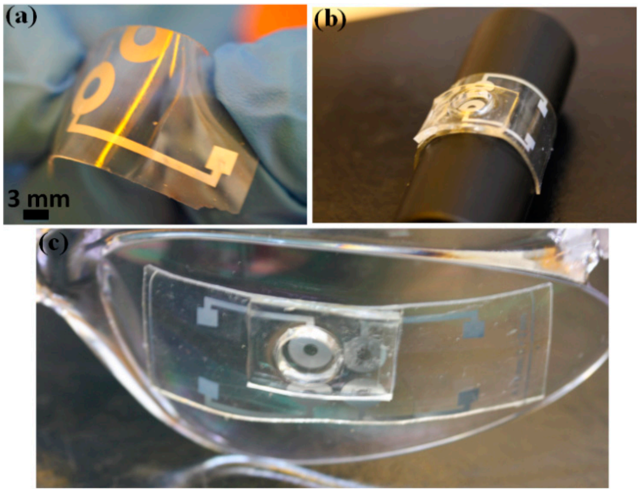

3. Results and Discussion

3.1. Experiment Results

The shape change of the droplet within the microlens is monitored by a goniometer (OCA 15+, DataPhysics Instruments Inc., Filderstadt, Germany). Figure 4 shows the cross-section images of the silicone oil droplet when the applied voltage, 500 Hz Alternating Current (AC), varies between 0 and 100 V. The volume of the oil droplet is 54 μL. When the voltage increases, the effective surface energy on the substrate increases, and thus the substrate turns more hydrophilic. Therefore, the water squeezes the oil droplet, reducing the radius of curvature (*R*) of the oil-water interface. The focal length is thus to decrease with increasing voltages.

Figure 4. Shape change of oil droplet with increasing voltage. As the applied voltage increases, the oil droplet is squeezed by the surrounding waters and bulges up into a shape with smaller radius of curvature.

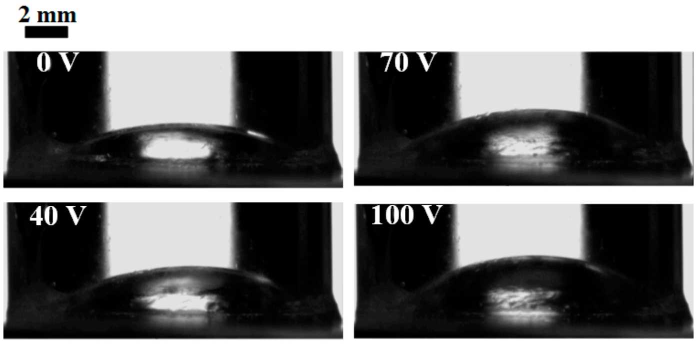

The focal length of the lens was measured on both a flat and a curved transparent surface. The curved surface, which is the eyeglass in Figure 3c, has zero optical power. Figure 5 shows the focal length *f* versus the applied voltage. On both substrates, the focal length varies in a similar trend with increasing voltages; however the lens has a slightly longer focal on the curved surface. The possible source of the focal length change will be discussed in Section 3.2. The resolving power of the lens is measured by imaging a 1951 United States Air Force (USAF) resolution test chart and the smallest features to resolve were 25.39 line pairs per mm.

Figure 5. Focal length versus applied voltage. The curved surface is the protection glass shown in Figure 3c and it has no optical power. On the curved surface, the lens has a slightly longer focal length than that on a flat surface.

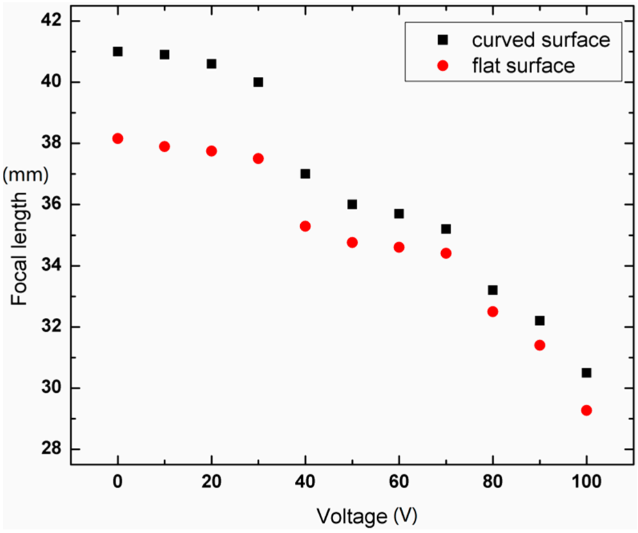

3.2. Discussion of Focal Length Change

As shown in Figure 5, the liquid microlens exhibits slightly longer focal length on a curved surface than that on a flat surface. The change could have two sources: (1) the oil droplet forms a different shape on the curved PDMS substrate; (2) the curved PDMS substrate changes the overall optical power of the system. Based on the current fabrication process, the microlens cannot be wrapped onto a curved substrate that has comparable radius of curvature to that of the oil droplet. In other words, the curved substrate has a much larger radius compared to the liquid lens. Therefore, it is reasonable to assume that the shape of the oil droplet did not change much when the microlens was wrapped onto the curved surface.

Next, we consider the effect of the optical power of the curved PDMS substrate. Figure 6a illustrates the optical system when the microlens is on curved surface. The water-oil interface has a focal length $f_1 = 38$ mm. The curved PDMS substrate functions as a diverging lens with focal length $f_2 = -426$ mm. By lensmakers' formula, the overall focal length is calculated by:

$$\frac{1}{f} = \frac{1}{f_1} + \frac{1}{f_2} - \frac{d}{n_1 f_1 f_2} \tag{2}$$

where $d \approx 3$ mm and $n_1 = 1.47$ (oil's refractive index). Therefore, the estimated overall focal length is 41.5 mm, which is close to the experiment result, 41 mm. To sum up, for the current microlens device the curved PDMS substrate is the dominant cause of the focal length change and the diverging lens formed by it makes the system focal length slightly longer than that on a flat substrate.

Figure 6. (**a**) Schematic of the overall optical system when the liquid lens is on a curved surface. The PDMS substrate forms a diverging lens and its focal length is around −426 mm; (**b**) contact angle of an oil droplet on curved PDMS substrate.

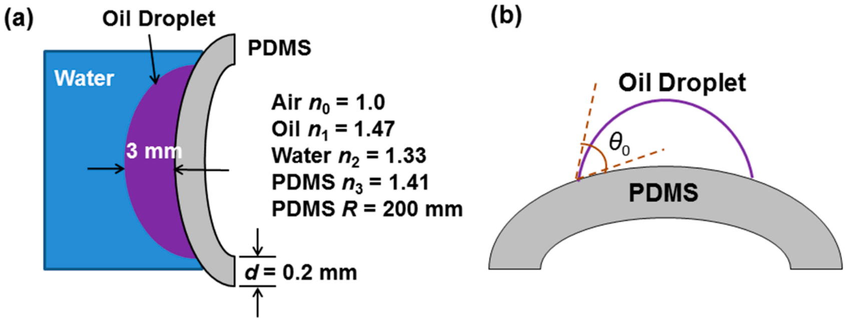

$$f_{PDMS} = [\frac{n_3 - n_2}{R} + \frac{n_0 - n_1}{R} - \frac{d(n_3 - n_2)(n_0 - n_1)}{R^2}]^{-1} = \text{-426 mm}$$

In the future, with improved fabrication process, the lens could be wrapped onto a convex substrate with much shorter radius of curvature than that of the current one. Under such circumstances, the shape change of the oil droplet must be taken into consideration. Under ideal conditions, such as that the liquid droplet is deposited on the substrate symmetrically and that the hysteresis in contact angle is neglected, the contact angle between substrate-liquid surface tangent and the liquid-liquid surface tangent is the same as the θ_0 in Equation (1) [27], as shown in Figure 6b. As a result, the focal length of the liquid lens will be shorter on the curved substrate, excluding the effect of the curved PDMS substrate.

4. Conclusions

In summary, we have demonstrated a new design of flexible EWOD microlens which is made of soft flexible PDMS structure. The process to fabricate robust electrodes on PDMS thin substrate is also introduced. Parylene C thin film is used as an intermediate layer to strengthen the bonding between PDMS and aluminum electrode and to address the porosity problem of PDMS. The liquid lens is formed by a silicone oil droplet and the water covering it. All the functioning layers implementing EWOD mechanism are deposited on the substrate. Therefore, when a lens is wrapped onto a curved surface, the effect of stress on the water-oil interface is reduced as the peripherals of the oil droplet are pinned on the substrate. The microlens is a converging lens at any voltage. When the applied voltage increases, the water squeezes the oil droplet, and thus both the radius of curvature of the droplet and the focal length decreases. The focal length is 29–38 mm on a flat surface and 31–41 mm on a curved surface. The curved PDMS substrate forms a diverging lens and makes the overall focal length slightly longer on the curved surface. The aberration of the lens is measured by a Shack-Hartmann wavefront sensor and its Zernike coefficients are reported. In the future, the driving voltage of the lens can be further reduced by exploring dielectric materials which have high dielectric constants and are compatible with our flexible polymer structure. The fabrication process can be improved to make the lens structure compatible with a more curved substrate. A contact lens integrated with a flexible low-voltage EWOD microlens provides a better solution for presbyopia correction. Meanwhile, EWOD microlens array can also be fabricated by the current fabrication process and it can be formed on a spherical surface to provide a micro-optical system with very wide field of view [6].

Acknowledgments

This work was supported by the US National Institute of Health (Grant number: 1DP2OD008678). The authors thank Yong Xu and Hongen Tu for assistance in the deposition of paralene C, and Yen-Sheng Lu, Bader Aldalali, and Xuezhen Huang for technical discussion and assistance.

Author Contributions

Chenhui Li performed part of the theoretical analysis, and all of the device fabrication, experiments and results analysis. Hongrui Jiang contributed to the overall design of the flexible EWOD lens and part of the theoretical analysis.

Conflicts of Interest

The authors declare no conflict of interest.

References

1. Kuiper, S.; Hendriks, B.H.W. Variable-focus liquid lens for miniature cameras. *Appl. Phys. Lett.* **2004**, *85*, 1128–1130.
2. Liu, C.; Park, J.; Choi J. A planar lens based on the electrowetting of two immiscible liquids. *J. Micromech. Mcroeng.* **2008**, *18*, doi:10.1088/0960-1317/18/3/035023.
3. Cheng, C.C.; Chang, C.A.; Yeh, J.A. Variable focus dielectric liquid droplet lens. *Opt. Express* **2006**, *14*, 4101–4106.
4. Dong, L.; Agarwal, A.K.; Beebe, D.J.; Jiang, H. Adaptive liquid microlenses activated by stimuli-responsive hydrogels. *Nature* **2006**, *442*, 551–554.
5. Binh-Khiem, N.; Matsumoto, K.; Shimoyama, I. Polymer thin film deposited on liquid for varifocal encapsulated liquid lenses. *Appl. Phys. Lett.* **2008**, *93*, doi:10.1063/1.2988467.
6. Zhu, D.; Zeng, X.; Li, C.; Jiang, H. Focus-tunable microlens arrays fabricated on spherical surfaces. *J. Microelectromech. Syst.* **2011**, *20*, 389–395.
7. Kim, Y.; Park, J.H.; Choi, H.; Jung, S.; Min, S.W.; Lee, B. Viewing-angle-enhanced integral imaging system using a curved lens array. *Opt. Express* **2004**, *12*, 421–429.
8. IJzerman, W.L.; de Zwart, S.T.; Dekker, T. Design of 2D/3D Switchable Displays. In *SID Symposium Digest of Technical Papers*; Blackwell Publishing Ltd.: Hoboken, NJ, USA, 2005; pp. 98–101.
9. Lee, B.; Jung, S.; Min, S.W.; Park, J.H. Three-dimensional display by use of integral photography with dynamically variable image planes. *Opt. Lett.* **2001**, *26*, 1481–1482.
10. Song, Y.M.; Xie, Y.; Malyarchuk, V.; Xiao, J.; Jung, I.; Choi, K.J.; Rogers, J.A. Digital cameras with designs inspired by the arthropod eye. *Nature* **2013**, *497*, 95–99.
11. Krupenkin, T.; Yang, S.; Mach, P. Tunable liquid microlens. *Appl. Phys. Lett.* **2003**, *82*, 316–318.

12. Li, C.; Jiang, H. Electrowetting-driven variable-focus microlens on flexible surfaces. *Appl. Phys. Lett.* **2012**, *100*, doi:0.1063/1.4726038.
13. Niu, X.Z.; Peng, S.L.; Liu, L.Y.; Wen, W.J.; Sheng, P. Characterizing and patterning of PDMS-based conducting composites. *Adv. Mater.* **2007**, *19*, 2682–2686.
14. Bowden, N.; Brittain, S.; Evans, A.G.; Hutchinson, J.W.; Whitesides, G.M. Spontaneous formation of ordered structures in thin films of metals supported on an elastomeric polymer. *Nature* **1998**, *393*, 146–149.
15. Eddings, M.A.; Johnson, M.A.; Gale, B.K. Determining the optimal PDMS–PDMS bonding technique for microfluidic devices. *J. Micromech. Microeng.* **2008**, *18*, doi:10.1088/0960-1317/18/6/067001.
16. Duffy, D.C.; Schueller, O.J.; Brittain, S.T.; Whitesides, G.M. Rapid prototyping of microfluidic switches in poly (dimethyl siloxane) and their actuation by electro-osmotic flow. *J. Micromech. Microeng.* **1999**, *9*, doi:10.1088/0960-1317/9/3/301.
17. Rousche, P.J.; Pellinen, D.S.; Pivin, D.P., Jr.; Williams, J.C.; Vetter, R.J. Flexible polyimide-based intracortical electrode arrays with bioactive capability. *IEEE Trans. Biomed. Eng.* **2001**, *48*, 361–371.
18. Engel, J.; Chen, J.; Liu, C. Development of polyimide flexible tactile sensor skin. *J. Micromech. Microeng.* **2003**, *13*, doi:10.1088/0960-1317/13/3/302.
19. Takeuchi, S.; Ziegler, D.; Yoshida, Y.; Mabuchi, K.; Suzuki, T. Parylene flexible neural probes integrated with microfluidic channels. *Lab Chip* **2005**, *5*, 519–523.
20. Rodger, D.C.; Fong, A.J.; Li, W.; Ameri, H.; Ahuja, A.K.; Gutierrez, C.; Tai, Y.C. Flexible parylene-based multielectrode array technology for high-density neural stimulation and recording. *Sens. Actuators B Chem.* **2008**, *132*, 449–460.
21. Lee, H.; Cho, J. Development of Conformal PDMS and Parylene Coatings for Microelectronics and MEMS Packaging. In Proceedings of the ASME International Mechanical Engineering Congress and Exposition, Orlando, FL, USA, 5–11 November 2005.
22. Shih, C.Y.; Harder, T.A.; Tai, Y.C. Yield strength of thin-film parylene-C. *Microsys. Technol.* **2004**, *10*, 407–411.
23. Hassler, C.; von Metzen, R.P.; Ruther, P.; Stieglitz, T. Characterization of parylene C as an encapsulation material for implanted neural prostheses. *J. Biomed. Mater. Res. B Appl. Biomater.* **2010**, *93*, 266–274.
24. Shin, Y.S.; Cho, K.; Lim, S.H.; Chung, S.; Park, S.J.; Chung, C.; Chang, J.K. PDMS-based micro PCR chip with parylene coating. *J. Micromech. Microeng.* **2003**, *13*, doi:10.1088/0960-1317/13/5/332.
25. Mukhopadhyay, R. When PDMS isn't the best. *Anal. Chem.* **2007**, *79*, 3248–3253.
26. Datta, A.; Eom, I.Y.; Dhar, A.; Kuban, P.; Manor, R.; Ahmad, I.; Dasgupta, P.K. Microfabrication and characterization of Teflon AF-coated liquid core waveguide channels in silicon. *IEEE Sens. J.* **2003**, *3*, 788–795.
27. Wang, Y.; Zhao, Y.P. Electrowetting on curved surfaces. *Soft Matter* **2012**, *8*, 2599–2606.

CO_2 Laser Manufacturing of Miniaturised Lenses for Lab-on-a-Chip Systems

Mazher-Iqbal Mohammed and Marc Phillipe Yves Desmulliez

Abstract: This article describes the manufacturing and characterisation of plano-convex miniaturised lenses using a CO_2 laser engraving process in PMMA substrates. The technique allows for lenses to be fabricated rapidly and in a reproducible manner at depths of over 200 μm and for lens diameters of more than 3 mm. Experimental characterisation of the lens focal lengths shows good correlation with theory. The plano-convex lenses have been successfully embedded into capillary microfluidic systems alongside planar microlenses, allowing for a significant reduction of ancillary optics without a loss of detection sensitivity when performing fluorescence measurements. Such technology provides a significant step forward towards the portability of fluorescence- or luminescence-based systems for biological/chemical analysis.

Reprinted from *Micromachines*. Cite as: Mohammed, M.-I.; Desmulliez, M.P.Y. CO2 Laser Manufacturing of Miniaturised Lenses for Lab-on-a-Chip Systems. *Micromachines* **2014**, *5*, 457–471.

1. Introduction

Lab-on-a-chip technologies have revolutionised biological- and chemical-based processes for diagnostics-based applications. In particular, optical-based interrogation techniques have become the most prevalent means of end-point quantification. Such techniques are, however, typically performed using bulky assisting instrumentation, thereby negating the advantages of device miniaturisation [1,2]. An elegant approach to remedy this bottleneck with respect to true device portability and miniaturisation includes the use of embedded on chip microlenses and microlens arrays [3–10] for not only lab-on-a-chip systems, but also for alternative applications, ranging from optical storage/communications, high definition displays to a host of biomedical instrumentation [11].

Various microlenses and microarray structures have been fabricated in a range of substrates using techniques, such as photolithography/reactive ion etching [3–7], surface tension-based curing [10,11], laser ablation, engraving and thermal expansion [8,9,12–14], thermal reflow [15,16], embossing [17,18] and inkjetting [19,20]. Of these fabrication processes, CO_2 laser engraving is an attractive alternative to established micro-manufacturing techniques for the production of optical components, and such a technology has a rapid turnaround time and does not require fixed photomasks, embossing tools or a clean room environment and is suited to polymer manufacturing, a substrate most commonly used for the fabrication of various microsystems [8,9,21–25]. However, without adequate post-processing, the quality of manufactured microfluidics and the surface quality of the lenses are poor compared to techniques, such as photolithography or thermal reflow.

This article describes a manufacturing process whereby plano-convex lens structures are formed by CO_2 laser etching of poly(methyl methacrylate) (PMMA) polymer surfaces, using a graded power function with raster scanning. The resulting lens structures are then polished to a high degree of clarity using simple, backend processing of the lens surface, comprising abrasive hand sanding and polishing with rubbing compounds, followed by thermal annealing. The final lens structures can be fabricated with a high degree of reproducibility, rapidly and with the versatility to readily alter the physical parameters of the lens, providing considerable scope for tailoring of the focal lengths of the lens. CO_2 laser systems have been used previously to form planar lens structures [8,9] and lens structures upon optical fibres [14]. However, this is the first such demonstration of the CO_2 laser engraving using a graded power function by which to produce both single and arrays of plano-convex lenses in a bulk polymer material. Additionally, we demonstrate how both 2D planar and 3D plano-convex lenses can be readily integrated into microfluidics-based systems, providing a usable lab-on-a-chip platform for a range of optical-based test inspection and biological/chemical-based reaction end-point quantification.

2. Experimental Section

2.1. Materials and Fabrication

All microlens and microfluidic structures demonstrated in this work were manufactured using a Class 2 CO_2 laser etching system (Helix 24, Epilog, Golden, CO, USA), which operates at a maximum power of 40 W, a maximum scan speed of 96 mm s^{-1}, a wavelength of 10.6 μm with a spot size of 76–127 μm. All devices were manufactured from CLAREX® precision thin sheet PMMA, made by a specialist cell-casting technique, which ensures very high surface uniformity, and was purchased precast from Weatherall Equipment & Instruments Ltd (Bucks, UK). Designs of the plano-convex lenses were created using Corel Draw X4 (Corel Software, Ottawa, ON, Canada) interfaced directly with the CO_2 laser.

Within the Epilog system, the CO_2 laser is mounted in the device, such that its focal point is directed into reflecting and focusing optical elements, which translate the beam in the *x*- and *y*-directions through the use of two stepper motors. Samples to be processed are brought into focus with the laser upon a working stage, which is translatable in the *z*-direction. PMMA is processed based on its ability to absorb the radiation produced by the laser, with the power required to etch a given thickness depending on the melting and vaporisation temperatures of the polymer. The laser power and scan speed can be adjusted across a percentage scale in 1% increments, across either vector or raster power modes, as described in previous articles [21,22].

For the final manufacturing phase, the devices were constructed from a double-layer PMMA laminate, with the microfluidic channels and 2D lenses on the lower 1 mm-thick layer and plano-convex lenses on the upper layer. The upper layer also acts as a seal for the microfluidic channels and provides entry and exit ports for the test fluid, with flow being initiated and maintained through capillary action. Microchannels were fabricated in a single pass using a laser scan speed of 35% and power of 30%, with the laser set to low power raster mode, creating microchannels approximately 300 μm in depth. 2D lenses were created in a single pass of the laser with a scan speed of 30% and power of 80%, with the laser set to the high power vector mode to cut through the PMMA substrate, creating a 2D lens structure with a thickness equal to that of the substrate. The 2D lenses were singulated from the substrate to ease the polishing of the surfaces. They were also cut into a squared section of PMMA, such that they can be slotted back into the chip containing the channels for the subsequent bonding process. The polishing of the 2D lens surfaces is performed in an identical fashion to the plano-convex lenses, as described in Section 2.2.

The devices were bonded using a thermal compressive bonding procedure, described in [21]. The entire bonding procedure can be completed within approximately 2–3 h and leads to a permanent bonding of the PMMA through the controlled melting and re-solidification of the surfaces of the two PMMA layers. Briefly, the two laminate layers were covered with borosilicate glass microscope slides over the top and bottom layers and then placed between two 10 mm-thick steel plates and compressed together. The plates were then placed into a convection oven and heated under a slow thermal gradient (2–3 °C min^{-1}) above the glass transition temperature of the PMMA (170 °C), for a period of approximately 40 min. Following this, the oven is cooled to 80 °C and held for duration of 30 min before being cooled to room temperature.

2.2. Plano-Convex Lens Modelling and Fabrication

In addition to the unique manufacturing process that makes use of the graded power function of the laser engraving system, the 3D plano-convex lenses in this work yield several distinct advantages compared to the use of our previously demonstrated 2D lens structures. Firstly, the 2D lenses only allow for light to be directed within the plane of the chip, and the 3D lenses allow for light to be collected, or directed, orthogonal to the chip plane, making both lenses suitable for distinctly different applications. Therefore, collecting emission light orthogonal to the chip plane removes the cross-talk from excitation and emission light, thereby maximising the detection signal. For orthogonal chip light emission detection, the 2D lenses are not suitable. However, the 3D plano-convex lenses readily allow for this orientation, and their fabrication within the bulk chip substrate layer means that they can easily be integrated into the laminate chip bonding method used in this work. Additionally, the 3D lenses provide a greater collection efficiency of light, allowing for a near 2π collection angle, whereas collection with 2D lenses approximately has a collection angle of π. Ultimately, this makes the 2D lens structures ideal for excitation purposes, where light generally needs to be delivered in the chip plane, and the 3D plano-convex lenses are suited for emission collection optics.

In our previous work, we have demonstrated the CO_2 laser operating with either power on or off [8,21]. In this work, the laser was used in an analogue fashion to yield greater functionality during fabrication to create the 3D features. In that regard, a circular design, which comprises the plano-convex lens, was superimposed upon a rectangular area. The rectangular area is removed by direct etching using the laser system. The use of the rectangular area surrounding the lens is required to allow space for polishing of the lens surface post engraving. The power distribution of the laser was graded from full power at the rectangle area and circle edges and gradually moving to zero power at the centre of the circle. This resulted in the creation of a plano-convex lens in the centre of the rectangular etched area within the PMMA. The curvature of the lens can be adjusted depending upon the radius of the circle design and by control of the depth of etching in the low power, raster scan mode of the laser. Using the CO_2 laser at maximum power in raster scan mode, Figure 1 illustrates the attained average lens depth of etch as a function of the laser scan speed for a 5-mm diameter lens fabricated into a 2 mm-thick PMMA substrate. Tests were also performed using multiple passes of the laser over a single target area, allowing for the maximum depth of etch to be extended beyond that of a single pass. During the subsequent passes, the laser spot is out of focus and imparts less power onto the target area. This has the effect of partially "cleaning" residual, condensed PMMA material. For this work, 2 passes were performed with the power set to maximum and with speeds of 45% and 60% for the first and second pass, respectively. This produced a lens structure with an approximate depth of 600 ± 30 µm, which was used as a standard depth to investigate various diameter lens structures.

Figure 1. Ablation depth as a function of laser scan speed for maximum raster mode laser power.

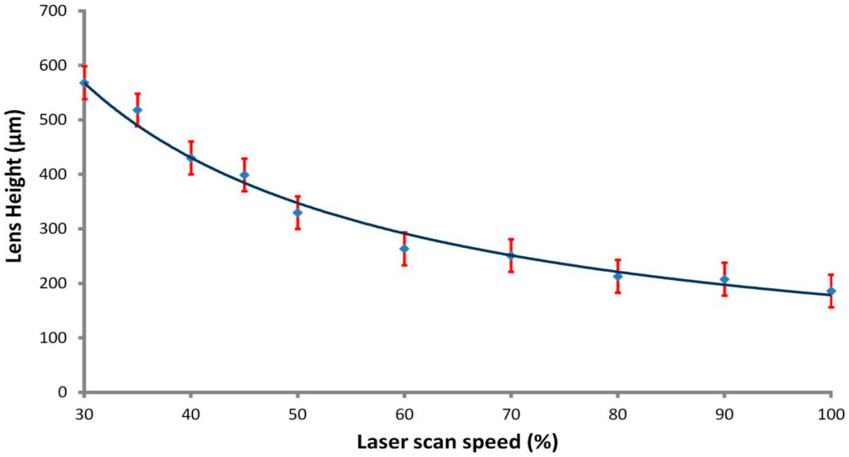

Optical simulations were performed using OptiCAD 7.0 (OptiCAD Corporation, Santa Fe, NM, USA) modelling the focusing of light from a collimated white light source through a plano-convex spherical lens and onto a virtual detection area. This model mimics our experimental set-up allowing for the determination of the focal length of the lens. In all simulations, a refractive index for PMMA of 1.49 was used. Figure 2 shows ray path simulations for a 5 mm-diameter plano-convex lens. Several lens diameters were examined, and a summary of the lens properties and predicted focal distances can be found in Table 1. The simulations revealed the spherical aberrations that would be present in such a lens design, which results in a range over which the true focal distance of the lens will be found, and this range is expressed in Table 1.

Figure 2. (**a**) Simulated results of the focusing of a collimated light source through a 5-mm plano-convex lens showing (**i**) 3D and (**ii**) a plan view of the lens and light rays; (**b**) A diagram illustrating the parameters of the fabricated lenses within a PMMA bulk substrate, as stated in Table 1.

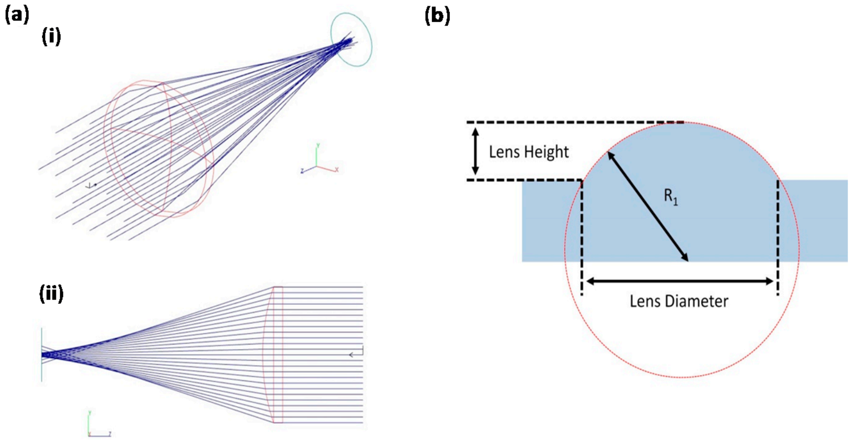

Table1. Theoretical results for various lens diameters and their respective focal lengths. R_1 is defined in Figure 2.

Lens diameter (mm)	Lens height (mm)	R_1 (mm)	Simulated focal range (mm)
0.25	0.6	12.5	0.19–0.21
0.5	0.6	0.25	0.44–0.46
1	0.6	0.5	0.92–0.95
3	0.6	2.35	4.2–4.3
5	0.6	6	11.2–11.5

The plano-convex lenses were fabricated in a similar fashion to PMMA-based laser-ablated 2D lenses [8]. The surfaces of the lenses were found to be rough, due to the nature of the thermal vaporisation and condensation process, as observed in Figure 3a-i. Following the initial laser etching, the lenses were then polished manually by hand, by firstly sequentially sanding using 60, 240, 600, 1200, 2400 and 4000 grit wet and dry sandpaper to remove major defects. Lenses were sanded by placing a 1 cm^2 piece of wetted sand paper over the lens, applying light pressure with the index finger and rotating the paper in a clockwise circular manner, with the whole procedure taking approximately 5–6 min. This was followed by a two-stage hand polishing with an acrylic polymer cutting compound (Glass Polish Ltd., Tolworth, UK) to remove the majority of remaining abrasions and scratches, with this procedure taking approximately 5 min. Following polishing, the lenses underwent a final stage of thermal processing, whereby the substrate is heated above the glass transition temperature of the PMMA for 30 min, resulting in the liquefaction of the lens surface. At this stage, the surface tension effects during liquefaction remove any remaining minor defects, resulting in a high quality finish to the lens surface, as can be seen in Figure 3a-ii,b. The process of defect removal had measured effects on the radius and height, and each was quantified by taking the average across 10 independently manufactured 5 mm-diameter lenses. The radiuses of the lenses were found to contain negligible differences, with an average reduction of 5–10 µm over the 5 mm of diameter. The height at the centre of the lens relative to the original substrate height was found to be reduced by approximately 250 ± 20 µm. These changes were factored into the optical simulations to reflect the true geometry of the manufactured lenses.

The graded spatial thermal processing of the PMMA substrate was examined over varying lens diameters to determine the limitations to the geometry of the manufactured lenses. The CO_2 laser system has a minimum manufacturing resolution of approximately 100–150 µm. The smallest manufacturable size is likely to be significantly larger for the laser stepper motor to create the lens curvature upon the PMMA surface. Various-sized lenses were manufactured with diameters of 5 mm, 3 mm, 2 mm, 1 mm and 750 µm, and the quality of the final structures was assessed to determine the limitations of the proposed manufacturing process, as described later in the article. It was determined that the 5 mm-larger diameter lens structure was likely to be the most practical for implementation into a working device, given its focal length and the need to manually align the photodetector with the chip system. Therefore, work was focused primarily on the characterisation of this type of lens.

Figure 3. (**a**) Photographs of a 5 mm, spherical PMMA lens (**i**) post-laser ablation and (**ii**) post-polishing and thermal annealing; (**b**) The same PMMA post-polished and thermally annealed lens in (**i**) side profile and (**ii**) overhead profile.

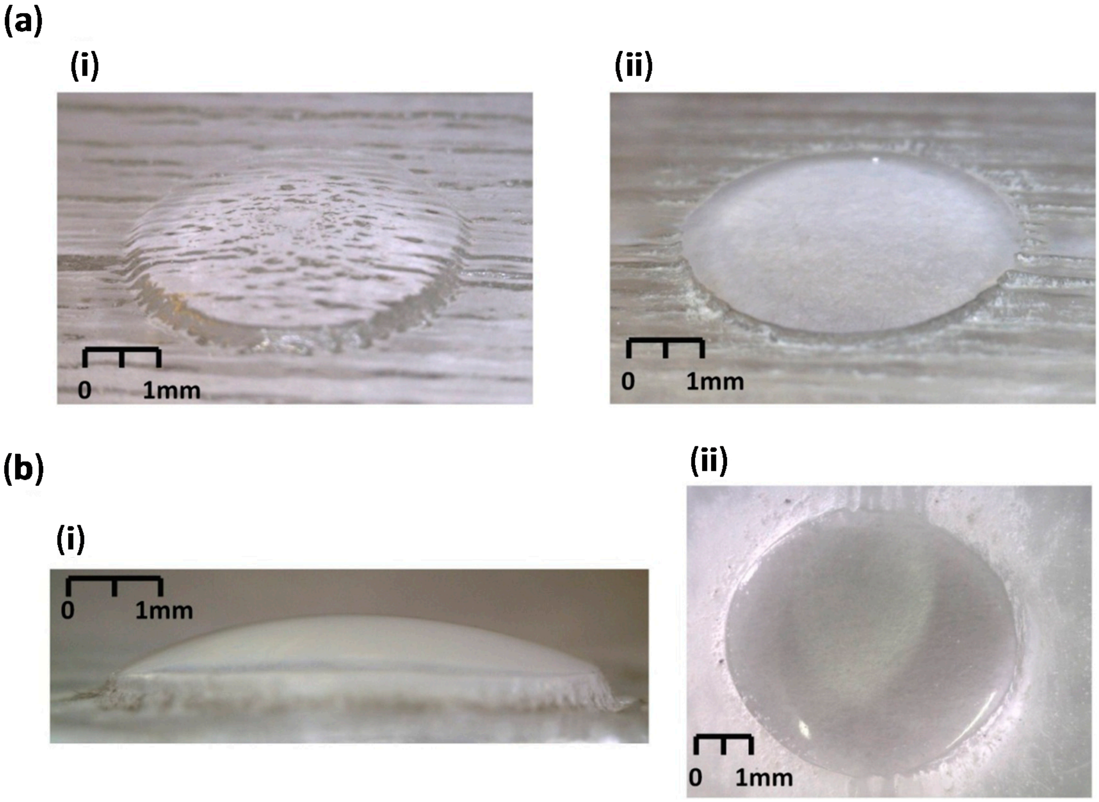

2.3. Fluorescence and Light Detection

The manufactured lenses were validated through the detection of both light from various LED sources and from the emission of excited fluorophores placed into microfluidic systems. For all characterisation-based experiments, detection was achieved using a USB-based spectrometer (USB2000+, Ocean Optics, Dunedin, FL, USA) in conjunction with a 200-µm coupling optical fibre (Numerical Aperture (NA) = 0.22) mounted upon an *x*-*y*-*z* translational stage. Focal length determinations were achieved using a blue collimated LED source (M470L3-C1, Thorlabs, Ely, UK) and the diameter of the light column controlled by an in-house build optical aperture. A schematic of the experimental setup can be seen in Figure 4a.

For testing in the microfluidic system, serial dilutions of fluorescein isothiocyanate (FITC) dye ($\lambda_{\text{Excitation}}$ = 494 nm and $\lambda_{\text{Emission}}$ = 518 nm) were used as a demonstrator for fluorescence detection. In this work, a 1-nM FITC solution was used for all testing of lens properties. This was made fresh in a stock solution combined on the first instance with ethanol, following the manufacturer's recommendations, and then subsequently diluted with deionised water. As ethanol degrades PMMA, which was used as the vessel for FITC, a water-based dilution methodology was used to preserve the integrity of the microfluidic channels. Excitation of the fluorophores was achieved using a 3-mm Nichia ultra-bright blue LED (NSPB300A, RS Components, Glasgow, UK) and a band pass excitation filter (FB490-10, Thorlabs, UK) with λ_{Trans} = 490 ± 5 nm (approximately 48% transmission), both mounted into a custom-built holder cradle. Fluorescence detection measurement was achieved using a H9858 photosensor module (Hamamatsu, Welwyn Garden City, UK), in conjunction with an FITC-optimised band pass emission filter (HQ535-50m, Chroma, Bellows Falls, VT, USA), $\lambda_{\text{Trans}} = 535 \pm 25$ nm (approximately 75%–80% transmission). A schematic of the experimental set up can be seen in Figure 4b. The photodetector and emission filter were both housed within a custom-built cradle, to preserve the alignment of the two components and to reduce background light from entering the active area of the detector. A secondary rig was built to house the excitation LED/emission filter and to create a cradle into which the chip could be placed, such that its final orientation would leave the 2D planar lens and microchamber of the fluidic chip in direct alignment with the LED and photodetector, respectively. The photomultiplier module, LED and filters were set up in a configuration as illustrated in Figure 5b, and the photodetector was mounted a distance of 40 mm above the bottom of the chip holding cradle. As a benchmark comparison, fluorescence measurements were performed using a 10× microscope objective (Thorlabs, UK) as the light collection optics, placed approximately 500 μm above the fluidic microchamber, in a configuration described previously [8]. Such a system has been demonstrated previously by our group to provide FITC detection limits of 10 fM, which is comparable to the detection capabilities of commercial fluorescence reader systems. The use of this benchmark setup allows us to examine the efficiency of the optical component only, as we shall keep the excitation and detection apparatus the same. This therefore eliminates the variability from factors, such as detector sensitivity and excitation power emission, that have a different fluorescence setup being used, thereby providing a more fair comparison of the devised plano-convex lenses against commercial-grade optics.

Figure 4. Schematic of the experimental setup to determine (**a**) the lens focal length and (**b**) the FITC fluorescence intensity measurements.

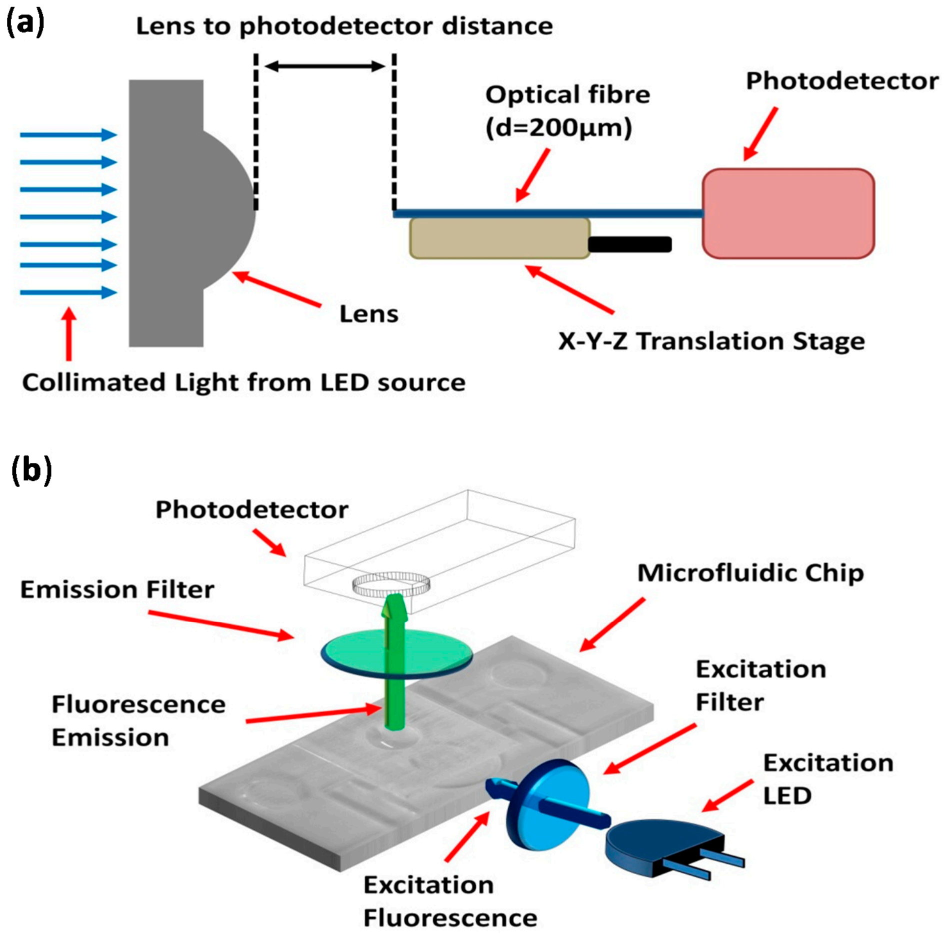

3. Results

3.1. Manufacturing Limitations and Characterisation

Investigations were initially performed to validate the smallest repeatable lens size that could be manufactured by the proposed fabrication process. Figure 5a shows images of several lens structures ranging from 3 mm to 750 μm in a single array. The defect removal procedure was focused on the lenses only and not on the bulk of the PMMA substrate material, which had been engraved away using the CO_2 laser. The ability to use a manual polishing methodology was constrained by the size of the lens structure and the ability to physically feel the surface of the lens during hand sanding. Additionally, the qualitative nature of the process limits the roundness precision of the lenses, which were found to suffer a discrepancy between what could be achieved and the desired lens curvature. Errors in precision were quantified to be on average a minimum of 1–2 μm and a maximum of 30–40 μm above or below the intended curvature respectively. This discrepancy was found to be uniform across the various lens diameters from the average measurement of several lens surfaces under a microscope and has the influence of increasing the spherical aberrations. As the discrepancy in the roundness was found to be uniform, their influence is most pronounced for smaller lens diameters, negatively impacting the ability to achieve a tight focus of a light source or to produce a sharp image when used for magnification purposes. Through qualitative testing, for lens diameters of over 3 mm, the influence on achieving a tight focus from a light source or producing a sharp image of a magnified test structure was found to be negligible. Despite the demonstrated qualitative adequacy of the hand sanding/polishing method, it would be desirable to standardize the polishing procedure through the automated use of an industrial, sanding, lapping and polishing device. These devices could potentially provide more uniform pressure and sanding/polishing action across the surface of the lens, improving the roundness of the lenses and, thereby, reducing spherical aberrations. Tests were also performed to use the Epilog laser system to polish the surface of the manufactured lenses using a methodology described previously [26], but attempts were unsuccessful at adequately removing defects. Given greater control of the laser parameters (raster speed, power, *etc.*), the current CO_2 laser could potentially be used to polish the surface of the lenses. We aim to investigate the feasibility of such measures in future work.

For diameters of less than 750 μm, the laser was incapable of forming the desired lens structure in a reproducible manner, due to limitations in the resolution of the *x*-*y* translation stage of the Epilog equipment. It was therefore concluded that the smallest repeatable diameter of lens manufacturable by the described process was above 3 mm.

Figure 5. (**a**) Photographs of spherical PMMA lenses (**i**) of sizes of 3 mm, 2 mm, 1 mm and 750 um; and (**ii**) a 5 mm lens array, post-polishing and thermal annealing; (**b**) Results for the average focal length determination of several 5 mm-diameter spherical lenses.

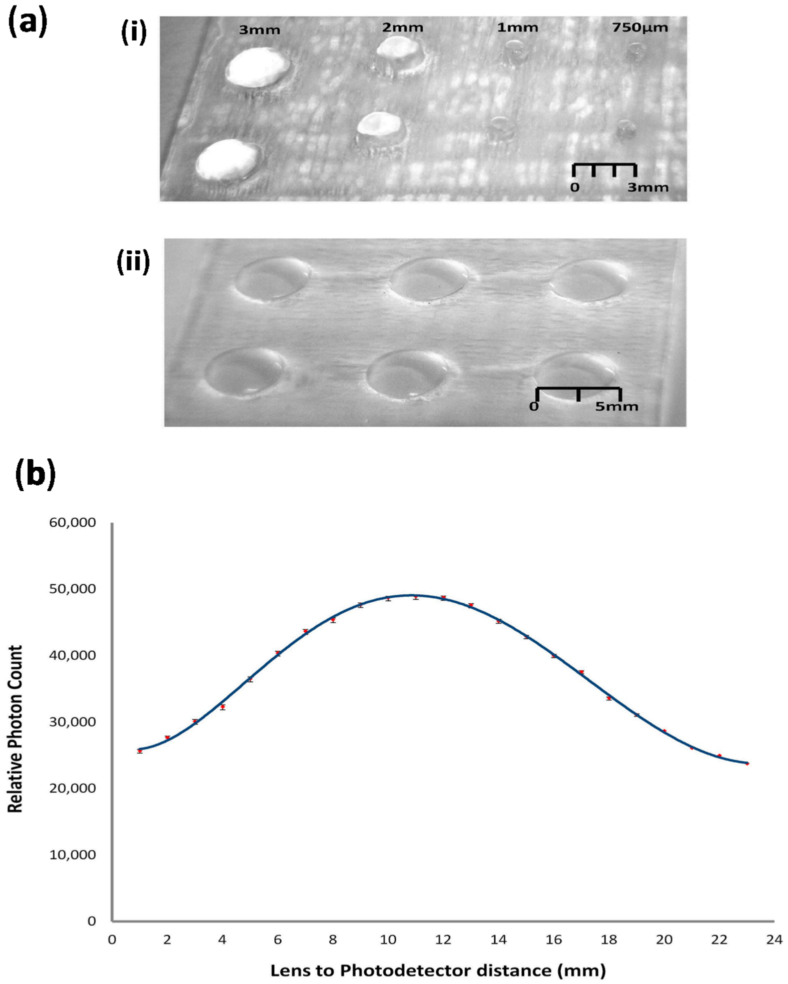

Given the greater level of repeatability of larger diameter lens structures, the remainder of this work focused on the characterisation of the 5 mm-diameter plano-convex lenses. Each lens was characterised using the experimental setup illustrated in Figure 4a, whereby an optical fibre, 200 µm in diameter (0.22 NA ≈ 25° full angle of acceptance), connected to a photodetector, was placed at the midpoint of the lens and ,using a translational stage, was moved progressively away from the lens in 1 mm increments. Light was then shone from a collimated LED source, through a lens, where it was focused into the direct path of the optical fibre. It was believed that, given the limited acceptance angle, as the fibre was moved closer to the focal point of the lens, the intensity measured by the photodetector would increase. Conversely, as the fibre moves away from the focal point, the intensity would also decrease. Results for the average over five lenses are illustrated in Figure 5b, were a focal point of approximately 10.9 mm was determined from extrapolation of a line of best fit. This result is in good agreement with the predicted result of 11.2–11.5 mm, with any discrepancies being explained by the minor variations in the lens height and the alignment of the optical fibre during experimentation.

It was possible given the agile nature of the laser engraving process that lens arrays could be produced and applied to the multiplex focusing of multiple sources, such as those found in multiplate well systems.

Figure 5a-ii shows a picture of a 5 mm-diameter lens array, fabricated with a spacing of 5 mm from each edge of the lens structure.

3.2. Microfluidic Chip Integration

The rapid prototype manufacturing process was investigated to integrate the plano-convex lens directly into a microfluidic chip design, in a similar fashion as the integration of 2D planar lenses achieved by our group in previous works [8,9]. The aim of such a device would be to operate as an integrated excitation and detection platform for fluidic and solid phase-based biological and chemical processes, such as fluorescence/luminescent DNA- [27,28] and protein- [8,9,29,30] based reactions. Such a design would provide a lab-on-a chip solution that completely eliminates complementary, off-chip optical elements. As our aim in this work is to focus on aspects pertaining to micro-optical systems integration, we shall not elaborate on the dynamics of the fluidics components, which we have characterised previously [22].

Figure 6a illustrates the complete microfluidic chip design, with the lower laminate layer containing the microfluidic channel, micro-chamber and 2D planar lenses and the upper layer containing the entry/exit ports and the plano-convex lens. The chip had approximate dimensions of 60 mm × 25 mm × 3 mm. For visualisation of all the chip components, the bulk engraved area surrounding the plano-convex lens has been left intact. Prior to a measurement, this area is covered with a layer of blackened masking tape, leaving only the lens exposed, in order to remove any unwanted scattering of the excitation and emission light on the roughened surface from entering the active area of the photodetector, thereby improving detection sensitivity. For experimentation, one of the ports was loaded with 20 μL of the 1 nM FITC dye, which migrated to fill the fluidic system through capillary forces. Following loading of the test dye, the microfluidic chip was placed into the cradle of the custom-built excitation and fluorescence reader, and the emitted fluorescence was measured.

Initial tests were performed on a fluidic chip with the 600-μm depth, 5 mm-diameter plano-convex microlens engraved into a 2-mm substrate, placing the lens at a distance of approximately 1.4 mm from the upper surface of the FITC loaded micro-chamber. Following this measurement, additional microfluidic chips were fabricated to include the 2D planar lens and a blank 1 mm-thick upper sealing layer, with only entry and exit ports. This allowed for a plano-convex lens engraved substrate and spacers to be placed upon the chip surface to examine the change in measured fluorescence with increased separation distance. To increase the separation distance, various 1 mm-thick PMMA substrates, of equal size to the chip, were placed in between the unmodified upper layer chip and a PMMA layer containing the plano-convex microlens. Results of the fluorescence detection can be seen in Figure 6b, where it was found that the use of the lens significantly increased the detected fluorescence emission in comparison to when no lens was placed on the chip. The largest increase in detected fluorescence was achieved for a separation distance of approximately 9.4 mm, which provided an increase in fluorescence signal by approximately a factor of 2–2.5. Examining the results against the measurement using the collection optics benchmark, it was found that the maximum intensity achieved using the plano-convex lens system was comparable to the use of the microscope objective, as can be seen in Figure 6b. The lenses were significantly smaller in dimensions, being a height of 600 μm and a radius of 5 mm, compared to a height of 50 mm and maximum radius of 30 mm for the microscope objective. It is the aim of future work to develop the system further to reduce the separation distance of the lens to the microchannel by means of altered single lens geometry or the use of a compound multi-lens system. However, even with the added height of the separation distance, the 10 mm total height of the system compares favourably to the microscope objective benchmark. This, in addition to the integration of the lenses, provides significant advantages of the demonstrated system in terms of overall device portability, a bottleneck still to be fully addressed in current lab-on-a-chip and microfluidic systems.

Figure 6. (**a**) (**i**) Photograph of the complete microfluidic chip with integrated planar and spherical lenses and (**ii**) annotated schematic of the microchip cross section; (**b**) Detected fluorescence intensity from a 1-nM sample of FITC within the chip as a function of the distance of the lens from the micro-chamber. As a comparison, results are shown for systems with no spherical lens and additional collection optics; and no spherical lens and a 10× microscope objective for emission collection.

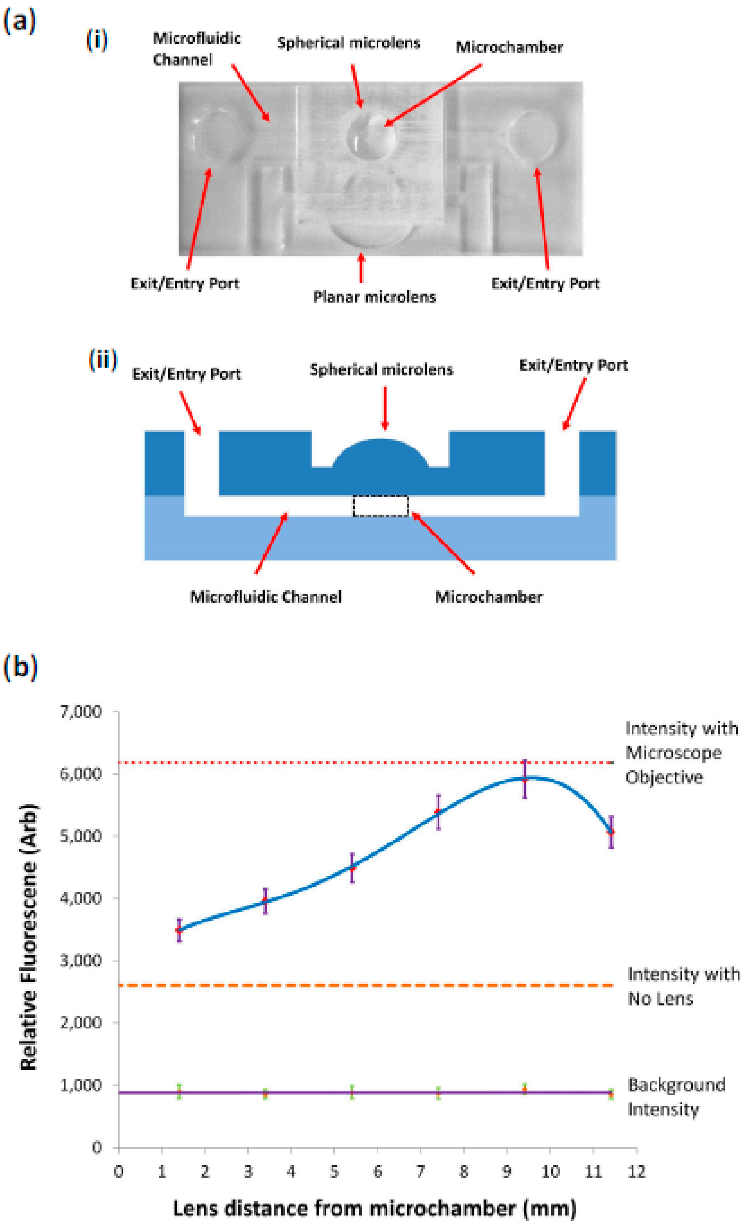

4. Conclusions

In this paper, we have reported the creation of plano-convex microlens structures within PMMA substrates by means of 3D CO_2 laser engraving. The lenses can be made rapidly and in a reproducible manner, at depths of over 200 μm and for lens diameters larger than 3 mm. Good agreements with optical simulation results were obtained as far as the calculation of the focal length was concerned. The plano-convex lenses have been successfully integrated into capillary microfluidics and have demonstrated significant improvements, compared with their no-lens counterparts, in the detected fluorescence intensity of a fluorescent dye placed within the microfluidics. The performance of the system has also been demonstrated to be comparable to that of larger, commercial optical components, but at a fraction of the size and price, thus enhancing the overall portability of the system. The complete microfluidic system, when used in conjunction with 2D planar and 3D plano-convex lenses, reduces the instrumentation required to just simple excitation and detection sources and filters. The presented system has demonstrated a usable format by which microfluidics could be translated to true portable use and could find usefulness in a range of fluorescent/luminescent-based applications for biological and chemical analysis.

Acknowledgments

The authors would like to thank Stephan Wilhelm for his technical discussion regarding the laser manufacturing process.

Author Contributions

All experimental and theoretical work was conducted by Mazher Mohammed in conjunction with Marc Desmulliez.

Conflicts of Interest

The authors declare no conflict of interest.

References

1. Kuswandi, B.; Nuriman, J.; Huskens, J.; Verboom, W. Optical sensing systems for microfluidic devices: A review. *Anal. Chim. Acta* **2007**, *601*, 141–155.
2. Myers, F.B.; Lee, L.P. Innovations in optical microfluidic technologies for point-of-care diagnostics. *Lab Chip* **2008**, *8*, 2015–2031.
3. Camou, S.; Fujita, H.; Fujii, T. PDMS 2D optical lens integrated with microfluidic channels: Principle and characterization. *Lab Chip* **2003**, *3*, 40–45.
4. Guo, H.; Zhao, P.; Xiao, G.; Zhang, Z.; Yao, J. Optical manipulation of microparticles in an SU-8/PDMS hybrid microfluidic chip incorporating a monolithically integrated on-chip lens set. *IEEE J. Sel. Top. Quantum. Electron.* **2010**, *16*, 919–926.
5. Rosenauer, M.; Bechugger, W.; Finoulst, I.; Verhaert, P.; Vellekoop, M. Miniaturized flow cytometer with 3D hydrodynamic particle focusing and integrated optical elements applying silicon photodiodes. *Microfluid. Nanofluidics* **2011**, *10*, 761–771.

6. Seo, J.; Lee, L.P. Disposable integrated microfluidics with self-aligned planar microlenses. *Sens. Actuators B* **2004**, *99*, 615–622.
7. Roulet, J.C.; Voelkel, R.; Herzig, H.P.; Verpoorte, S.; de Rooij, N.F.; Daendliker, R. Microlens systems for fluorescence detection in chemical microsystems. *Opt. Eng*. **2001**, *40*, 814–821.
8. Mohammed, M.I.; Desmulliez, M.P.Y. Planar lens integrated capillary action microfluidic immunoassay device for the optical detection of troponin I. *Biomicrofluidics* **2013**, *5*, doi:10.1063/1.4837755.
9. Mohammed, M.I.; Desmulliez, M.P.Y. Autonomous capillary microfluidic system with embedded optics for improved troponin I cardiac biomarker detection. *Biosens. Bioelectron*. **2014**, 61, 478–484.
10. Lee, B.K.; Park, J.M.; Kim, D.S.; Kwon, T.H. A simple fabrication and integration technique of microlens for microfluidic lab-on-a-chip by overflow of UV resin through holes. *Curr. Appl. Phys*. **2001**, *11*, 909–913.
11. Ho, J.R.; Shih, T.K.; Cheng, J.W.J.; Sung, C.K.; Chen, C.F. A novel method for fabrication of self-aligned double microlens arrays. *Sens. Actuators A* **2007**, *135*, 465–471.
12. Kim, K.R.; Jeong, H.W.; Lee, K.S.; Yi, J.; Yoo, J.C.; Cho, M.W.; Cho, S.H.; Choi, B. Rapid laser fabrication of microlens array using colorless liquid photopolymer for AMOLED devices. *Opt. Commun.* **2011**, *284*, 405–410.
13. Chiu, C.C.; Lee, Y.C. Fabricating of aspheric microlens array by excimer laser micromachining. *Opt. Lasers Eng*. **2011**, *49*, 1232–1237.
14. Malki, A.; Bachelot, R.; van Lauwe, F. Two-step process for micro-lens-fibre fabrication using a continuous CO_2 laser source. *J. Opt. A Pure Appl. Opt.* **2001**, *3*, 291–295.
15. Lian, Z.J.; Hung, S.Y.; Shen, M.H.; Yang, H. Rapid fabrication of semi ellipsoid microlens using thermal reflow with two different photoresists. *Microelectron. Eng*. **2014**, *115*, 46–50.
16. Li, F.; Chen, S.H.; Luo, H.; Zhou, Y.F.; Lai, J.J.; Gao, Y.Q. Fabrication and characterization of polydimethylsiloxane concave microlens array. *Opt. Laser Technol.* **2012**, *44*, 1054–1059.
17. Huang, T.C.; Chan, B.D.; Ciou, J.K.; Yang, S.Y. Fabrication of microlens arrays using a CO_2-assisted embossing technique. *J. Micromech. Microeng*. **2009**, *19*, doi:10.1088/0960-1317/19/1/015018.
18. Wu, J.T.; Chu, Y.T.; Yang, S.Y.; Li, C.C. Low-temperature embossing technique for fabrication of large-area polymeric microlens array with supercritical carbon dioxide. *Microelectron. Eng.* **2010**, *87*, 2620–2624.
19. Luo, Y.; Wang, L.; Ding, Y.; Wei, H.; Hao, X.; Wang, D.; Shi, J. Direct fabrication of microlens arrays with high numerical aperture by ink-jetting on nanotextured surface. *Appl. Surf. Sci.* **2013**, *279*, 36–40.
20. Lin, X.; Hosseini, A.; Dou, X.; Subbaraman, H.; Chen, R.T. Low-cost board-to-board optical interconnects using molded polymer waveguide with 45 degree mirrors and inkjet-printed micro-lenses as proximity vertical coupler. *Opt. Express* **2013**, *21*, 60–69.
21. Mohammed, M.I.; Desmulliez, M.P.Y. The manufacturing of packaged capillary action microfluidic systems by means of CO_2 laser processing. *Microsyst. Technol*. **2013**, 19, 80–818.
22. Mohammed, M.I.; Desmulliez, M.P.Y. Characterisation and theoretical analysis of rapidly prototyped capillary action autonomous microfluidic Systems. *J. Microelectromech. Syst.* **2014**, doi:10.1109/JMEMS.2014.2314470.

23. Klank, H.; Kutter, J.P.; Geschke, O. CO_2-laser micromachining and back-end processing for rapid production of PMMA-based microfluidic systems. *Lab Chip* **2002**, *2*, 242–246.
24. Malek, C.G.K. Laser processing for bio-microfluidics applications part I. *Anal. Bioanal. Chem.* **2006**, *385*, 1351–1361.
25. Nayak, N.C.; Lam, Y.C.; Yue, C.Y.; Sinha, A.T. CO_2-laser micromachining of PMMA: The effect of polymer molecular weight. *J. Micromech. Microeng*. **2008**, *18*, doi:10.1088/0960-1317/18/9/095020.
26. Nowak, K.M.; Baker, K.M.; Hall, D.R. Efficient laser polishing of silica micro-optic components. *Appl. Opt*. **2006**, *45*, 162–171.
27. Mohammed, M.I.; Sills, G.J.; Brodie, M.J.; Ellis, E.; Girkin, J.M. A complete miniaturised genotyping system for the detection of single nucleotide polymorphisms in human DNA samples. *Sens. Actuators B* **2009**, *139*, 83–90.
28. Girkin, J.M.; Mohammed, M.I.; Ellis, E.M. A miniaturised integrated biophotonic point-of care genotyping system. *Faraday Discuss.* **2010**, *149*, 115–123.
29. Dacres, H.; Dumancic, M.M.; Horne, I.; Trowell, S.C. Direct comparison of fluorescence- and bioluminescence-based resonance energy transfer methods for real-time monitoring of thrombin-catalysed proteolytic cleavage. *Biosens. Bioelectron*. **2009**, *24*, 1164–1170.
30. Dacres, H.; Michie, M.; Anderson, A.; Trowell, S.C. Advantages of substituting bioluminescence for fluorescence in a resonance energy transfer-based periplasmic binding protein. *Biosens. Bioelectron*. **2013**, *41*, 459–464.

An Optofluidic Lens Array Microchip for High Resolution Stereo Microscopy

Mayurachat Ning Gulari, Anurag Tripathi, Mostafa Ghannad-Rezaie and Nikos Chronis

Abstract: We report the development of an add-on, chip-based, optical module—termed the Microfluidic-based Oil-immersion Lenses (μOIL) chip—which transforms any stereo microscope into a high-resolution, large field of view imaging platform. The μOIL chip consists of an array of ball mini-lenses that are assembled onto a microfluidic silicon chip. The mini-lenses are made out of high refractive index material (sapphire) and they are half immersed in oil. Those two key features enable submicron resolution and a maximum numerical aperture of ~1.2. The μOIL chip is reusable and easy to operate as it can be placed directly on top of any biological sample. It improves the resolution of a stereo microscope by an order of magnitude without compromising the field of view; therefore, we believe it could become a versatile tool for use in various research studies and clinical applications.

Reprinted from *Micromachines*. Cite as: Gulari, M.N.; Tripathi, A.; Ghannad-Rezaie, M.; Chronis, N. An Optofluidic Lens Array Microchip for High Resolution Stereo Microscopy. *Micromachines* **2014**, *5*, 607–621.

1. Introduction

Stereo microscopes are low-end, low-cost, imaging instruments, mainly used in the field of biology and medicine [1]. They provide 3D images; have long working distances, large field of view and depth of focus. They are also modular, as the manufacturers provide a wide variety objectives, stands and illumination accessories. Because of these advantages, they are commonly used in the lab or in the hospital for bacteria counting, organism and tissue imaging, as well as for dissecting and inspecting specimens [2–5]. Stereo microscopes are also used in geology and archaeology as well as for inspecting microparts and electronics, making jewelry and repairing watches [6].

Despite the advantages mentioned above, stereo microscopes have limited resolution (typically 10–20 μm) and magnification (1×–6× without considering the magnification from the eyepiece) [6] when compared to the submicron resolution and magnification of up to 100× of expensive compound microscopes. In particular, low resolution is a critical shortcoming in low-end imaging systems as it prevents their use in clinical applications where cellular and sub-cellular imaging is needed.

Research efforts towards low cost, compact imaging systems have focused on utilizing microlenses [7–10] and microlens arrays [11–26] optofluidic microscope [27,28] or even tomographic imaging methods [29,30]. Although these approaches demonstrated high-resolution imaging, they typically lack the flexibility and versatility of a stereo microscope where the user can easily adjust the focus and magnification or the illumination conditions depending on the sample that is being imaged. An add-on optical module, e.g., a lens attachment for high-resolution imaging [21,31–34], would be an attractive solution in order to maintain the intended generic use of a stereo-microscope.

Here, we report the development of a compact and inexpensive optical, add-on module that transforms any stereo microscope into a high resolution imaging system without compromising the field of view. The add-on module—a Microfluidic-based Oil-immersion Lens (μOIL) chip—consists of an array of ball mini-lenses of excellent optical quality, which are microfluidically connected and half immersed in oil. The use of the µOIL chip is simple as it can be mounted on top of any biological sample and imaged through the stereo microscope by simply adjusting the focus. The µOIL chip is microfabricated on a wafer-level process, while the ball lenses are commercially available. The combined stereo microscope/µOIL chip system is an ideal tool for research studies and clinical applications where sub-micron and large field of view imaging is required.

2. The µOIL Chip

2.1. Architecture of the µOIL Chip

The µOIL chip consists of a 4 × 4 array of 1 mm in diameter ball mini-lenses. They are precisely seated on top of an array of 970 µm diameter microwells, etched on a silicon chip (Figure 1a,b). We use the term "ball mini-lenses" to indicate that they are small in size but they are not microfabricated. Those commercially available, ball mini-lenses are made of a high refractive index material (sapphire, refractive index 1.77, Edmund Optics, Barrington, NJ, USA, catalogue number 43-638) that greatly increases the numerical aperture (NA) of the system. They are half immersed in microscope oil, and half exposed to air. As a result, they act as doublet lenses, resembling the front end of a high-end, oil immersion microscope objective. We choose those mini-lenses as they have optical quality surface finish, tight tolerances (diameter, sphericity) and excellent broadband transmission. The silicon microwells are connected to each other through an open-air microfluidic network that distributes the oil uniformly to the entire array. The silicon chip is bonded to a thin glass substrate in order to seal the bottom of the microwells. The dimensions of the various elements of the µOIL chip were chosen, such that the focal plane of the ball mini-lenses is located at the bottom surface of the glass chip.

The sample, which typically sits on a transparent substrate (e.g., a microscope glass slide), is placed underneath the µOIL chip at a fixed distance from the ball mini-lens array. That distance is accurately defined by the thickness of a spacer. The spacer can be a thin photoresist film that is patterned on the bottom of the glass substrate or stacked glass chips (typically 100–300 µm thick) placed underneath each side of the µOIL chip. The latter option is recommended when a large field of view (FOV) is desired and high resolution is not that critical. When the sample/µOIL chip assembly is imaged through a stereoscope (Figure 1c), a high resolution and magnified image of the sample is obtained. Using an array of 16 ball lenses fully assembled on the µOIL chip (Figure 1b), one can observe simultaneously multiple areas of interest.

Figure 1. (**a**) Cross section schematic of the μOIL chip; (**b**) A picture (**left**) of the microfabricated μOIL chip (scale bar: 3 mm) and a close up view (**right**) of the microwell array with no ball mini-lenses (scale bar, 1 mm); and (**c**) The combined μOIL chip/stereo microscope system. The μOIL chip is placed directly on top of the sample of interest.

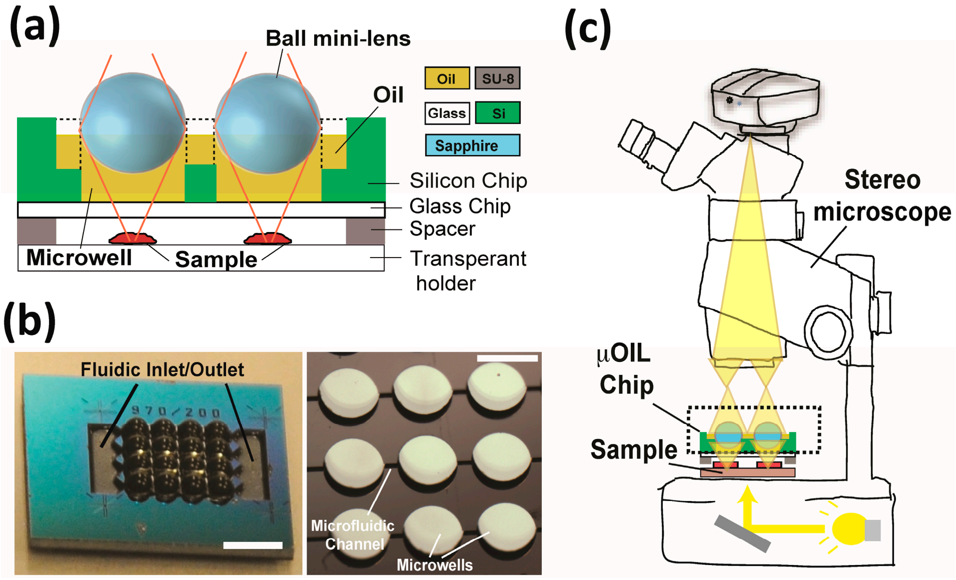

2.2. Microfabrication

The μOIL chip is fabricated using a 2-mask, standard silicon micromachining processes. The fabrication process consists of the following steps (Figure 2a): (1) A 400 μm thick silicon wafer is thermally oxidized to form a 200 nm thick SiO_2 film. The SiO_2 film is photolithographically patterned and Hydrofluoric acid-etched to create a hard masking layer for etching the microfluidic network; (2) A 5 μm thick photoresist film is then patterned using the second mask that contains the microwell array and a deep reactive ion etching (DRIE) step is performed to partially etch 200 μm out of the 400 μm microwell total thickness; (3) The photoresist is then stripped to expose the SiO_2 film. A wafer-through DRIE step is then performed to obtain the 200 μm thick microfluidic network and the microwells; (4) The silicon wafer is anodically bonded to a 100 μm thick Pyrex wafer and the bonded wafer is diced. A 5 μm thick SU-8 film—the spacer is patterned at the bottom of each individual chip. Instead of using the SU-8 film, multiple glass coverslips can be stacked on top of each other and glued on the sides of the chip if it is desired to increase the distance between the μOIL chip and the sample; (5) The microfluidic network is filled with microscope immersion oil (Cargillis labs #159, Cedar Grove, NJ, USA, refractive index 1.52 and (6) the ball mini-lenses are manually assembled on the top of the oil-filled microwell array and kept in place by surface tension. They are separated from the bottom surface of the microwell array by ~20 μm. Before use, the μOIL module is placed on a flat surface for 30 min to let oil evenly distribute into the microwell array. The assembled μOIL module is then ready for use: It can then be placed on top of any specimen to obtain high resolution images through a stereoscope. The μOIL module can be re-used indefinitely as long as it is kept in a dry environment (to minimize oil evaporation). It can also be cleaned and re-assembled if needed. For long term use, a thin parylene film can also be deposited to completely seal the μOIL module.

Figure 2. (**a**) Microfabrication process and (**b**) Critical dimensions of the µOIL chip. The focal length measured from the center of the ball mini-lens is ~620 µm. The dotted lines represent the microwell sidewalls that are not visible in the highlighted cross section.

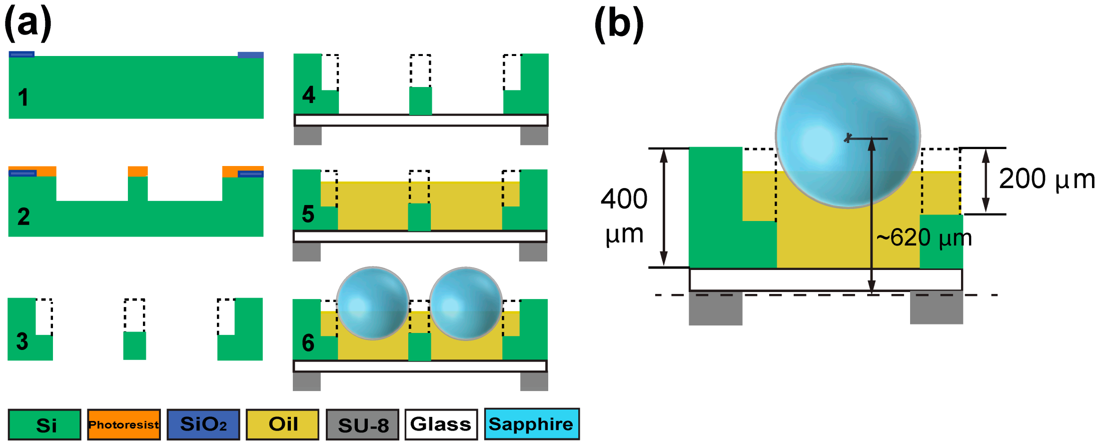

3. Results and Discussion

3.1. The µOIL Module

3.1.1. Material Considerations

The amount of light collected by a lens that also affects its resolution can be quantified by its numerical aperture (NA):

$$NA = n_M \cdot \sin\theta \tag{1}$$

where n_M is the refractive index of the medium that the lens is immersed into and θ is the half angle of the cone of rays collected by the lens. The maximum half angle θ and therefore the maximum NA can be obtained when the sample is located at the focal length of the lens. In order to increase the NA, one should increase the refractive index of the medium and/or increase the angle θ. The former task can be achieved by using media that have high refractive index (e.g., oil or water). The latter one can be achieved by combining the high refractive index media with a high refractive index lens.

Our µOIL chip has similar behavior, which can be described by Equation (1): The effect of the refractive index of the medium and the ball lens material are critical for achieving high NA. We choose to use microscopy oil as a medium in order to match the refractive index of the glass chip that seals the bottom of the microwell array. The use of oil reduces the total internal reflection of optical rays at the glass/oil interface, resulting in an increase in angle θ (the focal length also increases in this case but the effect compared to the increase in angle θ is less significant) (Figure 3a). Microscopy oil also does not fluoresce and does not evaporate as fast as other media. In addition, by using a high refractive index lens material (e.g., sapphire, refractive index n_L = 1.77), the focal length decreases and the optical cone widens (angle θ increases) (Figure 3b).

Figure 3. The effect of the refractive index of the immersion medium (**a**) and ball lens (**b**) on the ray collection angle θ₀ Values for angle θ₀ are theoretically estimated by thick-lens equations (see supplementary materials and Figure S1).

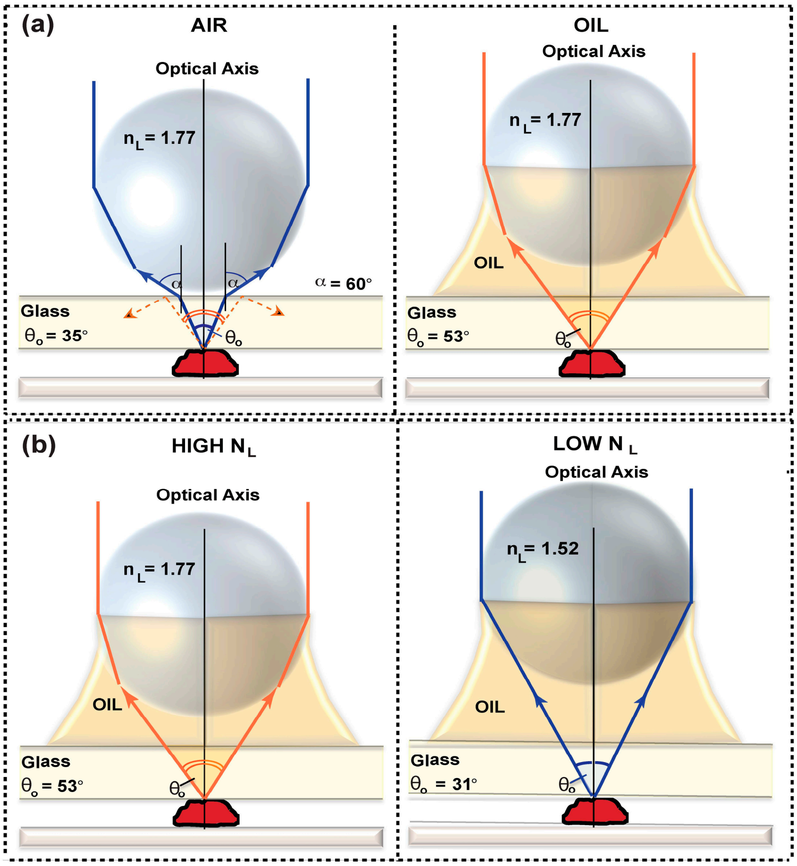

This specific combination of materials results in a high optical performance of the µOIL module (Table 1) which is excellent for high-resolution imaging (see supplementary materials for calculating the various optical properties of the µOIL module). We should emphasize that due to the modular assembly of the ball mini-lenses, the oil and the silicon/glass chip, the end user has the ability to custom-make his/her µOIL module.

Table 1. Properties of µOIL chip.

Parameter	Value
Ball mini-lens Diameter (*D*)	*D* = 1 mm
Ball mini-lens Refractive index (n_L)	n_L = 1.77 (sapphire)
Back Focal Length (BFL)	124 µm (see supplementary materials)
Numerical Aperture (NA)	1.2 (from Equation (2))
Lens power (φ)	1.6 mm^{-1} (from Equation (3))
Magnification	~130× (see Figure 5)
Resolution (center)	0.7 µm (see Figure 7)
Depth of Field (DOF)	0.38 µm (from λ/NA^2) [13,19]
Field of View (FOV)	60–140 µm/lens (see Figure 8)
F-number	0.62 (from EFL */*D*)

Notes: * EFL: the effective focal length (see supplementary materials); λ: the wavelength.

3.1.2. The Numerical Aperture (NA) of the μOIL Chip

In order to estimate the NA of the μOIL module, we modeled the ball lens as a thick lens [35] that is half immersed in medium and half immersed in air. We neglected any refraction of light that might take place between the focal plane and the medium. In this case, the NA can be expressed as a function of refractive index of the lens material (n_L), the refractive index of the medium (n_M), the lens power (φ) and the lens radius (see supplementary materials):

$$\mathrm{NA} = n_{\mathrm{M}}\left(\frac{\varphi R n_{\mathrm{L}}}{\varphi R n_{\mathrm{L}} + n_{\mathrm{M}} n_{\mathrm{L}} - 2(n_{\mathrm{L}} - 1) n_{\mathrm{M}}}\right) \tag{2}$$

$$\varphi = \frac{1}{R}\left(n_{\mathrm{M}} + 1 - \frac{2 n_{\mathrm{M}}}{n_{\mathrm{L}}}\right) \tag{3}$$

To better understand the dependence of NA on n_M and n_L, we plotted the NA *versus* n_L, when the ball mini-lens is immersed in four different media: air, water, oil and polydimethylsiloxane (Figure 4). Air, water and oil are widely used media in standard optical microscopy. To cover the low end of the n_M spectrum, we choose PDMS as an alternative low-cost solution. The n_L of the lens was varied from 1.4 to 2, as those values represent refractive indices of off-the-shelve ball lenses (e.g., N-BK7 ($n_L = 1.516$), Ruby ($n_L = 1.77$), S-LAH79 ($n_L = 2$), *etc.*). In all calculations, we did not take into account the aperture created by the silicon well (the silicon well is 30 μm smaller in diameter than the ball lens diameter) and we assumed that the top half of the ball-lens is exposed to air. We want to note that in reality, the size of the holder aperture (*i.e.*, silicon well) needs to be taken into account since light blocked by the smaller aperture will reduce the maximum cone angle of the rays thus effect NA value. For all practical purposes, we also assumed that the sample is located at the focal plane. The results quantitatively validate our expectations: the higher the n_M and n_L the higher the NA. For ball mini-lenses of small refractive index (n_L = 1.5–1.6), an increase of the refractive index of the immersion medium does not result a significant increase in the NA. The effect of refractive index of the immersion medium on the NA is significant (up to ~50%) when ball mini-lenses with high refractive indices are used (e.g., $n_L > 1.7$). The combination of microscope immersion oil ($n_M = 1.516$) and sapphire ball mini-lens ($n_L = 1.77$) results in a numerical aperture of NA = ~1.2 which is comparable to high-end oil or water immersion microscope objectives. For the result we report in this paper, the effective aperture is 320 μm in diameter allowing a light collection cone angle of 53° based on the geometry of Figure 3b.

Figure 4. Numerical Aperture (NA) of the μOIL chip *versus* refractive index of the ball mini-lens (n_L) for four different cases of immersion media as theoretically predicted by Equation (2).

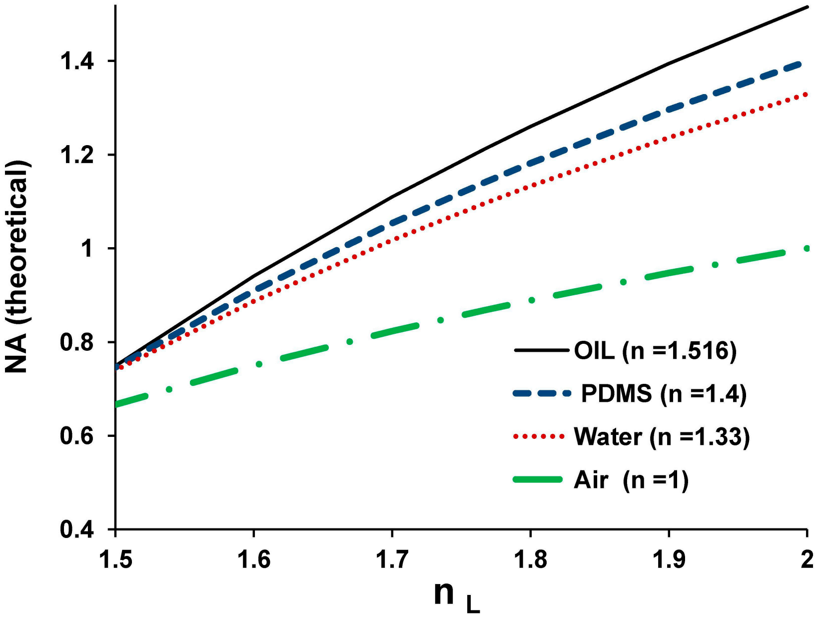

3.1.3. Magnification and NA *versus* Spacer Thickness

We performed optical simulations using Optics Software for Layout and Optimization (OSLO) software to obtain the magnification and numerical aperture as a function of the distance of the sample from the focal plane of the μOIL chip (the focal plane is located at the bottom glass surface of the μOIL chip). This distance coincides with the thickness of the spacer. For all practical purposes, we assumed a minimum spacer thickness of 5 μm (that is the thickness of the SU-8 film) and that the medium between the sample and the bottom glass surface of the μOIL chip is water. In this case, the numerical aperture and magnification are ~1× and ~130× respectively. As expected, when the spacer thickness increases, both the magnification and NA decrease. Spacer thickness has a major impact on the magnification, as the magnification decay has an exponential trend. At a spacer thickness of 900 μm the magnification and the NA is 1× and ~0.01 respectively (data not shown), beyond that point the sample is being demagnified. We want to emphasize that this is the magnification obtained from the μOIL chip alone. For the combined stereo microscope/μOIL chip system, the total magnification is calculated by multiplying the magnification of the μOIL chip and the magnification from the stereo microscope.

Figure 5. Dependence of the magnification and NA of the µOIL chip on spacer thickness.

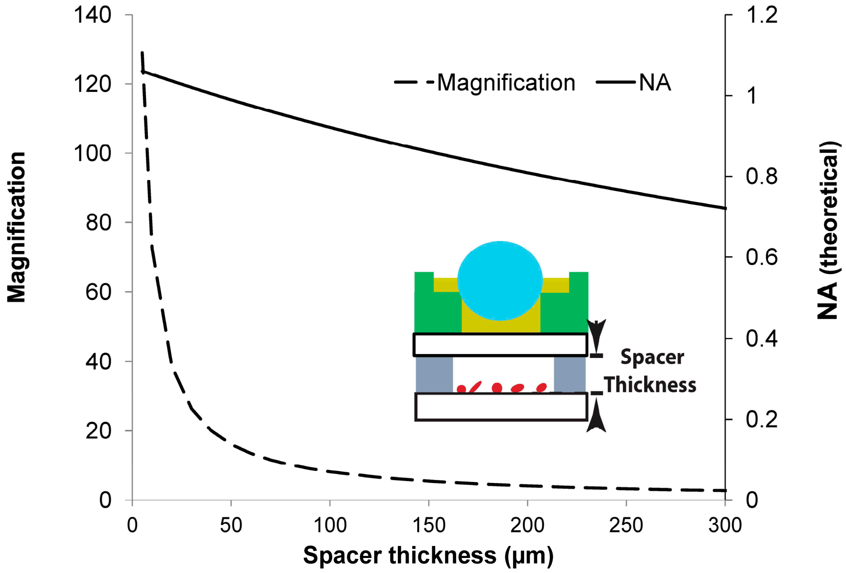

3.2. The Combined µOIL Chip/Stereo Microscope Assembly

We evaluated the optical performance of a standard stereo microscope (Olympus SZ61, Tokyo, Japan) when the µOIL chip is used as an add-on module. We placed the µOIL module on top of various samples (test charts, blood cells) and analyzed the obtained images. The stereo microscope we used had a magnification range from 0.67× to 4.5× and was equipped with a 3.3 megapixel CCD (MicroPublisher 3.3RTV, with 0.5× de-magnifying lens in from of the camera, British Columbia, Canada). In all tests described below, we set the magnification of the stereo microscope to its maximum value of 4.5× that corresponds to a maximum NA of ~0.07 and a maximum resolution of ~10 µm [36]. We used bright field illumination in transmission mode by adjusting the mirror at the base of the stereoscope at ~45°. The use of the µOIL chip as a module greatly enhances the resolution of the stand-alone stereo microscope (Figure 6). Using the stereo microscope alone, the finest pattern from a standard resolution plate (U.S. Air Force-USAF1951) is blurred and none of the lines can be resolved (Figure 6a). When the µOIL chip is placed on top of the resolution plate, the narrowest lines (0.775 µm in width) are resolved (Figure 6b). Although, there is noticeable aberration away from the center of field of view.

3.2.1. Resolution

To obtain the optical resolution of the combined system, we measured the image contrast of a resolution plate (USAF1951) that has equally spaced line patterns of decreasing width. The dependence of the image contrast on the line width represents the modulation transfer function of the combined system, which is a widely accepted method for obtaining the resolution of an optical system [37]. The acquired images were taken within 30 µm of the center of the field of view and analyzed using Metamorph software and the percentage of the image contrast averaged over all color channels *versus* the number of line pairs per millimeter was obtained (Figure 7). In addition, we tested the effect on the resolution of a thin (~125 nm) parylene film that was deposited on top of the µOIL chip. As discussed above, the parylene film can permanently seal the µOIL chip in order to prevent evaporation of the oil as well as to serve as an anti-reflective coating [38].

Figure 6. Images of a resolution plate (USAF1951) obtained from a stereo microscope alone (**a**) and from the combined µOIL chip/stereo microscope system (**b**). Scale bar: 10 µm in (**a**) and (**b**).

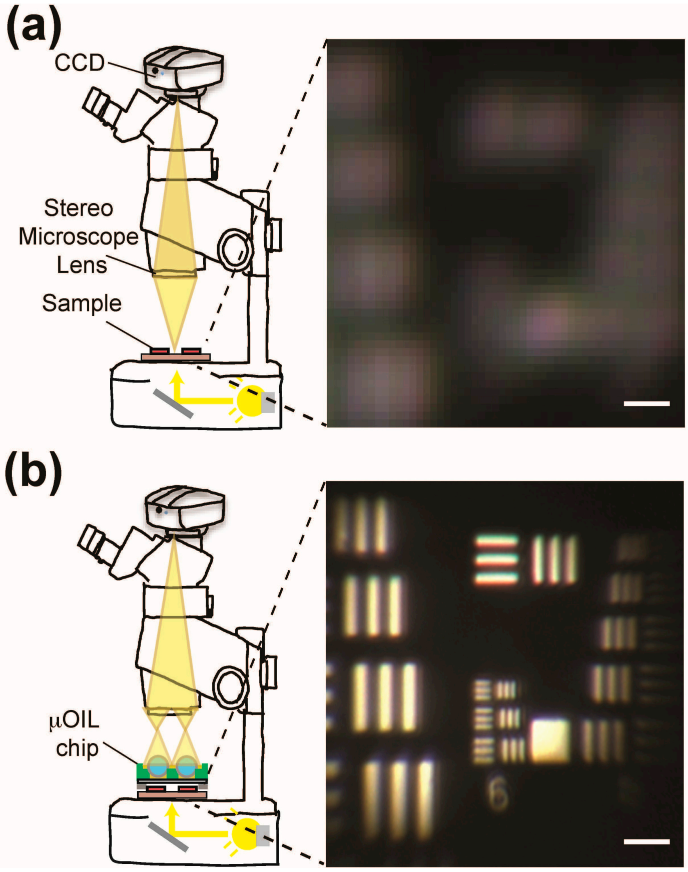

Figure 7. Image contrast (%) *versus* line pairs per mm for the combined system. The sample was a resolution plate that was imaged in air. The spacer thickness was 5 µm and NA (theoretical) is ~0.79.

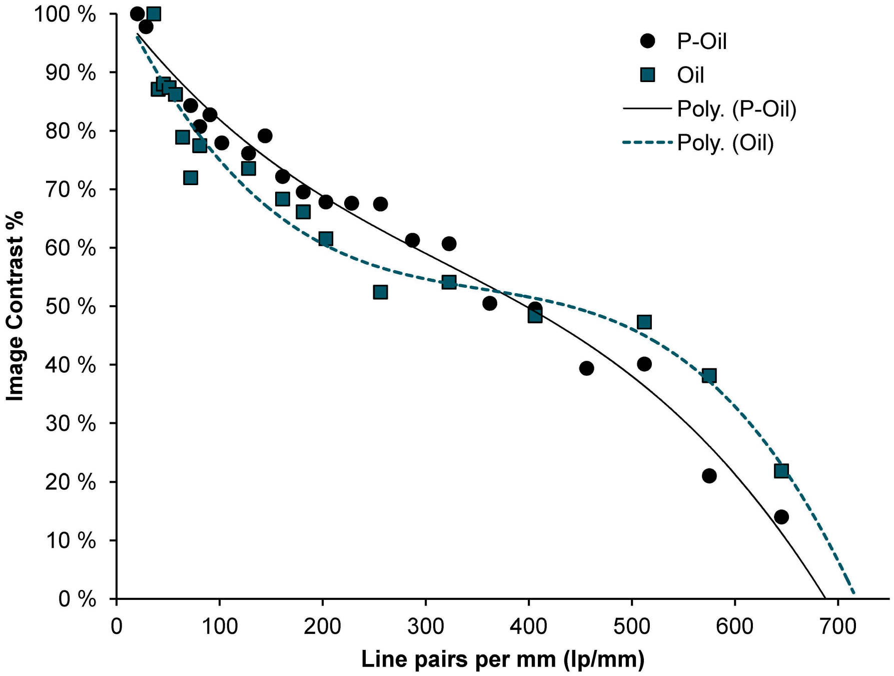

The experimental results indicate that the image contrast percentage decreases continuously as the number of line pairs per mm increases. All the lines from the resolution plate even the smallest lines with a width of 0.775 µm (corresponding to 645 line pairs/mm) can be imaged clearly using both the non-coated µOIL chip and the parylene-coated µOIL chip. However, at 400 line pairs/mm and above, the parylene-coated µOIL chip resulted in a slight degradation in the optical performance as compared to the non-coated µOIL chip. As the minimum feature size of the resolution plate is larger than the anticipated maximum resolution, we can only estimate the latter one by extrapolating the modulation transfer function until the image contract becomes zero. Using this approach, the theoretical resolution for the non-coated and the parylene-coated µOIL chip is 715 lp/mm (0.7 µm line width) and 690 lp/mm (0.73 µm line width) respectively. We should also emphasize that the obtained results are not limited by the camera resolution which was measured to be 0.15 µm/pixel at maximum magnification.

3.2.2. Field of View (FOV)

We experimentally obtained the change in the FOV of the combined system *versus* spacer thickness (Figure 8). The FOV was measured by imaging a commercially available grid distortion target (Thorlabs, catalog number R1L3S3P, Newton, NJ, USA,) that consists of 10 µm wide metal squares. For each spacer thickness, we obtained the one dimensional intensity profile across the grid pattern (see supplementary Figure S2). The medium between the sample and the bottom glass surface of the µOIL chip is water. The intensity was uniform at the center of the ball mini-lens where minimum image distortion is observed. The FOV was defined as the diameter of an area where the intensity is above 80% of the maximum intensity. Although such a criterion is subjective, we experimentally observed that the 80% cut-off threshold was a rather conservative value for most practical application (e.g., for cell counting). For high-resolution imaging, the spacer thickness needs to be minimized (e.g., 5 µm), which results in a minimum FOV in the range of ~60 µm/lens. Increasing the spacer thickness resulted in a linear increase in the FOV at the expense of resolution.

Figure 8. (**a**) Field of view (FOV) and NA *versus* spacer thickness. The theoretical NA values were calculated from thick-lens equation (see supplementary). (**b**) Image of 10 µm grid using a 5 µm spacer (**I**) and a 250 thick µm spacer (**II**). Scale bar: 20 µm in (**b**).

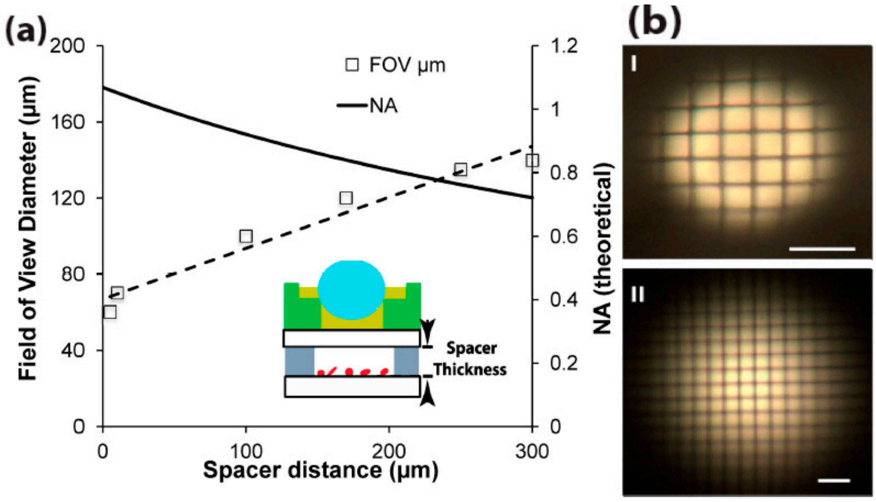

3.2.3. Biological Imaging

In order to demonstrate the practical usefulness of the µOIL module, we imaged various biological samples using the combined system. In particular, we imaged: a whole, undiluted blood smear obtained from a patient diagnosed with sickle-cell disease (Figure 9a,b). Cells were stained with Wright and Giemsa stain and imaged using transmission brightfield illumination (as illustrated in Figure 9). White, normal red and sickle red blood cells and platelets were clearly visible and distinguishable. If the µOIL module is removed, then the stereomicroscope alone cannot resolve single cells (Figure 9c,d).

Figure 9. Wright and Giemsa stained blood smear from a patient with sickle-cell disease: neutrophils (**a**) and sickle cells (**b**) are clearly visible. In (**c**, **d**), the same blood smear sample as imaged from the stereo microscope alone. Scale bars: 10 µm in **(a)**, **(b)**, **(d)**; 50 µm in **(c)**.

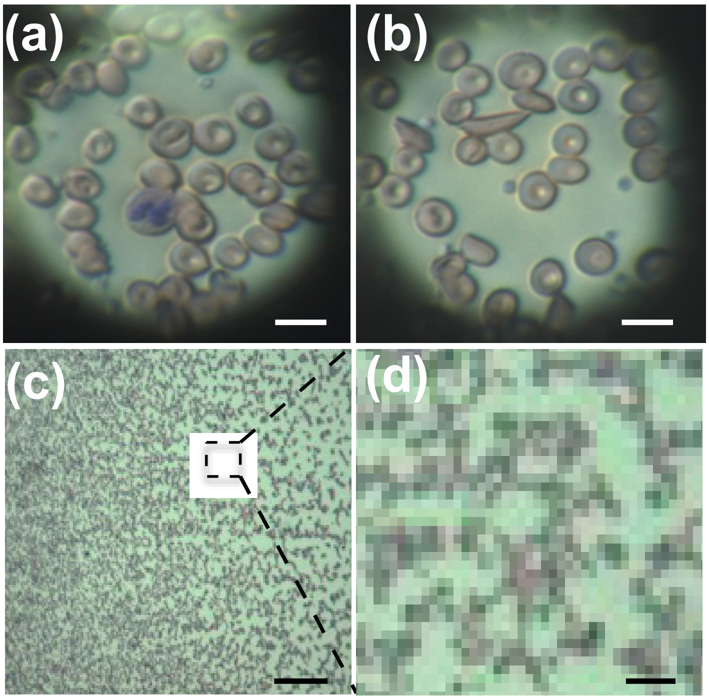

In all the above experiments, the magnification of the stereo microscope was 4.5×. In this magnification, the combined system with the 1 inch CCD detector can simultaneously obtain images from 4 to 6 mini-lenses. To increase the FOV and image the entire µOIL chip (all 16 mini-lenses), one has to decrease the magnification of the stereo microscope to ~2×. Even in this case the FOV is ~60 µm/lens the shape of single cells from a smear test (Figure 10) is still visible. In order to obtain a sharp image from all mini-lenses in the array, minor focus adjustments using the stereomicroscope focus knob (within the array, it is possible to have variation up to 50 µm) might be required as imperfections in the microfabrication and mini-lens assembly process result in a lens-to-lens variation in the focal length within the array. Our future work will incorporate a better design of the µOIL chip, better control of the fabrication process and tighter quality control assembly to improve the focal plan uniformity of the array.

Figure 10. Left image: Imaging a blood smear using the entire μOIL chip (from all 16 ball mini-lens). The magnification of the stereo microscope was set to 2×. **Right image** is the magnified version of the image from the lens in the square box shown in the left image. Scale bar: 20 μm.

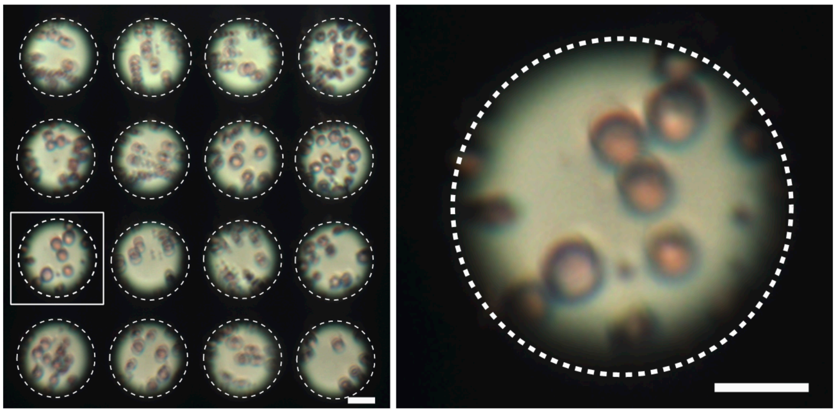

4. Conclusions

We have developed a simple-to-use, reusable and compact, microfabricated imaging module for high resolution, large field of view imaging applications. The key element of the design is the integration of a microfluidic chip with an array of 16 liquid-immersed, high refractive index ball mini-lenses. The integrated chip—termed the μOIL—chip mimics the working principle of the front end of expensive, oil-immersion microscope objectives. The μOIL chip alone has a maximum numerical aperture of 1.2 and a magnification of 130×. It is attached directly to the sample of interest and then imaged under a standard micro stereoscope by simply adjusting the focus and/or the magnification of the stereo microscope.

We demonstrated that, when it is used as an add-on module to a stereo microscope, it can resolve submicron micron features (maximum resolution of 0.7 μm) from a variety of biological samples. We believe that the μOIL chip can bring high resolution, large field of view imaging capabilities to research and medical laboratories and clinics where a stereo microscope is the only available imaging tool.

Supplementary Materials

Supplementary materials can be accessed at: http://www.mdpi.com/2072-666X/5/3/607/s1.

Acknowledgments

This research made possible in part with support by the National Institutes of Health (NIH) Microfluidics in Biomedical Sciences Training Program (T32 EB005582-05) and the NIH Director's New Innovator Award (DP2OD006458). The authors would like to thank Onnop Srivannavit, Maria Daphne Bazopoulou, Amrita Ray Chaudhury, Alexandros Pantazis and Eleni Gourgou for useful discussions. We also want to thank Usha Kota and Christine Falkiewicz at the hematology lab, University of Michigan hospital for disease diagnostic training and providing sickle cell blood smear sample. All the devices were fabricated at the Lurie Nanofabrication Facility at the University of Michigan.

Author Contributions

Mayurachat Ning Gulari performed the design, microfabrication, testing of the μOIL chip, analyzed the data and wrote the manuscript. Anurag Tripathi and Mostafa Ghannad-Rezaie contributed on the design and microfabrication of the μOIL chip. Nikos Chronis had oversight over the experiments and manuscript writing.

Conflicts of Interest

The authors declare no conflict of interest.

References

1. Bradbury, S.; Bracegirdle, D.B. *Introduction to Light Microscopy*; BIOS Scientific Publishers Limited: Milton Park, UK, 1998; p. 123.
2. Spellman, F.R. The Microscope. In *Microbiology for Water and Wastewater Operators (Revised Reprint)*; CRC Press: Boca Raton, FL, USA, 1999; pp. 11–17.
3. Peyman, G.A.; Koziol, J.E.; Fried, W.I.; Sanders, D.R. Operating Microscope with Two Pairs of Stereo Eye-Piece Lenses. U.S. Patent 4,138,191, 6 February 1979.
4. Muller, O.; Biber, K.; Jakubowski, H.; Hanemann, G. Operation Microscope. U.S. Patent 4,448,498, 15 May 1984.
5. Fukaya, T.; Hamada, M.; Nakamura, S.; Hanzawa, T.; Kinukawa, M.; Ishikawa, T.; Fujiwara, H.; Tokunaga, S. Stereomicroscope. U.S. Patent 5,552,929, 3 September 1996.
6. Woolnough, L. Starting with Stereomicroscopes—Quekett Microscopical Club. Available online: http://www.quekett.org/starting/stereo-microscopes/stereo-microscopes (accessed on 8 May 2014).
7. Krupenkin, T.; Yang, S.; Mach, P. Tunable liquid microlens. *Appl. Phys. Lett.* **2003**, *82*, 316–318.
8. Cadarso, V.J.; Llobera, A.; Villanueva, G.; Dominguez, C.; Plaza, J.A. 3-D modulable PDMS-based microlens system. *Opt. Express* **2008**, *16*, 4918–4929.
9. Dong, L.; Agarwal, A.K.; Beebe, D.J.; Jiang, H. Adaptive liquid microlenses activated by stimuli-responsive hydrogels. *Nature* **2006**, *442*, 551–554.
10. Chen, J.; Wang, W.; Fang, J.; Varahramyan, K. Variable-focusing microlens with microfluidic chip. *J. Micromech. Microeng.* **2004**, *14*, 675–680.
11. Chronis, N.; Liu, G.; Jeong, K.H.; Lee, L. Tunable liquid-filled microlens array integrated with microfluidic network. *Opt. Express* **2003**, *11*, 2370–2378.
12. He, M.; Yuan, X.C.; Ngo, N.; Bu, J.; Tao, S. Low-cost and efficient coupling technique using reflowed sol-gel microlens. *Opt. Express* **2003**, *11*, 1621–1627.
13. Nussbaum, P.; Volkrl, R.; Herzig, H.P.; Eisner, M.; Haselbeck, S. Design, fabrication and testing of microlens arrays for sensors and microsystems. *Pure Appl. Opt.* **1996**, *6*, 617–636.
14. Aristizabal, S.L.; Cirino, G.A.; Montagnoli, A.N.; Sobrinho, A.A.; Rubert, J.B.; Hospital, M.; Mansano, R.D. Microlens array fabricated by a low-cost grayscale lithography maskless system. *Opt. Eng.* **2013**, *52*, doi:10.1117/1.OE.52.12.125101.

15. Kozma, P.; Lehmann, A.; Wunderlich, K.; Michel, D.; Schumacher, S.; Ehrentreich-Förster, E.; Bier, F.F. A novel handheld fluorescent microarray reader for point-of-care diagnostic. *Biosens. Bioelectron.* **2013***, 47*, 415–420.
16. Orth, A.; Crozier, K. Microscopy with microlens arrays: High throughput, high resolution and light-field imaging. *Opt. Express* **2012**, *20*, 13522–13531.
17. Kim, J.Y.; Pfeiffer, K.; Voigt, A.; Gruetzner, G.; Brugger, J. Directly fabricated multi-scale microlens arrays on a hydrophobic flat surface by a simple ink-jet printing technique. *J. Mater. Chem.* **2012**, *22*, 3053–3058.
18. Tripathi, A.; Chronis, N. A doublet microlens array for imaging micron-sized objects. *J. Micromech. Microeng.* **2011**, *21*, doi:10.1088/0960-1317/21/10/105024.
19. Volkel, R.; Herzig, H.P.; Nussbaum, P.; Dandliker, R.; Hugle, W.B. Microlens array imaging system for photolithography. *Opt. Eng.* **1996**, *35*, 3323–3330.
20. Aldalali, B.; Kanhere, A.; Fernandes, J.; Huang, C.C.; Jiang, H. Fabrication of polydimethylsiloxane microlenses utilizing hydrogel shrinkage and a single molding step. *Micromachines* **2014**, *5*, 275–288.
21. Gulari, M.N.; Tripathi, A.; Chronis, N. Microfluidic-based oil-immersion lenses for high resolution microscopy. In Proceedings of the 16th International Conference on Miniaturized Systems for Chemistry and Life Sciences (μTAS'12), Okinawa, Japan, 28 October–1 November 2012; pp. 49–51.
22. Brückner, A.; Duparre, J.; Wippermann, F.; Leitel, R.; Dannberg, P.; Brauer, A. Ultra-compact close-up microoptical imaging system. *Proc. SPIE* **2010**, *7786*, doi:10.1117/12.860025.
23. Knieling, T.; Shaf, M.; Lang, W.; Benecke, W. Microlens array production in a microtechnological dry etch and reflow process for display applications. *J. Eur. Opt. Soc. Rap. Publ.* **2012**, *7*, doi:10.2971/jeos.2012.12007.
24. Tripathi, A.; Chokshi, T.V.; Chronis, N. A high numerical aperture, polymer-based, planar microlens array. *Appl. Opt.* **2009**, *17*, 19908–19918.
25. Pang, S.; Han, C.; Erath, J.; Rodriguez, A.; Yang, C. Wide field-of-view Talbot grid-based microscopy for multicolor fluorescence imaging. *Opt. Express* **2013**, *21*, 14555–14565.
26. Schonbrun, E.; Gorthi, S.S.; Schaak, D. Microfabricated multiple field of view imaging flow cytometry. *Lab Chip* **2012**, *12*, 268–273.
27. Cui, X.; Lee, L.; Heng, M.X.; Zhong, W.; Sternberg, P.W.; Psaltis, D.; Yang, C. Lensless high-resolution on-chip optofluidic microscopes for Caenorhabditis elegans and cell imaging. *Proc. Natl. Acad. Sci. USA* **2008**, *105*, 10670–10675.
28. Wu, J.; Zheng, G.; Lee, L.M. Optical imaging techniques in microfluidics and their applications. *Lab Chip* **2012**, *12*, 3566–3575.
29. Itatani, J.; Levesque, J.; Zeidler, D.; Niikura, H.; Pépin, H.; Kieffer, J.C.; Corkum, P.B.; Villeneuve, D.M. Tomographic imaging of molecular orbitals. *Nature* **2004**, *432*, 867–871.
30. Chen, Z.; Milner, T.E.; Dave, D.; Nelson, J.S. Optical Doppler tomographic imaging of fluid flow velocity in highly scattering media. *Opt. Lett.* **1997**, *22*, 64–66.
31. Foldscope: Microscopy for everyone. Available online: http://www.foldscope.com/ (accessed on 3 June 2014).

32. Bogoch, I.I.; Andrews, J.R.; Speich, B.; Utzinger, J.; Ame, S.M.; Ali, S.M.; Keiser, J. Mobile phone microscopy for the diagnosis of soil-transmitted helminth infections: A proof-of-concept study. *Am. J. Trop. Med. Hyg.* **2013**, *88*, 626–629.
33. Arpa, A.; Wetzstein, G.; Lanman, D.; Raskar, R. Single lens off-chip cellphone microscopy. In Proceedings of Computer Vision and Pattern Recognition Workshops (CVPRW), 2012 IEEE Computer Society Conference on, Providence, RI, USA, 16–21 June 2012; pp. 23–28.
34. Smith, Z.J.; Chu, K.; Espenson, A.R.; Rahimzadeh, M.; Gryshuk, A.; Molinaro, M.; Dwyre, D.M.; Lane, S.; Matthews, D.; Wachsmann-Hogiu, S. Cell-phone-based platform for biomedical device development and education applications. *PLoS One* **2011**, *6*, doi:10.1371/journal.pone.0017150.
35. Frank, S.J.; Pedrotti, L.; Pedrotti, L.M.; Pedrotti, L.S. *Introduction to Optics*; Pearson Education: Upper Saddle River, NJ, USA, 2008.
36. Solinski, W. Olympus, Tokyo, Japan. Personal communication, 2012.
37. Basic Concepts and Formulas in Microscopy: Resolution. Available online: http://www.microscopyu.com/articles/formulas/formulasresolution.html (accessed on 22 May 2014).
38. Hubers, H.W.; Schubert, J.; Krabbe, A.; Birk, M.; Wagner, G.; Semenov, A.; Goltsman, G.; Voronov, B.; Gershenzon, E. Parylene anti-reflection coating of a quasi-optical hot-electron-bolometric mixer at terahertz frequencies. *Infrared Phys. Technol.* **2001**, *42*, 41–47.

Fabrication of Polydimethylsiloxane Microlenses Utilizing Hydrogel Shrinkage and a Single Molding Step

Bader Aldalali, Aditi Kanhere, Jayer Fernandes, Chi-Chieh Huang and Hongrui Jiang

Abstract: We report on polydimethlysiloxane (PDMS) microlenses and microlens arrays on flat and curved substrates fabricated via a relatively simple process combining liquid-phase photopolymerization and a single molding step. The mold for the formation of the PDMS lenses is fabricated by photopolymerizing a polyacrylamide (PAAm) pre-hydrogel. The shrinkage of PAAm after its polymerization forms concave lenses. The lenses are then transferred to PDMS by a single step molding to form PDMS microlens array on a flat substrate. The PAAm concave lenses are also transferred to PDMS and another flexible polymer, Solaris, to realize artificial compound eyes. The resultant microlenses and microlens arrays possess good uniformity and optical properties. The focal length of the lenses is inversely proportional to the shrinkage time. The microlens mold can also be rehydrated to change the focal length of the ultimate PDMS microlenses. The spherical aberration is 2.85 μm and the surface roughness is on the order of 204 nm. The microlenses can resolve 10.10 line pairs per mm (lp/mm) and have an f-number range between f/2.9 and f/56.5. For the compound eye, the field of view is 113°.

Reprinted from *Micromachines*. Cite as: Aldalali, B.; Kanhere, A.; Fernandes, J.; Huang, C.-C.; Jiang, H. Fabrication of Polydimethylsiloxane Microlenses Utilizing Hydrogel Shrinkage and a Single Molding Step. *Micromachines* **2014**, *5*, 275–288.

1. Introduction

The utilization of microlenses has increased dramatically in many different applications including optical communications, imaging, and printing [1]. Due to this demand, different techniques to fabricate microlenses have emerged, including ink-jet printing [2], greyscale lithography [3], and photoresist thermal reflow [1]. The ink-jet printing method uses expensive equipment that requires very precise alignment in order to produce uniform arrays, while greyscale lithography faces difficulty in fitting the desired microlens shape into the different shades of grey [4,5]. In the case of the photoresist reflow method, the lenses are usually used as a mold since they have a high optical absorption under white light and need to be transferred to more optically transparent and stable substrates in a double transfer process [5–7]. There are other approaches that could generate the microlens mold; however, these approaches rely on accurate pressure or temperature control to achieve uniformity among the microlenses [8–10]. These approaches also rely on double transfer for ultimate formation of the microlenses which further elongates and complicates the fabrication process. It is thus highly desirable to develop low-cost, versatile, and simple microlens fabrication methods.

Another appealing feature of microlens arrays that gained popularity recently is their ability to be fabricated onto curved surfaces to increase their field of view (FOV), mimicking the compound eyes of insects [11–15]. Most of the existing fabrication methods rely on ultrafast lasers to fabricate the microlenses, which is very expensive [11,16]. Other methods rely on stress-alleviating bridges between the microlenses, which decreases the fill factor and requires a hard spherical shell under the microlenses to provide the desired curvature [13]. Another available low-cost fabrication method relies on the deformation of the microlens substrate by applying force to provide curvature, which is a very sensitive process and might damage the microlenses [15].

To provide a low-cost, simple fabrication process for microlenses on both planar and curved surfaces, we utilize the capabilities of advanced materials such as hydrogels [17,18]. Due to the high water content, hydrogels could shrink in air as they dry out [17]. We could take advantage of this natural shrinkage property of hydrogels in air to produce smooth concave microlenses and then transfer the microlenses to other more optically transparent and flexible substrates to form convex microlenses using a single molding step.

2. Fabrication

The fabrication process is divided into two segments. The first segment describes the process of fabricating the microlenses by liquid phase photopolymerization and hydrogel shrinkage. The second segment describes the added steps needed to fabricate the artificial compound eye structure using the hydrogel based microlenses.

2.1. Equipment and Materials

All photopolymerization processes were done using a desktop EXFO Acticure 4000 ultra-violet (UV) light source (EXFO Photonic Solutions, Inc, Missisauge, ON, Canada). Photomasks were printed using high-resolution films (3000 dpi, Imagesetter, Inc., Madison, WI, USA).

Two polymers were used to fabricate the microlens mold. A photopolymerizable prepolymer, isobornyl acrylate (IBA), made as per the recipe found in [19] was used as the structure that defines the microlens apertures. The other polymer is a photopolymerizable polyacrylamide (PAAm) based pre-hydrogel. The PAAm pre-hydrogel solution included a monomer, crosslinker, photoinitiator, and water as a solvent and was made as per the recipe in [20]. The PAAm was used as the mold for the microlenses. PDMS (Sylgard 184, Dow Corning Corporation, Midland, MI, USA) was used as the microlens material.

For the compound eye structure, in addition to PDMS, another polymer called Solaris (Smooth-on, Easton, PA, USA) was used as an alternative for the substrate of the compound eye. Solaris is a transparent silicone polymer which is widely used as a protective layer on top of solar cells [21].

2.2. Microlens Array Fabrication

Figure 1 shows fabricated PDMS microlenses with 0.7-mm diameter (called hereafter 0.7-mm microlenses). The fabrication process is shown in Figure 2. A polycarbonate cartridge well (40-mm × 22-mm × 0.36-mm, HybriWells, Grace Bio-Labs Inc., Bend, OR, USA) was utilized to define the apertures of the microlenses. The cartridge well consisted of two top and bottom plates connected by a 360-µm-thick adhesive spacer which defined the depth of the well. The bottom surface was first peeled off and the remaining surface with the spacer was placed onto a plastic slide. IBA was flowed into the well using a transfer pipette. The prepolymer IBA was then exposed to ultraviolet (UV) light at 10 mW/cm^2 for 25s with a mask defining the microlens apertures. Photopolymerizable IBA acts as a negative photoresist when exposed to UV light. After exposure, the top plate was peeled off and unpolymerized IBA was rinsed away with ethanol.

Figure 1. (**a**) Optical image of a 0.7-mm microlens array. (**b**) Scanning electron microscopy image of 0.7-mm microlens.

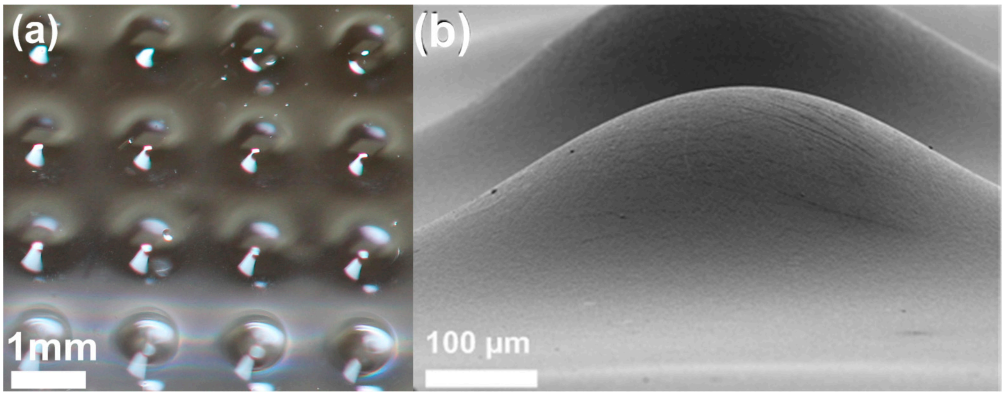

At this point, the structure included a polymerized IBA (poly-IBA) surface with an array of apertures on top of a plastic slide as in Figure 2b. The surface of the poly-IBA was then treated with oxygen plasma by a reactive ion etching RIE system (Unaxis 790, Unaxis Wafer Processing, Schwyz, Switzerland) using the following parameters: power supply = 100 W, treatment time between 30 s and 3 min. Oxygen plasma only rendered the top surface and sidewalls of the poly-IBA hydrophilic since the bottom surface was attached to the plastic slide and hence protected from the plasma. A hydrophobic-hydrophilic boundary was created between the bottom surface of the poly-IBA and the remaining structure, which was utilized to form the microlenses. A double-sided adhesive (250–300 µm thick) was added to a glass slide to define a chamber. The plastic slide along with the poly-IBA, was then flipped onto the glass slide. The plastic slide was peeled off as can be seen in Figure 2c.

At this step, the structure consisted of an array of poly-IBA apertures on top of a 280-µm-high chamber. Epoxy was then applied around the boundary of the structure to prevent any leakage. Using a syringe, a photopolymerizable polyacrylamide (PAAm) based pre-hydrogel was then flowed through one of the holes and was allowed to fill the chamber as well as the top surface of the poly-IBA as in Figure 2d. The PAAm pre-hydrogel was then flood exposed under UV light at 25 mW/cm^2 for 90 s. The PAAm hydrogel was then allowed to dry in air for 24 h.

After exposure, the PAAm hydrogel shrunk in air due to the high water content. In this solution, PAAm contained 85% water. In similar solutions, with 80% water, PAAm shrunk to 36% of its initial volume [17]. The hydrogel shrunk until it reached the top surface of the poly-IBA apertures where it was pinned at the boundary of the hydrophobic top surface and the hydrophilic sidewall. This resulted in a concave lens as shown in Figure 2e. Figure 3 shows the PAAm before and after shrinking. The PAAm substrate was placed on top of an array of the letter "W" and images were taken using the stereoscope. In Figure 3a, the PAAm fully covers the aperture array and hence no lenses have formed. In Figure 3b, the PAAm has started to shrink and has formed a concave lens at the boundary of the apertures. An erect minified image "W" can be seen below the aperture array.

Figure 2. Fabrication process of the polydimethlysiloxane (PDMS) microlenses by hydrogel shrinkage. (**a**) Isobornyl acrylate (IBA) prepolymer was flowed into the cartridge and exposed under ultraviolet light. The IBA was flowed using a pipette until it filled the chamber. The IBA was exposed at 10-mW/cm^2 for 25 s. (**b**) Top plastic plate is peeled off exposing the patterned aperture array and uncured IBA was washed away using ethanol. The top surface and sidewalls of the aperture array were treated with oxygen plasma. (**c**) Treated structure was flipped onto a glass slide with a 250–300 µm spacer. (**d**) Photopolymerizable polyacrylamide (PAAm) based pre-hydrogel is flowed into the chamber and allowed to fill the whole aperture array including the top surface. (**e**) The PAAm is allowed to dry in air for 24 h. The PAAm will shrink through the apertures and be pinned at the hydrophobic-hydrophilic boundary. (**f**) The microlens mold is then treated with octadecyltrichlorosilane to decrease the adhesion of PDMS to the mold. (**g**) Uncured PDMS is then flowed on top of the mold and allowed to cure. (**h**) Cured PDMS is then peeled off. (**i**) The final PDMS microlens array.

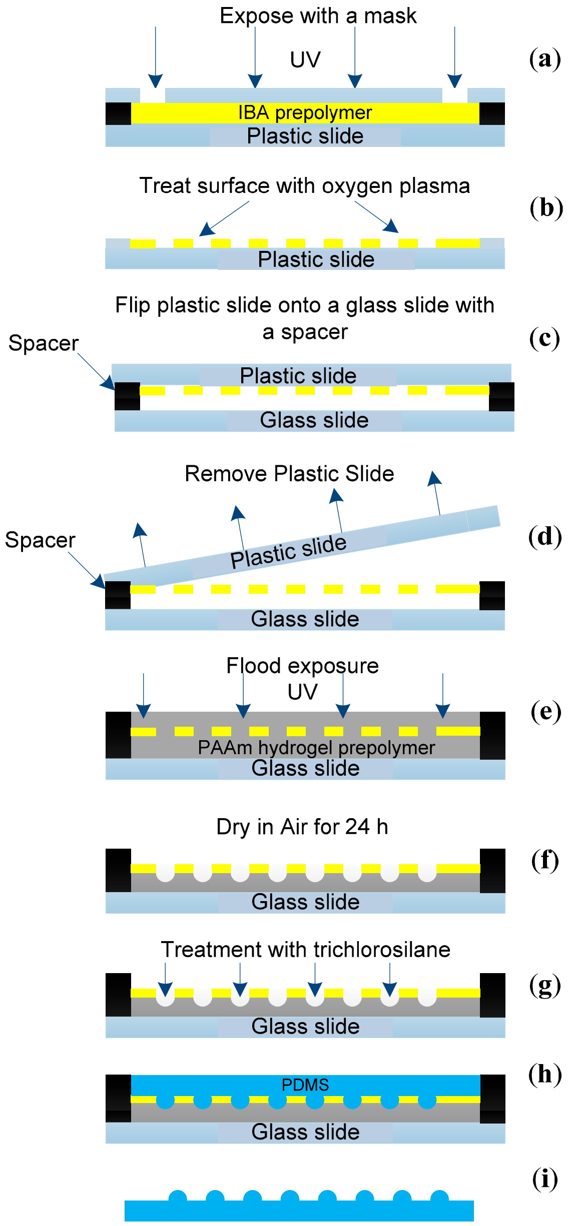

A key parameter during the fabrication process is the initial amount of PAAm pre-hydrogel. If too little PAAm is flowed, the hydrogel will shrink into the chamber, and if too much is flowed, the hydrogel will not reach the top poly-IBA aperture surface. PAAm should also be flowed uniformly on top of the aperture array to ensure uniform shrinking and eventually more uniform microlens arrays. However, since the top surface of the poly-IBA has been treated to make it hydrophobic, the PAAm that flows on top of the aperture array would tend to combine together and form a bubble-like profile. To overcome that, the PAAm pre-hydrogel was overflowed until it formed a relatively flat layer on top of the aperture array.

After 24 h, the PAAm surface was then treated with octadecyltrichlorosilane (OTS) in a vacuum for an hour rendering it even more hydrophobic [22]. After the OTS treatment, PDMS prepolymer mixed with the curing agent at a weight ratio of 10:1 was also placed in vacuum for an hour and then poured over the PAAm surface. The PDMS was then cured at 70 °C overnight and then peeled off.

Figure 3. Images of the PAAm hydrogel on top of the poly-IBA. (**a**) Shows the PAAm right after exposure and before shrinking. (**b**) Shows clear images of "W" under the poly-IBA apertures. The images are erect, minified and are visible between the object plane and the aperture array, hence concave lenses.

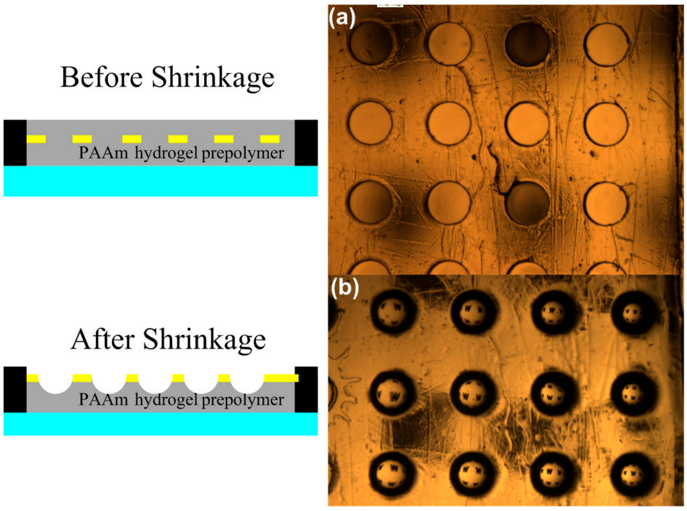

2.3. PDMS Compound Eye Fabrication

Figure 4 shows the added steps required to fabricate the compound eye structure. The fabrication process was inspired by the hemispherical camera work in [14]. PDMS was flowed on top of a plastic hemispherical shell with a 1.1-cm diameter. After curing, the PDMS was peeled off and placed on top of a cork with a diameter of 1.5-cm as in Figure 4b.The PDMS was then stretched from four opposite directions to realize a flat PDMS surface on top of the cork. On the other end, uncured PDMS was placed on top of a hydrogel microlens mold that has been allowed to shrink for at least 24 h. This minimum time requirement allows the PDMS to be easily peeled off later on in the fabrication process. The flattened PDMS and cork structure was then flipped onto the uncured PDMS and allowed to contact. It was very important to maintain a very thin layer of PDMS on top of the mold since a thick layer of PDMS will deform the hemispherical structure. The whole cork and mold structure was then placed in the oven at 75 °C to cure overnight. After the PDMS was cured, the whole structure was carefully peeled away from the hydrogel mold and the adhesive tape was then removed to allow the PDMS to retain its original shape.

2.4. Solaris Compound Eye Fabrication

We later substituted PDMS with Solaris to achieve a higher FOV. Solaris can be elongated to a length of 290% before breakage, which allows for utilizing most of the hemisphere [21]. In the same manner as PDMS, Solaris was cured by mixing the Solaris pre-polymer with the curing agent in a weight ratio of 1:1. Using a pipette, small volumes of uncured Solaris were dropped onto the hemispherical shell. Solaris was then cured on a hotplate at 80 °C for 10 min.

The trade-off with using Solaris is that the substrate became much softer compared to PDMS. This means that any excessive weight on the substrate will cause it to deform and not retain its spherical shape when it is finally released. In order to strengthen the Solaris structure, after curing the Solaris and removing it from the hotplate, another layer of uncured Solaris was placed on the first layer and cured again on the hotplate for 10 min. After the two-layered Solaris hemispherical substrate was cured, the rest of the fabrication process of Figure 4b–d was followed to produce the compound eye structure. The only other variation to the fabrication process of Figure 4 was that a larger cork was used (diameter = 1.8 cm).

Figure 4. Fabrication process of compound eye. (**a**) Uncured PDMS is flowed on top of plastic hemispherical shell and allowed to cure. (**b**) PDMS hemisphere is placed on top of the cork and stretched until it matches the diameter of the cork. (**c**) Uncured PDMS is placed on top of the hydrogel mold fabricated in Figure 2. Stretched PDMS on top of the cork is then flipped on top of the hydrogel mold. (**d**) Cured PDMS is peeled off from hydrogel mold. The cork is removed which released the stretched PDMS into its original hemispherical shape.

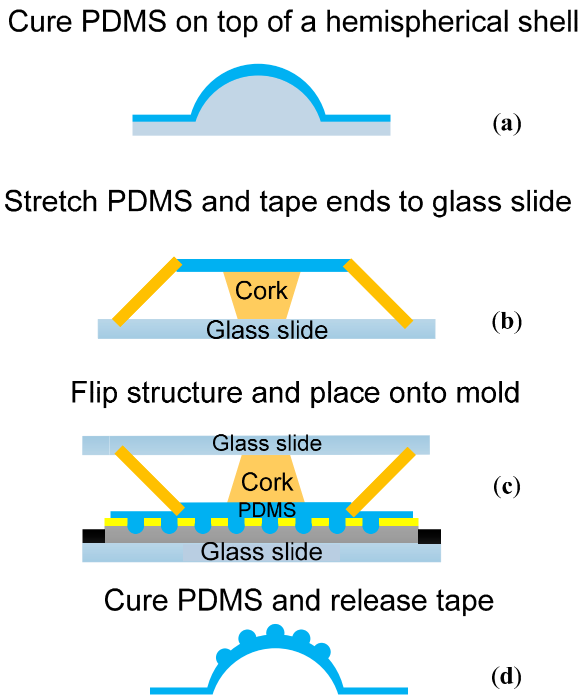

3. Results and Discussion

3.1. Microlens Analysis

Figure 5 shows the three dimensional profile of the 0.7-mm microlens using the white light interferometer (Zygo New View 6300).The microlenses were sputtered with a thin layer of reflective metal (gold or aluminum) prior to being placed under the interferometer to make the surface more reflective. The metal only alters the surface roughness of the microlenses and not the profile [8].As can be seen from Figure 5, the profile is of a 0.7-mm microlens with a height of approximately 31 µmother profile shows good uniformity of curvature across the entire microlens surface.

Figure 5. Three-dimensional profile of the 0.7-mm PDMS microlenses. The profile is taken using a ZYGO white light interferometer. The curvature is uniform across the surface of the microlens.

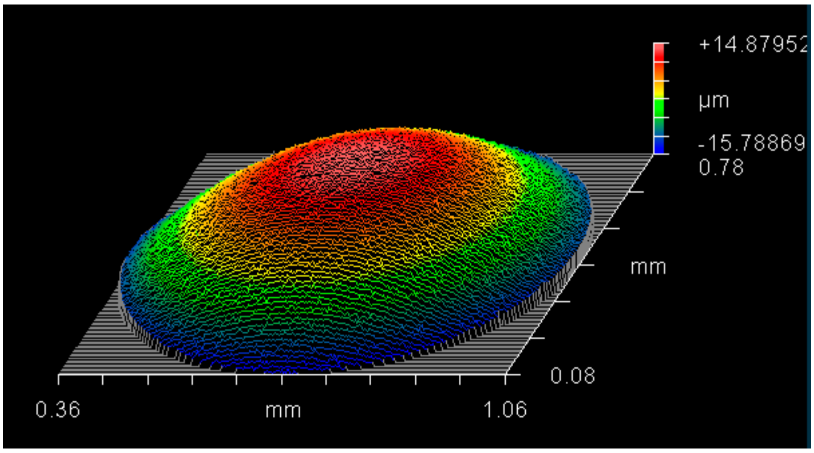

3.2. Image Analysis

The fabrication process can also be used to produce uniform microlens arrays. Figure 6 shows an image of an array of inverted “W”s using a stereoscope and imaged through a 2 × 4 0.7-mm microlens array. As can be seen from Figure 6, the image of the “W”s is clear and sharp for all eight microlenses. The largest percent difference of focal length between four neighboring microlenses is 2.59%. Figure 7 shows images acquired by the PDMS microlenses. In Figure 7a, a 0.7-mm microlens was used to image an inverted “UW”. In Figure7b, the United States Air Force (USAF) 1951 resolution test chart was used to determine the resolution of a 0.7-mm microlens. Table 1 shows the resulting optical properties of the microlenses in different sizes. The microlenses can be fabricated with f-numbers varying from f/2.9 to f/56.5.

Figure 6. Image of an array of inverted "W"s imaged through a 2 × 4 microlens array. The eight inverted images are clear and sharp which shows good uniformity among the neighboring microlenses.

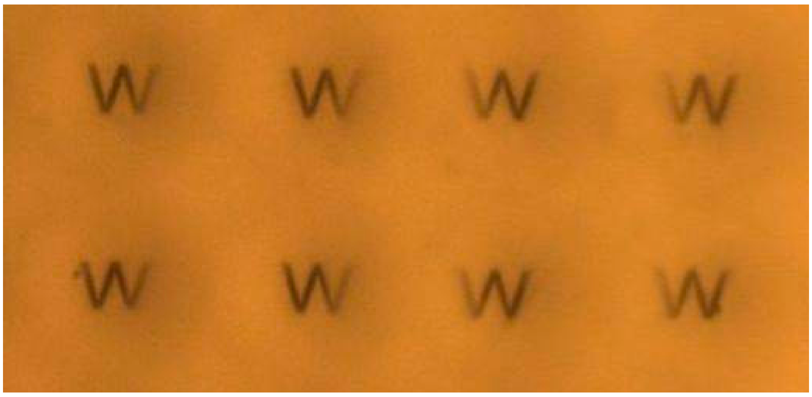

Figure 7. Images under the 0.7-mm PDMS microlenses. (**a**) Shows an image of an inverted "UW" under a 0.7-mm microlens. (**b**) Shows an image of the USAF1951 resolution test chart under a 0.7-mm microlens. The microlens can resolve lines in group 3, element 2.

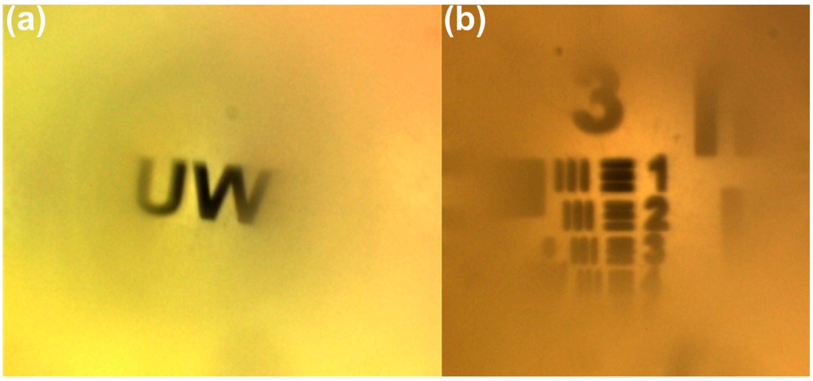

Table 1. Optical properties of PDMS microlenses with different sized apertures.

Parameter	**0.7-mm**	**1-mm**
Focal length (mm)	5.417	2.94
Spherical aberration (μm)	2.85	31.276
Resolution (lp/mm)	8.98	7.13
Roughness (nm)	204	320

Table 2. Optical properties of PDMS microlenses with different shrinkage times.

Parameter	**Shrinkage (h)**			
	9	**12**	**18**	**24**
Focal length (mm)	39.57	16.2	11.55	5.63
Spherical aberration (μm)	0.634	2.147	3.59	9.66
Roughness (nm)	110	204	255	187

3.3. Shrinkage

The relationship between hydrogel shrinkage and resultant optical properties has also been studied. Table 2 shows the resulting optical properties for 0.7-mm microlens arrays that were allowed to shrink for different durations before PDMS molding. The arrays included 5 × 7 microlenses and the size of the overall array was 2 × 1 call the arrays had an initial PAAm pre-hydrogel volume of 1ml prior to photopolymerization. The shortest duration as can be seen from Table 2 is 9 h. Shorter shrinkage times resulted in the PDMS sticking to the substrate and preventing it from being peeled off. This was due to the high water content still present in the hydrogel. It should be noted that both uniformity and yield increased with shrinkage time, especially between 9 and 12 h.

It can be seen from Table 2 that as the shrinkage time is increased, the focal length decreases, while both the spherical aberration and the surface roughness increases. The increase in surface roughness is due to the loss of water in the hydrogel as it shrinks. The increase in focal length is due to the fact that as the shrinking time increases the hydrogel shrinks down further through the aperture which increases both the height and curvature of the PDMS microlens. The height of the microlens and the focal length are related by the following two equations [23,24]:

$$R = \frac{h^2 + \left(\frac{d}{2}\right)^2}{2h} \tag{1}$$

and

$$f = \frac{R}{n-1} \tag{2}$$

where R is the radius of curvature of the microlens, h is the height, d is the diameter, and n is the refractive index which in the case of PDMS is 1.43 [25].

3.4. Rehydration

After the PDMS has been peeled off the mold, the mold can still be utilized to produce microlenses with different focal lengths than the original mold. This is achieved by rehydrating the mold with water. Rehydrating the mold allowed the hydrogel to swell up and produce a new curvature. The mold was then allowed to shrink and PDMS was then poured and cured on the rehydrated mold. Using the same mold, we measured three different samples of 1-mm microlenses that were hydrated to different levels. Between the three samples, the focal length varied from 4.4 mm to 20.59 mm. The surface roughness also varied from 686 nm to 195 nm. This capability allows control over the focal length and surface requirement even after the microlens mold is fabricated.

3.5. Compound Eye

Figure 8 shows the compound eye structure on a hemispherical shell which was fabricated as per Figure 4. The initial compound eye structure as can be seen from Figure 8 is made from PDMS. The FOV achieved by the PDMS compound eye is ~94°. As per the fabrication process in Figure 4, the FOV is dependent on how much the PDMS substrate can be stretched from a sphere onto a flat surface.

Theoretically, the PDMS can be elongated before breaking to 156% of its original size [26]. Note that the images in Figure 8c–d are taken using a stereoscope where an array of the letters "UW" are placed under the compound eye and on top of the light source of the stereoscope. The focus is then adjusted until it reaches the focal distance of some of the microlenses of the compound eye

The FOV achieved by the Solaris compound eye is ~113°. The FOV for both the PDMS and Solaris compound eye was calculated by placing a laser source at the periphery of a rotational stage (RBB12, Thorlabs Inc, Newton, NJ, USA) and placing the compound eye in the middle of the stage. The laser was aligned with a microlens at one end of the compound eye. The laser was then rotated across a line of microlenses and the FOV was equivalent to the rotation angle from the first focused spot to the last focused spot of the line of microlenses. When the laser passes through the microlens, the spot size should converge into a focal spot; however, in this case due to the small size of the microlenses and the laser beam, the focal spot was hard to observe. We therefore looked instead at the far-field diffraction pattern. If the far-field diffraction pattern was an Airy disk, then the laser source is aligned with one of the microlenses. If any other pattern is visible, then the laser beam is either between the microlenses or outside the FOV.

Figure 8. Artificial compound eye. (**a**) PDMS compound eye with 0.7-mm microlenses. Field of view achieved by the compound eye is 94°. (**b**) Solaris compound eye with 0.7-mm microlenses. Field of view achieved by the compound eye is 113°. (**c**) Images acquired by PDMS compound eye. (**d**) Images acquired by Solaris compound eye.

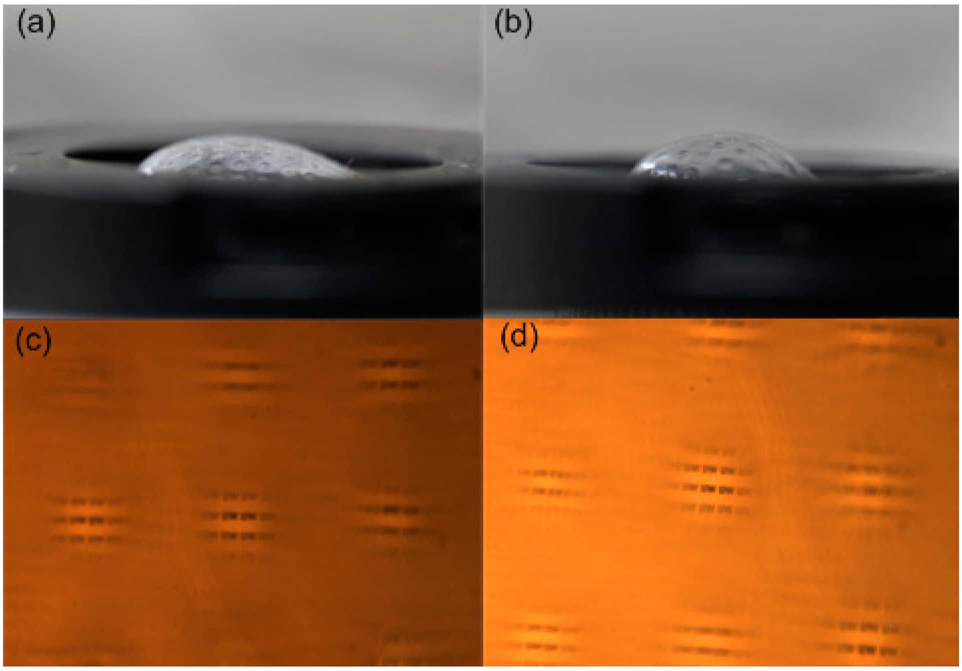

3.6. Aperture Limitation

It should be noted that there is an upper limit on the aperture size that can be achieved using the hydrogel shrinkage fabrication process. The main reason behind the limitation is due to the fact that as the aperture size increases, surface tension forces which are necessary for forming the required microlens profile become far less dominant when compared to the gravitational forces which become more dominant as the aperture size is increased [27]. Also in this case, gravitational forces would have a bigger impact compared to other fabrication techniques since we are fabricating concave lenses with profiles that are curved towards the gravitational force and not against it.

3.7. Time Sensitive Fabrication Process

When treating the surface of the IBA hydrophilic to create a hydrophobic and hydrophilic boundary, it should be noted that it is only a temporary process and the substrate will recover its natural hydrophobic state with time [9]. That means that the PAAm surface has to be flowed into the IBA chamber within hours after treatment or the surface will reverse into its original hydrophobic status. If the PAAm is flowed within the allocated time slot and exposed, the polymerized hydrogel will retain the lens curvature and is not time sensitive anymore.

4. Conclusions

We demonstrated PDMS microlenses and uniform microlens arrays fabricated through shrinking of a hydrogel and a single transfer step. The microlenses can be fabricated with lesser control requirements and can provide a wide range of f-numbers. The resulting aberrations are minimal for the small microlenses but increase with increasing apertures. Focal length is inversely proportional to the shrinkage time of the hydrogel while spherical aberration and surface roughness are directly proportional to the shrinkage time. The hydrogel mold can be rehydrated to produce microlenses with different focal lengths. An artificial compound eye based on the hydrogel shrinkage microlenses has also been demonstrated using two kinds of flexible polymers. Future work will focus on increasing the field of view of the compound eye as well as coupling microlenses with charge-coupled devices to produce complete optical system. Work will also include study of the correlation between the IBA mask size and the aperture size and shape of the resulting microlenses. In addition, work will include researching polymers that are more robust than PDMS to sustain long-term use.

Acknowledgments

The authors thank C. Li for technical discussions and help. This research utilizes National Science Foundation supported facilities at the University of Wisconsin. This work was supported by the U.S. National Science Foundation through the Emerging Frontiers in Research and Innovation program (EFRI 0937847). The work of the first author was supported by Kuwait University through its graduate student scholarship program.

Author Contributions

B. Aldalali performed most of the fabrication, analysis, and wrote the manuscript. A. Kanhere worked on the experiments pertaining to the hydrogel mold and planar PDMS microlenses. C. Huang performed the oxygen plasma processes, the PDMS compound eye, as well as the SEM images. J. Fernandes worked on both the Solaris and PDMS compound eye and on the analysis of the microlenses. H. Jiang had overall oversight over the experiments and manuscript writing.

Conflicts of Interest

The authors declare no conflict of interest.

References

1. Yang, H.; Chao, C.-K.; Wei, M.-K.; Lin, C.-P. High fill-factor microlens array mold insert fabrication using a thermal reflow process. *J. Micromech. Microeng.* **2004**, *14*, 1197–1204.
2. Beihl, S.; Danzebrikn, R.; Oliveira, P.; Aegerter, M.A. Refractive microlens fabrication by ink jet process. *J. Sol-Gel Sci. Technol.* **1998**, *13*, 177–182.
3. Rogers, J.D.; Karkkainen, A.H.O.; Tkaczyk, T.; Rantala, J.T.; Descour, M.R. Realization of refractive microoptics through grayscale lithographic patterning of photosensitive hybrid glass. *Opt. Express* **2004**, *12*, 1294–1303.
4. Yu, X.; Wang, Z.; Han, Y. Microlenses fabricated by discontinuous dewetting and soft lithography. *Microelectron. Eng.* **2008**, *85*, 1878–1881.
5. Huang, L.-C.; Lin, T.-C.; Huang, C.-C.; Chao, C.-Y. Photopolymerized self-assembly microlens arrays based on phase separation. *Soft Matter* **2011**, *7*, 2812–2816.
6. Daly, D. *Microlens Arrays*; Taylor and Francis: New York, NY, USA, 2001.
7. Park, S.; Jeong, Y.; Kim, J.; Choi, K.; Kim, H.C.; Chung, D.S.; Chun, K. Fabricaton of poly(dimethylsiloxane) microlens for laser-induced fluorescence detection. *Jpn. J. Appl. Phys. Part 1 Regul. Pap. Short Notes Rev. Pap.* **2006**, *45*, 5614–5617.
8. Zeng, X.; Jiang, H. Polydimethylsiloxane microlens arrays fabricated through liquid-phase photopolymerization and molding. *J. Microelectromech. Syst.* **2008**, *17*, 1210–1217.
9. Kim, H.-K.; Yun, K.-S. Fabrication of PDMS Microlenses with Various Curvatures Using a Water-Based Molding Method. In Proceedings of the 12th International Conference on Miniaturized Systems for Chemistry and Life, San Diego, CA, USA, 12–16 October 2008; pp. 994–996.
10. Yu, H.; Zhou, G.; Chau, F.S.; Lee, F. Fabrication and characterization of PDMS microlenses based on elastomeric molding technology. *Opt. Lett.* **2009**, *34*, 3454–3456.
11. Qu, P.; Chen, F.; Liu, H.; Yang, Q.; Lu, J.; Si, J.; Wang, Y.; Hou, X. A simple route to fabricate artificial compound eye structures. *Opt. Express* **2012**, *20*, 5775–5782.
12. Jeong, K.-H.; Kim, J.; Lee, L.P. Biologically inspired artificial compound eyes. *Science* **2006**, *312*, 557–561.
13. Zhu, D.; Zeng, X.; Li, C.; Jiang, H. Focus-tunable microlens arrays fabricated on spherical surfaces. *J. Microelectromech. Syst.* **2011**, *20*, 389–395.
14. Ko, H.C.; Stoykovich, M.P.; Song, J.; Malyarchuk, V.; Choi, W.M.; Yu, C.-J.; Geddes, J.B., III; Xiao, J.; Wang, S.; Huang, Y.; Rogers, J.A. A hemispherical electronic eye camera based on compressible silicon optoelectronics. *Nature* **2008**, *454*, 748–753.
15. He, Q.; Liu, J.; Yang, B.; Dong, Y.; Yang, C. Fabrication and characterization of biologically inspired curved-surface artificial compound eyes. *J. Microelectromech. Syst.* **2013**, *22*, 4–6.
16. Radtke, D.; Duparré, J.; Zeitner, U.D.; Tünnermann, A. Laser lithographic fabrication and characterization of a spherical artificial compound eye. *Opt. Express* **2007**, *15*, 3067–3077.

17. Das, A.L.; Mukherjee, R.; Katiyer, V.; Kulkarni, M.; Ghatak, A.; Sharma, A. Generation of sub-micrometer-scale patterns by successive miniaturization using hydrogels. *Adv. Mater.* **2007**, *19*, 1943–1946.
18. Dong, L.; Agarwal, A.K.; Beebe, D.J.; Jiang, H. Adaptive liquid microlenses activated by stimuli-responsive hydrogels. *Nature* **2006**, *442*, 551–554.
19. Agarwal, A.K.; Beebe, D.J.; Jiang, H. Integration of polymer and metal microstructures using liquid-phase photopolymerization. *J. Micromech. Microeng.* **2006**, *16*, 332–340.
20. Sridharamurthy, S.S.; Dong, L.; Jiang, H. A microfluidic chemical/biological sensing system based on membrane dissolution and optical absorption. *Meas. Sci. Technol.* **2007**, *18*, 201–207.
21. Smooth-on Corp Homepage. Available online: http://www.smooth-on.com (accessed on 5 April 2013).
22. Aldalali, B.; Zhu, D.; Jiang, H. Fabrication of Polydimethylsiloxane Microlens Arrays on Curved Surfaces. In Proceedings of the 16th International Conference on Optical MEMS and Nanophotonics Istanbul, Istanbul, Turkey, 2011; pp. 239–240.
23. Zappe, H. Micro-optics: A micro-tutorial. *Adv. Opt. Technol.* **2012**, *1*, 117–126.
24. Nussbaum, P.; Volkel, R.; Herzig, H.P.; Eisner, M.; Haselbeck, S. Design, fabrication and testing of microlens arrays for sensors and microsystems. *Pure Appl. Opt.* **1997**, *6*, 617–636.
25. Chang-Yen, D.A.; Eich, R.K.; Gale, B.K. A monolithic PDMS waveguide system fabricated using soft-lithography techniques. *J. Lightwave Technol.* **2005**, *23*, 2088–2093.
26. Huang, N.; Lee, R.; Li, S. Engineering of aligned skeletal muscle by micropatterning. *Am. J. Transl. Res.* **2010**, *2*, 43–55.
27. Zeng, X.; Jiang, H. *Microlenses: Properties, Fabrication and Liquid Lenses*; Taylor and Francis: Boca Raton, FL, USA, 2013.

Bio-Inspired Wide-Angle Broad-Spectrum Cylindrical Lens Based on Reflections from Micro-Mirror Array on a Cylindrical Elastomeric Membrane

Chi-Chieh Huang and Hongrui Jiang

Abstract: We present a wide-angle, broad-spectrum cylindrical lens based on reflections from an array of three-dimensional, high-aspect-ratio micro-mirrors fabricated on a cylindrical elastomeric substrate, functionally inspired by natural reflecting superposition compound eyes. Our device can perform one-dimensional focusing and beam-shaping comparable to conventional refraction-based cylindrical lenses, while avoiding chromatic aberration. The focal length of our cylindrical lens is 1.035 mm, suitable for micro-optical systems. Moreover, it demonstrates a wide field of view of 152° without distortion, as well as modest spherical aberrations. Our work could be applied to diverse applications including laser diode collimation, barcode scanning, holography, digital projection display, microlens arrays, and optical microscopy.

Reprinted from *Micromachines*. Cite as: Huang, C.-C.; Jiang, H. Bio-Inspired Wide-Angle Broad-Spectrum Cylindrical Lens Based on Reflections from Micro-Mirror Array on a Cylindrical Elastomeric Membrane. *Micromachines* **2014**, *5*, 373–384.

1. Introduction

Cylindrical lenses possess a spherical radius only in a single axis, enabling them to focus or expand a collimated beam into a one-dimensional (1-D) line image. Owing to the unique 1-D focusing and beam shaping capabilities, they are widely utilized in a variety of applications such as laser diode collimation, barcode scanning, slit detector array illumination, optical microscopy, holography, microlens arrays, and digital projection display and finger print scanning [1–10]. Conventional cylindrical lenses are predominantly refraction-based and hence inherently subject to two major disadvantages: chromatic aberration and lower transmission due to dispersion and absorption of light by the lens materials, respectively. In addition, fabrication of these cylindrical lenses requires high precision due to the lack of spherical symmetry, posing a great challenge in manufacturing and inevitably increasing the cost [11]. To address these optics-related issues, reflective cylindrical mirrors can achieve dispersion-free 1-D focusing with minimum chromatic aberration; however, its implementation into existing micro-optical systems requires that the imager of similar dimensions to other components be placed on the same side of the mirror as the light source, thus blocking part of the incoming light source and limiting the field of view (FOV).

In nature, some decapods (e.g., shrimps, lobsters and crayfish) possess reflecting superposition compound eyes (RSCEs) that image based on reflection rather than refraction [12,13]. Studying and mimicking this unique imaging mechanism has provided great insight into overcoming all the above challenges with a single optical design, as well as adding many features beyond those available with conventional optical technologies [14]. These advantages, including wide-angle field of view (FOV), minimum chromatic aberration and enhanced sensitivity to motion [15,16], can be implemented into existing optical devices and systems to further improve the afore-mentioned applications. Here, we report a wide-angle, miniaturized cylindrical lens suitable for 1-D focusing and beam shaping within the wide visible spectrum based on reflections from an array of three-dimensional (3-D), high-aspect-ratio micro-mirrors fabricated on a flexible cylindrical membrane to achieve minimum chromatic aberration and modest spherical aberrations by functionally mimicking the optical features of the natural RSCEs.

2. Operating Principles

Figure 1a schematically illustrates the operating principle of our bio-inspired cylindrical lens. Here, a collimated beam is applied as the light source and only a part of the device is displayed to elucidate the focusing mechanism. From the cross-section view, high-aspect-ratio micro-mirrors with reflecting sidewalls are spherically arranged onto a thin, transparent, cylindrical elastomeric membrane (radius of curvature: r) to focus the incident light by reflection. The orientation of each micro-mirror aims directly at the geometric center of the cylinder, as shown in the upper half of the cylinder in Figure 1a. The incident rays are reflected by the sidewall of each micro-mirror and then converged in an overlapping fashion onto a cylindrical focal plane with the radius of curvature of $r/2$ (Figure 1a), thus, enhancing the light sensitivity of the device [17]. Due to the spherical symmetry across the longitudinal axis of the cylinder, the focusing behavior of our device is almost equivalent to that by a cylindrical mirror with the same radius of curvature r as shown in the bottom half of the cylinder in Figure 1a. In this case, since the height of each micro-mirror (*i.e.*, 80 μm) is much smaller than r (*i.e.*, 2.07 mm) of the cylindrical substrate, reflection is assumed to occur at the top surface of the cylinder. Therefore, the incident paraxial light is focused in the same way with a focal length f of $r/2$ (*i.e.*, 1.035 mm). The way our device focuses, thus, only differs from the cylindrical mirrors in that the object and the real image are located on the opposite sides of the device, much like a conventional refractive cylindrical lens, so that the imager does not obstruct the incoming light at all, as would happen in reflective cylindrical mirrors. Hence, a theoretical FOV up to 180° can ideally be achieved if a sufficiently large array of micro-mirrors covers the entire cylindrical substrate. An equivalent 3-D representation of Figure 1a is shown in Figure 1b to demonstrate the 1-D focusing and beam shaping mechanism of our device. The structure of our device consists of an array of distributed, 3-D, high aspect-ratio micro-mirrors with smoothened sidewalls curved into a cylindrical configuration. A beam of collimated rays is first reflected by the sidewalls and then focused into a straight line image along the longitudinal axis of the cylindrical focal plane with a radius of curvature of $r/2$. In other words, the height of the image is expanded without altering its width. This schematic clearly shows the ability of such a device to elongate the focused image in only one axis (*i.e.*, 1-D), equivalent to that of the conventional refraction-based cylindrical lens.

Figure 1. (**a**) Schematic representing the operating principle of our device with radius of curvature *r* under collimated illumination. The way the incoming light is reflected by an array of micro-mirrors is equivalent to that by a mirrored cylindrical surface with the same radius *r* (see both half of the circle). Due to the spherical symmetry, both have a same cylindrical focal plane with radius of curvature of *r*/2; (**b**) An equivalent, 3-D representation of (**a**) to demonstrate the 1-D focusing and beam shaping mechanism of our device.

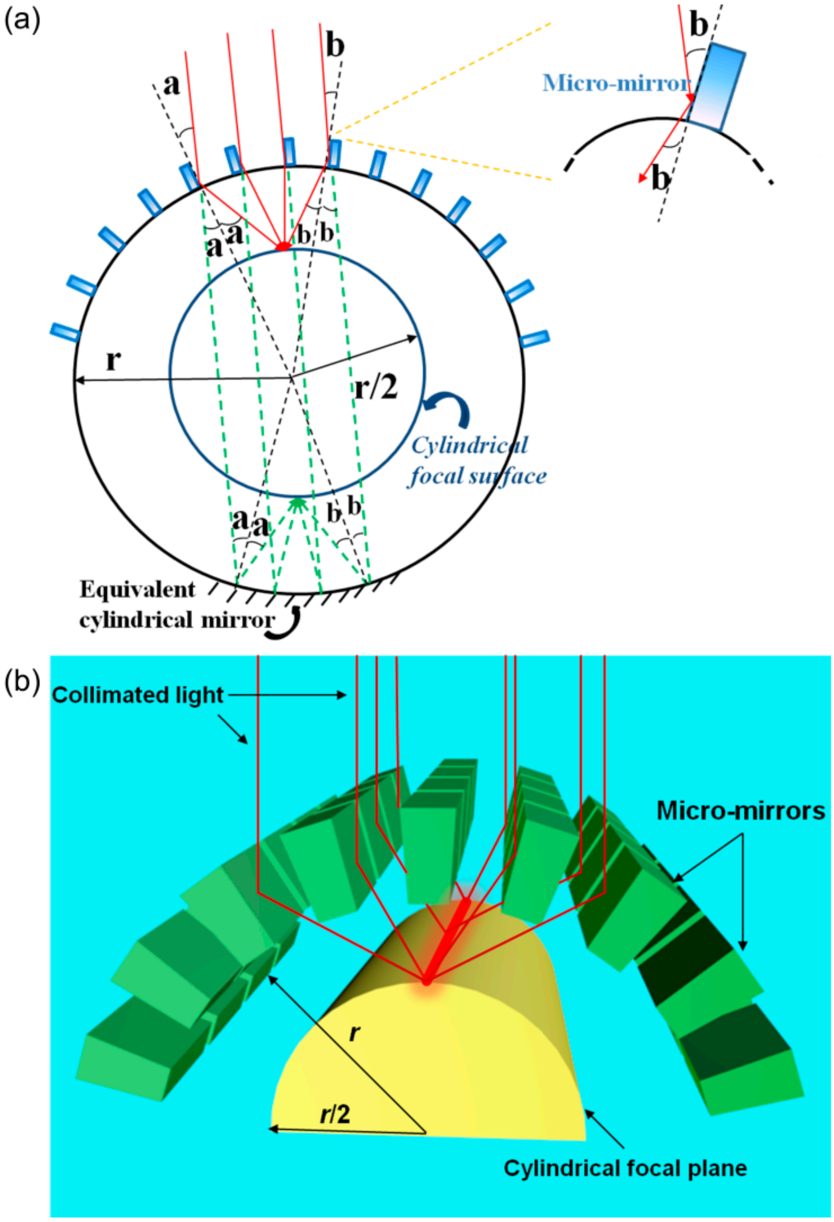

3. Fabrication

The detailed fabrication process flow for our bio-inspired cylindrical lens by a peeling micro-transfer printing method is illustrated in Figure 2 [18,19]. The process began with a large-scale array of 3-D, high aspect-ratio silicon (Si) micro-mirrors with highly vertical and smoothened sidewalls on a p-type, (100) silicon-on-insulator (SOI) wafer (80 µm-thick device layer and a 2 µm-thick buried oxide (BOX) layer) via contact-mode lithography, reactive ion etching (RIE) and inductively coupled plasma-based (ICP) deep reactive ion etching (DRIE), as shown in Figure 2a–d, respectively. The height, width, length and spacing of each micro-mirror were 80 µm, 40 µm, 120 µm, and 60 µm, respectively. Prior to the actual transfer-printing step (Figure 2g), a couple of process optimizations had to be performed to guarantee that (1) sidewalls of each micro-mirror were smoothened to serve as perfect reflectors to focus light without undesirable aberrations and distortions in the images due to scattering; and (2) large-area surface coverage of the micro-mirror array on the cylindrical polymeric membrane to maximize the FOV of the device. First, the sidewall scalloping induced by the DRIE process was removed by a 45% potassium hydroxide (KOH, Fisher Scientific, Waltham, MA, USA) wet-etching process at 40 °C for 5 min [20]. Second, the BOX layer was selectively undercut by a 6:1 buffered oxide etch (BOE, Fisher Scientific) to a level that all micro-mirrors were just slightly adhered to the underlying substrate and were ready to be transferred onto the elastomeric membrane. These two steps were represented in Figure 2e. A layer of 400-nm aluminum with reflectivity over 90% in the visible spectrum was subsequently sputtered onto the smoothened facets of the Si micro-mirrors, as shown in Figure 2f. Next, the preparation of a thin, transparent elastomeric membrane was made via a spin-coating process (spin rates 4000 rpm for 30 s) on a flat plastic substrate. The elastomeric membrane (refractive index $n = 1.43$ and thickness $t = 400$ µm) was made of pre-polymers of polydimethylsiloxane (PDMS, Sylgard 184, Dow Corning, Midland, MI, USA) with a mass ratio of 10:1 between the base and curing agent and later cured at 75 °C in a baking oven for 6 h. The width of the PDMS membrane was measured to be 6.5 mm. Once curved into a cylindrical configuration, the radius of curvature r of our device was equivalent to 2.07 mm accordingly. The optical and mechanical properties of PDMS include high transparency at the visible wavelengths and excellent flexibility, making them ideal candidates for substrate materials of our cylindrical lens. Next, the SOI wafer was brought into a conformal contact with the PDMS membrane (Figure 2g). In fact, prior to the actual contact, a thin, partially cured PDMS of the same mixing ratio was coated onto the PDMS membrane to serve as a glue layer to enhance the adhesion between the membrane and the micro-mirror array. The Si micro-mirrors were successfully transfer-printed to the flat PDMS membrane by a peeling force exerted in the lateral direction, as shown in Figure 2h,i. Figure 2j concluded the fabrication process as an array of micro-mirrors built on a flexible PDMS membrane was curved into a cylindrical configuration. The radius of curvature r was measured to be 2.07 mm, making the theoretical focal length of our device to be 1.035 mm.

Figure 2. Schematic illustrating the detailed fabrication process of the peeling micro-transfer-printing method applied to realize our device. (**a**) A large-area array of micro-mirrors fabricated on an SOI wafer by the following steps: (**b**) Contact-mode standard lithography; (**c**) Etching of oxide hard mask by RIE; (**d**) DRIE process; (**e**) Si sidewall smoothening by a 45% KOH wet-etching process. Plus, a selective undercut etching of the BOX layer by BOE solution; (**f**) Al sputtered onto the Si pillars to create an array of micro-mirrors; (**g**) A transparent, flexible PDMS membrane pressed against the structured SOI wafer to achieve conformal contact; (**h**) A peeling stress in the lateral direction lifting the micro-mirror array onto the PDMS membrane; (**i**) Micro-mirror array successfully transferred onto the PDMS membrane; (**j**) The fabrication concluded with the production of an array of micro-mirrors on a cylindrical PDMS membrane. The dimensions in this figure are not to scale.

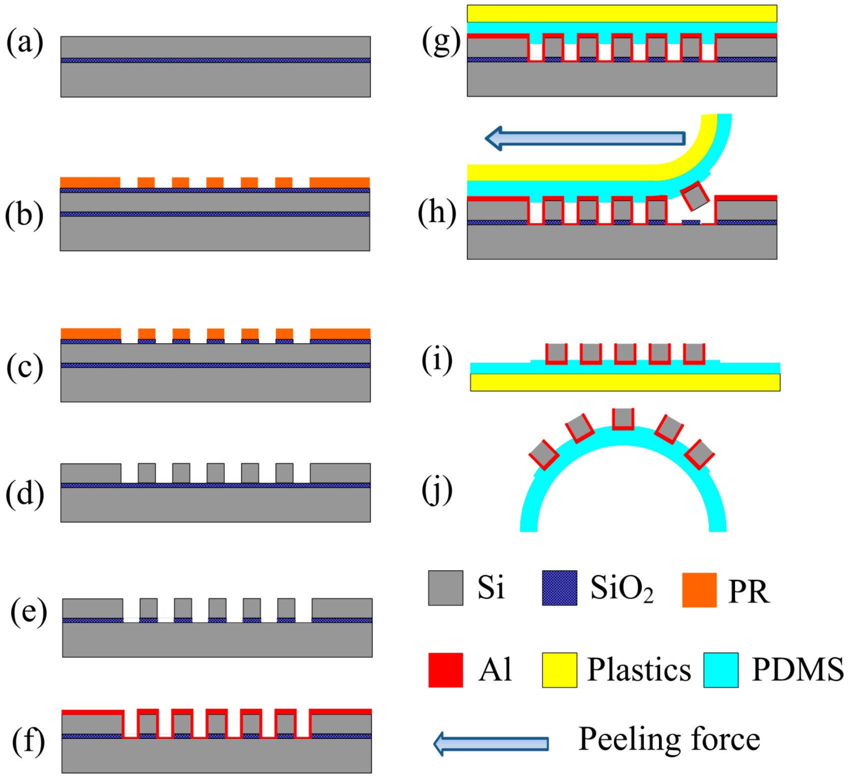

4. Results and Discussion

Figure 3 shows scanning electron microscopy (SEM) images representing part of a 55-by-50 array of 3-D, high aspect-ratio Si micro-mirrors (a) fabricated on the SOI wafer and (b) transferred onto a thin, transparent and flexible PDMS membrane. Figure 3c highlights the highly vertical and smoothened facets of the micro-mirror covered with aluminum, which are critical to an optical reflector. Figure 3d presents the picture of the micro-mirror array curved into a cylindrical configuration by a cylindrical lens holder. Again, the radius of curvature *r* and the theoretical focal length were measured to be 2.07 mm and 1.035 mm, respectively. The yields of the fabrication process were high as more than 90% of the micro-mirrors have been reproducibly transferred from the SOI wafer to the PDMS substrate.

Figure 3. Representative images of the detailed microstructures of a bio-inspired cylindrical lens. SEM images of a portion of a 55-by-50 array of 3-D, high aspect-ratio Si micro-mirrors (**a**) fabricated on the SOI wafer and (**b**) transferred onto a flat PDMS membrane; (**c**) SEM image highlighting the uniformly aluminum-covered, smoothened facets of the micro-mirror where the reflection takes place; (**d**) close-up picture of the micro-mirror array on the PDMS membrane curved into a cylindrical configuration by a lens holder.

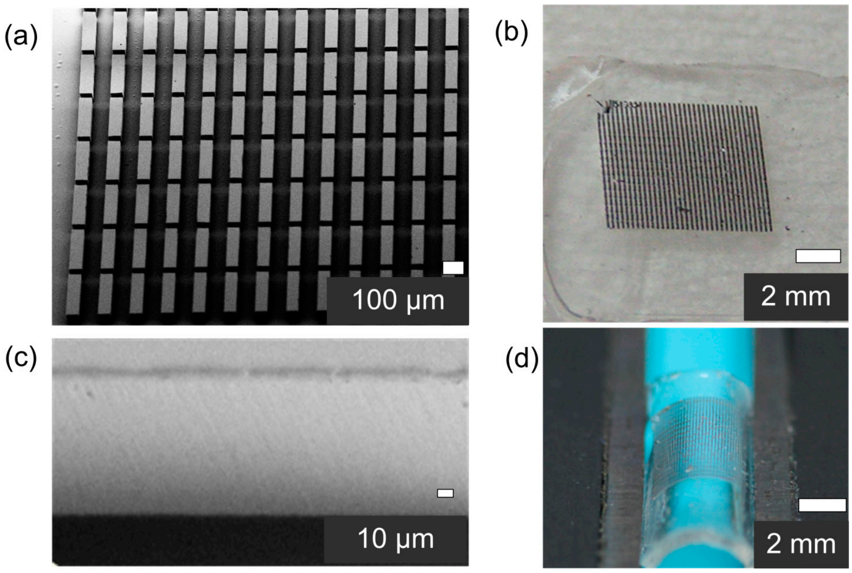

The primary functions of a conventional cylindrical lens are focusing and beam-shaping because it expands light in only one axis. Here, an extensive theoretical study was performed to compare the focusing behavior between our device, a conventional refractive cylindrical lens and a thin cylindrical PDMS membrane utilizing the optical simulation tool Zemax. Figure 4d–f shows simulated intensity profiles of various corresponding devices of our micro-mirror array on a cylindrical PDMS substrate (Figure 4a), a conventional refractive cylindrical lens (Figure 4b) and a cylindrical PDMS membrane itself, with a collimated, rectangular incoming light source (Figure 4c). For simplicity, an 11-by-5 array of reflective Si micro-mirrors radially arranged on a transparent, cylindrical PDMS membrane (refractive index $n = 1.43$, thickness $t = 400$ μm and radius of curvature $r = 1.3$ mm) was modeled to represent our device, as shown in Figure 4a. A Gaussian beam profile was applied to represent a collimated laser beam. Well-focused line images shown in Figure 4d,e can be obtained by both Figure 4a and Figure 4b but not by Figure 4c, indicating that our device has a 1-D focusing and beam-shaping capability equivalent to that of a conventional cylindrical lens, consistent with the operating principles shown in Figure 1b. One thing should be noted that the focal length of our device calculated in the Zemax was almost 0.65 mm, agreeing to theory.

To characterize the optical performances of our device in terms of focusing and beam-shaping, real focused images generated by our device (Figure 4g) and a commercial cylindrical lens (Figure 4h) were captured and compared to those simulated by theoretical modeling shown in Figure 4a,b. Both focused images were obtained without any post-image processing. A He–Ne laser (wavelength = 630 nm, JDS Uniphase 1107, Milpitas, CA, USA) was applied to produce a collimated light source. The device under test was placed at the lens holder (Edmund Optics, Barrington, NJ, USA). The holder pinched our device by the edges of the PDMS membrane to curve it into a cylindrical shape with radius of curvature close to 2 mm. The output focused images were first projected on a planar paper screen and then captured by a single lens reflex camera (Canon, EOS 60D, Tokyo, Japan) from behind. The entire optical characterization system was built on an optical linear translation stages and track (Edmund Optics) to ensure excellent alignment, stability and precise focal length measurement see Figure 5a for the system set-up. For our device, the focal length was measured to be approximately 1 mm in Figure 4g, equivalent to the *r*/2. Again, the focusing characteristics of our device were consistent with theory. More importantly, the overall beam-shaping performance in terms of the quality and clarity of the focused line image generated by our device (Figure 4g) was qualitatively comparable to those acquired by a commercial cylindrical lens with comparable size (*H* = 10.0 mm, *L* = 12.0 mm, *f* = 10.0mm, N-BK7 plano-convex lens, Thorlabs, Newton, NJ, USA) in Figure 4h. One thing should be noted: the periodic oscillation observed in the simulated image in Figure 4a stems from (a) the artifact of the periodic structures of the micro-mirror array within our device and (b) part of the incident light rays are directly passing through our device without reflecting upon the sidewalls. Both results in a somewhat blurry background expose around the focal line. This happens mostly in such area so that the effect is further enhanced. It is difficult to observe in the experimental image in Figure 4g due to its small size and more importantly, its dimmer intensity compared to the focused image. In addition, the exposure setting of the camera was kept low and hence made it even harder to be seen due to the limited dynamic range of the camera.

Figure 4. Zemax simulated intensity profiles (**d**)–(**f**) of various corresponding devices of (**a**) our micro-mirror array on a cylindrical PDMS substrate; (**b**) a conventional cylindrical lens; and (**c**) a cylindrical PDMS membrane itself, with a collimated light source. The device structures in (**a**)–(**c**) are schematically drawn. Pictures of focused line images produced by (**g**) our device and (**h**) a commercial refractive cylindrical lens. Note that the beam-shaping performances of both focused line images are almost comparable. The wavelength of the laser beam was 633 nm.

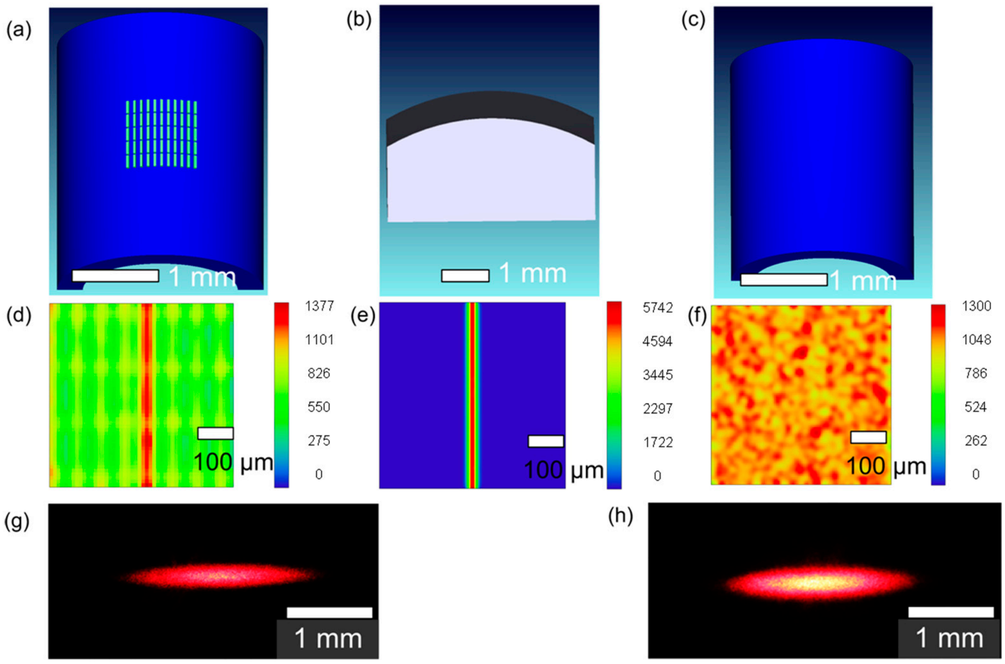

The focusing performance of our device primarily depends on two factors: dimensions of the micro-mirrors and the aspect ratio of each mirror. The former directly dictates the degree of diffraction, *i.e.*, the smaller the inter-mirror spacing, the worse diffraction can be observed. Since the smallest dimensions within our device are still much larger than the wavelength, the effect of diffraction is considered little. The aspect ratio of each mirror determines the number of reflections of the incident light rays while passing through our device. The focusing behavior is contributed by one-time reflection on the sidewalls of the micro-mirror, while two-time reflection can cause the light rays deviate from the focal point. As the aspect ratio of each micro-mirror increases, the number of two-time reflections increases accordingly and broadens the spatial light distribution. As a result, the focusing performance is degraded. In our study, the aspect ratio of 2:1, similar to that found in natural RSCEs (*i.e.*, 2:3), can allow the majority of the incident rays to focus via one-time reflections and thus serves as the basis to determine the aspect ratio and dimensions of our device.

The ability of our device to achieve minimum chromatic aberrations in the focused line images is best demonstrated and compared in Figure 6a,b. A rectangular, non-collimated white light was applied as the source. Focused line image produced by the same commercial refractive plano-convex cylindrical lens in Figure 6a showed strong chromatic aberration (*i.e.*, fringes of purple and yellow at the center and along the boundaries of the image, respectively), while that generated by our device in Figure 6b revealed no signs of chromatic aberration. Identical camera exposure settings were applied to capture both images. The dimmer aura surrounding the focused line image in Figure 6b resulted from the fact that few of the incident rays were reflected twice by the micro-mirror array before exiting our device. The reason that this aura was revealed in Figure 6b was due to larger exposure setting of the camera than those used in Figure 4g. The superior advantage of minimum chromatic aberration found in our device enables it to perform dispersion-free imaging operations over a wide visible light spectrum.

Spherical aberration, coma and astigmatism are commonly used to quantitatively characterize the extent of deviation from the normal performance in a given optical system. For our cylindrical lens, these parameters were measured with a Shack-Hartmann wavefront sensor (Thorlabs, WFS series) [21–24]. Based on the results, our device showed modest aberrations since the measured aberrations (*i.e.*, coma, tilt, spherical aberration, astigmatism) were modest and comparable to those measured from the same commercial refractive lens described above, as shown in Table 1. All parameters displayed here are in the unit of waves.

Table 1. Zernike coefficients of our device and a commercial refractive cylindrical lens (N-BK7) characterized by Shack-Hartmann wavefront sensor system.

Zernike Polynomial	Our device	N-BK7 lens	Physical meaning
$2\rho\cos(\theta)$	0.095	0.039	Tilt in *x*-axis
$2\rho\sin(\theta)$	0.272	0.442	Tilt in *y*-axis
$\rho^2\cos(2\theta)$	3.259	3.933	Primary Astigmatism
$(3\rho^2 - 2\rho)\cos\theta$	−0.135	−0.028	Coma in *x*-axis
$(3\rho^2 - 2\rho)\sin\theta$	−0.035	−0.057	Coma in *y*-axis
$6\rho^4 - 6\rho^2 + 1$	−0.07	−0.095	Spherical aberration

Another fascinating feature of our device lies in its ability to achieve a wide angle (FOV) of 152° enabled by the spherical geometry across the longitudinal axis [25,26], as demonstrated in Figure 6c The FOV measurement started with the sequential illumination of our device placed on a fixed stage at the center of the circular rotating breadboard (RBB12, Thorlabs) by a He-Ne laser mounted on the circumference (see Figure 5b for the system set-up). Three focused line images captured from three different angles, −76° (left), 0° (center), and 76° (right), in one dynamic scan were selected to represent the total 152° viewing angle. Identical camera exposure settings were used to capture all three representative figures. The result clearly demonstrates the system's ability to achieve wide-angle FOV. Owing to fact that our cylindrical lens possessed spherical symmetry in any cross section perpendicular to the longitudinal axis of the device and hence no primary optical axis was specified, all representative focused images showed comparable clarity without noticeable distortion and blur commonly seen in most wide-angle fish-eye lenses. The image quality of the focused line images in terms of clarity and brightness remained identical over the entire scanning path corresponding to the 152° FOV.

Figure 5. Photograph of the optical setup used for (**a**) image acquisition and (**b**) FOV measurement.

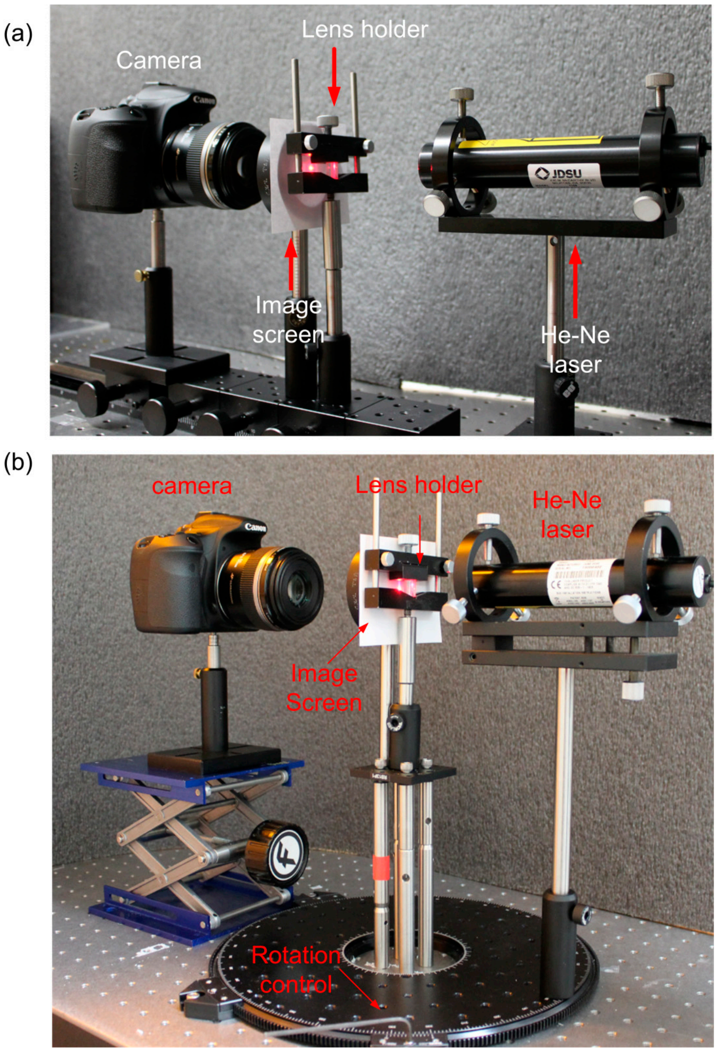

Figure 6. Focused line images produced by (**a**) a commercial plano-convex refractive cylindrical lens revealing strong chromatic aberration and (**b**) our device without chromatic aberration. These two images demonstrated clear evidence highlighting the distinctive differences in focused images with and without chromatic aberration due to different focusing mechanisms: refraction *vs.* reflection; (**c**) composite schematic and pictures representing 152° of FOV achieved by our device captured at three representative angles of incidence: −76° (left), 0° (center) and 76° (right).

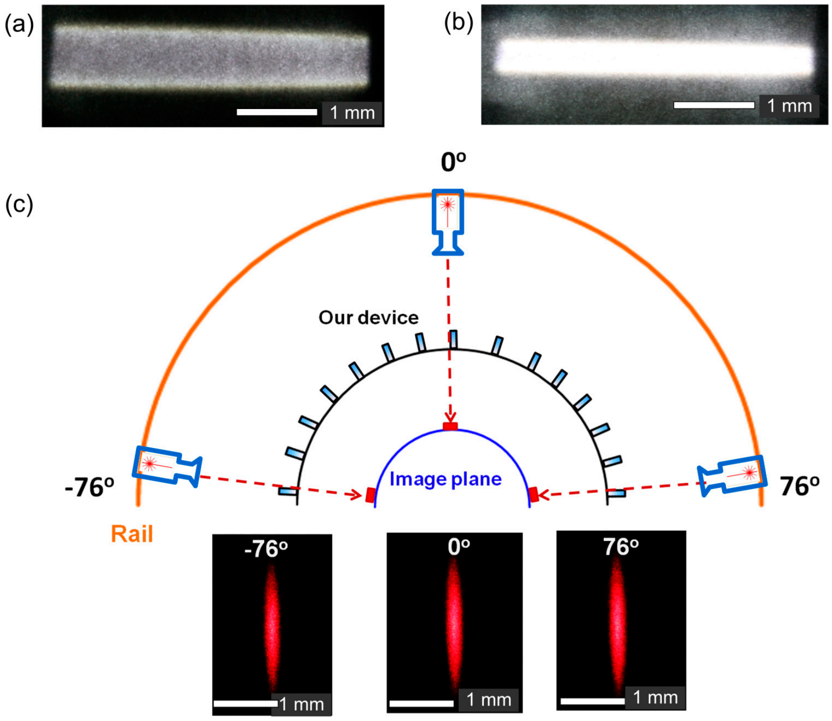

5. Conclusions

In summary, we have realized a bio-inspired wide-FOV, broad-spectrum cylindrical lens possessing optical features such as 1-D focusing, minimum chromatic aberration, exceptional 152° FOV without distortion and modest spherical aberrations. Given its small radius of curvature (2.07 mm) and focal length (1.035 mm), it can be readily implemented into micro-optical systems. Our work finds applications in laser diode collimation, barcode scanning, holography, digital projection display, optical microscopy, temporal shaping of femtosecond pulses, and so on. In the future, the same optical design concept can be applied to other spectrums ranging from infrared to X-ray wavelengths due to its reflection-based imaging mechanism. In addition, we will conduct extensive studies on the performance optimization within our optical design with regard to the dimensions and the aspect ratios of the micro-mirrors. In addition, since curving the PDMS membrane into a cylindrical configuration with a lens holder is only a tentative plan, we will directly fabricate a cylindrical PDMS substrate by casting and curing the pre-polymers of PDMS with a cylindrical rod as a mold. Prior to the transfer, the curved PDMS membrane can be elastically stretched into a flat configuration by a unidirectional tension. Finally, in order to expand the spectrum of its applications, we could deposit multiple layers of interference dielectric coatings on the Si structures instead of using a single Al layer to make our device polarization dependent.

Acknowledgments

This research was supported by U.S. National Science Foundation through the Emerging Frontiers in Research and Innovation program (EFRI 0937847). This research utilized NSF-supported shared facilities at the University of Wisconsin. The authors would like to thank Difeng Zhu, Bader Aldalali, Young Min Song, Viktor Malyarchuk, and John. A. Rogers for technical assistance and discussion.

Author Contributions

Chi-Chieh Huang and Hongrui Jiang designed the experiments, Chi-Chieh Huang performed the experiments, simulations and analysis, and Chi-Chieh Huang and Hongrui Jiang wrote the manuscript.

Conflicts of Interest

The authors declare no conflict of interest

References

1. Snyder, J.J.; Reichert, P.; Baer, T.M. Fast diffraction-limited cylindrical microlenses. *Appl. Opt.* **1991**, *30*, 2743–2747.
2. Kaestner, P. Laser Diode Collimation Optics. U.S. Patent 4,185,891, 29 January 1980.
3. Fu, Y.; Bryan, N.K.A.; Shing, O.N. Integrated micro-cylindrical lens with laser diode for single-mode fiber coupling. *IEEE Photonics Technol. Lett.* **2000**, *12*, 1213–1215.
4. Schwartz, E.D.; Hubben, E.B.; Jovanovski, B.L.; Hunter, V.L.; McCall, M.D.; Beckhusen, G.F. Adjustable Illumination System for a Barcode Scanner. U.S. Patent 6,371,374B1, 16 April 2002.
5. Sheppard, C.J.R.; Mao, X.Q. Confocal microscopes with slit apertures. *J. Modern Opt*. **1988**, *35*, 1169–1185.
6. Huang, B.; Wang, W.; Bates, M.; Zhuang, X. Three-dimensional super-resolution imaging by stochastic optical reconstruction microscopy. *Science* **2008**, *319*, 810–813.
7. Hanari, J.; Higuchi, Y. Fingerprint Image Input Apparatus Including a Cylindrical Lens. U.S. Patent 5,146,102A, 8 September 1992.
8. Huff, L.; Fusek, R.L. Color holographic stereograms. *Opt. Eng*. **1980**, *19*, 691–695.
9. Dong, L.; Agarwal, A.K.; Beebe, D.J.; Jiang, H. Variable-focus liquid microlenses and microlens arrays actuated by thermoresponsive hydrogels. *Adv. Mater*. **2007**, *19*, 401–405.
10. Sun, W.S. Using the Toroidal and Cylindrical Lenses to Project the RGB LEDs Sources on the Lens Array with Elliptic Solid Angle Calculation for the DLP Projector. In Proceedings of SPIE 8841, Current Developments in Lens Design and Optical Engineering XIV, 884110, San Diego, CA, USA, 25 September 2013.
11. Fischer, R.F.; Tadic-Galeb, B.; Yoder, P.R. *Optical System Design*; McGraw Hill Professional: New York, NY, USA, 2008; Chapter 17.
12. Vogt, K. Die Spiegeloptik des Flußkrebsauges *J. Comp. Physiol.* **1980**, *135*, 1–19. (In Germany)
13. Lee, L.P.; Szema, R. Inspirations from biological optics for advanced photonic systems. *Science* **2006**, *310*, 1148–1150.

14. Huang, C.C.; Wu, X.; Liu, H.; Aldalali, B.; Rogers, J.A.; Jiang, H. Large-field-of-view wide-spectrum artificial reflecting superposition compound eyes. *Small* **2014**, doi:10.1002/smll.201400037.
15. Land, M.F.; Nillson, D.E. *Animal Eyes*; Oxford University Press: Oxford, UK, 2002; Chapter 8.
16. Land, M.F. Superposition images are formed by reflection in the eyes of some oceanic decapod Crustacea. *Nature* **1976**, *263*, 764–765.
17. Land, M.F. Eyes with mirror optics. *J. Opt. A* **2000**, *2*, 44–50.
18. Huang, C.C.; Zeng, X.; Jiang, H. Fabrication of large-area three-dimensional microstructures on flexible substrates by micro-transfer printing methods. *J. Microelectromech. Syst.* **2012**, *21*, 749–755.
19. Zeng, X.; Jiang, H. Fabrication of complex structures on non-planar surfaces through a transfer method. *J. Microelectromech. Syst.* **2011**, *20*, 6–8.
20. Shikida, M.; Inagaki, N.; Sasaki, H.; Amakawa, H.; Sato, K. The mechanism of selective corrugation removal by KOH anisotropic wet etching. *J. Micromech. Microeng.* **2010**, *20*, 1–9.
21. Li, C.; Hall, G.; Zhu, D.; Li, H.; Eliceiri, K.; Jiang, H. Three-dimensional (3D) surface profile measurement of microlenses using Shack-Hartmann wavefront. *J. Microelectromech. Syst.* **2012**, *21*, 530–540.
22. Li, C.; Hall, G.; Zeng, X.; Zhu, D.; Eliceiri, K.; Jiang, H. Three-dimensional surface profiling and optical characterization of liquid microlens using a Shack-Hartmann wavefront sensor. *Appl. Phys. Lett.* **2011**, *98*, doi:10.1063/1.3583379.
23. Jeong, T.M.; Menon, M.; Yoon, G. Measurement of wave-front aberration in soft contact lenses by use of a Shack-Hartmann wave-front sensor. *Appl. Opt.* **2005**, *44*, 4523–4527.
24. Pfund, J.; Lindlein, N.; Schwider, J.; Burow, R.; Blümel, T.; Elssner, K.E. Absolute sphericity measurement: A comparative study of the use of interferometry and a Shack-Hartmann sensor. *Opt. Lett.* **1998**, *23*, 742–744.
25. Floreano, D.; Pericet-Camara, R.; Viollet, S.; Ruffier, F.; Brückner, A.; Leitel, R.; Buss, W.; Menouni, M.; Expert, F.; Juston, R.; *et al.* Miniature curved artificial compound eyes. *Proc. Natl. Acad. Sci. USA* **2013**, *110*, 9267–9272.
26. Song, Y.M.; Xie, Y.; Malyarchuk, V.; Xiao, J.; Jung, I.; Choi, K.J.; Liu, Z.; Park, H.; Lu, C.; Kim, R.H.; *et al.* Digital cameras with designs inspired by the arthropod eye. *Nature* **2013**, *497*, 95–99.

Wafer-Level Hybrid Integration of Complex Micro-Optical Modules

Peter Dannberg, Frank Wippermann, Andreas Brückner, Andre Matthes, Peter Schreiber and Andreas Bräuer

Abstract: A series of technological steps concentrating around photolithography and UV polymer on glass replication in a mask-aligner that allow for the cost-effective generation of rather complex micro-optical systems on the wafer level are discussed. In this approach, optical functional surfaces are aligned to each other and stacked on top of each other at a desired axial distance. They can consist of lenses, achromatic doublets, regular or chirped lens arrays, diffractive elements, apertures, filter structures, reflecting layers, polarizers, *etc*. The suitability of the separated modules in certain imaging and non-imaging applications will be shown.

Reprinted from *Micromachines*. Cite as: Dannberg, P.; Wippermann, F.; Brückner, A.; Matthes, A.; Schreiber, P.; Bräuer, A. Wafer-Level Hybrid Integration of Complex Micro-Optical Modules. *Micromachines* **2014**, *5*, 325–340.

1. Introduction

Although discussed extensively in recent years, wafer level optics is a well-established technology, which had been introduced decades ago in the field of miniaturized or micro-structured optics. Here, the wafer concept was simply related to the lithographical generation of micro-optical structures, such as microlens arrays or diffractive optical elements. In analogy to micro-electronics, a large number of optical chips with thousands or millions of microstructures can be generated in parallel. Lithography involves the structuring of several layers, aligned to each other, and, thus, offers an integration capability. More than ten years ago, UV polymer on glass replication [1] using a modified mask aligner as a lithography related fabrication tool was introduced as a precise and cost effective technology for the generation of wafer-scale miniaturized optical systems and for hybrid integration [2]. Parallel fabrication is especially useful in cases of miniaturized systems because one can obtain a high number of chips from a wafer and in cases where several structural layers have to be aligned to each other. Thus, similar wafer-level concepts were introduced and optimized in recent years for the fabrication of miniaturized cameras [3–5]. However, the technological and application potential of wafer-level miniaturized optics is not restricted to miniature camera lenses.

In the present paper we present a refined wafer-level fabrication technology involving UV polymer molding, coating and lithography which is based on earlier work [2] but is characterized by a much higher degree of variety and complexity. Within the frame of this paper, the main focus will be on the diversity of systems that have been realized using this technology, as well as on the fabrication details, range of parameters, and on the potential and limits of the approach. The paper is organized as follows: the mastering of micro-optical elements, UV replication, and further key elements of the fabrication process will be discussed in the next chapter “Technology”. Our focus is on the interaction and compatibility of process steps in order to generate systems with high lateral and axial complexity. This will be illustrated in the subsequent chapter “Experimental examples and characterization” by discussing special aspects of three different micro-optical systems. Finally, a summary of typical systems, their performance and main technological parameters will be given and conclusions will be drawn.

2. Technology

2.1. UV Polymer Molding

The centerpiece of the presented technology is a UV polymer molding process using a mask aligner. In the typical UV replication, a thin layer of polymer is cured in between a replication tool and a rigid inorganic substrate such as glass. In fact, the low coefficient of thermal expansion (CTE), good optical homogeneity and low total thickness variation of state-of-the-art float glass wafers, such as Borofloat B33 or D263T (Schott), are essential in order to realize the necessary lateral and axial precision of micro-optical systems on a wafer level. UV polymer (cured at room temperature and normal pressure) is used to realize high precision, rapid replication, and good adhesion to the substrate and high thermal and environmental stability of the element. There are numerous acrylate- or epoxy-based UV curing resins with tailored properties, such as viscosity, refractive index, or shrinkage, which are compatible with the described UV-molding process. Inorganic-organic hybrid polymers like ORMOCOMP® [6,7] show enhanced stability compared to their purely organic counterparts.

A contact mask aligner is ideally suited to generate thin, uniform and plane-replicated polymer layers on arbitrary substrates as a result of a sequence of dispensing, alignment, proximity exposure through a UV-transparent mold, and separation. In our experiments we used a MA8e 200 mm aligner (SUSS MicroTec AG, Munich, Germany) featuring a unique UV molding software and a special tooling with exposure gap control realized by three-point inductive z-measurement and closed-loop piezo-driven z-axis movement for sub- µm gap control. Furthermore the piezo-driven z-movement is designed to apply the necessary force to spread the dispensed polymer resin across a 200 mm wafer area.

For proper focusing of the individual systems on the wafer a high axial precision is essential. This is achieved by the precise mask aligner tooling, especially the top load mask holder approach and due to soft elastomer-on-glass molds, which were fabricated using the same mask aligner, thus, compensating for some of the deviations. In the MA8e, the substrate thickness can be as high as 10 mm, and the mask or replication tool can be as thick as 15 mm in order to ensure superior planarity. Alternatively, thinner replication tools can be reinforced by a vacuum-attached, planar, transparent glass plate. As a result, it is possible to replicate UV cured, insoluble polymer films on either side of arbitrary substrates, even on top of each other with a lateral precision of about ±1 µm across 200 mm substrates and an axial accuracy in the range of ±5 µm. Typically the overall polymer thickness exceeds the lens sag, forming a uniform polymer layer in order to accomplish axial alignment and as a means for shrinkage compensation. For a lens sag <150 µm, we found that for a polymerization shrinkage below 5% (volume) it is not necessary to apply some form of mold precompensation in order to maintain the diffraction limited lens accuracy during the molding step.

In the UV molding technology, the adhesion to the mold is kept low by a proper choice of the mold material (*i.e.*, polydimethyl siloxane/PDMS) or by applying an anti-sticking layer onto the mold surface. Thus, the mold can be separated from the molded part after UV curing. On the other hand, when treated with an adhesion promoter, two parts can be aligned and glued together using the same process (without the separation). That means the technology is not restricted to single- or double-side polymer on glass replication but can be extended to stacks of wafers. An example concerning multi-aperture cameras is given in Chapter 3.3.

2.2. Coating and Structuring

Apertures filter structures, anti-reflection, or other coatings are an essential part in the design of more complex optical systems and have to be implemented in the wafer-level approach. The UV polymer on glass technology allows for a variety of different materials and arrangements of structural layers: a glass wafer can be coated and patterned before the replication, *i.e.*, by sputter coating of metal, lithography, and wet etching. In this way, apertures or reflector elements were generated in chromium, low reflective chromium, titanium, aluminum and silver.

Additionally, the glass wafer can be structured using photopatternable polymer materials (like PSK2000 and PSC resists/Brewer science). Thus, apertures or color filters can be generated by spin coating, lithography, and hard bake. The choice of metal or polymer apertures depends on the actual design. PSK2000 apertures have very low reflection (<1%) in a wide spectral and angular range and are easily generated, while low reflective chromium structures demonstrate better spatial resolution and stability. Lens replication on top of apertures or filters results in buried structures.

Plane, transparent polymer layers can be added by UV-molding, defining additional structural layers or acting as spacers.

Surfaces can be coated with large-area dielectric layer systems, *i.e.*, as IR cutoff or other filters anti-reflection coatings or mirrors. Plasma assisted evaporation (APS) coating technology for polymer surfaces is a well-established technology [8] and can be applied to optical wafers in every stage of the fabrication. Typically, UV polymer is subject to a thermal post-curing (hardbake) before coating (30 min at 180 °C under protective gas (Nitrogen) for ORMOCOMP®). We found that long-term radius changes of the ORMOCOMP® polymer lenses after hard bake were well below 1%.

2.3. Compatibility

As a matter of course, blank glass substrates can be structured in various ways. UV polymer replication is compatible with blank glass substrates, as well as with structured ones. Surface profiles will be planarized in the molding step and absorbing layers, apertures etc. are uncomplicated when using a UV-transparent replication tool. The crosslinked nature of UV-cured resins enables UV molding of several polymer layers directly on top of each other. Adhesion at interfaces is promoted by common silane treatment of glass or other oxidic surfaces [9], by proper choice of polymer materials, and by oxygen plasma treatment of polymer surfaces [8,10]. Dielectric coatings can be treated with silane adhesion promoters in the same way as glass as the final layer is usually SiO_2. In this way, black matrix polymer apertures can for instance be created directly on top of anti-reflection coated lenses. The alternate stacking of UV-replicated polymer layers in the form of computer generated holograms and of dielectric color filter layers has already been demonstrated [11]. Shrinkage and CTE mismatch might cause problems like stress, wafer bowing, or delamination in the described stacks of different materials. This can limit the maximum polymer thickness especially in the case of thin glass substrates. As an alternative, a large area polymer layer can be subdivided into a multitude of smaller areas by proper tooling, by selective UV curing, or by a chipwise dispensing approach. Furthermore, symmetrical polymer-glass-polymer designs and/or flexible polymer resins can reduce bowing.

The chemical stability of crosslinked UV-cured polymer films enables subsequent coating and lithographic patterning, *i.e.*, the generation of metal structures/apertures by sputtering of titanium, spin-coating, baking, and structuring of photoresist, wet chemical etching, and resist stripping on top of a replicated optical surface [12].

The compatibility of the dimensional scaling of different structural layers is achieved by the consistent use of photolithography. A set of photomasks normally consists of a mask for the lens mastering (see below), the apertures, the filter structures and the spacers, including the respective features for alignment, process monitoring, dicing, *etc*. The lithographical patterning of all features, the tooling and UV molding including the alignment of all layers is done in the same mask aligner under comparable conditions.

As a preliminary conclusion it can be stated that the compatibility of UV polymer on glass replication, coating and lithography is the key factor for the variety of different systems that can be generated as it will be shown below. Figure 1 shows a schematic flow chart of the wafer-level fabrication of micro-optical systems using the described process steps.

2.4. Thermal Behavior

Refractive index as well as geometry changes with temperature, have to be considered in the optical design of imaging systems; for lens array applications a temperature dependent pitch can be critical. Thermo-optical coefficients of a 100 µm thick polymer layer on a B33 glass substrate were measured and are typically on the order of $-0.0002\ \mathrm{K}^{-1}$. Geometry changes were determined by measuring polymer-on-glass microlens arrays in a mechanical profiler (Taylor Hobson Form Talysurf) at different temperatures, thus, taking the polymer on glass configuration into account. In Figure 2 changes of pitch and radius of curvature of a polymer (ORMOCOMP®) on glass (Borofloat 33/Schott) microlens array are plotted, as far as we know for the first time. Due to the scatter in the lenslet parameters it is crucial to compare corresponding lenslets, and to scan across a higher number of lenslets in order to improve the measurement contrast. The measured pitch variation corresponds to the CTE of the glass substrate ($+3.3 \times 10^{-6}\ \mathrm{K}^{-1}$) and is almost two orders of magnitude smaller than for thermoplastic polymers. As a consequence of the restricted lateral expansion there is a slight decrease of the lens radius with temperature ($1/R \times \mathrm{d}R/\mathrm{d}T$ of $0.00016\ \mathrm{K}^{-1}$), thus, the radius change can partially compensate for the thermo-optical changes of focal length. We could not detect a temperature change of the <30 nm rms. form deviation of the lenslets.

Figure 1. Flowchart of the technology based on UV-molding, coating, and lithography.

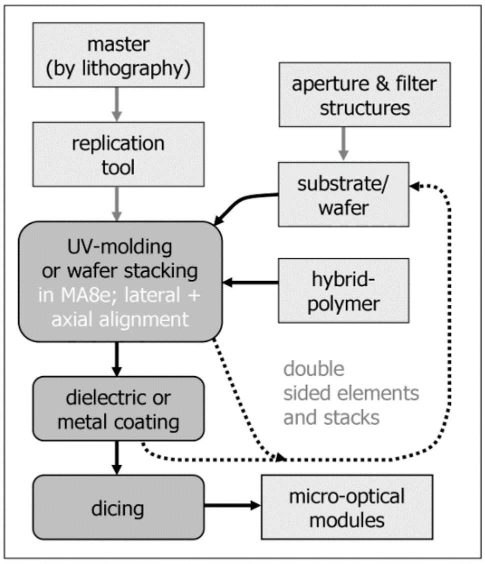

Figure 2. Temperature dependent pitch (**left** hand side) and radius (**Right** hand side) changes of an ORMOCOMP® on B33 glass lens array measured using a mechanical profiler (FormTalysurf PGI/ Taylor Hobson).

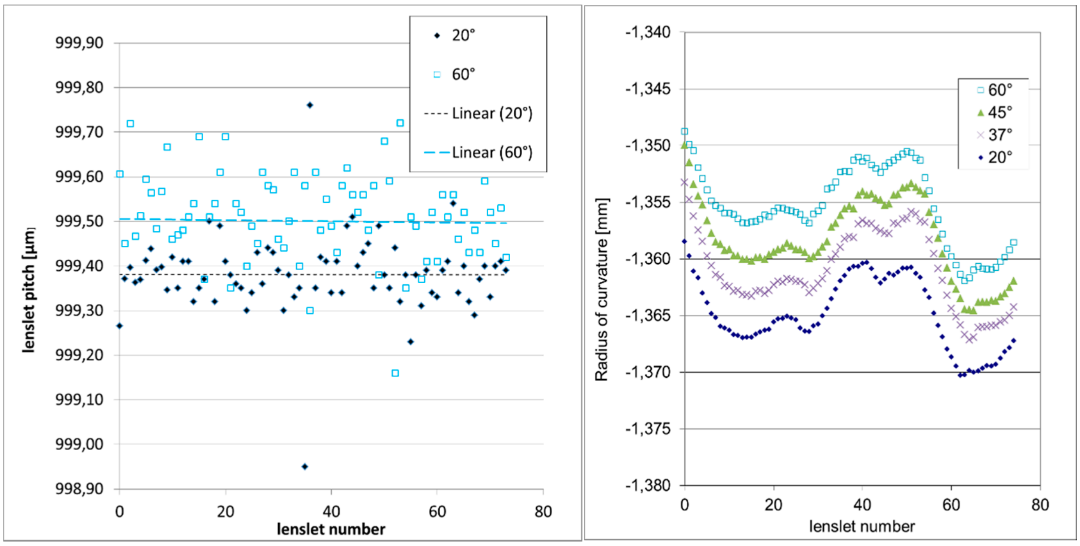

2.5. Mastering by Photolithography

The reflow of photoresist patterned by binary photolithography is well established to generate a large number of microlens structures with precise positioning and diffraction limited surface accuracy on a single wafer [13–15]. The main limitations of the technology are the radius scatter depending on the amount of photoresist which is available per lenslet in the reflow step, and the limited flexibility of the lens profiles, both making reflow lenses less attractive for high-resolution imaging.

Nevertheless, in all of the applications discussed below we used reflow lens mastering successfully. Several extensions of the standard process enabling higher complexity of the systems will be discussed in the following paragraphs: hybrid refractive-diffractive elements, chirped lens arrays, and RIE assisted mastering.

Hybrid refractive-diffractive elements: here, the reflow process forming the refractive lens is carried out at reduced temperature so that the resist can still be patterned by further lithographical steps afterwards. In the example shown in Figure 3, we used variable dose laser writing to generate the diffractive correction element on top of the refractive microlens [16].

Chirped lens arrays: Figure 4 shows the scheme of a two-mask process where the lateral layout of the lens array is defined using mask #1. The structures are transferred to a ~100 nm thin base layer by dry etching, forming chemically stable lens pedestals. Then the proper resist thickness for the reflow process is added by spin coating. The volume of each lenslet (and thus its radius of curvature) is now defined by patterning a smaller resist area onto every pedestal using mask #2. As a result, the lateral lens layout (process #1) can be defined with exceptional high accuracy and high resolution, and can be chosen independently of the corresponding radius of curvature. In other words: every lenslet on the wafer can be designed to have its own position, orientation, size (mask #1), and focal length (mask #2). We used this enhanced design freedom in the randomization of arrays for homogenization [17], the channel-wise aberration correction of multichannel imaging optics [18] or simply the lateral arrangement of elements with different parameters on the same wafer [19]. A means to simulate "generalized" chirped or stochastic lens arrays in the ray tracing design and routines to calculate the corresponding mask data for each lenslet were implemented in our fabrication process [20].

Figure 3. Mastering of hybrid microlenses: refractive lens combined with a diffractive phase correction element by combining reflow and laser lithography.

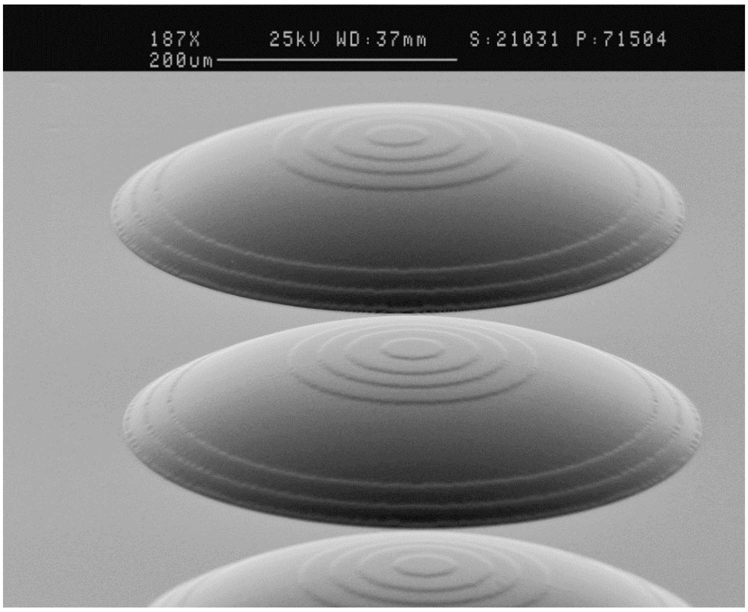

Figure 4. Scheme of a two-mask process to generate chirped lens arrays.

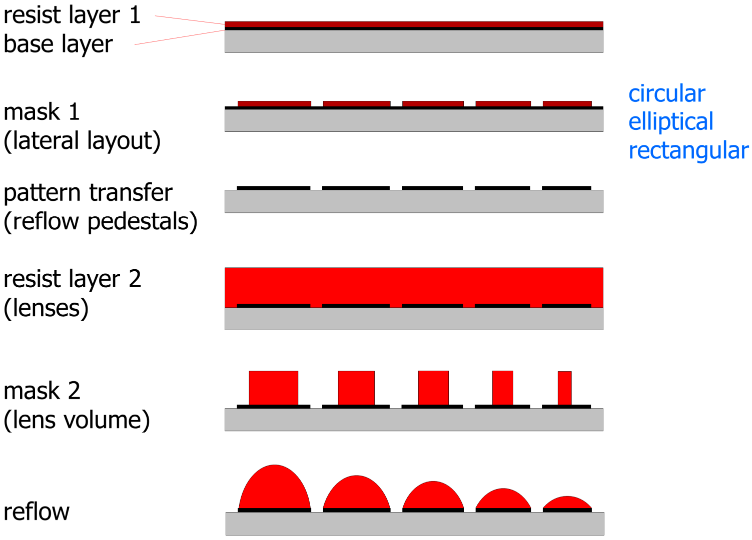

RIE assisted lens mastering: Reactive ion etching (RIE) of polymer structures like reflow lenses is a well established technology for proportional transfer of lenses to fused silica or other inorganic substrates [21]. Furthermore, an initially spherical lens profile can be shaped by changing the transfer rate during the etch process resulting in well-defined aspheres [22]. The fabricated aspheres can be used as a master for UV replication [12]. The preferred substrate material in the RIE process is fused silica due to its etching characteristics, low CTE and UV transparency.

Because of the highly isotropic nature of the RIE, the fill factor of arrays of convex lenses decreases during the transfer process. On the other hand, with concave lens arrays it is constantly enhanced during the etching process until the gap between adjacent lenslets vanishes, leading to a 100% fill factor. Thus, a limitation of microlenses based on photoresist reflow can be overcome as shown in Figure 5. These arrays can again be used as a tool for subsequent UV replication.

Figure 5. Microscope photograph of a UV molded hexagonal convex lens array with 100% fill factor.

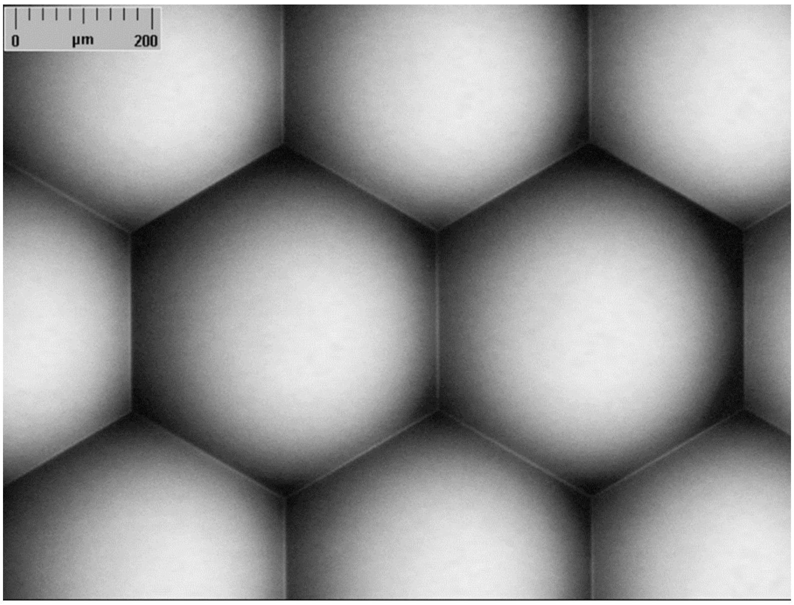

RIE assisted mastering is subject to limitations inherent to the RIE process. In particular, the feature height should be well below 100 μm and slope angles below 35°.

The implementation of these more complex processes to achieve microlenses with improved performance is justified for volume production because the elevated efforts apply only to the mastering while the replication process remains unchanged.

2.6. Options and Add-ons

The UV polymer in the molding process is typically cured in a large area flood exposure. As the mask aligner is originally designed for proximity exposure through a mask, one can, without hardware modification achieve a local photopolymerisation by combining the mold with a photomask and performing a directed exposure with a fraction of the necessary dose of a full UV cure. The UV polymer acts as a negative resist, and uncured material can be removed after separation from the mold by rinsing with a solvent, typically methyl isobutyl ketone. After drying, a diffuse flood exposure fully cures the molded structures. An example (lens arrays on Si CMOS detector arrays) is given in the next chapter.

There are a number of commercial UV curing resins with different dispersion characteristics, mainly depending on their refractive index n ~1.45–1.65. Abbe numbers (v) range typically from 25 to about 60 allowing for the achromatization of systems in an all-polymer approach. As UV molding does not require plane surfaces, achromatic doublets were easily fabricated by performing two molding steps on top of each other using different UV resins.

Further material combinations can be used, one proposal being the implementation of UV curing/ photopatternable birefringent liquid-crystal polymer layers [23]. Glass substrates with polarizers [24] can be integrated, *i.e.*, for sensor applications.

As mentioned above, the mask aligner can be used for the stacking and bonding of two or more micro-optical wafers in a similar way as in the UV molding process. This has been demonstrated e.g., in a multi-aperture camera application, and in the wafer scale fabrication of miniaturized Mirau interferometer lenses [25].

As a final step, a commercial wafer saw DAD3350 (Disco, Tokyo, Japan) is used to separate wafers or wafer stacks into individual chips providing an alignment accuracy of <10 μm. Even polymer-glass-silicon composites can be cut without problems. Separated chips are available on standard tape for further processing (also see Figure 6).

3. Experimental Examples and Characterization

3.1. Lens Arrays on Si Detector Arrays

The direct replication of lens arrays onto detector arrays including lateral and axial alignment was already proposed [2]. In particular, selective UV curing using a partially UV-transparent replication tool allows for the electrical bonding of separated chips. In the following we show first results of molding on functional complementary metal–oxide–semiconductor (CMOS) substrates. Figure 6 is a photograph of a six-inch silicon wafer with a cylindrical lens arrays for fill factor enhancement.

In contrast to other studies [26], we focused on rather large lenslets where the designed pitch and polymer thickness were in the range of 100 μm, which is ideal for UV replication. The detail in Figure 6 shows that selective curing can be used to keep the bond pads free of polymer despite the possible stray light from metal or from via or mesa structures in the CMOS substrate. Before UV molding, the CMOS passivation layer was treated with a coupling agent (methacryloxypropyl trimethoxy silane) for optimum adhesion. Polymer thickness homogeneity across the wafer was ±5 µm. The Silicon CMOS wafer with UV-molded microlens arrays turned out to be compatible with further process steps like dicing (see Figure 6), handling by a pick and place robot, electrical bonding, reflow soldering at 260 °C, and testing.

Figure 6. Silicon CMOS wafer with UV molded cylindrical lenslets after dicing. Detail: selective UV curing leaves the bond pads open for electrical bonding.

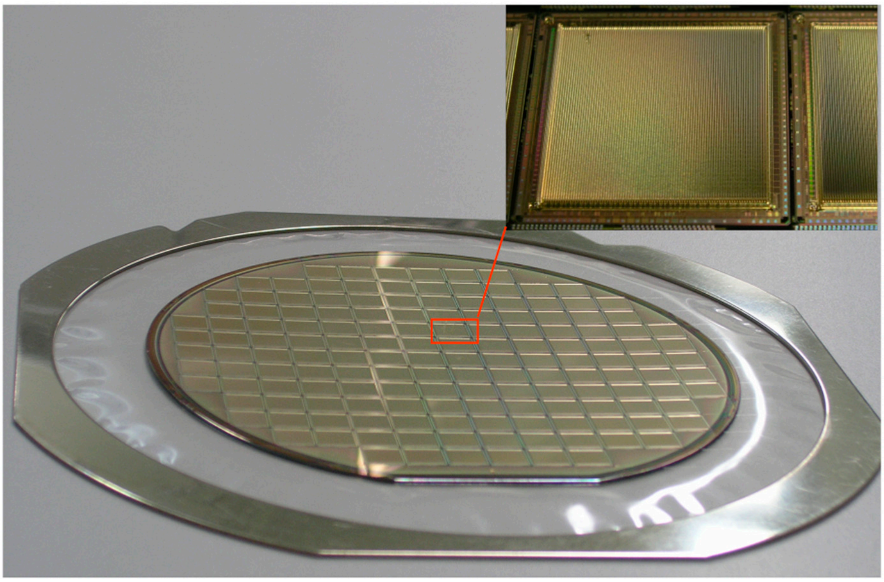

3.2. LED Spot Array Illumination

Figure 7a shows a beam shaping device where a lens array is illuminated by a LED in a pupil splitting approach to generate an array of 21 × 21 spots with field-of-view of 40° × 40° [27]. The lens array as the central element was integrated with an aperture array to obscure the space between lenslets. As an additional feature, a buried color filter array was implemented in order to demonstrate the opportunity to color code each individual spot. Apertures and filters were patterned onto blank glass wafers and hard baked before lens replication. A chirped lens array was generated by the approach illustrated in Figure 4 in order to compensate for aberrations of the plano-convex projection lens. Here, the chirp of the microlens position (see Figure 7b) compensates for the distortion while the chirp in the focal length (see Figure 7c) reduces field curvature. As a result we obtained equally spaced spots (period 19 mm) with a distortion <0.5%, and equal spot size of 4 mm [27].

3.3. Multi-Aperture Cameras and Channel Isolation

Multi-aperture imaging concepts implementing microlens arrays are currently investigated to be used as the optics of compact vision sensors for automotive, machine vision, or measurement applications [28]. A main technological difficulty in all multi-aperture systems is the fabrication of features, which serve as channel isolation in order to suppress scattering and optical cross talk which would lead to ghost images. We found that one approach which is compatible to the presented technology is the stacking of thin, plane diaphragm arrays in several layers, with axial separation and diameters designed in a way that scattered light is blocked before impinging upon the adjacent detector. This concept typically involves three different diaphragm layers. Figure 8 shows the cross section of an electronic cluster eye with VGA resolution [29], consisting of an upper wafer with the system aperture stop, as well as an imaging lens array, and the diaphragm stack for channel isolation as the lower part. The diaphragm layers are designed as PSK2000 black matrix polymer layers between thin D263T glass substrates laminated on top of each other using UV curing glue (OG146, Epoxy Technology, Billerica, MA, USA). Chirped lens arrays were generated on the upper wafer for a channel-wise minimization of aberrations. Figure 9 represents measured lens radii across several chips on the wafer. It can be seen that even subtle changes in the design radius (to compensate for field curvature) can be precisely generated—defined by mask 2 of the process described in Figure 4.

Figure 7. LED illuminated array of 21 × 21 spots (**a**) configuration consisting of LED, condenser, chirped lens array and relay lens; (**b**) photograph of a separated chirped lens array including apertures and filters; (**c**) measured surface profile across a regular array and chirped arrays. Detail resolves single lenslets.

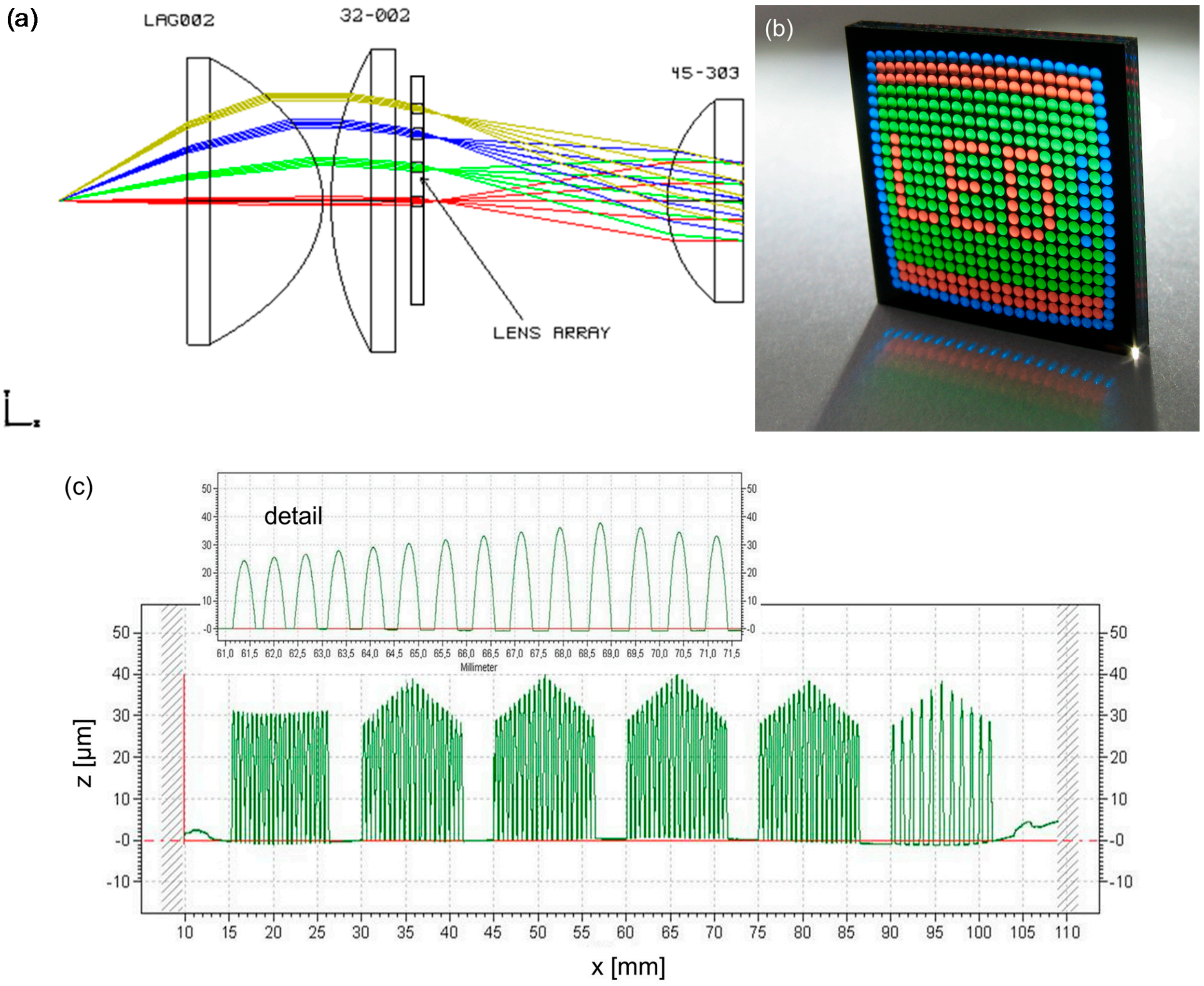

Figure 8. Schematic cross section of a multiaperture imaging system with VGA resolution.

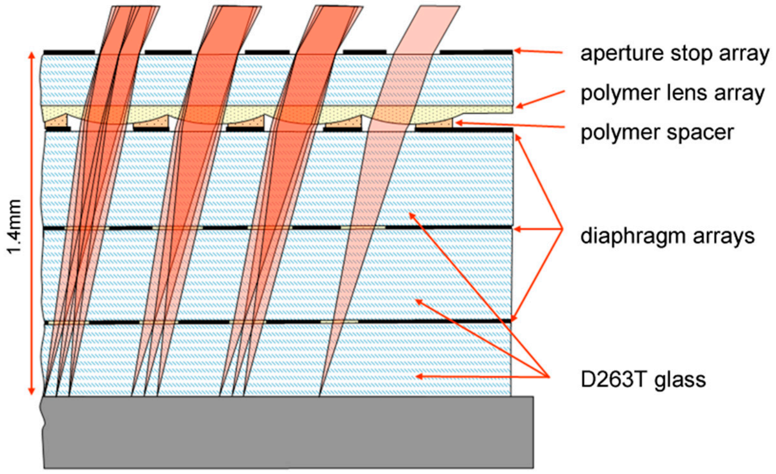

Figure 9. Chirped lens arrays: Design (**hollow** squares) and measurement data (**full** triangles) of lens radii across a row of chips.

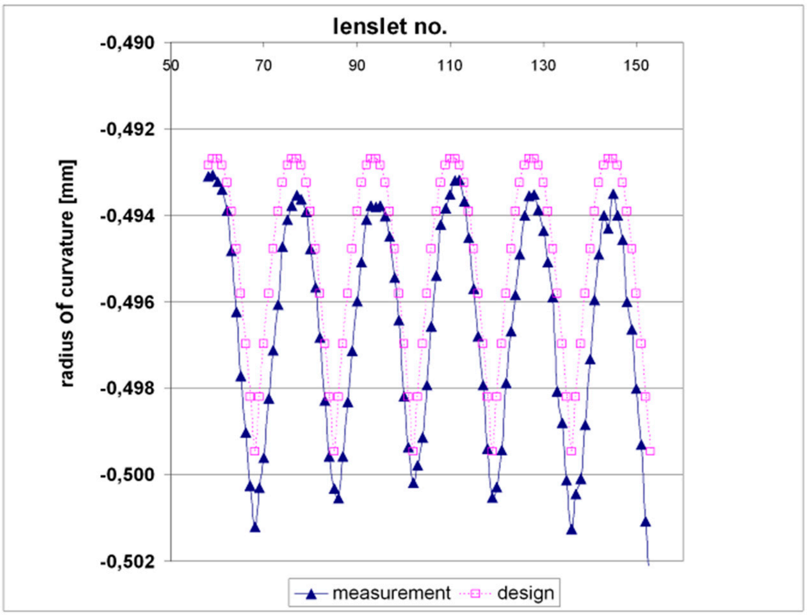

A spacer layer was generated on top of the lenses by selective UV molding and subsequent rinsing of uncured resin so that the openings correspond to the optically active areas of the lenslets (see Figure 8). The spacer surface was then coated with a thin layer of UV curing adhesive before upper and lower parts were loaded into the mask-aligner, aligned in x, y direction, brought into contact ($z = 0$) and bonded together by diffuse UV exposure. The thickness of the bonding adhesive in this example was below 3 µm in order to avoid the lenses being contaminated with excess material, and to achieve the desired axial accuracy of the stack. On the other hand, the adhesive layer was thick and homogenous enough to form tight cavities for each lens, which were not affected in the dicing process. For testing purposes, the optics and imager (without cover glass) were mounted on a chip scale after dicing. Proper focusing within about ±10 µm was achieved solely by the control of lens radii and glass and polymer spacer thickness.

4. Summary and Conclusions

In the present paper we describe a technology for the generation of hybrid-integrated micro-optical systems on wafer scale. Polymer on glass UV molding of microlenses, diffractive elements, or other structures in a specially equipped eight-inch mask aligner combines precision and cost-effective fabrication via replication. The demonstrated high lateral accuracy of ~1 µm is essential for the wafer-scale approach and is suitable for applications where the precise matching to the pitch of detector or fiber arrays is required. Compared to all-polymer technology (like injection molding) the elements show considerably higher stability and lower lateral CTE.

We demonstrated that fabricating a variety of rather complex systems becomes feasible by using UV molding, precise float glass or silicon wafers, dielectric or metal coating, and lithography as patterning and mastering technologies. The process is completed by wafer stacking and dicing. Figure 10 represents a block diagram showing numerous examples, which were realized using this technology. Every example, (**a**) to (**u**), is presented as schematic cross sectional view, and a typical application is mentioned. As discussed above, the diversity of systems can be generated because of the compatibility of molding, coating, and lithographical patterning processes. Current technological parameters of our processes are summarized in Table 1.

Figure 10. Survey of realized micro-optical modules shown as schematic cross section.

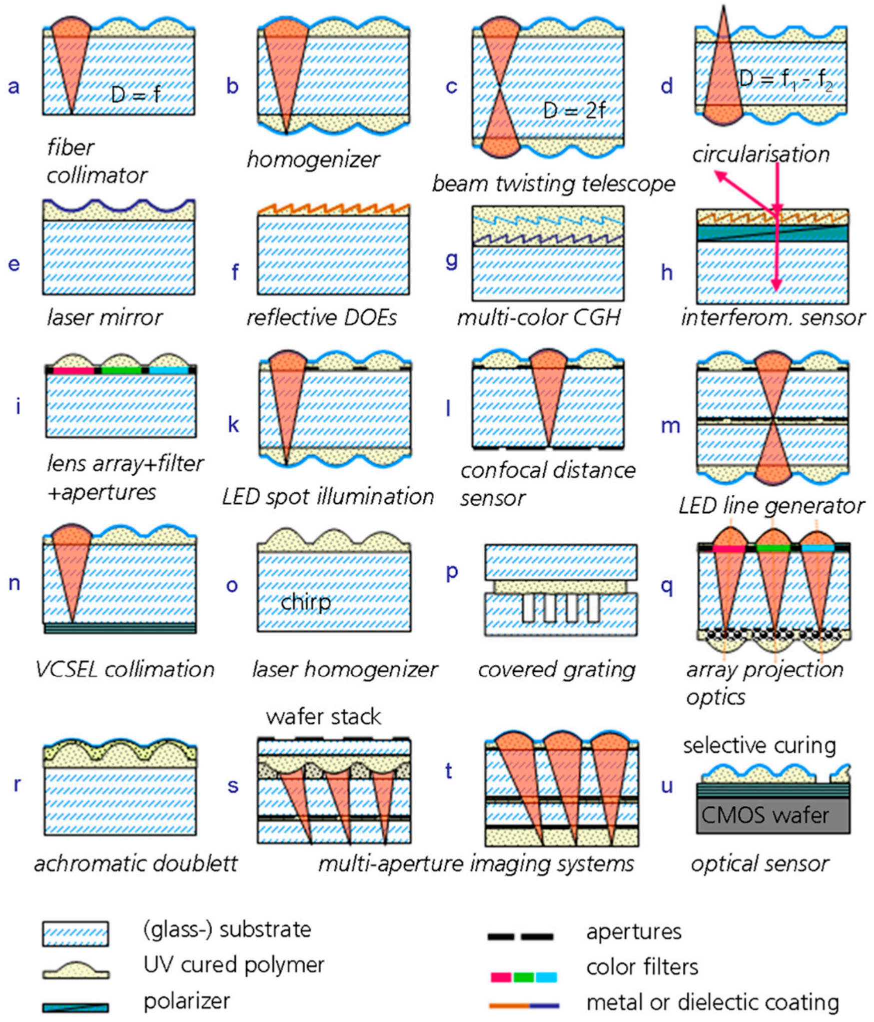

Mastering and patterning by means of lithography is especially useful when complex layout information has to be processed, as in the case of diffractive elements, (chirped or stochastic) microlenses, aperture or filter arrays and their repetition on the wafer, and additional structures like alignment and dicing marks, test and control structures, *etc*.

Microlenses mastered by photoresist reflow show diffraction limited performance in a wide parameter range (see Table 1). RIE assisted mastering can extend the design rules towards 100% fill factor of arrays, which was shown for the first time. We demonstrated the feasibility of aspheres and achromatic doublets and their benefits in multi-aperture imaging systems. However, reflow lenses show limited homogeneity of their focal length across the wafer (~1%, see also Figure 2), which causes problems beyond VGA imaging resolution. As a possible alternative, ultra precision machined lens masters with higher accuracy and uniformity, larger size and more complex profiles of the single lenslet can be introduced to the wafer-level concept [5], e.g., by generation of large-area UP machined lens arrays [30,31] or step and repeat replication of a single lenslet in the tooling process. Further extensions of the technology could be the implementation of mechanical actuators or OLED illumination.

Table 1. Summary of essential technology parameters and typical values realized.

Parameter	Value	Remark
lenslet master structure	spherical, elliptical, cylindrical	refined photoresist reflow technology
lateral size of lenslet	10 µm to several millimeters	
gap between lenslets	>1 µm	no gap with RIE assisted master
lens sag	<200 µm, virtually no minimum	diffraction limited: <100 µm
wafer size	Ø200 mm, 150 mm, 100 mm, die	200 mm × 200 mm also possible
wafer thickness	0.15 nm to 10 mm	Ø200 mm: $d > 0.4$ mm
glass thickness variation	<10 µm total (TTV)	*i.e.*, D263T or B33 (Schott)
mask-aligner	MA8e/ SUSS Microtec	closed loop piezo z axis control
top-/ bottom side alignm.	Yes	assisted alignment possible
lateral alignment/ posit.	±1 µm	maximum BSA distance 6 mm
axial alignment/ position	±5 µm to (±10 µm)	depending on substrates *etc.*
polymer material	UV curing acrylate or epoxy	*i.e.*, inorganic-organic hybrids [6]
temperature stability	>180 °C for ORMOCOMP [5]	270 °C for t <2 min
polymer index/Abbe#	1.45 to 1.65/60 to 25	commercial UV curing resin
thermo-optical coefficient	$-0.00024\ \mathrm{K}^{-1}$	ORMOCOMP® hybrid polymer
polymer thickness	typically 10 µm to 300	matching the sag limit of reflow lenslets
transmission range	400 nm to 1700 nm	-
black aperture resolution	CD ~10 µm (PSK2000, Brewer)	$T < 0.1\%$, $R < 5\%$ (300 nm to 700 nm)
dicing/ maximum size	thickness <6 mm, Ø < 300 mm	DISCO DAD3350

Acknowledgments

Part of this work has been funded by the German Federal Ministry of Education and Research (BMBF) within the projects ”Insect inspired imaging” and “Consumer Micro Camera”.

Furthermore, the authors like to express their gratitude to Sylke Kleinle and Antje Oelschlaeger who participated in the fabrication of the microoptics modules.

Author Contributions

Frank Wippermann and Andreas Brückner were mainly involved in design, technology concepts and optical characterization of multi-aperture imaging, Peter Schreiber for illumination systems. Peter Dannberg and André Matthes did element design, experiments, process development, and geometrical characterization. Andreas Bräuer conceived microoptical systems concepts, coordinated design and technology interactions and approved the final manuscript. All authors discussed the results and commented on the manuscript.

Conflicts of Interest

The authors declare no conflict of interest.

References

1. Zwiers, R.J.M.; Dortant, G.C.M. Aspherical lenses produced by a fast high-precision replication process using UV-curable coatings. *Appl. Opt.* **1985**, *24*, 4483–4488.
2. Dannberg, P.; Erdmann, L.; Bierbaum, R.; Krehl, A.; Bräuer, A.; Kley E.B. Micro-optical elements and their integration to glass and optoelectronic wafers. *Microsyst. Technol.* **1999**, *1*, 41–47.
3. Rossi, M.; Rudmann, H.; Marty, B.; Maciossek, A. Wafer-Scale Micro-Optics Replication Technology. In Proceedings of Optical Science and Technology, SPIE's 48th Annual Meeting International Society for Optics and Photonics, San Diego, CA, USA, 4 November 2003; pp. 148–154.
4. Jeong, H.S.; Kim, S.H.; Shin, D.I.; Lee, S.C.; Jin, Y.S.; Noh, J.E.; Oh, H.R.; Lee, K.U. Camera imaging lens fabrication using wafer-scale UV embossing process. *J. Opt. Soc. KR.* **2006**, *10*, 124–129.
5. Dagan, Y. Wafer-Level Optics Enables Low Cost Camera Phones. In Proceedings of SPIE, San Jose, CA, USA, 24 January 2009; Volume 7218, pp. 1–8.
6. Hybrid polymers commercially. Available on line: http://www.microresist.de/products/ormocers/overview_ormocers_en.htm (accessed on 26 March 2014).
7. Rose, K.; Wolter, H.; Glaubitt, W. Multifunctional Acrylate Alkoxysilanes for Polymeric Materials. In Proceedings of MRS, Pittsburgh, PA, USA, January 1992; Volume 271, pp. 731–734.
8. Schulz, U.; Schallenberg, U.B.; Kaiser, N. Antireflective coating design for plastic optics. *Appl. Opt.* **2003**, *42*, 1346.
9. Gentle, T.E.; Schmidt, R.G.; Naasz, B.M.; Gellman, A.J.; Gentle, T.M. Organofunctional silanes as adhesion promoters direct characterization of the polymer/silane interphase. *J. Adhes. Sci. Technol.* **1992**, *6*, 307–316.
10. Liston, E.M.; Martinu, L.; Wertheimer, M.R. Plasma Surface Modification of Polymers for Improved Adhesion: A Critical Review. In *Plasma Surface Modification of Polymers Relevance to Adhesion*; Strobel, M., Lyons, C., Mittal, K.L., Eds.; VSP BV: Utrecht, the Netherlands, 1994; pp. 3–39.
11. Kämpfe, T.; Kley, E.B.; Tünnermann, A.; Dannberg, P. Design and fabrication of stacked computer generated holograms for multicolour image generation. *Appl. Opt.* **2007**, *46*, 5482–5488.

12. Stollberg, K.; Brückner, A.; Duparré, J.; Dannberg, P.; Bräuer, A.; Tünnermann, A. The Gabor super lens as an alternative wafer-level camera approach inspired by superposition compound eyes of nocturnal insects. *Opt. Express* **2009**, *17*, 15747–15759.
13. Popovich, Z.D.; Sprague, R.A.; Conell, G.A.N. Technique for monolithic fabrication of microlens arrays. *Appl. Opt.* **1988**, *27*, 1281–1284.
14. Daly, D.; Stevens, R.F.; Hutley, M.C.; Davies, N. The manufacture of microlenses by melting photoresist. *J. Meas. Sci. Technol.* **1990**, *1*, 759–766.
15. Lim, C.H.; Jeung, W.K.; Choi, S.M. LED Packaging Using High Sag Rectangular Microlens Array. In Proceedings of SPIE 6185, Micro-Optics, VCSELs, and Photonic Interconnects II: Fabrication, Packaging and Integration, Strasbourg, France, 21 April 2006; Volume 618516, doi:10.1117/12.662358.
16. Zeitner, U.D.; Dannberg, P. Double-Sided Hybrid Microoptical Elements Combining Functions of Multistage Optical Systems. In Proceedings of SPIE 4440, Lithographic and Micromachining Techniques for Optical Component Fabrication, San Diego, CA, USA, 9 November 2011; Volume 44, doi:10.1117/12.448057.
17. Wippermann, F.; Zeitner, U.D.; Dannberg, P.; Bräuer, A.; Sinzinger, S. Beam homogenizers based on chirped microlens arrays. *Opt. Express* **2007**, *15*, 6218–6223.
18. Duparré, J.; Wippermann, F.; Dannberg, P.; Reimann, A.; Chirped arrays of refractive ellipsoidal microlenses for aberration correction under oblique incidence. *Opt. Express* **2009**, *13*, 10539–10551.
19. Schreiber, P.; Dannberg, P.; Hoefer, B.; Beckert, E. Chirped Microlens Arrays for Diode Laser Circularization and Beam Expansion. In Proceedings of *SPIE* 5876, Laser Beam Shaping VI, San Diego, CA, USA, 30 August 2005; Volume 58760K, doi:10.1117/12.616988.
20. Wippermann, F.; Radtke, D.; Zeitner, U.; Duparré, J.W.; Tünnermann, A.; Amberg, M.; Sinzinger, S.; Reinhardt, C.; Ovsianikov, A.; Chichkov, B.N. Fabrication Technologies for Chirped Refractive Microlens Arrays. In Proceedings of SPIE 6288, Current Developments in Lens Design and Optical Engineering VII, San Diego, CA, USA, 31 August 2006; Volume 62880O, doi:10.1117/12.680585.
21. Nussbaum, P.; Völkel, R.; Herzig, H.P.; Eisner, M.; Haselbeck, S. Design fabrication and testing of microlens arrays for sensors and microsystems. *Pure Appl. Opt.* **1997**, *6*, 617–636.
22. Voelkel, R.; Eisner, M.; Weible, K. Fabrication of Aspherical Microlenses in Fused Silica and Silicon. In Proceedings of SPIE 4440, Lithographic and Micromachining Techniques for Optical Component Fabrication, San Diego, CA, USA, 9 Novmber 2001; Volume 40, doi:10.1117/12.448056.
23. Harding, R.; Gardiner, I.; Yoon, H.J.; Perrett, T.; Parri, O.; Skjonnem, K. Reactive Liquid Crystal Materials for Optically Anisotropic Patterned Retarders. In Proceedings of SPIE Lithography Asia, Taipei, Taiwan, 4 December 2008; Volume 71402J, doi:10.1117/12.805378.
24. CODIXX standard polarizer products. Available online: http://www.codixx.de/cms/polarizers/polarizer.html (accessed on 26 March 2014).
25. Albero, J; Bargiel, S.; Passilly, N.; Dannberg, P.; Stumpf, M; Zeitner, U.D.; Rousselot, C.; Gastinger, K.; Goreck, C. Micromachined array-type mirauinterferometer for parallel inspection of MEMS. *J. Micromech. Microeng.* **2011**, *21*, 065005; doi:10.1088/0960-1317/21/6/065005.
26. Kim, S.M.; Kim, H.M.; Kang, S.; Development of an ultraviolet imprinting process for integrating a microlens array onto an image sensor. *Opt. Lett.* **2006**, *31*, 10–12.

27. Schreiber, P.; Dannberg, P.; Wippermann, F. Chirped Lens-Array LED Spot-Array Generator with Individually Colored Spots. In Proceedings of SPIE 7716, Micro-Optics 2010, Brussels, Belgium, 13 May 2010; Volume 771617, doi:10.1117/12.854415.
28. Duparré, J.; Wippermann, F. Micro-optical artificial compound eyes. *Bioinsp. Biomim.* **2006**, *1*, R1; doi:10.1088/1748-3182/1/1/R01.
29. Brückner, A.; Duparré, J.; Dannberg, P.; Leitel, R.; Bräuer, A. Driving Microoptical Imaging Systems Towards Miniature Camera Applications. In Proceedings of SPIE 7716, Micro-Optics 2010, Brussels, Belgium, 12 May 2010; Volume 77160J, doi:10.1117/12.853976.
30. Rømer Holme, N.C.; Geltzer Dinesen, P.; Attar, Z.; Oliver, S.D.; Voelkel, R. New technologies enable precise and cost effective waferlevel optics. *Laser Focus World* **2009**, *37*, 87–90.
31. Wafer-level optics tooling. Available online: http://www.kaleido-technology.com/Applications/Wafer-level%20optics%20tooling.pdf (accessed on 26 March 2014).

The Five Ws (and one H) of Super-Hydrophobic Surfaces in Medicine

Francesco Gentile, Maria Laura Coluccio, Tania Limongi, Gerardo Perozziello, Patrizio Candeloro and Enzo Di Fabrizio

Abstract: Super-hydrophobic surfaces (SHSs) are bio-inspired, artificial microfabricated interfaces, in which a pattern of cylindrical micropillars is modified to incorporate details at the nanoscale. For those systems, the integration of different scales translates into superior properties, including the ability of manipulating biological solutions. The five Ws, five Ws and one H or the six Ws (6W), are questions, whose answers are considered basic in information-gathering. They constitute a formula for getting the complete story on a subject. According to the principle of the six Ws, a report can only be considered complete if it answers these questions starting with an interrogative word: who, why, what, where, when, how. Each question should have a factual answer. In what follows, SHSs and some of the most promising applications thereof are reviewed following the scheme of the 6W. We will show how these surfaces can be integrated into bio-photonic devices for the identification and detection of a single molecule. We will describe how SHSs and nanoporous silicon matrices can be combined to yield devices with the capability of harvesting small molecules, where the cut-off size can be adequately controlled. We will describe how this concept is utilized for obtaining a direct TEM image of a DNA molecule.

Reprinted from *Micromachines*. Cite as: Gentile, F.; Coluccio, M.L.; Limongi, T.; Perozziello, G.; Candeloro, P.; di Fabrizio, E. The Five Ws (and one H) of Super-Hydrophobic Surfaces in Medicine. *Micromachines* **2014**, *5*, 239–262.

1. Introduction

Super-hydrophobic surfaces (SHSs) are bio-inspired, artificial microfabricated interfaces, in which a pattern of cylindrical micropillars is modified to incorporate details at the nanoscale [1–3]. For these systems, the integration of different scales translates into superior properties, including a vanishingly small friction coefficient, on account of which biological solutions of medical interest can be manipulated.

The five Ws, five Ws and one H or the six Ws (6W) are questions whose answers are considered basic in information-gathering. They are often mentioned in journalism, research and police investigations. The 6W task seeks to summarize the information essential to understanding a phenomenon by distilling it into the answers to the 6W questions: why, who, what, where and when; where the H stands, instead, for how [4]. In the above description, these five questions are presented in an order that seems logical to the authors; in practice, the approach becomes iterative: it does not matter much where you begin, since answering one question often reveals important aspects of the other questions that you had not yet considered.

In what follows, super-hydrophobic surfaces and some of the most promising applications thereof are reviewed following the scheme of the 6W. The Introduction is dedicated to a discursive articulation of these six theses. The experimental section presents and describes a family of different devices and the nanotechnology methods required for their fabrication. The modeling and theory paragraphs describe the physics of small drops on a surface, providing the mathematical tools for the rational design of those systems. In the Results, some of the most recent biological applications of SHSs are recapitulated, especially pertaining to the early detection of tumors.

Why: A large number of studies confirm that blood contains thousands of intact proteomic molecules coming from the tissues or as products of enzymatic proteolysis in the circulating flux. What has been until only recently considered as a "waste deposit" might reveal itself as an extraordinary mine of data for the evaluation of the health status of tissues or districts of the human body. Single, exclusive markers, or rather, biomarker patterns, integrated with each other, express a high sensitivity and specificity and may be employed to discriminate diseases [5,6]. The major drawback of this approach is the very low abundance of the proteins of study [5,6]. Very rarely, biologists deal with or are able to detect single molecules, and hence, their understanding of molecular events is blurred by a poor experimental resolution. This is the reason why there is an increasing demand for high quality biomolecular sensors. The ability to perform sensing measurements at femto- or atto-molar sample concentrations with single molecule resolution is an outstanding achievement in the field of biosensors. The past decade has seen tremendous progress in the development of micro- and nanoscale sensors with impressive performance. Detection limits down to the single-molecule level have been achieved, with potential applications ranging from the early diagnosis of disease to the fast sequencing of genomes. However, in practical applications, transporting target molecules and particles in extremely dilute solutions to these tiny sensors is a significant challenge that often involves impractical timescales [7]. The physics of diffusion governs the random movement of molecules in a solution and their binding kinetics to the sensor. At ultralow concentrations, it takes an unacceptably long amount of time for a molecule to diffuse to the sensor for detection, which may render the sensor impractical [7,8]. Scientists are now attempting to minimize the time taken for target molecules to bind to such sensors.

Who: Super-hydrophobic surfaces (SHSs) are bio-inspired, nanotechnology artifacts, which feature a reduced friction coefficient, whereby they can be used for a variety of practical applications [1,3,9]. SHSs are typically fabricated using micro- and nano-fabrication techniques, in which a two-dimensional lattice is created by the repetition, or tessellation, of a regular pattern or motif. In doing so, an artificial, periodic pattern is obtained, where the smallest unit of the pattern can be a silicon or polymeric cylindrical micropillar (Figure 1).

The most practical property of SHSs is a reduced friction coefficient that is responsible for a number of advantages over conventional surfaces, namely: (i) the geometry and positioning of liquid droplets can be easily controlled; (ii) micropatterns can be prefilled with aqueous solutions without the need for surfactants; (iii) droplets can be positioned extremely close to each other on a surface; (iv) super-hydrophobic regions can be used to create patterns to control bio-adhesion; and (v) the discontinuous dewetting effect arising from the extreme difference in contact angle hysteresis between the super-hydrophilic and super-hydrophobic regions can be used to passively dispense aqueous solution into the super-hydrophilic spots without wetting the super-hydrophobic background.

Figure 1. Cartoon representation of a super-hydrophobic surface (**a**); here, the pattern at the microscale recovers a hexagonal periodic lattice (**b**); each silicon micropillar is covered by features at the nanoscale that can be, for instance, an array of silver nanograins; the entire device is covered by a Teflon thin film, which assures hydrophobicity (**c**).

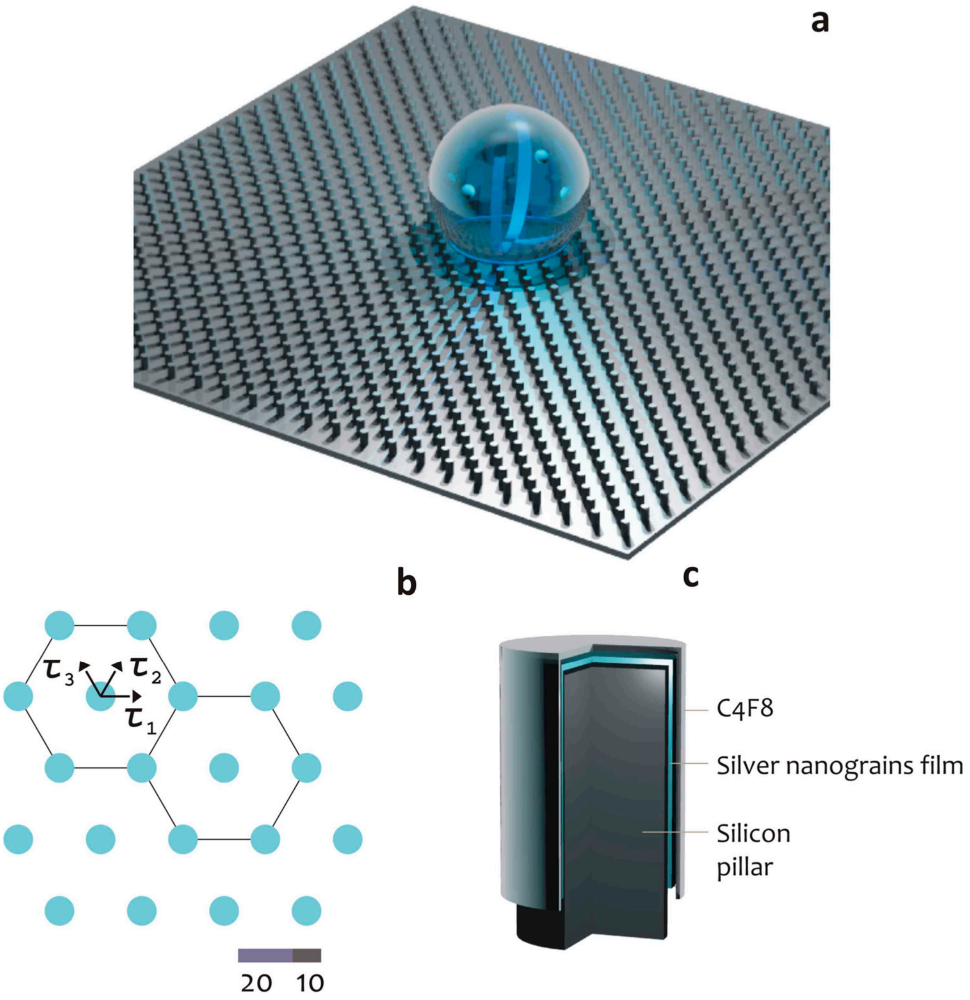

Those advantages, in turn, may be exploited for applications spanning specific areas of the physical, engineering and biological sciences, sometimes bridging traditional disciplines. These applications comprise, but are not restricted to: the pattering of complex geometries with liquids [10,11], the separation of oil from water [12], anti-biofouling coatings [13,14], controlling the adhesion of proteins or bacteria on a surface [15–18], guiding the aggregation of primary neurons into three-dimensional architectures [19], imaging DNA fibers and gaining exclusive information of the double helix [20] and advances in the very large area of cell microarray technology [21]. Perhaps more important than all this, SHSs can be utilized for efficiently delivering molecules in femto-/atto-molar solutions to a nanoscale plasmonic sensor [7,8,22–24], thus bypassing the diffusion limit. This technique involves the integration of plasmonic structures into super-hydrophobic surfaces.

What: Hydrophobic materials repel water; a well-known, natural example of a water repellent material is the lotus leaf: if deposited upon this, a water droplet would assume the form of a sphere without wetting or spreading on the surface [1,2]. Inspired by the lotus effect, we developed super-hydrophobic surfaces that mimic the morphology of the lotus leaf using techniques, such as nano-patterning, polymer coating, plasma etching and the electrochemical assembly of nanoparticles [22–24]. We created such a super-hydrophobic surface from arrays of silicon micropillars and optimized the size, periodicity and aspect ratio of those pillars to enable a large contact angle and low-friction forces that were independent of the sample droplet radius. Therefore, we allowed a water droplet containing the molecules of interest to evaporate and slide on the super-hydrophobic surface, leaving very little solution behind. As it evaporated, the solution became increasingly concentrated, until the droplet finally collapsed onto one of the pillars, thus confining the solute to a suspended region of a few square micrometers. In tests with rhodamine 6G molecules as a solute, we found that our silicon pillar surface provided a concentration factor 10,000 times that of a conventional, flat plasmonic substrate [22]. With λ-DNA molecules, we showed that DNA filaments cross-link to form a network that covers several pillars [22]. As a result, this simple "drop and dry" scheme provides the good localization and immobilization of molecules for fluorescent and Raman spectroscopic measurements. We developed this concept even further, as reported in the remainder of the paper. Some of these developments are reported in the Results section.

Where: Although Raman spectroscopy is a very useful tool for detecting and identifying the molecular constituents of a sample, the Raman signal is intrinsically very weak at the few-molecule level, which makes it difficult to extract from any background noise. Strong localization of the molecules during the drying process enhances the Raman spectroscopic signature. To boost the Raman signal further, we integrated a range of plasmonic structures into their super-hydrophobic silicon pillars. These metal structures, presented in Figure 2, and described in the Experimental Section, serve as "hot spots" that intensify the local electric fields and consequently enhance the Raman signal by several orders of magnitude. To put it in a nutshell, we combined these surfaces with bio-photonic devices to obtain an integrated lab-on-a-chip system, where, at the first stage, the SH surface would transport the analytes of interest into a small area, and at the second stage, the biosensors would permit, in that area, the detection of the solute with the resolution of a single molecule.

How: Small drops of de-ionized water, containing the moieties at study, should be positioned on the substrate and allowed to evaporate. In sight of a simple balance of forces, the line of contact at the solid interface would recede with time, and thus, the footprint of the drop would also gradually reduce. When the drop gets sufficiently small, a transition to a more stable state occurs, whereby the drop is firmly attached to the substrate, and the scale-down of the area of contact is prevented. This results in the accumulation of a few molecules into a very small region, an increased density and the attainment of the limits of detection.

When: The droplet evaporation time, which takes from a few seconds to several minutes, depending on its size, dramatically shortens the long waiting time of hours or even days for the traditional diffusion process. The transport of a trace inside a slowly evaporating drop on a substrate and the consequent particle deposition is a complex phenomenon that has generated interest for potentials in applications, such as molecular sieves [25], optoelectronic devices [26], drug delivery [27,28] and for the absorption and separation of the low molecular weight content of human plasma [29–31]. Despite its complexity, to the first approximation, this mechanism can be regarded (and analyzed) as the superposition of simpler effects. These effects are: (i) the displacement of particles inside an evaporating drop driven by convection and diffusion [32,33]; and (ii) the translocation or capture of a molecule through a nanopore [30,34–36].

Figure 2. SEM micrographs of the textures of silicon micropillars (**a**,**b**); the top of those pillars can be tailored with random patterns of silver nanoparticles (**c**,**d**) or regular arrays of metallic nanodots (**e**,**f**) for surface-enhanced Raman scattering (SERS).

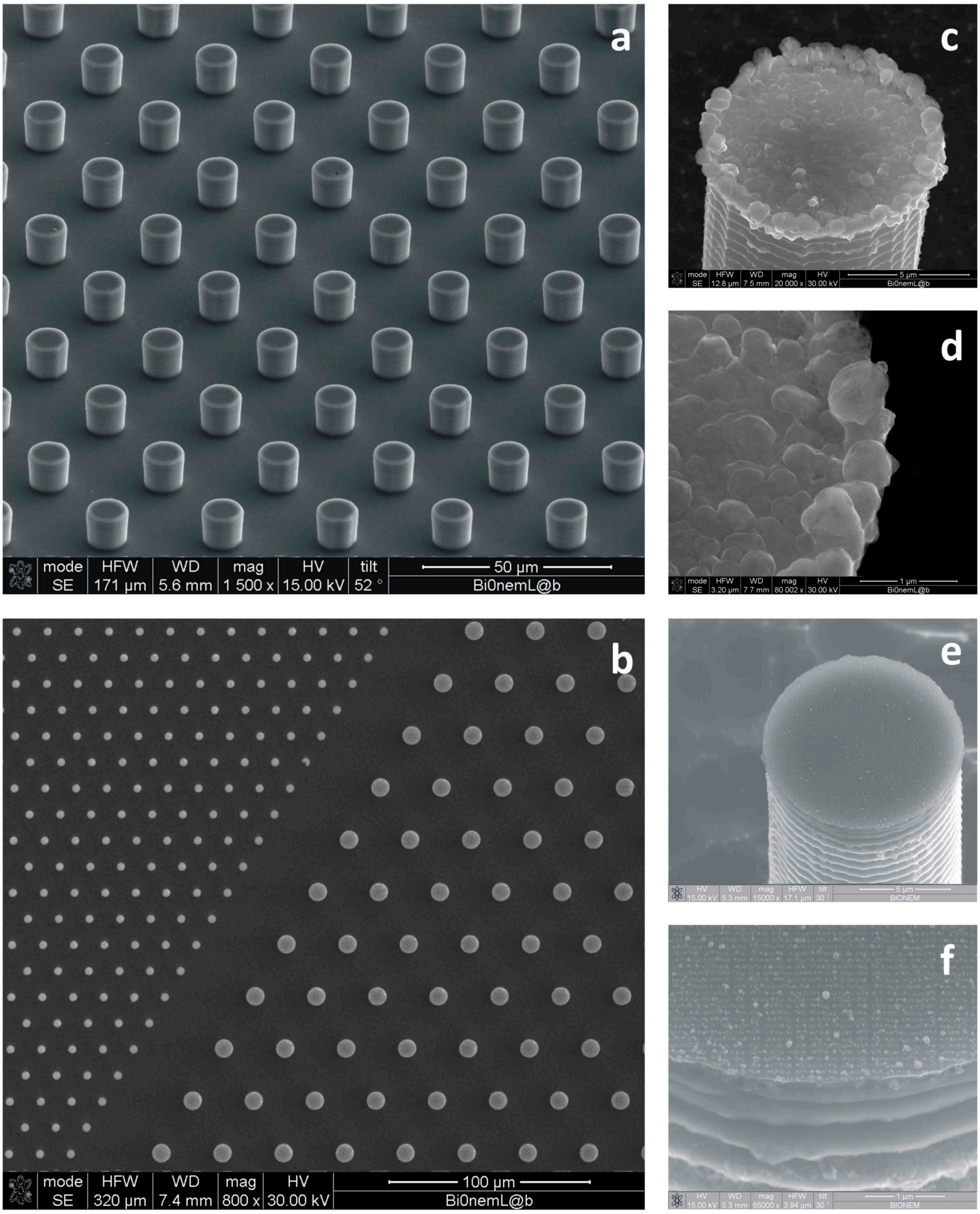

In brief, the aim of this paper is to expound the contributions that the integration of the super-hydrophobic theme with nano-geometry-based sensors (optical sensors) can possibly offer to clinical medicine, specifically in the discipline of early diagnostics. This is technically viable only if an array of silicon pillars is used like a workable platform, into which micro- or nano-lenses are implanted, and this is described in the rest of paper. That is why we shall mainly focus on artificial, ordered arrays of cylindrical micropillars, disregarding other, still mirable, approaches. This essay is dedicated to the articulation of this specific perspective. It is not a review of the many important contributions that have formed and made scientifically significant the field of super-hydrophobicity.

In the literature, one may find several examples of super-hydrophobic devices created out of plastic, cellulose or other natural (and in-expensive) materials; nevertheless, they are often limited to the still important issue of controlling and driving a droplet in a plane, and they do this either by: (i) changing the curvature/shape of patterns of ink on a flexible paper [37,38]; or (ii) fabricating surfaces with heterogeneous contact angle hysteresis [39]; and, this enables the splitting of the droplet on the surface. The described devices depart from ours in that they do not present any hierarchical nanostructure (nano-lenses) that may manipulate the electromagnetic field around them. The novelty of our approach is represented by the combined use of the super-hydrophobic scheme and nano-optics, which may resolve the issue of detecting biomolecules in an extremely low diluted solution; in this sense, the super-hydrophobic theme is only half of the story.

2. Experimental Section

A large variety of different super-hydrophobic devices is reported in the literature. Those surfaces typically comprise micropillars disposed on the substrate to form a regular hexagonal motif; in some cases, the periodicity of the pillars may be broken to introduce an increased degree of complexity into the geometry of the devices. The pillars are therefore modified to incorporate details at the nanoscale, ranging from bio-photonic devices to nanoporous silicon films. Those extra non-continuous scales would provide the device with additional, sometimes surprising, functions. Moreover, on account of their hierarchical structures bridging different length scales, those devices exhibit an increased hydrophobicity with contact angles as large as nearly 170°. Mathematical modeling and computer simulations can be conveniently used to describe the physics of small drops on a surface; those models, in turn, can be utilized to fabricate the devices on the basis of rational design.

Small drops of DI water containing infinitesimal amounts of analytes are gently positioned upon the surfaces, and the entire process of evaporation is followed over time. The process enables one to concentrate very tiny amounts of agents over micrometric areas. The evaporation process is performed in a clean room to reduce the presence of external contaminants and lasts approximately 30 min. The residual solute may be observed using scanning electron microscope (SEM), transmission electron microscopy (TEM), fluorescent microscopy and Raman spectroscopy techniques.

2.1. SHSs Tailored with Nanosensors

Artificial super-hydrophobic textures comprise a periodic hexagonal lattice of cylindrical silicon (Si) micropillars with a certain diameter and pitch. Nanosized geometries appropriately positioned on the pillars would assure giant surface-enhanced Raman scattering (SERS) enhancement [22,24]. (100) silicon wafers are cleaned with acetone and isopropanol to remove possible contaminants and then etched with a 4% wet hydrofluoric acid (HF) solution. The wafers are then rinsed with DI water and dried with N2. Standard optical lithography techniques are employed to dig out regular arrays of disks within a layer of positive resist that was precedently spin-coated onto clean silicon wafers. Electroless deposition techniques are employed to grow silver nanograins within the holes. Upon removal of the residual resist with acetone, a Bosch reactive ion etching process is utilized, whereby the final structures were obtained in the form of cylindrical pillars with an aspect ratio greater than 2. The electroless grown Ag layer served as a mask during the reactive ion etching (RIE) process, while its characteristic granular structure allowed for the enhancement of the SERS signal. The substrates, as a whole, are then covered with a thin (few nm) film of a Teflon-like (C_4F_8) polymer to assure hydrophobicity. The masks necessary for optical lithography are typically fabricated using standard electron beam lithography methods. Figure 2 reports some examples of the final devices. Electroless deposition is a technique whereby metal ions are reduced as atoms on specific patterned sites of a reducing surface, in our case, a silicon dangling bonding surface, to form nanoparticulates with the desired chemical and structural characteristics. The electroless deposition on a substrate is based on an autocatalytic or a chemical reduction of aqueous metal ions. This process consists of an electron exchange between metal ions and a reducing agent. In this work, Si substrate was used itself as a reducing agent. A fluoridric acid (HF) solution containing silver nitrate ($AgNO_3$) is used, where Ag was reduced to metal form by the Si substrate oxidation. In particular, the patterned silicon wafer is dipped in a 0.15 M HF solution containing 1 mM silver nitrate for 60 s at a constant temperature $T = 313$ K. After the growth process, the silicon wafer is rinsed with water and dried under nitrogen flux. The driving force in this process is the difference between redox potentials of the two half-reactions, which depends on solution temperature, concentration and pH. Consequently, these parameters influence the particles size and density. In the deposition process, the kinetics of chemical reaction is some two orders of magnitude faster than diffusion; therefore, a diffusion-limited aggregation model can be utilized to reproduce the results of the process [40].

2.2. SHSs Covered with Nanoporous Silicon Films

In some cases [41], the surface of the silicon pillars is treated to incorporate nanoporous silicon (NPSi) films (Figure 3). NPSi films are prepared upon the pillars through a process of Si anodic dissolution. While simple, untreated Si is intrinsically hydrophilic, and NPSi manifests an apparent contact angle as large as 130°; these micro-/nano-hierarchical structures reveal an increased contact angle approaching 170°, and this may be explained by a dual scale roughness, as reported in [42–45], and recapitulated in the Theory Section. The major advance of these devices is the simultaneous use of super-hydrophobicity and NPSi films. The nanoporous matrix furnishes to the device the capability of extracting the low molecular weight (LMW) content of a solution, that is a potential source of diagnostic markers for diseases [5,6]. PSi substrates with a pore diameter lower or equal to 10 nm are obtained by Si anodization using an electrolyte mixture of HF, DI water and ethanol (by Sigma-Aldrich, Milan, Italy) (1:1:2, *v*/*v*/*v*). A constant current density of 20 mA/cm^2 for 5 min at 25 °C is applied. The photoluminescence properties of the PSi substrate are verified using an ultraviolet lamp, in the long wave ultraviolet limit.

Figure 3. Nanoporous silicon devices (**a**); the silicon micropillars (**b**) reveal, at smaller scales, pores with an average pore size of 10 nm (**c**–**e**).

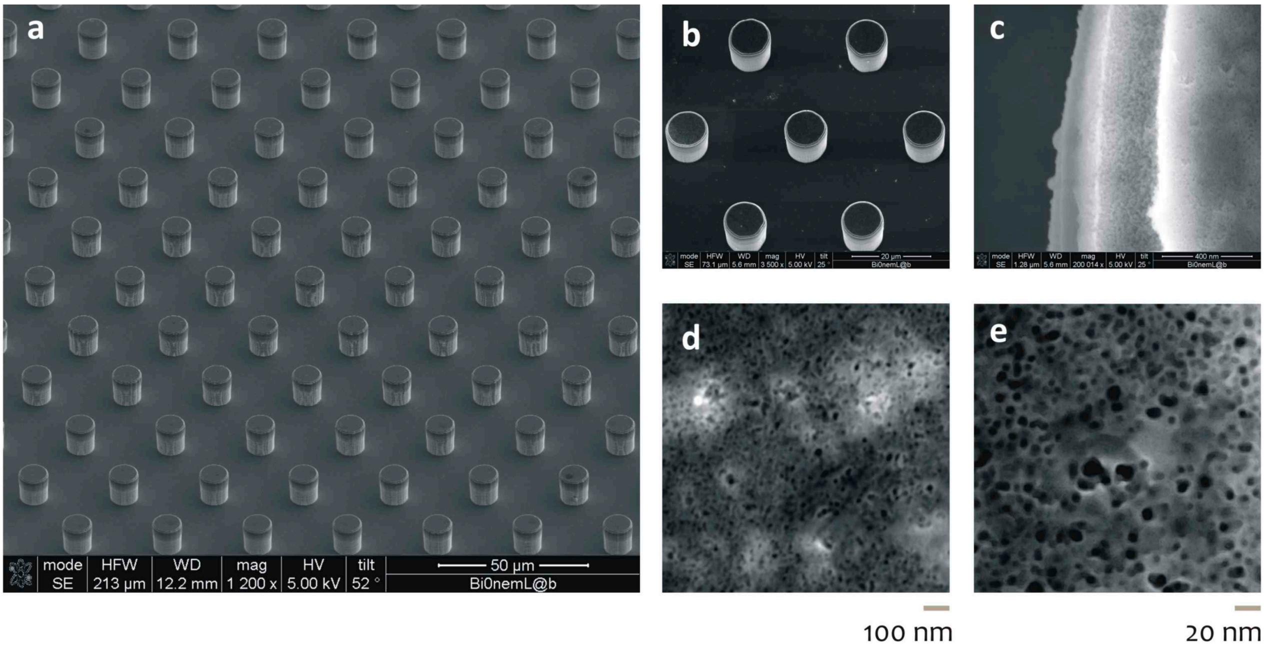

2.3. AG NPs/Nanoporous SH Hybrid Devices

The scheme reported in the former paragraph was developed even further in [46]. Silver nanoparticles were implanted into the super-hydrophobic NPSi film to guarantee superior SERS capabilities (Figure 4). In doing so, multifunctional devices are obtained, revealing different functions. Those functions only arise due to the heterogeneous scales of the system and, namely, the micro, on account of which the substrate is super-hydrophobic, and the nano, which is the typical length scale of the pores and of the silver particles dispersed into the pores. In sight of its hierarchical nature, the device may serve as a biosensor with the ability of: (i) concentrating diluted solutions; (ii) transporting and selecting the biomolecules of interest to the active areas of the device; and (iii) analyzing these molecules with extreme accuracy. Chains of silver nanograins are implanted into the porous matrix using an electroless deposition process, as described in Section 2.1. Silver nanograins are obtained with an average dimension strictly smaller than the pore size.

Figure 4. Micro-textures of nanoporous silicon pillars where electroless silver nanoparticles are infiltrated into the pores. In (**a**), at a smaller scale, you may observe the micro-pillar covered with the nano-porous silicon film. In (**b**–**e**), at larger scale, you can notice the morphology of the nano-porous matrix and of the silver nano-particles infiltrated into the pores.

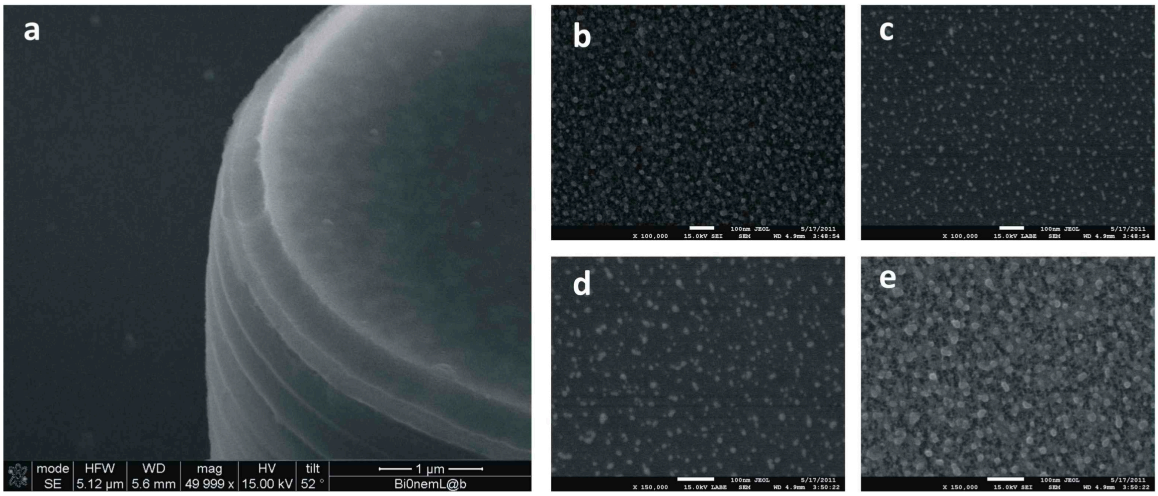

2.4. TEM Transparent SHSs

The super-hydrophobic concept was utilized in a recent article to obtain a direct image of a DNA molecule [20]. Transmission electron microscopy (TEM) is a technique that allows imaging with intrinsic spatial resolution at the atomic scale. When working with few biomolecules, there are some factors that worsen the final resolution of the obtained images: (i) the poor phase (or absorption) contrast of atomic species constituting the molecule compared to that of the substrate where the molecule is sitting; and (ii) the tendency of the molecule to be rapidly damaged when investigated by a high energy electron beam.

Silicon micropatterned hydrophobic devices allow one to control the deposition of few DNA molecules, which can be suspended, or stretched, between two adjacent pillars. In creating several passing through the holes between the pillars constituting the super-hydrophobic surface (Figure 5), the free passage of the electron beam during TEM measurements (background free imaging) is allowed; in doing so, we circumvent the conventional TEM resolution limitations described above.

Super-hydrophobic (SH) surfaces are designed and microfabricated. These comprise silicon micropillars arranged to form a regular hexagonal motif (A); the devices are therefore modified to incorporate, throughout the substrate, a pattern of holes, B, conveniently aligned with the pillars, which would permit the passage of the electron beam. The process of the fabrication of these devices is basically reduced to: (i) creating Pattern A; (ii) creating Pattern B; and (iii) positioning, as precisely as possible, Pattern A with respect to Pattern B. Pattern A is realized following the methods described in Section 2.1. Pattern B is realized using a deep reactive ion etching (DRIE) process; where the diameter of the holes (6 μm) is sufficiently large to allow practical use in TEM imaging. In the fabrication, conveniently positioned on the substrate, a number of alignment markers are used as a reference for the correct positioning of the holes with respect to the pillars.

Figure 5. Super-hydrophobic surfaces are designed and microfabricated. These comprise silicon micropillars arranged to form a regular hexagonal motif; the devices are therefore modified to incorporate, throughout the substrate, a pattern of holes, conveniently aligned with the pillars, which would permit the passage of the electrons beam. Figure **a**–**f** reports the device's geometry at different magnifications.

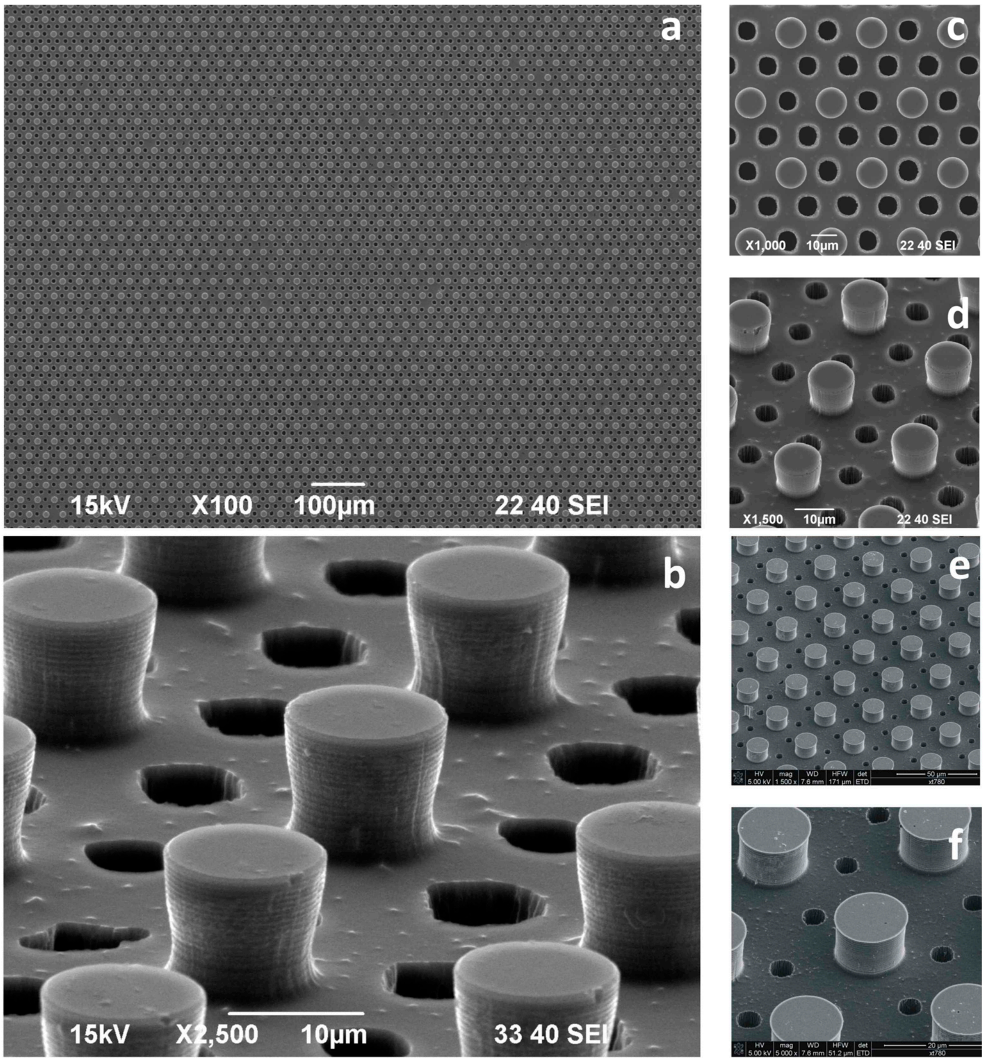

2.5. Non-Periodic SHSs

In all of the cited examples, the pattern of the pillars is periodic, that is, the substrate can be obtained as the repetition of a primitive cell, where the cell is the basis for the lattice. The disadvantage of regular arrays of pillars is that the analytes, upon evaporation, would randomly target the substrate, with a lack of precision in positioning the species of interest on specific points of the surface. This limitation can be circumvented on introducing gradients of wettability in the pattern [47]. This is practically done realizing a non-periodic array of micropillars, that is, a distribution, where the pitch, δ, between the pillars is not constant, and it would instead smoothly transition from an external region, where δ is large, to an inner region, where δ is small (Figure 6). By doing so, the hydrophobicity would not be constant over the substrate; rather, some regions would be more hydrophilic than others; on account of this augmented hydrophilicity, a solute, upon evaporation, would preferentially target these hydrophilic regions, which would therefore be the active sites of the devices, and in these sites solely, superior nanosensors can be embedded. The fabrication of these surfaces is the same as that required for regular geometries, as in Section 2.1, except for the fact that the optical masks necessary for the lithographies are generated on the basis of a mathematical model described in [47]. The non-uniform profile of pillars can be obtained using a contraction, which is a mathematical operation that, on a metric space and with respect to a fixed point, would displace the pillars in a fashion that their mutual distance would vary following a certain law. The surface energy of the substrate can be therefore determined and, on deriving that with respect to space, the non-uniform field of forces exerted on the drop during evaporation. This has some similarity with the general theory of relativity, where mass warps space-time to create gravitational fields. Examples of super-hydrophobic devices with a variable pitch are shown in Figure 6.

Figure 6. In the figure are presented devices where gradients of wettability are artificially introduced into the pattern of pillars. This is practically done realizing a non-periodic array of micropillars, that is, a distribution where the pitch, δ, between the pillars is not constant, and it would instead smoothly transition from an external region, where δ is large, to an inner region, where δ is small. Figure **a**–**c** shows a non-uniform pattern of pillars with different magnifications and points of view.

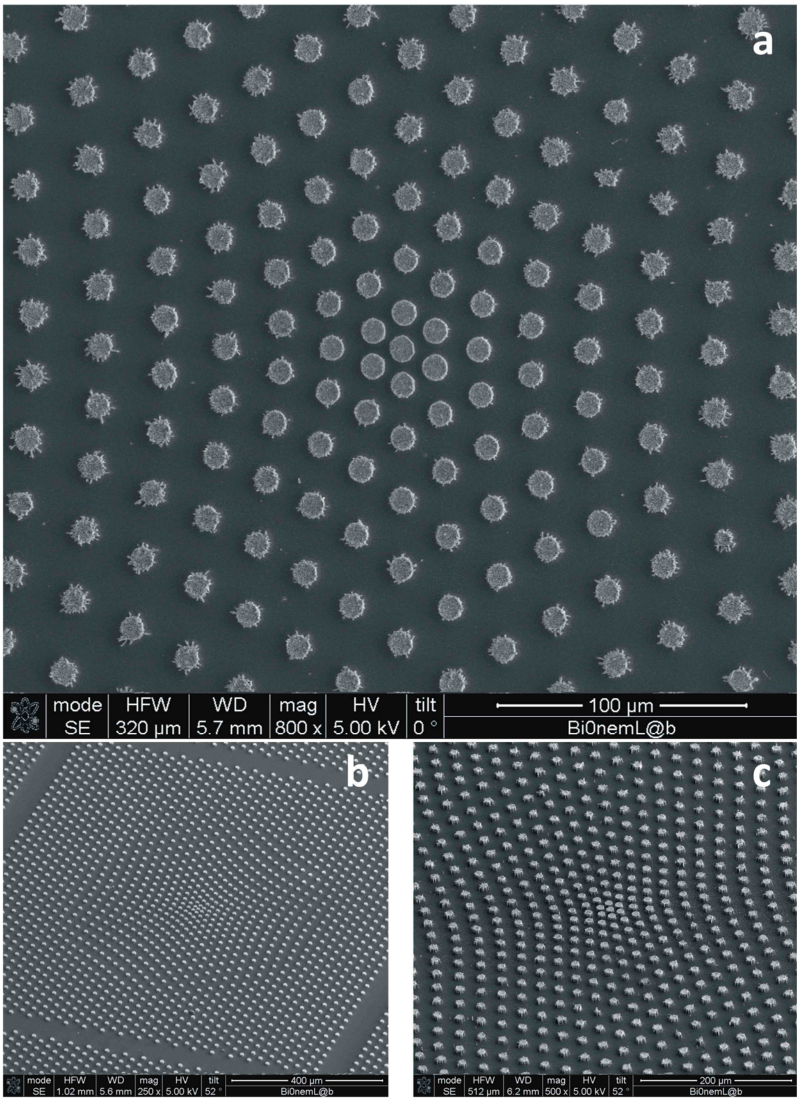

2.6. Rational Design of SHSs

It is well known that the physics of micrometric or sub-millimetric drops is correctly governed by surface tension solely [48]. The angle of contact, θ, at the solid/air/liquid interface indicates the propensity of a droplet of whether wetting or not a surface. Surfaces where $\theta > 150°$ are super-hydrophobic. A drop of water, positioned on such surfaces, would maintain a quasi-spherical shape, with a contact angle at the air-solid interface that can be theoretically predicted with excellent accuracy. In the celebrated model of Cassie and Baxter, the wetting behavior of the surface is lumped in the sole parameter, ϕ, that is, the ratio of the solid to the total projected area [49]:

$$\cos\theta_c = -1 + \phi(\cos\theta + 1) \tag{1}$$

at the limit of ϕ going to zero, $\phi \rightarrow 0$, $\theta_c \rightarrow 180°$, and the droplet would resemble a perfect sphere. For a periodic hexagonal lattice of cylindrical pillars, where the diameter, d, of the pillars and the distance, δ, between those pillars may be arbitrarily imposed, the fraction, ϕ, can be derived as $\phi = \pi d^2/(d + \delta)^2$. If ϕ is small, and thus θ_c is large, the contact line would jump inward from a thread of pillars to another, while the drop evaporates. Therefore, in the first approximation, one would produce structures where the distance between the pillars is large and ϕ is small. Unfortunately, the collateral effect of small ϕ is that a drop would collapse at the early stage of evaporation. Equation (2), below, reveals the minimum radius of a drop before impalement, whereby an irreversible transition to a pinned state occurs. In this situation, no further contact area shrinkage is possible:

$$r_{\min} = \frac{\delta}{\cos\theta} \tag{2}$$

In what follows, a criterion is discussed that would guarantee the best trade-off between sufficiently dense forests of pillars, which prevent the early collapse of the drop and avoid dispersion, and diluted structures, which instead assure a large contact angle. Let the surface be patterned as to reproduce a regular lattice described by d and δ, where the significance of these symbols is given above. If d is fixed, then the system would be determined given the sole δ. The aim here is to determine the optimal δ that would induce large θ, while still retaining the advantages of a small $r_{\min}$. To do this, we introduce the function, Ψ, which is the superposition of the two non-dimensional contributions $\Psi = \Psi_1 + \Psi_2$.

Ψ_1 accounts for the effects of the microstructure on the contact line, $\Psi_1 = r/R$, where R is the initial radius of the drop.

Ψ_2 accounts for the effects of the microstructure upon the smallest radius of contact before collapse:

$$\Psi_2 = \frac{r_{\min}}{d} = \frac{1}{\cos\theta}\frac{1-\phi^{1/2}}{\phi^{1/2}} \tag{3}$$

Ψ is not monotonic with respect to δ. A value of δ can be determined where Ψ attains a minimum (Figure 7), and this would the best gap for a fixed d. Figure 7 shows, in the plane d-δ, the area of optimal design according to this criterion.

Figure 7. The diagram shows the region of optimal design, that is, the subset of pattern configurations, in terms of d and δ, which guarantee large contact angles, still retaining the advantages of a small radius of collapse (**a**). This working distance is obtained on minimizing the function, Ψ, as explained in the modeling section (**b,c**).

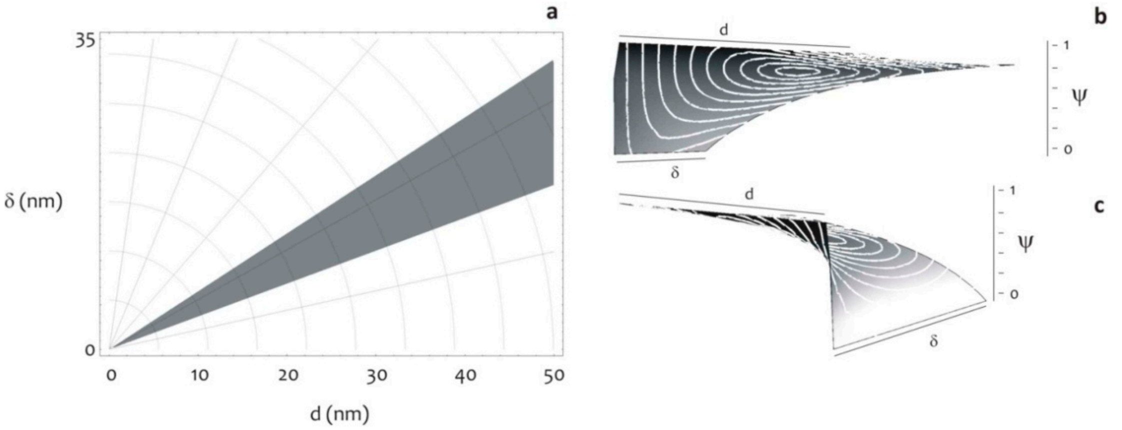

2.7. Non-Continuum Description of Hierarchical Hydrophobicity

In Section 2.3, we presented devices where the increased hydrophobicity depends on thin nanoporous films. Porous silicon, or nanoporous silicon (NPSi), is a form of Si containing a layer of nanosized pores artificially introduced in its microstructure, thus revealing an increased surface-to-volume ratio. NPSi exhibits certain promising properties, including highly controllable and reproducible pore size and distribution; bio-reactivity; biocompatibility; biodegradability in physiological environment; photo luminescence at room temperature and hydrophobicity [50]. Nevertheless, some NPSi-related phenomena are still not well understood or, at best, their explanation is controversial. This would be the case of the increased hydrophobicity of NPSi films, whereby the observed contact angle of a drop of water settles down to extremely high values, well beyond those predicted by Cassie–Baxter's classical theories. Considering that those nanoporous surfaces have, on average, a porosity of about $p = 0.4$, expressed as the fraction of the volume of voids over the total volume, and that the porosity can be, in turn, rephrased in terms of ϕ as $\phi = 1 - p$, it follows that for those NPSi films, $\phi = 0.6$. Upon using this value in the classical Cassie and Baxter formula Equation (1), a contact angle as large as 95° is predicted, considerably smaller than that revealed by direct experiments, where θ instead approaches 140°. In [42], a new theory has been presented that explains this discrepancy. This theory explores the wettability mechanisms on a randomly patterned surface at a non-continuum level.

Fractals are mathematical objects that are too irregular to be described by conventional geometry. They all retain, to different extents, certain properties that may be reviewed as follows: (i) they reveal details on arbitrarily small scales (fine structure); (ii) they can be generated (and thus described) by short algorithms (perhaps recursively); (iii) they exhibit a fractal dimension, Df, strictly greater than the classical topological dimension. The latter property reserves particular attention, in that it claims that a surface, under a fractal point of view, may have a dimension, Df, even greater than 2, and the more Df is close to 3, the more the fractal set fills the space it is embedded in. On account of this, an NPSi surface, to an extent, depending upon its fractal dimension, would be hierarchical: thus revealing, on different scales, the same self-affine structure. We shall denote, here, with n, the scale factor (that is, the level of detail describing the set at study). Accordingly, the classical Cassie and Baxter expression for the contact angle, θ, may be rephrased in terms of a recursive function in, n [42]:

$$\cos\theta_{n+1} = -1 + \phi(\cos\theta_n + 1) \tag{4}$$

Notice that, for $n = 1$, Equation (4) recapitulates the classical Cassie and Baxter equation. While, the larger n, the more the substrate is hydrophobic. The issue, here, is identifying the correct n. To do this, the surface area magnification factor, σ (that, to a certain measure, is connected to the length of the profile under examination), is deduced according to two different procedures, and from the comparison of these, n would be determined. In the first approach, σ is expressed in terms of the fractals parameters Λ, λ and Df [42]:

$$\sigma = \left(\frac{\Lambda}{\lambda}\right)^{Df-2} \tag{5}$$

where Λ and λ are the upper and lower limits of the fractal behavior and Df has the meaning explained above. Notice that the parameters in Equation (2) may be deduced experimentally from the Power Spectrum PS, and thus, given an AFM profile, σ would be determined. In the second approach, the definition of σ is used:

$$\sigma = \frac{\Gamma}{\gamma} \tag{6}$$

In Equation (6), γ is a length of base (that is, the length of the profile in the continuous limit $n = 1$), while Γ is the fractal, actual length of the profile. On expanding Equation (6), one would obtain:

$$\sigma(n) = \frac{1}{\gamma}\begin{cases} \Gamma = \int_0^{\gamma}\left(1+\left(\dfrac{\partial y}{\partial x}\right)^2\right)^{\frac{1}{2}} & (n=1) \\ \Gamma = \int_0^{\gamma}\left(1+\left(\dfrac{\partial(y/n^{2-Df})}{\partial(x/n)}\right)^2\right)^{1/2} & (n>1) \end{cases} \tag{7}$$

Additionally, on comparing Equations (5) and (7), one would obtain the right n to use in Equation (4).

3. Results

3.1. SEM Verification of the Samples

The devices presented heretofore were verified against the deposition, concentration and detection of a few molecules of Rhodamine 6G (R6G). R6G was used for the evaluation of the devices in that its utilization in biotechnology applications is very well assessed; it is a supplement to fluoresceins, as it offers longer wavelength emission maxima; and it is conveniently and extensively used for standard and non-standard labelling essays. Solutions were prepared containing R6G molecules with a concentration as low as 10^{-18} M. Evaporation processes of small drops of solution were followed over time until an irreversible transition to a pinning state occurred. Few molecules were conveniently forced to confine into a small area, at the limit, upon a single pillar. Figure 8 shows an array of SEM images of the residual solute of R6G at different magnifications ranging from 150× to 2500×. The initial footprint of the drop measures up to about 1.6 mm, and on average, 1.2 mm, while the solution, at the final stage of the process, sediments in a bounded region sized a few tens of microns or less (Figure 8b–d) and, in some cases, upon one single pillar (Figure 8e). Considering bi-dimensional scale effects solely, the device is capable of concentrating a solution some $(1200/40)^2{\sim}10^3$ times. More importantly, all the deposits are suspended upon the pillars, the residual R6G is arranged in complex forms or agglomerates that wrap the pillars, connecting them one to the other, without touching the bottom of the substrate.

Figure 8. SEM micrographs showing the concentration ability of super-hydrophobic surfaces (SHSs). At the end of an evaporation process, a few molecules of solute are forced into a micrometric area; in this case, Rhodamine 6G, as it is used as a solute. From **a**–**f**, you can notice the residual solute upon evaporation, suspended upon few pillars. In some cases, as in **f**, the residue links adjacent pillars.

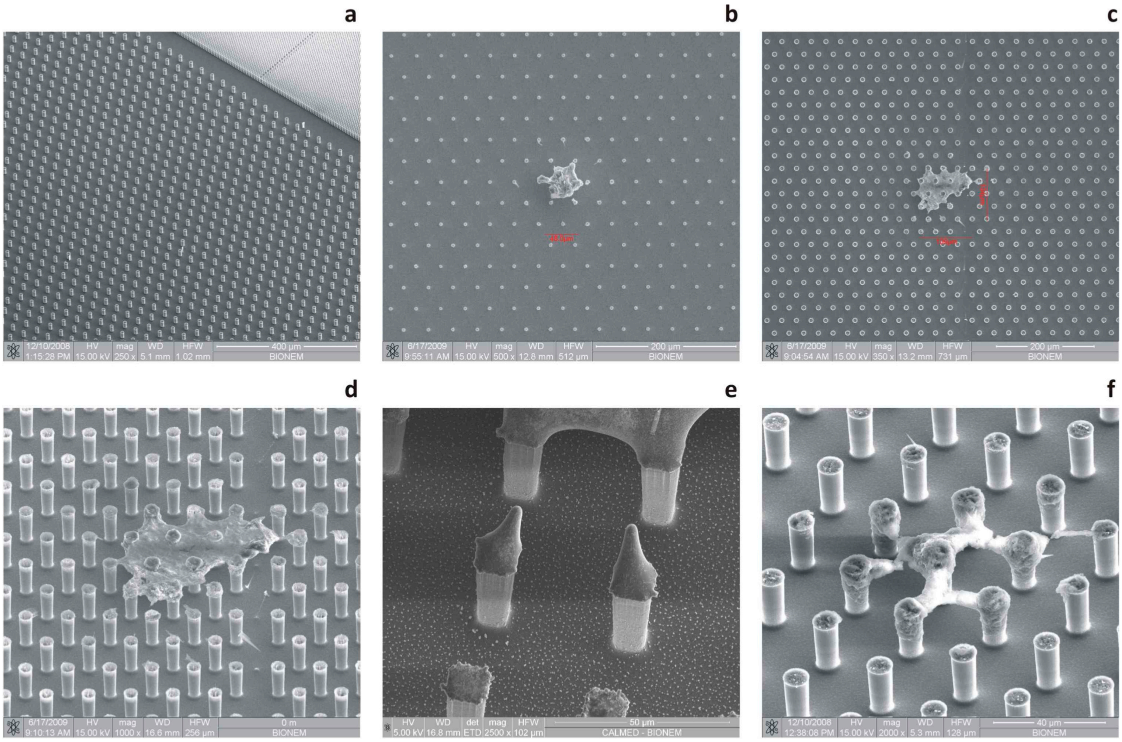

3.2. Confocal and SERS Measurements of the Samples

The evaporation sequence of a drop upon a super-hydrophobic surface is reported in (Figure 9a–c), where the volume of the solvent steadily diminishes with the time parameter, *t*, varying from *t* = 0 min, in Figure 9a, to *t* = 30 min, in Figure 9c. This scheme allows one to concentrate a few molecules in a restricted area, as reported in the SEM images above. Fluorescent images in (Figure 9d–f) would prove that the identification of a residue, such as R6G, is correct, and it is not instead constituted by debris or other refuse. The intensity of fluorescence is directly proportional to the quantity of substance deposited on the pillars, and thus, in the central part of the substrate, the amount of R6G is higher and diminishes as we move towards the sides. Notice the high degree of precision with which the intensity of the signal of fluorescence recovers the mass of the solute distributed upon the substrate. Micro-Raman mapping measurements (Figure 9g–i) were performed to further substantiate the method. The mapping analysis was performed by referencing the band centered at 1650 cm^{-1}. In the figures, mapping images in surface mode are overlapped onto the scanning area, and this clearly highlights the variation of intensity as a function of the position within the area of interest. Figure 9g–i shows measurements for an initial concentration of 10^{-18} M, and in the present case, the Raman signal comes prevalently from the central region of the deposit, as expected.

Figure 9. Droplet evaporation scheme showing the volume evolution of a drop on a super-hydrophobic surface over time (**a**–**d**). Fluorescent images (**d**–**f**) prove that identification of the residue as R6G is correct, and it is not instead constituted by debris or other refuse. The intensity of fluorescence is directly proportional to the quantity of substance deposited on the pillars, and thus, in the central part of the substrate, the amount of Rhodamine 6G (R6G) is higher and diminishes as we move towards the sides. Raman SERS measurements of the samples (**g**–**i**).

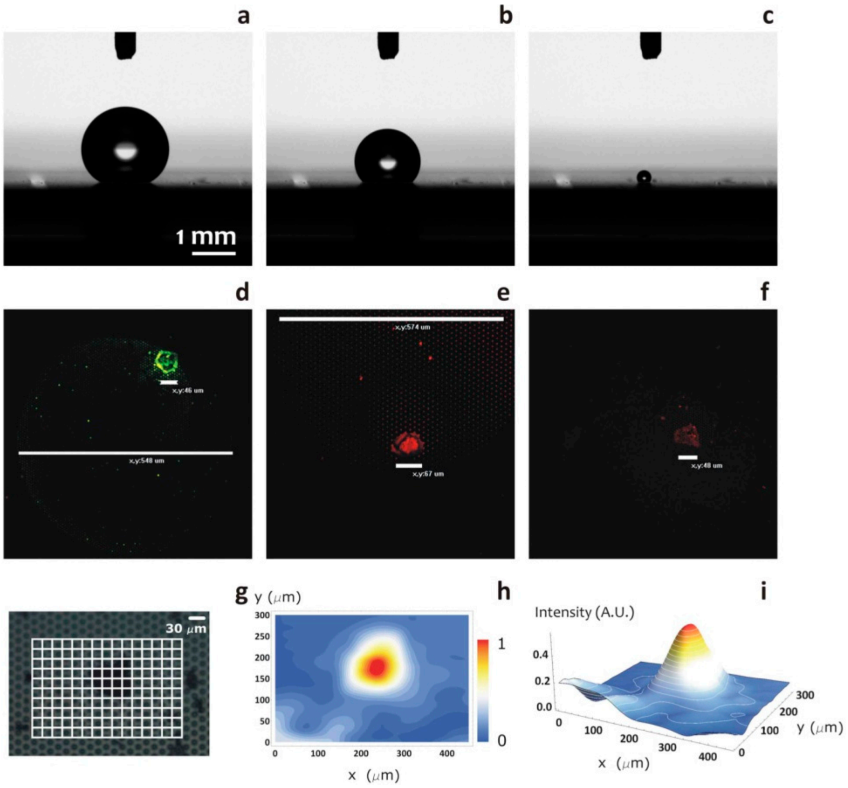

3.3. TEM Measurements of DNA fibers

Here, we show the potentials of SHSs in imaging single filaments of DNA using transmission electron microscopy (TEM) techniques. These results have been presented in [20]. The preparation in view of the TEM imaging was obtained by allowing the water to evaporate from the original liquid sample. The super-hydrophobic surface was treated in a way that the adhesion force between it and the water was very low (a friction coefficient of about 0.02), and during the evaporation, pinning of the drop was avoided. As a result, DNA molecules could be deposited, suspended and well tensed between the pillars, and more importantly, several DNA bundles resulted in being suspended in correspondence with the holes Figure 10. The suspended DNA bundles have a well-reproducible diameter, between eight and 200 nm. In Figure 10e, DNA bundles with strong mechanical stability under an electron beam up to 100-keV accelerating energy and beam current in the pA range are shown. This method was used in [20] to image in detail the 10 periods of DNA, where the period measures 2.7 ± 0.2 nm, corresponding to that known for ds λ-DNA in the A conformation.

Figure 10. Super hydrophobic surfaces (**a**,**b**) with very low adhesion forces allow one to avoid the pinning of the drop during evaporation. As a result, DNA molecules are deposited, suspended and well tensed between the pillars (**a**), and more importantly, several DNA bundles resulted in being suspended in correspondence with the holes (**c**–**e**).

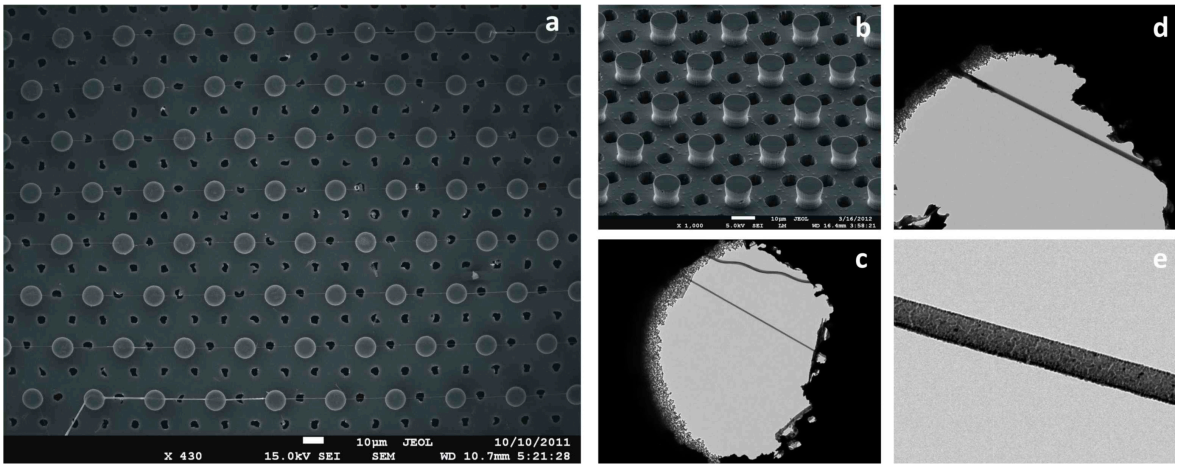

4. Discussion

Surface plasmons are waves that propagate along the surface of a conductor. By altering the structure of a metal's surface, the properties of surface plasmons—in particular, their interaction with light—can be tailored, which offers the potential for developing new types of photonic devices. This could lead to miniaturized photonic circuits with length scales that are much smaller than those currently achieved [51]. Surface plasmons and the properties thereof may be directly correlated to Raman scattering. This effect is named after C.V. Raman, who experimentally discovered it in 1928 [52]. When light interacts with matter, it may scatter inelastically from vibrational quantum states. During that process, photons may lose energy to, or gain it from, vibrational excitations. A change in the photon energy must produce a concomitant shift in the frequency of the scattered light. While the Raman effect alone is relatively modest, and thus, it offers an effective, but limited instrument to investigate matter and the properties thereof, it may be artificially incremented by several orders of magnitude (to obtain a substrate-enhanced Raman scattering (SERS) effect) basically in two ways.

An increased Raman signal appears due to a magnification of both incident and Raman-scattered fields, an effect known as electromagnetic enhancement. Moreover, the electronic interaction between molecule and metal can modify the scattering process itself and produce an effectively larger cross-section than would occur by scattering light from the molecule alone, an effect known as electronic or chemical SERS. The total enhancement is a product of the two mechanisms. Here, we shall discuss the metal-radiation interaction mechanism solely.

In the close proximity of metal nanoclusters, field enhancement occurs because of the resonant interaction between the optical fields and surface plasmons in the metal [51–53]. In essence, the light from a laser beam excites the surface plasmons, which are collective oscillations of conduction electrons. Those plasmons then radiate a dipolar field. The coherent interaction of the incoming electric field with the dipolar field leads to a redistribution of electric-field intensities in areas around the metal clusters. A molecule nearby or adsorbed on the metal feels an enhanced excitation intensity. Therefore, its Raman-scattered field is enhanced in the same way that the incident laser field is. Indeed, one can liken the metallic clusters to tiny antennas that enhance and transmit the Raman-scattered light. The enhancement depends on the type of metal, its degree of roughness—the sizes and shapes of the clusters that form—and the frequency of the incident light [54–56]. In this scenario, the precise and tight control of the morphology of metallic structures at the nanoscale is a major requisite for the design of efficient SERS substrates.

The new revolution in nanoscience, engineering and technology is being driven by our ability to manipulate matter at the molecular, nanoparticle and colloidal level to create designer structures. The discovery and understanding of the fundamental principles of how nanoscale systems of building blocks assemble enables us to nano-engineer new materials, where their physical properties depend intimately on their structure [57]. The organization of individual building blocks into ordered structures is ubiquitous in nature and found at all length scales. Examples include simple and complex crystals in atomic systems, liquid and plastic crystals in molecular materials and super-lattices of nanoparticles and colloids. The formation of atomic materials structures can be rationalized, to the first approximation, from geometric considerations and from a delicate balance of entropy, diffusion, chemical and atomic forces [58–60]. Mechanisms that cause nanoparticles to assemble into near-ordered structures are desirable for the correct control of those forces and for the precise organization of these particles into inorganic super-clusters.

Those super-clusters, in turn, may be the constituents (the fundamental building blocks) of efficient SERS substrates, for which one should control as accurately as possible: (i) the size of the features, which should have a characteristic length scale comparable with $\lambda/10$ (λ is the electromagnetic wavelength); and (ii) the distance between the elementary nanostructures that, differently from size, should have a characteristic length scale comparable with $\lambda/100$. These two length scales are the reason why nanoplasmonics and nanofabrication are tightly connected [55].

While randomly rough surfaces still induce a sensible enhancement in the signal of the electric (E) field [23,61], regular geometries are the best building blocks for advanced optical devices, where a good theoretical control can be achieved for a desired optical response. For certain architectures, this response can be extremely strong, with $|E|^2$ enhancement up to six orders of magnitude [54,56,62–67]. Recalling that the Raman signal in SERS substrates scales with the fourth power of the electric field, similar geometries would guarantee a Raman increment of the order of 10^{12}, which is a giant enhancement of the spectroscopy signal, which would be sufficient to reveal, in theory, the signature of a single molecule. With unprecedented applications in fields spanning the physical and biological sciences, including the early detection of cancers or other pathologies, whose evolution in time is related to the release in blood of biomarkers in extremely low abundance ranges.

The fabrication of similar geometries is result that has been achieved. In Figures 2, 4 and 6 and the captions thereof, we report nano-lenses on a pillar surface, where those lenses are either disordered random ensembles of silver nanoparticles in a plane (Figure 2c,d, Figure 6), or ordered arrays of nanoparticles (Figure 2e,f) or networks of metal grains infiltrated in a matrix of nanoporous silicon. In all of the described cases, the size and spacing of the structures is controlled at the nanometer level. Similar nano-geometries were realized using electroless deposition methods, ultra-high resolution Electron Beam Lithography EBL pattering methods or a combination of these, as described in the Experimental Section and, in detail, elsewhere [55,68–72].

Nevertheless, the presented nanomaterials, while they are advanced in the terms of the overall architecture and potential use as nano-lenses, may be ineffective if utilized directly as biosensors, in that the transport of the target species towards the cited sensors, driven by diffusion, would take impractical (unacceptably long) time scales, and this has been scrupulously discussed in the Introduction. Thus, the efficiency of similar sensors is hampered by diffusion.

Recently, a breakthrough strategy has been proposed that delivers the promise to surpass the described limitation, where the adjective, breakthrough, is justified by the fact that a similar strategy relies on a mechanism that is completely different from either plasmonic resonance or diffusion.

Instead, it is based on non-wettable, super-hydrophobic materials.

In this paper, using the original scheme of the five Ws, we reviewed and commented on a new family of devices in which diverse sensitive nanomaterials (that are, silver nanoparticles, nanoporous silicon, ordered arrays of micropillars) and the properties thereof (nanoplasmonics and SERS effects, super-hydrophobicity, nano-filter capabilities) are combined to beat diffusion [22] and use the described nano-lenses more efficiently.

5. Conclusions

Non-invasive analysis in biological fluids is gaining increasing interest in the diagnosis and experimental assessment of diseases. As an example, it is very well understood that malignancies can be identified based on their molecular expression profiles. Exclusive markers extracted from serum, other biological fluids or any sample obtained through minimally invasive techniques can be realistically employed to discriminate cancers or other pathologies. The possibility to realize innovative sensing devices to measure specific analytes without any pain for the patient is a novel frontier in health control. Super-hydrophobic surfaces are biomimetic, microstructured solids with a texture given by a regular hexagonal lattice of micropillars. They deliver great potentials in biotechnology, because they reveal superior properties compared to conventional flat surfaces, including extremely low friction coefficients. On account of this, a millimetric drop would maintain a spherical shape if positioned upon those surfaces. Most importantly, during evaporation, the molecules contained in the drop can be concentrated, localized or transported into specific points of the substrate. These properties may be used for a variety of applications of medical interest. In this work, using the scheme of the 6W, the most promising applications of SHSs are reviewed. On integrating similar substrates with nano-geometrical SERS devices, molecules have been detected in very low abundance ranges, with femto- to zepto-molar sensitivity; DNA fibers have been imaged, thus gaining exclusive information about the double helix; and a few, small Rhodamine molecules have been separated from large albumin proteins using nanoporous silicon as a molecular sieve.

Acknowledgments

This work has been partially funded from the EU Commission, the European Social Fund and the Calabria Region (POR Calabria FSE 2007–2013), from the Italian Minister of Health ("Cancer biomarker detection using microstructured/super-hydrophobic surfaces and advanced spectroscopy techniques", CUP J65C13001370001, Project No. GR-2010-2320665) and from the Cariplo Foundation under the project "New Frontiers in Plasmonic Nanosensing" (Grant No. 2011-0338).

Author Contributions

F. Gentile conceived the idea of writing a review of super-hydrophobic surfaces in the form of the 5 Ws and wrote the manuscript. M.L. Coluccio, T. Limongi, G. Perozziello and P. Candeloro discussed the results and commented on the manuscript, and helped in writing the manuscript. E. Di Fabrizio designed the experimental plan, supervised the work and wrote the manuscript.

Conflicts of Interest

The authors declare no conflict of interest.

References

1. Blossey, R. Self-cleaning surfaces—Virtual realities. *Nat. Mater.* **2003**, *2*, 301–306.
2. Lafuma, A.; Quéré, D. Superhydrophobic states. *Nat. Mater.* **2003**, *2*, 457–460.
3. Ueda, E.; Levkin, P.A. Emerging applications of superhydrophilic-superhydrophobic micropatterns. *Adv. Mater.* **2013**, *25*, 1234–1247.
4. Parton, K.; McKeown, K.R.; Coyne, R.; Diab, M.T.; Grishman, R.; Hakkani-Tür, D.; Harper, M.; Ji, H.; Ma, W.-Y.; Meyers, A.; *et al.* Who, What, When, Where, Why? Comparing Multiple Approaches to the Cross-Lingual 5W Task. In Proceedings of the Joint Conference of the 47th Annual Meeting of the ACL and the 4th International Joint Conference on Natural Language Processing of the AFNLP, Suntec, Singapone, 2–7 August 2009; pp. 423–431.
5. Gentile, F.; Ferrari, M.; Decuzzi, P. The transport of nanoparticles in blood vessels: The Effect of vessel permeability and blood rheology. *Ann. Biomed. Eng.* **2008**, *2*, 254–261.
6. Liotta, L.A.; Ferrari, M.; Petricoin, E. Clinical proteomics: Written in blood. *Nature* **2003**, *425*, 905.
7. Sheehan, P.E.; Whitman, L.J. Detection limits for nanoscale biosensors. *Nano Lett.* **2005**, *4*, 803–807.
8. Peng, K.; Zhu, J. Morphological selection of electroless metal deposits on silicon in aqueous fluoride solution. *Electrochim. Acta* **2004**, *49*, 2563–2568.
9. McHale, G.; Shirtcliffe, N.; Newton, M. Super-hydrophobic and super-wetting surfaces: Analytical potential? *Analyst* **2004**, *129*, 284–287.
10. Hancock, M.J.; He, J.; Mano, J.F.; Khademhosseini, A. Surface-tension-driven gradient generation in a fluid stripe for bench-top and microwell applications. *Small* **2011**, *7*, 892–901.
11. Liu, Z.; Lee, H.; Xiong, Y.; Sun, C.; Zhang, X. Far-field optical hyperlens magnifying sub-diffraction-limited objects. *Science* **2007**, *315*, 1686.

12. Wang, C.; Yao, T.; Wu, J.; Ma, C.; Fan, Z.; Wang, Z.; Cheng, Y.; Lin, Q.; Yang, B. Facile approach in fabricating superhydrophobic and superoleophilic surface for water and oil mixture separation. *ACS Appl. Mater. Interfaces* **2009**, *1*, 2613–2617.
13. Genzera, J.; Efimenkoa, K. Recent developments in superhydrophobic surfaces and their relevance to marine fouling: A review. *Biofouling: J. Bioadhes. Biofilm Res.* **2006**, *22*, 339–360.
14. Zhang, X.; Shi, F.; Niu, J.; Jiang, Y.; Wang, Z. Superhydrophobic surfaces: From structural control to functional application. *J. Mater. Chem.* **2008**, *18*, 621–633.
15. Accardo, A.; Gentile, F.; Mecarini, F.; de Angelis, F.; Burghamme, M.; di Fabrizio, E.; Riekel, C. Micro- and nano-patterned super-hydrophobic PMMA surfaces with high optical and X-ray transparency fabricated by optical lithography and plasma etching. *Langmuir* **2010**, *26*, 15057–15064.
16. Hook, A.L.; Voelcker, N.H.; Thissen, H. Patterned and switchable surfaces for biomolecular manipulation. *Acta Biomater.* **2009**, *5*, 2350–2370.
17. Na, K.; Jung, J.; Shin, B.; Hyun, J. Micropatterning of cell-repellent polymer on a glass substrate for the highly resolved virus microarray. *Langmuir* **2006**, *22*, 10889–10892.
18. Pauloehrl, T.; Delaittre, G.; Bruns, M.; Meisler, M.; Borner, H.G.; Bastmeyer, M.; Barner-Kowollik, C. (Bio)Molecular surface patterning by phototriggered oxime ligation. *Angew. Chem. Int. Ed.* **2012**, *51*, 9181–9184.
19. Limongi, T.; Cesca, F.; Gentile, F.; Marotta, R.; Ruffilli, R.; Barberis, A.; Maschio, M.D.; Petrini, E.M.; Santoriello, S.; Benfenati, F.; *et al*. Nanostructured superhydrophobic substrates trigger the development of 3D neuronal networks. *Small* **2013**, *9*, 402–412.
20. Gentile, F.; Moretti, M.; Limongi, T.; Falqui, A.; Bertoni, G.; Scarpellini, A.; Santoriello, S.; Maragliano, L.; Zaccaria, R.P.; di Fabrizio, E. Direct Imaging of DNA Fibers: The Visage of Double Helix. *Nano Lett.* **2012**, *12*, 6453–6458.
21. Geyer, F.L.; Ueda, E.; Liebel, U.; Grau, N.; Levkin, P.A. Superhydrophobic–superhydrophilic micropatterning: Towards genome-on-a-chip cell microarrays. *Angew. Chem. Int. Ed.* **2011**, *50*, 8424–8427.
22. De Angelis, F.; Gentile, F.; Mecarini, F.; Das, G.; Moretti, M.; Candeloro, P.; Coluccio, M.; Cojoc, G.; Accardo, A.; Liberale, C.; *et al*. Breaking the diffusion limit with super hydrophobic delivery of few molecules to plasmonic nanofocusing structures. *Nat. Photonics* **2011**, *5*, 682–687.
23. Gentile, F.; Coluccio, M.; Coppedè, N.; Mecarini, F.; Das, G.; Liberale, C.; Tirinato, L.; Leoncini, M.; Perozziello, G.; Candeloro, P.; *et al*. Superhydrophobic surfaces as smart platforms for the analysis of diluted biological solutions. *ACS Appl. Mater. Interfaces* **2012**, *4*, 3213–3224.
24. Gentile, F.; Tirinato, L.; Battista, E.; Causa, F.; Liberale, C.; di Fabrizio, E.; Decuzzi, P. Cells preferentially grow on moderately rough substrates. *Biomaterials* **2010**, *31*, 7205–7212.
25. Yiu, H.H.P.; Wright, P.A. Enzymes supported on ordered mesoporous solids: A special case of an inorganic-organic hybrid. *J. Mater. Chem.* **2005**, *15*, 3690–3700.
26. Sel, O.; Sallard, S.; Brezesinski, T.; Rathousky, J.; Dunphy, D.R.; Collord, A.; Smarsly, B.M. Periodically ordered meso and macroporous SiO_2 thin films and their induced electrochemical activity as a function of pore hierarchy. *Adv. Funct. Mater.* **2007**, *17*, 3241–3250.

27. Ananta, J.S.; Godin, B.; Sethi, R.; Moriggi, L.; Liu, X.; Serda, R.E.; Krishnamurthy, R.; Muthupillai, R.; Bolskar, R.D.; Helm, L.; *et al.* Geometrical confinement of gadolinium-based contrast agents in nanoporous particles enhances T1 contrast. *Nat. Nanotechnol.* **2010**, *5*, 815–821.
28. Decuzzi, P.; Gentile, F.; Granaldi, A.; Curcio, A.; Causa, F.; Indolfi, C.; Netti, P.; Ferrari, M. Flow chamber analysis of size effects in the adhesion of spherical particles. *Int. J. Nanomed.* **2007**, *2*, 689–696.
29. Gaspari, M.; Cheng, M.M.-C.; Terracciano, R.; Liu, X.; Nijdam, J.; Vaccari, L.; di Fabrizio, E.; Petricoin, E.F.; Liotta, L.A.; Cuda, G.; *et al.* Nanoporous surfaces as harvesting agents for mass spectrometric analysis of peptides in human plasma. *J. Proteome Res.* **2006**, *5*, 1261–1266.
30. Hu, Y.; Bouamrani, A.; Tasciotti, E.; Li, L.; Liu, X.; Ferrari, M. Tailoring of the nanotexture of mesoporous silica films and their functionalized derivatives for selectively harvesting low molecular weight protein. *ACS Nano* **2010**, *4*, 439–451.
31. Terracciano, R.; Gaspari, M.; Testa, F.; Pasqua, L.; Tagliaferri, P.; Cheng, M.M.-C.; Nijdam, J.; Petricoin, E.F.; Liotta, L.A.; Cuda, G.; *et al.* Selective binding and enrichment for low-molecular weight biomarker molecules in human plasma after exposure to nanoporous silica particles. *Proteomics* **2006**, *6*, 3243–3250.
32. Gelderblom, H.; Bloemen, O.; Snoeijer, J.H. Stokes flow near the contact line of an evaporating drop. *J. Fluid Mech.* **2012**, *709*, 69–84.
33. Masoud, H.; Felske, J.D. Analytical solution of Stokes flow inside an evaporating sessile drop: Spherical and cylindrical cap shapes. *Phys. Fluids* **2009**, *21*, 042102; doi:10.1063/1.3112002.
34. Astier, Y.; Data, L.; Carney, R.P.; Stellacci, F.; Gentile, F.; di Fabrizio, E. Artificial surface-modified si3n4 nanopores for single surface-modified gold nanoparticle scanning. *Small* **2010**, *7*, 455–459.
35. Lee, P.-H.; Helms, V.; Geyer, T. Coarse-grained Brownian dynamics simulations of protein translocation through nanopores. *J. Chem. Phys.* **2012**, *137*, 145105; doi:10.1063/1.4757265.
36. Yusko, E.C.; Johnson, J.M.; Majd, S.; Prangkio, P.; Rollings, R.C.; Li, J.; Yang, J.; Mayer, M. Controlling protein translocation through nanopores with bio-inspired fluid walls. *Nat. Nanotechnol.* **2011**, *6*, 253–260.
37. Balu, B.; Berry, A.; Patel, K.; Breedveld, V.; Hess, D. Directional mobility and adhesion of water drops on patterned superhydrophobic surfaces. *J. Adhes. Sci. Technol.* **2011**, *25*, 627–642.
38. Balu, B.; Berry, A.D.; Hess, D.W.; Breedveld, V. Patterning of superhydrophobic paper to control the mobility of micro-liter drops for two-dimensional lab-on-paper applications. *Lab Chip* **2009**, *9*, 3066–3075.
39. Li, L.; Breedveld, V.; Hess, D.W. Hysteresis controlled water droplet splitting on superhydrophobic paper. *Colloid Polym. Sci.* **2013**, *291*, 417–426.
40. Gentile, F.; Coluccio, M.; Toma, A.; Rondanina, E.; Leoncini, M.; de Angelis, F.; Das, G.; Dorigoni, C.; Candeloro, P.; di Fabrizio, E. Electroless deposition dynamics of silver nanoparticles clusters: A diffusion limited aggregation (DLA) approach *Microelectron. Eng.* **2012**, *98*, 359–362.
41. Gentile, F.; Accardo, A.; Coluccio, M.; Asande, M.; Cojoc, G.; Mecarini, F.; Das, G.; Liberale, C.; de Angelis, F.; Candeloro, P.; *et al.* NanoPorous- micropatterned- superhydrophobic surfaces as harvesting agents for low molecolar weight molecules. *Microelectron. Eng.* **2011**, *88*, 1749–1752.

42. Gentile, F.; Battista, E.; Accardo, A.; Coluccio, M.; Asande, M.; Perozziello, G.; Das, G.; Liberale, C.; de Angelis, F.; Candeloro, P.; *et al.* Fractal structure can explain the increased hydrophobicity of nanoporous silicon films. *Microelectron. Eng.* **2011**, *88*, 2537–2540.
43. Nosonovsky, M.; Bhushan, B. Biomimetic superhydrophobic surfaces: A multiscale approach. *Nano Lett.* **2007**, *7*, 2633–2637.
44. Nosonovsky, M.; Bhushan, B. Hierarchical roughness optimization for biomimetic superhydrophobic surfaces. *Ultramicroscopy* **2007**, *107*, 969–979.
45. Patankar, N. Mimicking the lotus effect: Influence of double roughness structures and slender pillars. *Langmuir* **2004**, *20*, 8209–8213.
46. Gentile, F.; Coluccio, M.; Accardo, A.; Marinaro, G.; Rondanina, E.; Santoriello, S.; Marras, S.; Das, G.; Tirinato, L.; Perozziello, G.; *et al.* Tailored Ag nanoparticles/nanoporous superhydrophobic surfaces hybrid devices for the detection of single molecule. *Microelectron. Eng.* **2012**, *97*, 349–352.
47. Gentile, F.; Coluccio, M.L.; Rondanina, E.; Santoriello, S.; di Mascolo, D.; Accardo, A.; Francardi, M.; de Angelis, F.; Candeloroa, P.; di Fabrizio, E. Non periodic patterning of super-hydrophobic surfaces for the manipulation of few molecules. *Microelectron. Eng.* **2013**, *111*, 272–276.
48. Medasani, B.; Park, Y.H.; Vasiliev, I. Theoretical study of the surface energy, stress, and lattice contraction of silver nanoparticles. *Phys. Rev. B* **2007**, *75*, 235436–235436.
49. Cassie, A.B.D.; Baxter, S. Wettability of porous surfaces. *Trans. Faraday Soc.* **1944**, *40*, 546–551.
50. Gentile, F.; Rocca, R.L.; Marinaro, G.; Nicastri, A.; Toma, A.; Paonessa, F.; Cojoc, G.; Liberale, C.; Benfenati, F.; di Fabrizio, E.; *et al.* Differential cell adhesion on mesoporous silicon substrates. *ACS Appl. Mater. Interfaces* **2012**, *4*, 2903–2911.
51. Barnes, W.L.; Dereux, A.; Ebbesen, T.W. Surface plasmon subwavelength optics. *Nature* **2003**, *424*, 824–830.
52. Kneipp, K. Surface-enhanced raman scattering. *Phys. Today* **2007**, *60*, 40–47.
53. Das, G.; Mecarini, F.; Gentile, F.; Candeloro, P.; Liberale, C.; de Angelis, F.; Kumar, H.; Cuda, G.; di Fabrizio, E. Nano-patterned SERS substrate: Application for protein analysis *vs.* temperature. *Biosens. Bioelectron.* **2009**, *24*, 1693–1699.
54. Aravind, P.; Rendell, R.; Metiu, H. A new geometry for field enhancement in surface-enhanced spectroscopy. *Chem. Phys. Lett.* **1982**, *85*, 396–403.
55. Coluccio, M.L.; Gentile, F.; Francardi, M.; Perozziello, G.; Malara, N.; Candeloro, P.; di Fabrizio, E. Electroless deposition and nanolithography can control the formation of materials at the nano-scale for plasmonic applications. *Sensors* **2014**, *14*, 6056–6083.
56. Inoue, M.; Ohtaka, K. Surface enhanced raman scattering by metal spheres. I. cluster effect. *J. Phys. Soc. Jpn.* **1983**, *52*, 3853–3864.
57. Phillips, C.L.; Anderson, J.A.; Huber, G.; Glotzer, S.C. Optimal filling of shapes. *Phys. Rev. Lett.* **2012**, *108*, 198304.
58. Damasceno, P.F.; Engel, M.; Glotzer, S.C. Predictive self-assembly of polyhedra into complex structures. *Science* **2012**, *337*, 453.
59. Glotzer, S. Nanotechnology: Shape matters. *Nature* **2012**, *481*, 450–452.

60. Xia, Y.; Nguyen, T.D.; Yang, M.; Lee, B.; Santos, A.; Podsiadlo, P.; Tang, Z.; Glotzer, S.C.; Kotov, N.A. Self-assembly of self-limiting monodisperse supraparticles from polydisperse nanoparticles. *Nat. Nanotechnol.* **2011**, *6*, 580–587.
61. Garcia-Vidal, F.; Pendry, J. Collective theory of surface enhanced raman scattering. *Phys. Rev. Lett.* **1996**, *77*, 1163–1166.
62. Hao, E.; Schatz, G. Electromagnetic fields around silver nanoparticles and dimmers. *J. Chem. Phys.* **2004**, *120*, 357–367.
63. Metiu, H. Surface enhanced spectroscopy. *Prog. Surf. Sci.* **1984**, *17*, 153–320.
64. Quinten, M. Local fields close to the surface of nanoparticles and aggregates of nanoparticles. *Appl. Phys. B: Lasers Opt.* **2001**, *73*, 245–255.
65. Xu, H.; Aizpurua, J.; Kall, M.; Apell, P. Electromagnetic contributions to single-molecule sensitivity in surface-enhanced Raman scattering. *Phys. Rev. E* **2000**, *62*, 4318–4324.
66. Xu, H.; Kall, M. Surface-plasmon-enhanced optical forces in silver nanoaggregates. *Phys. Rev. Lett.* **2002**, *89*, 246802.
67. Xu, H.; Kall, M. Polarization-dependent surface-enhanced raman spectroscopy of isolated silver nanoaggregates. *ChemPhyschem* **2003**, *4*, 1001–1005.
68. Babiaczyk, W.; Bonella, S.; Ciccotti, G.; Coluccio, M.; Gentile, F.; di Fabrizio, E. Silver self aggregation in a nanodevice for enhanced Raman spectroscopy: Experiments *vs.* simplified modeling via molecular dynamics. *Nanoscale* **2012**, *4*, 2362–2371.
69. Tao, A.; Sinsermsuksakul, P.; Yang, P. Polyhedral silver nanocrystals with distinct scattering signatures. *Angew. Chem. Int. Ed.* **2006**, *45*, 4597–4601.
70. Tao, A.R.; Habas, S.; Yang, P. Shape control of colloidal metal nanocrystals. *Small* **2008**, *4*, 310–325.
71. Tao, A.R.; Sinsermsuksakul, P.; Yang, P. Tunable plasmonic superlattices of silver nanocrystals. *Nat. Nanotechnol.* **2007**, *2*, 435–440.
72. Thaxton, C.S.; Elghanian, R.; Thomas, A.D.; Stoeva, S.I.; Lee, J.S.; Smith, N.D.; Schaeffer, A.J.; Klocker, H.; Horninger, W.; Bartsch, G.; *et al*. Nanoparticle-based bio-barcode assay redefines "undetectable" PSA and biochemical recurrence after radical prostatectomy. *Proc. Nat. Acad. Sci. USA* **2009**, *106*, 18437–18442.

MDPI AG
Klybeckstrasse 64
4057 Basel, Switzerland
Tel. +41 61 683 77 34
Fax +41 61 302 89 18
http://www.mdpi.com/

Micromachines Editorial Office
E-mail: micromachines@mdpi.com
http://www.mdpi.com/journal/micromachines

MDPI • Basel • Beijing • Wuhan
ISBN 978-3-03842-051-4
www.mdpi.com